

# **From Intermetallics to Intermetalloid Clusters**

## **Molecular Alloying of Aluminum and Gallium with Transition Metals**

Jana Weßing

Vollständiger Abdruck der von der Fakultät für Chemie der Technischen Universität München zur Erlangung des akademischen Grades eines

### **Doktors der Naturwissenschaften (Dr. rer. nat.)**

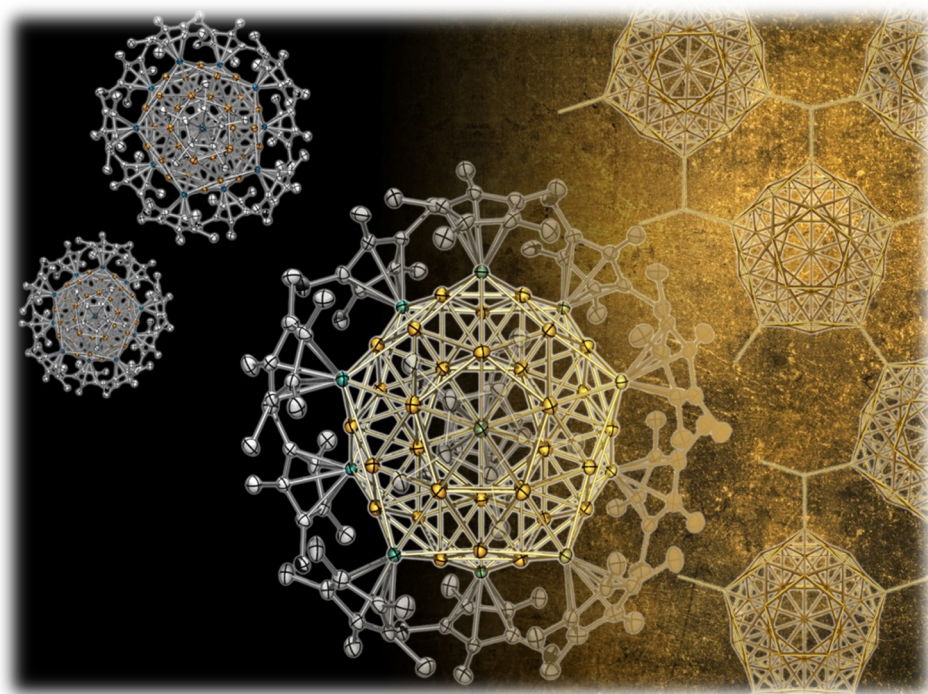
genehmigten Dissertation.

Vorsitzender: Prof. Dr. Thomas F. Fässler  
Prüfende der Dissertation: 1. Prof. Dr. Roland A. Fischer  
2. Prof. Dr. Jean-Yves Saillard  
3. Prof. Dr. Stefanie Dehnen

Die Dissertation wurde am 01.03.2018 bei der Technischen Universität München eingereicht und durch die Fakultät für Chemie am 30.04.2018 angenommen.

# FROM INTERMETALLICS TO INTERMETALLOID CLUSTERS

Molecular Alloying of Aluminum and Gallium with Transition Metals



**Dissertation**

Jana Weßing

Die vorliegende Arbeit wurde am Lehrstuhl für Anorganische Chemie II der Ruhr-Universität Bochum im Zeitraum von Januar 2014 bis März 2016, sowie am Lehrstuhl für Anorganische und Metallorganische Chemie der Technischen Universität München im Zeitraum von April 2016 bis März 2018 erstellt.

## Danksagung

In erster Linie gilt mein besonderer Dank

**Prof. Dr. rer. nat. Dr. phil. h.c. Roland A. Fischer**

für die Möglichkeit mich in den letzten Jahren in Ihrer fachlich, wie menschlich herausragenden Arbeitsgruppe verwirklichen zu können. Ihnen verdanke ich nicht nur ein faszinierendes wissenschaftliches Thema, das meine Aufmerksamkeit trotz diverser Tiefschläge im Labor wecken und kontinuierlich fesseln konnte, sondern vor Allem die Gelegenheit alte Strukturen zu verlassen und mich in allen Belangen an neuen Herausforderungen messen und weiterentwickeln zu können. Für Ihr mir dabei entgegengebrachtes Vertrauen und Ihre Unterstützung bin ich von Herzen dankbar.

Meiner Prüfungskommission danke ich für die bereitwillige und freundliche Übernahme des Koreferats.

Wie so oft haben auch an der Entstehung dieser Arbeit zahlreiche Menschen, bewusst oder unbewusst, mitgewirkt, deren Name nicht auf dem Deckblatt stehen. Ihnen allen gebührt an dieser Stelle ein großes **DANKESCHÖN**.

**Inbesondere möchte ich mich bedanken bei... / I am particularly thankful to...**

... **Dr. Christian Gemel** für seine stets offene Tür bei wissenschaftlichen Fragestellung aller Art, sowie seinen Enthusiasmus und die Kreativität in der Herangehensweise an eben diese.

... **Dr. Mariusz Molon** und **Dr. Ganesamoorthy Chelladurai**, dafür mein Interesse an der Organometallchemie nicht geweckt, aber befeuert zu haben und mir den Einstieg in die OM-Gruppe, sowie mein spannendes Promotionsthema geebnet zu haben.

... **Prof. Dr. Jean-Yves Saillard, Dr. Samia Kahlal and Dr. Rémi Marchal** for the quantum chemical calculations on  $[\text{Cu}_{43}(\text{AlCp}^*)_{12}]$  which finally round the topic off, and greatly contributed to this great chapter.

... **Prof. Olivier Cador** and **Prof. Birgit Weber**, as well as **Christoph Göbel** for magnetic susceptibility measurements.

... **Dr. Rüdiger Seidl** und **Dr. Alexander Pöthig**, sowie den "Pöthig Boys" **Philipp Altmann** und **Christian Jandl** für die Unterstützung bei kleineren und größeren kristallographischen Problemfällen, insbesondere jedoch für die Vertiefung meiner ursprünglich doch recht rudimentären Kristallographiekenntnisse.

... **Dr. Gabriele Raudaschl-Sieber** für das Ermöglichen teils recht kurzfristiger Festkörper-NMR-spektroskopischer Messungen und ihr Engagement insbesondere bei schwierigen Proben.

... **Julius Hornung** für quantenchemische Rechnungen und LIFDI-MS Messungen.

... **Tim Kratky** für abenteuerliche XPS Messungen unter Luftausschluss und die hilfsbereite Unterstützung bei deren Interpretation.

... den Bochumer und Münchener "Office Ladies" **Sabine Pankau, Jacinta Essling, Gabriele Querbach** und **Martin Schellerer**. Ohne eure stete Ansprechbarkeit sowie Unterstützung in allen administrativen Dingen wäre der Uni-Alltag bedeutend aufreibender. Danke dass ihr, viel zu oft unbemerkt, dafür sorgt, dass alles läuft.

... den hilfsbereiten Technikern und Angestellten von RUB und TUM, **Uschi Herrmann, Martin Gartmann, Jürgen Kudermann, Maria Weindl, Peter Richter, Tobias Kubo,**



**Rodica Dumitrescu, Ulrike Ammari, Petra Ankenbauer, Bircan Dilki und Carmen Hessner**, für ihre tatkräftige Unterstützung im (Labor-)Alltag und bei den Analysen.

... den Studenten, die ich im Rahmen von Forschungspraktika oder Abschlussarbeiten begleiten durfte: **Niklas Cibura, Patrick Wonner, Maximilian Göckeler, Cindy Beyer, Okan Yildirim, Jonas Bruckmoser, Alexander Engel und Christian Jakob**. Ganz besonderer Dank gebührt **Lena Staiger** für ihren Einsatz in der Masterarbeit und natürlich die weltbeste Ni(cdt) Synthese.

... dem **Fonds der Chemischen Industrie** und der **Gesellschaft Deutscher Chemiker** für die finanzielle Unterstützung in Form eines Promotionsstipendiums und Reisebeihilfe.

Abseits von allem Organisatorischem und Fachlichem ist doch das Menschliche ausschlaggebend für den Spaß an der Arbeit. Daher möchte ich von ganzem Herzen den lieben Menschen danken, die das Leben in und außerhalb des Laboralltags so lebenswert gemacht haben, mit denen ich kleine Erfolge feiern und große Misserfolge schönreden (oder unter den Tisch trinken) konnte, oder die Uni auch mal ganz vergessen durfte.

Daher danke ich **meinen Kollegen der jetzigen AMC**, insbesondere **Alexander Pöthig, Philipp Altmann, Suttipong Wannapiboon, David Mayer, Anna-Lisa Semrau, Konstantin Epp, Julius Hornung, Lena Staiger, Kathrin Kratzl und Pia Vervoorts** für eine großartige, teils ausgelassene Gruppenatmosphäre, den Zusammenhalt und diverse gemeinsame Aktivitäten in und außerhalb der Uni. Unserer OM-Gruppen "Mutti" **Kerstin Freitag** möchte ich für das Auffangen nach dem Umzug nach München danken, und für die geteilte Leidenschaft für schweißtreibende Wandertouren. Den **Mitgliedern der MolKat Arbeitsgruppe** bin ich außerdem dankbar für die herzliche Aufnahme an der TUM.

Mein herzlicher Dank gilt weiterhin meinen **Bochumer Leidensgenossen der ehemaligen ACII**, vor Allem aber weiten Teilen von Anjanas Kindergarten: **Alexander Sadlo, Stefan Cwik, Sarah Karle, Richard O'Donoghue, Jiyeon Kim und Daniel Peeters** für die gemeinsamen Kaffeepausen, die endlosen Abende im Bermudadreieck und Feierabendbier "vor vier". **Jiyeon Kim** und **Andreas Schneemann** bin ich dankbar für den "awesome roadtrip" durch Kanada und die USA im Anschluss an das ACS Fall Meeting 2015. **Clarissa Kroll** und **Jiyeon Kim** bin ich zudem dankbar für Korean BBQ und leider viel zu seltene "Girls Days". **Olesia Halbherr**, unserer ewigen Kaffeekönigin, danke ich von Herzen für ihre Freundschaft auch außerhalb der Uni, insbesondere für die vielen Gespräche bei literweise Kaffee, die gemeinsamen Spieleabende und dafür, dass du mich an deiner kleinen Familie teilhaben lässt. Furthermore, I am thankful to **Marissa Kerrigan**, whom I know "live" for just a couple of weeks, for her decision to cross the Atlantic for a research stay with the CVD group, and the resulting honest friendship.

Meinen Geschwistern **Dennis, Fabian und Benjamin** und meinen Eltern **Beate und Karsten Weßing** danke ich von Herzen für die liebevolle Unterstützung in den letzten Jahren, das aufgebrachte Verständnis in jeder Lebenssituation, das Auffangen in etwaigen kleineren und größeren Krisen und das hartnäckige Nachbohren, wann ich denn mal langsam fertig werde. Daran, dass es jetzt endlich soweit ist habt ihr einen wesentlichen Anteil!

Zu guter Letzt gilt mein zutiefster Dank **Daniel Peeters**. Ich kann wohl kaum in Worte fassen, wie unendlich dankbar ich dir bin, für deine großartige Unterstützung, deine unerschütterliche Gelassenheit und deine Fähigkeit mir immer wieder das Wesentliche vor Augen zu führen, vor Allem aber für deinen Humor und die kostbare gemeinsame Zeit. Ohne deinen Rückhalt in und außerhalb der Uni, die Aufmunterung an rabenschwarzen Tagen und dein uneingeschränktes Verständnis gerade in der letzten Zeit wäre diese Arbeit vermutlich nie so weit gekommen.

*“Curiosity is a descending stair...  
that leads to only who-knows-where.”*

— Jasper Fforde

## I Table of contents

I	Table of contents .....	i
II	List of figures .....	iv
III	List of schemes .....	viii
IV	List of tables .....	ix
V	List of abbreviations .....	x
1	MOTIVATION.....	1
2	SUMMARY.....	4
3	INTERMETALLIC PHASES AND CLUSTERS.....	12
1.1	Intermetallic phases .....	13
1.2	Top-Down! From solid-state phases to molecular clusters .....	29
1.3	Metal cluster compounds.....	32
1.4	Bottom-up! From a molecular view to the solid state .....	51
1.5	Hume-Rothery phase inspired molecular chemistry .....	55
4	RESULTS AND DISCUSSION.....	70
4.1	Laying the groundwork - $[\text{Cu}_6(\text{AlCp}^*)_6\text{H}_4]$ as an archetypical metalloid TM/E cluster .....	71
4.1.1	Excursus: Electron counting for the model compounds <b>1</b> and <b>2</b> - An effective tool to assess observed reactivities.....	74
4.1.2	Identifying new routines - Assessing the suitability of XPS as a classical solid-state characterization technique for the characterization of <b>1</b> .....	75
4.1.3	Concluding remarks .....	79
4.2	The intermetalloid CuAl cluster $[\text{Cu}_43(\text{AlCp}^*)_{12}]$ ( <b>3</b> ), a rare example of a heterometallic open-shell superatom with a Mackay-type $\text{M}_{55}$ two-shell icosahedral structure .....	80
4.2.1	Introductory remarks.....	80
4.2.2	Synthesis of $[\text{Cu}_43(\text{AlCp}^*)_{12}]$ ( <b>3</b> ) .....	81
4.2.3	Structural analysis of $[\text{Cu}_43(\text{AlCp}^*)_{12}]$ ( <b>3</b> ).....	82
4.2.4	Spectroscopic characterization of $[\text{Cu}_43(\text{AlCp}^*)_{12}]$ ( <b>3</b> ).....	84
4.2.5	Theoretical investigations of $[\text{Cu}_43(\text{AlCp}^*)_{12}]$ ( <b>3</b> ) .....	85
4.2.6	Magnetic characterization of $[\text{Cu}_43(\text{AlCp}^*)_{12}]$ ( <b>3</b> ).....	87
4.2.7	Concluding remarks .....	89

4.3	[Au <sub>a</sub> (AlCp*) <sub>6</sub> H <sub>x</sub> ] ( <b>4</b> ), an all-AlCp* ligated Au cluster of unapparent nuclearity .....	91
4.3.1	Introductory remarks .....	91
4.3.2	Synthesis of [Au <sub>a</sub> (AlCp*) <sub>6</sub> H <sub>x</sub> ] ( <b>4</b> ).....	91
4.3.3	Structural analysis of [Au <sub>a</sub> (AlCp*) <sub>6</sub> H <sub>x</sub> ] ( <b>4</b> ) .....	92
4.3.4	Rationalizing potential core geometries of [Au <sub>a</sub> (AlCp*) <sub>6</sub> H <sub>x</sub> ] ( <b>4</b> ) - available means to assess unapparent molecular structures.....	94
4.3.5	Theoretical investigations of a hypothetical [Au <sub>7</sub> (AlCp*) <sub>6</sub> H <sub>x</sub> ].....	96
4.3.6	Spectroscopic characterization of [Au <sub>a</sub> (AlCp*) <sub>6</sub> H <sub>x</sub> ] ( <b>4</b> ).....	98
4.3.7	Concluding remarks .....	100
4.4	[(Cp*Co) <sub>3</sub> Ga <sub>6</sub> (Cp* <sub>3</sub> Co <sub>3</sub> (μ <sub>3</sub> -CH))H <sub>x</sub> ] ( <b>6</b> ), an "inverse" TM/E cluster featuring a naked Ga <sub>6</sub> core inside a CoCp* shell.....	102
4.4.1	Introductory remarks .....	102
4.4.2	Synthesis of [(Cp*Co) <sub>3</sub> Ga <sub>6</sub> (Cp* <sub>3</sub> Co <sub>3</sub> (μ <sub>3</sub> -CH))H <sub>x</sub> ] ( <b>6</b> ) .....	102
4.4.3	Structural characterization of [(Cp*Co) <sub>3</sub> Ga <sub>6</sub> (Cp* <sub>3</sub> Co <sub>3</sub> (μ <sub>3</sub> -CH))H <sub>x</sub> ] ( <b>6</b> ) .....	103
4.4.4	Rationalizing the structure of [(Cp*Co) <sub>3</sub> Ga <sub>6</sub> (Cp* <sub>3</sub> Co <sub>3</sub> (μ <sub>3</sub> -CH))H <sub>x</sub> ] ( <b>6</b> ) on the basis of electron counting principles - a hypothetical excursus.....	105
4.4.5	Spectroscopic characterization of [(Cp*Co) <sub>3</sub> Ga <sub>6</sub> (Cp* <sub>3</sub> Co <sub>3</sub> (μ <sub>3</sub> -CH))H <sub>x</sub> ] ( <b>6</b> ).....	106
4.4.6	XPS spectroscopic characterization of [(Cp*Co) <sub>3</sub> Ga <sub>6</sub> (Cp* <sub>3</sub> Co <sub>3</sub> (μ <sub>3</sub> -CH))H <sub>x</sub> ] ( <b>6</b> ).....	110
4.4.7	Reactivity of [Co <sub>6</sub> H <sub>8</sub> (P <sup>i</sup> Pr <sub>3</sub> ) <sub>6</sub> ] towards AlCp* .....	112
4.4.8	Concluding remarks .....	113
4.5	The intermetalloid NiGa cluster [Ni <sub>8</sub> (GaCp*) <sub>6</sub> ] ( <b>8</b> ) - a structural chameleon bearing resemblance to binary NiGa phases .....	115
4.5.1	Introductory remarks .....	115
4.5.2	Synthesis and characterization of [Ni(cdt)(GaCp*)] ( <b>7</b> ).....	116
4.5.3	Synthesis of [Ni <sub>8</sub> (GaCp*) <sub>6</sub> ] ( <b>8</b> ).....	118
4.5.4	Spectroscopic characterization of [Ni <sub>8</sub> (GaCp*) <sub>6</sub> ] ( <b>8</b> ) .....	119
4.5.5	Structural characterization of [Ni <sub>8</sub> (GaCp*) <sub>6</sub> ] ( <b>8</b> ).....	122
4.5.6	Relation of [Ni <sub>8</sub> (GaCp*) <sub>6</sub> ] ( <b>8</b> ) to the solid state structures of binary NiGa phases .....	124
4.5.7	Theoretical investigations on the structure of [Ni <sub>8</sub> (GaCp*) <sub>6</sub> ] ( <b>8</b> ).....	125
4.5.8	Concluding remarks .....	127

4.6	Diverse Reactivity of ECp* towards low-coordinate transition metal amides [TM(bt <sub>s</sub> a) <sub>2</sub> ] (TM = Mn, Fe, Co, Zn): Insertion, Cp* transfer, and orthometalation.....	128
4.6.1	Introductory remarks.....	128
4.6.2	Synthesis and characterization of [Cp*Co(μ-H)(Al(κ <sub>2</sub> -(CH <sub>2</sub> SiMe <sub>2</sub> )NSiMe <sub>3</sub> )(bt <sub>s</sub> a))] ( <b>9</b> ) .....	128
4.6.3	Synthesis and characterization of [(Cp*Ga)Co(bt <sub>s</sub> a) <sub>2</sub> ] ( <b>10</b> ) and [(Cp*Ga) <sub>2</sub> Fe(bt <sub>s</sub> a) <sub>2</sub> ] ( <b>11</b> ).....	133
4.6.4	Synthesis and characterization of [(Zn(Al(η <sup>2</sup> -Cp*)(bt <sub>s</sub> a)) <sub>2</sub> ] ( <b>12</b> ) .....	137
4.6.5	Synthesis and characterization of [(Co(μ-H) <sub>4</sub> (Al(η <sup>2</sup> -Cp*)(bt <sub>s</sub> a)) <sub>2</sub> ] ( <b>13</b> ).....	139
4.6.6	Preliminary reactivity studies - attempts at the initiation of cluster growth by selective ligand abstraction.....	143
4.6.7	Concluding remarks .....	147
5	OUTLOOK.....	155
6	EXPERIMENTAL PART .....	158
6.1	Materials and Methods .....	159
6.2	Synthetic procedures .....	165
6.3	Supplementary data .....	174
6.3.1	Computational details .....	174
6.3.2	Crystallographic data .....	179
6.3.3	Synthetic procedure and molecular structure of [Ga <sub>10</sub> (CoCp*) <sub>6</sub> ].....	184
6.3.3	Supplementary analytical data .....	186
7	APPENDIX .....	I
	Active participation on scientific conferences.....	II
	Publications in scientific journals.....	III
	Curriculum Vitae .....	IV

## II List of figures

Figure 1.	Overview of the synthesized compounds <b>1-6</b> .	8
Figure 2.	Overview of the synthesized compounds <b>7-12</b> .	9
Figure 3.	Overview of the synthesized compounds <b>13-15</b> .	10
Figure 4.	Periodic table depicting the classification of metals into alkaline and earth alkaline metals (A1, green), transition metals (A2, violet), post-transition metals (B1, pink) and semi-metals (B2, blue).	13
Figure 5.	Classification of binary intermetallic systems based on the combination of A1, A2, B1, or B2 metals.	14
Figure 6.	Adapted van-Arken Ketelaar triangle showing the correlation of chosen intermetallics with their inherent bond natures.	15
Figure 7.	a) Crystal structure of the Laves phase $\text{MgCu}_2$ . b) and c) Frank Kasper polyhedra in $\text{MgCu}_2$ .	17
Figure 8.	Crystal structure of the prototypical Zintl phase $\text{NaTl}$ .	18
Figure 9.	Crystal structures of the Zintl phases a) $\text{K}_4\text{Sn}_9$ and b) $\text{KGa}_3$ .	20
Figure 10.	Phase sequences as observed in the copper-zinc system at room temperature.	21
Figure 11.	(a) The extended zone scheme of the electron band structure of a one-dimensional chain of atoms. (b) The corresponding X-ray diffraction pattern.	24
Figure 12.	Penrose tiling composed of a narrow and a wide diamond tile.	25
Figure 13.	Successive shell structures of atoms in the atomic clusters found in rhombic triacontahedral-type, Mackay icosahedral-type, and Tsai-type quasicrystals and their approximants.	26
Figure 14.	Molecular structures of exemplary intermetallic germanium clusters demonstrating the rich coordination chemistry of Zintl ions towards transition metals centers.	30
Figure 15.	Schematic presentation of a conventionalized spherical ligand-stabilized cluster.	33
Figure 16.	Molecular structures of exemplary metalloid transition metal clusters.	34
Figure 17.	Molecular structures of the metalloid group 13 clusters $[\text{Al}_{50}\text{Cp}^*_{12}]$ (a) and $[\text{Ga}_{84}(\text{N}(\text{SiMe}_3)_2)_{20}]^{4+}$ (b).	35

Figure 18.	Schematic presentation of the Pd <sub>59</sub> core of [Pd <sub>59</sub> (CO) <sub>32</sub> (PMe <sub>3</sub> ) <sub>21</sub> ] with highlighted relevant polyhedra for the cluster valence electron counting rules.....	38
Figure 19.	Central structural motif of the molecular structure of [Ga <sub>22</sub> (Si <sup>†</sup> Bu <sub>3</sub> ) <sub>8</sub> ]. .....	41
Figure 20.	Molecular structure of [Au <sub>102</sub> (p-MBA) <sub>44</sub> ].....	43
Figure 21.	Projected local density of states (PLDOS) for [Al <sub>50</sub> Cp* <sub>12</sub> ]. .....	44
Figure 22.	a) Molecular structure of [Pd <sub>3</sub> (μ-SPh) <sub>3</sub> (PPh <sub>3</sub> ) <sub>3</sub> ] <sup>+</sup> in the solid state. b) Selected molecular orbitals of [Pd <sub>3</sub> (μ-SPh) <sub>3</sub> (PPh <sub>3</sub> ) <sub>3</sub> ] <sup>+</sup> which contribute to delocalized 3c2e bonding between the three Pd atoms. ....	46
Figure 23.	Selected examples of metal analogues of σ-aromatic [H <sub>3</sub> ] <sup>+</sup> and π-aromatic C <sub>3</sub> H <sub>3</sub> <sup>+</sup> .....	47
Figure 24.	a) Molecular orbital pattern of ZnI <sub>8</sub> as derived from s-atom orbital contributions. b) Molecular structure of the cluster (Zn <sub>8</sub> (HL) <sub>4</sub> (L <sub>8</sub> ) <sup>12-</sup> . c) Electron localization function (ELF) calculations performed for ZnI <sub>8</sub> with depiction of the isosurface of the cube (a), and top views of the triangular (b), square (c) and diagonal rectangular (d) surfaces. ....	50
Figure 25.	a) Molecular structures of [AlCp*] <sub>4</sub> , [Al <sub>20</sub> Cp* <sub>8</sub> Br <sub>10</sub> ] and [Al <sub>50</sub> Cp* <sub>12</sub> ], and optimized structure of [Al <sub>8</sub> Cp*] <sub>4</sub> . b) Exemplary calculated energy diagram (kJ·mol <sup>-1</sup> ) for the disproportionation of [AlR] <sub>4</sub> (Al = Cp, Cp*) to elemental Al and AlR <sub>3</sub> via intermediate formation of [Al <sub>50</sub> R <sub>12</sub> ].....	52
Figure 26.	Molecular structures of the homoleptic, ECp*-stabilized palladium clusters a) [Pd <sub>2</sub> (GaCp*) <sub>5</sub> ], b) [Pd <sub>3</sub> (AlCp*) <sub>6</sub> ] and c) [Pd <sub>3</sub> (InCp*) <sub>8</sub> ]. .....	56
Figure 27.	Comparative illustration of two alternative ways to rationalize the structure of [Pd <sub>3</sub> (AlCp*) <sub>6</sub> ]. .....	57
Figure 28.	Molecular structures of [Mo(ZnCp*) <sub>3</sub> (ZnMe) <sub>9</sub> ] (MoZn <sub>12</sub> ), [Ru(ZnCp*) <sub>4</sub> (ZnMe) <sub>6</sub> ] (RuZn <sub>10</sub> ), [Rh(ZnCp*) <sub>3</sub> (ZnMe) <sub>6</sub> ] (RhZn <sub>9</sub> ) and [Pd(ZnCp*) <sub>4</sub> (ZnMe) <sub>4</sub> ] (PdZn <sub>8</sub> ) with highlighted Zn <sub>n</sub> coordination polyhedra.....	59
Figure 29.	Molecular structure of [(CuCNtBu) <sub>4</sub> (ZnCp*) <sub>4</sub> ] and nested polyhedra of γ-brass. ....	60
Figure 30.	Molecular structure of [(GaCp*) <sub>4</sub> (H)Ru(μ-Ga)Ru(H) <sub>2</sub> (GaCp*) <sub>3</sub> ].....	61
Figure 31.	One disorder site of the molecular structure of <b>1</b> , and nested polyhedra found in the solid-state structures of γ-brass.....	72



Figure 32.	Detailed view on the development of the aromatic PPh <sub>3</sub> signals during <i>in situ</i> <sup>1</sup> H NMR spectroscopic measurements of the reaction mixture of [PPh <sub>3</sub> CuH] <sub>6</sub> and AlCp* in C <sub>6</sub> D <sub>6</sub> .....	73
Figure 33.	Conceptual scheme of the hydride transfer reaction occurring upon coordination of one molecule of benzonitrile to <b>1</b> . ....	74
Figure 34.	XPS survey spectrum of [Cu <sub>6</sub> (AlCp*) <sub>6</sub> H <sub>4</sub> ] ( <b>1</b> ). ....	76
Figure 35.	High resolution scans of a) the Cu L <sub>3</sub> M <sub>45</sub> M <sub>45</sub> Auger peak and b) the Cu2p binding energy peaks of [Cu <sub>6</sub> (AlCp*) <sub>6</sub> H <sub>4</sub> ] ( <b>1</b> ). c) High resolution scan of the overlapping Cu3s and Al2s photoelectron peaks.....	78
Figure 36.	Molecular structure of [Cu <sub>43</sub> (AlCp*) <sub>12</sub> ] ( <b>3</b> ) in the solid state and multiple-shell structure of its intermetallic Cu <sub>43</sub> Al <sub>12</sub> kernel. ....	83
Figure 37.	Kohn-Sham orbital diagrams of [Cu <sub>43</sub> ] <sup>3+</sup> and [Cu <sub>43</sub> Al <sub>12</sub> Cp <sub>12</sub> ] <sup>3+</sup> in I <sub>h</sub> symmetry. ....	86
Figure 38.	Temperature-dependent magnetic measurements of <b>3</b> given as χ <sub>M</sub> vs. T plot (red) and 1/χ <sub>M</sub> vs. T plot (black; left), and field-dependent magnetic susceptibility measurements at 10, 50 and 200 K (right). ....	87
Figure 39.	a) Temperature-dependent magnetic susceptibility measurements of <b>3</b> given as χ <sub>M</sub> vs. T plot (red) and 1/χ <sub>M</sub> vs. T plot (black; left), corrected by contributions from ferromagnetic impurities. b) χ <sub>M</sub> T vs. T plot with the calculated value for S = 3/2 under assumption of g = 2 (red). ....	89
Figure 40.	Severely disordered molecular structure of [Au <sub>a</sub> (AlCp*) <sub>6</sub> H <sub>x</sub> ] ( <b>4</b> ; a = 6,7) in the solid state. ....	93
Figure 41.	Core geometries of literature-reported hexa-, hepta- and octanuclear gold-phosphine cluster compounds.....	95
Figure 42.	Different views on the optimized molecular structure of [Au <sub>7</sub> (AlMe <sub>6</sub> )H] ( <b>4'</b> ).....	97
Figure 43.	Molecular structure of [Au <sub>8</sub> (AlCp*) <sub>5</sub> (IMes)H <sub>x</sub> ] ( <b>5</b> ) in the solid state. ....	101
Figure 44.	Molecular structure of [(Cp*Co) <sub>3</sub> Ga <sub>6</sub> (Cp* <sub>3</sub> Co <sub>3</sub> (μ <sub>3</sub> -CH))H <sub>x</sub> ] ( <b>6</b> ) in the solid state.....	104
Figure 45.	Comparison of the disordered [Ga <sub>6</sub> Co <sub>6</sub> ] kernel of <b>6</b> with the nido-cluster structure expected according to Wade Mingos rules. ....	105
Figure 46.	Experimental and calculated isotopic distribution patterns of the molecular ion peak [MI] <sup>+</sup> of [(Cp*Co) <sub>3</sub> Ga <sub>6</sub> (Cp* <sub>3</sub> Co <sub>3</sub> (μ <sub>3</sub> -CH))H <sub>x</sub> ] ( <b>6</b> ) and its fragment [MI-CH] <sup>+</sup> .....	108

Figure 47.	XPS survey spectrum of [(Cp*Co) <sub>3</sub> Ga <sub>6</sub> (Cp* <sub>3</sub> Co <sub>3</sub> (μ <sub>3</sub> -CH))H <sub>x</sub> ] ( <b>6</b> ).....	110
Figure 48.	High resolution scans of a) the Ga L <sub>3</sub> M <sub>45</sub> M <sub>45</sub> Auger peak and b) the Ga2p binding energy peaks of [(Cp*Co) <sub>3</sub> Ga <sub>6</sub> (Cp* <sub>3</sub> Co <sub>3</sub> (μ <sub>3</sub> -CH))H <sub>x</sub> ] ( <b>6</b> ). c) and d) High resolution scan of the deconvoluted Co2p <sub>3/2</sub> peak with two and three contributions, respectively. ....	111
Figure 49.	Molecular structure of [Ni(cdt)(GaCp*)] ( <b>7</b> ) in the solid state. ....	118
Figure 50.	Experimental and calculated isotopic distribution patterns of the ..... molecular ion peaks [MI+Na] <sup>+</sup> and [MI+Li] <sup>+</sup> of [Ni <sub>8</sub> (GaCp*) <sub>6</sub> ] ( <b>8</b> ). ....	121
Figure 51.	Severely disordered molecular structure of [Ni <sub>8</sub> (GaCp*) <sub>6</sub> ] ( <b>8</b> ) in the solid state.....	122
Figure 52.	Calculation of the expected cve count of a hexacapped Ni <sub>8</sub> cube on the basis of the cluster fusion principle.....	124
Figure 53.	Crystal structures of the binary NiGa phases a) β-NiGa and b) Ni <sub>3</sub> Ga <sub>7</sub> . ....	125
Figure 54.	Optimized molecular structure of [Ni <sub>8</sub> (GaMe) <sub>6</sub> ] ( <b>8'</b> ).....	126
Figure 55.	Molecular structure of [Cp*Co(μ-H)(Al(κ <sup>2</sup> -(CH <sub>2</sub> SiMe <sub>2</sub> )NSiMe <sub>3</sub> )(btsa))] ( <b>9</b> ) in the solid state. ....	131
Figure 56.	Molecular structures of [(Cp*Ga)Co(btsa) <sub>2</sub> ] ( <b>10</b> ) and [(Cp*Ga) <sub>2</sub> Fe(btsa) <sub>2</sub> ] ( <b>11</b> ) in the solid state. ....	135
Figure 57.	Molecular structure of [(Zn(Al(η <sup>2</sup> -Cp*)(btsa)) <sub>2</sub> ] ( <b>12</b> ) in the solid state. ....	138
Figure 58.	Molecular structure of [(Co(μ-H) <sub>4</sub> (Al(η <sup>2</sup> -Cp*)(btsa)) <sub>2</sub> ] ( <b>13</b> ) in the solid state. ....	141
Figure 59.	Molecular structure of [(Cp*Co) <sub>2</sub> (μ-AlNMe <sub>3</sub> ) <sub>2</sub> H <sub>4</sub> ] ( <b>14</b> ) in the solid state. ....	144
Figure 60.	Molecular structure of [Al <sub>3</sub> H <sub>4</sub> (μ-H)(κ <sup>2</sup> -(CH <sub>2</sub> SiMe <sub>2</sub> )NSiMe <sub>3</sub> ) <sub>2</sub> ] ( <b>15</b> ) in the solid. ....	146
Figure 61.	Preparative steps in the synthesis of [Cu <sub>43</sub> (AlCp*) <sub>12</sub> ] ( <b>3</b> ).....	166
Figure 62.	Analytically pure [Cu <sub>43</sub> (AlCp*) <sub>12</sub> ] ( <b>3</b> ) in a sealed quartz glas ampulla. ....	167
Figure 63.	Different views on the optimized molecular structure of [Au <sub>8</sub> (AlMe <sub>6</sub> )] ( <b>4''</b> ).....	178
Figure 64.	Molecular structure of [Ga <sub>10</sub> (CoCp*) <sub>6</sub> ] in the solid state. ....	184

## III List of schemes

Scheme 1.	Synthesis of $[\text{Cu}_6(\text{AlCp}^*)_6\text{H}_4]$ ( <b>1</b> ) and $[\text{Cu}_6(\text{AlCp}^*)_6\text{H}_3(\text{N}=\text{CHPh})]$ ( <b>2</b> ).....	71
Scheme 2.	Synthesis of $[\text{Cu}_{43}(\text{AlCp}^*)_{12}]$ ( <b>3</b> ).....	81
Scheme 3.	Synthesis of $[\text{Au}_a(\text{AlCp}^*)_6\text{H}_x]$ ( <b>4</b> , $a = 6, 7$ ).....	91
Scheme 4.	Synthesis of $[(\text{Cp}^*\text{Co})_3\text{Ga}_6(\text{Cp}^*_3\text{Co}_3(\mu_3\text{-CH}))\text{H}_x]$ ( <b>6</b> ).....	102
Scheme 5.	Synthesis of $[\text{Ni}(\text{GaCp}^*)(\text{cdt})]$ ( <b>7</b> ).....	116
Scheme 6.	Synthesis of $[\text{Ni}_8(\text{GaCp}^*)_6]$ ( <b>8</b> ) <i>via</i> $[\text{Ni}(\text{cdt})(\text{GaCp}^*)]$ ( <b>7</b> , path A) or direct reaction of $[\text{Ni}(\text{cdt})]$ and $\text{GaCp}^*$ (path B).....	119
Scheme 7.	Synthesis of $[\text{Cp}^*\text{Co}(\mu\text{-H})(\text{Al}(\kappa^2\text{-}(\text{CH}_2\text{SiMe}_2)\text{NSiMe}_3)(\text{btsa}))]$ ( <b>9</b> ).....	129
Scheme 8.	One possible mechanistic pathway leading to the formation of the unusual [2.1.0] metallacycle as observed in compound <b>9</b> .....	130
Scheme 9.	Synthesis of $[(\text{Cp}^*\text{Ga})\text{Co}(\text{btsa})_2]$ ( <b>10</b> ) and $[(\text{Cp}^*\text{Ga})_2\text{Fe}(\text{btsa})_2]$ ( <b>11</b> ).....	134
Scheme 10.	Synthesis of $[(\text{Zn}(\text{Al}(\eta^2\text{-Cp}^*)(\text{btsa}))_2)]$ ( <b>12</b> ).....	137
Scheme 11.	Synthesis of $[(\text{Co}(\mu\text{-H})_4(\text{Al}(\eta^2\text{-Cp}^*)(\text{btsa}))_2)]$ ( <b>13</b> ).....	140
Scheme 12.	Reactivity of $[\text{Cp}^*\text{Co}(\mu\text{-H})(\text{Al}(\kappa^2\text{-}(\text{CH}_2\text{SiMe}_2)\text{NSiMe}_3)(\text{btsa}))]$ ( <b>9</b> ) towards hydride-bearing reducing agents.....	143
Scheme 13.	Reactivity of $\text{ECp}^*$ ( $\text{E} = \text{Al}, \text{Ga}$ ) towards $[\text{TM}(\text{btsa})_2]$ ( $\text{TM} = \text{Mn}, \text{Fe}, \text{Co}, \text{Zn}$ ).....	148

## IV List of tables

Table 1.	Overview of the synthesized compounds <b>1-15</b> with classification and chapter.....	11
Table 2.	Examples of intermetallic compounds with Laves phase structures.....	16
Table 3.	Valencies for some first row transition metals, as determined by a) Raynor and b) Mizutani <i>et al.</i> ....	27
Table 4.	Cve counts for representative metal cluster geometries.....	37
Table 5.	Correlation of sep counts and deltahedral structures of electron-deficient main group and transition metal clusters according to Wade-Mingos rules.....	39
Table 6.	Auger parameters of <b>1</b> , and selected Cu(0) and Cu(I) compounds.....	78
Table 7.	Shell-closing electron counts for $[\text{Au}_a(\text{AlCp}^*)_6\text{H}_x]$ in dependency of a and x.....	96
Table 8.	Experimental and calculated molecular weight distributions for $[\text{Au}_a(\text{AlCp}^*)_6\text{H}_x]$ ( <b>4</b> ) .....	99
Table 9.	Masses detected during LIFDI MS measurements of <b>8</b> and assigned fragments with calculated m/z values.....	121
Table 10.	Cartesian coordinates of the optimized structure of $[\text{Au}_7(\text{AlMe})_6\text{H}]$ ( <b>4'</b> ).....	175
Table 11.	Cartesian coordinates of the optimized structure of $[\text{Au}_8(\text{AlMe})_6]$ ( <b>4''</b> ).....	176
Table 12.	Cartesian coordinates of the optimized structure of $[\text{Ni}_8(\text{GaMe}_3)_6]$ ( <b>8'</b> ).....	177
Table 13.	Crystallographic data of compounds <b>1-3</b> . ....	179
Table 14.	Crystallographic data of compounds <b>4-6</b> . ....	180
Table 15.	Crystallographic data of compounds <b>7-9</b> . ....	181
Table 16.	Crystallographic data of compounds <b>10-12</b> . ....	182
Table 17.	Crystallographic data of compounds <b>13-15</b> . ....	183
Table 17.	Crystallographic data of $[\text{Ga}_{10}(\text{CoCp}^*)_6]$ .....	185

## V List of abbreviations

AAS	atom absorption spectrometry
AIM	atoms-in-molecules
AO	atomic orbital
ATR	attenuated total reflection
BAr <sub>4</sub> <sup>F</sup>	tetrakis[3,5-bis(trifluoromethyl)phenyl]borate
btsa	bis(trimethylsilyl)amide
Bz	Brillouin zone
cdt	1,5,9-cyclododecatriene
centr	centroid
CMA	complex metallic alloy
CN	coordination number
cod	1,5-cyclooctadien
Cp	cyclopentadienyl
Cp*	1,2,3,4,5-pentamethylcyclopentadienyl
crypt	cryptand
cve	cluster valence electron
ddp	2-((2,6-diisopropylphenyl)amino)-4-((2,6-diisopropylphenyl)imino)-2-pentene
DFT	density functional theory
Dipp	2,6-diisopropylphenyl
dmsO	dimethyl sulfoxide
DOS	density of states
dppe	1,2-bis(diphenylphosphino)ethane
DQC	decagonal quasicrystal
dvds	1,3-divinyl-(1,1,3,3-tetramethyl)disiloxane
e/a	valence electron concentration
ELF	electron localization function
EN	electronegativity
EPR	electron paramagnetic resonance
Et	ethyl
EXAFS	extended X-ray absorption fine structure
Fs	Fermi surface
FT	Fourier transform
HOMO	highest occupied molecular orbital
HR	Hume-Rothery
HR-TEM	high resolution transmission electron microscopy
ICSD	inorganic crystal structure database
IMes	1,3-bis(2,4,6-trimethylphenyl)imidazol-2-ylidene
IPr	1,3-bis(2,6-diisopropylphenyl)imidazol-2-ylidene
<sup>i</sup> Pr	<i>iso</i> -propyl
IQC	icosahedral quasicrystal
IR	infrared
L	ligand
LIFDI-MS	liquid injection field desorption ionization mass spectrometry

LUMO	lowest unoccupied molecular orbital
M	metal atom
m/z	mass-to-charge ratio
MALDI-MS	matrix assisted laser desorption/ionization mass spectrometry
MAS	magic angle spinning
mes	mesitylene
Me	methyl
MI	Mackay icosahedral
MI <sup>+</sup>	molecular cation
MO	molecular orbital
MOCVD	metalorganic chemical vapour deposition
NacNac <sup>Dipp</sup>	1,3-bis(2,6-diisopropylphenyl)-diketimine
NBO	natural bond orbital
NHC	N-heterocyclic carbene
NICS	nucleus independent chemical shift
NMR	nuclear magnetic resonance
OEt <sub>2</sub>	diethyl ether
OTf	trifluoromethanesulfonate
PDF	pair distribution function
Ph	phenyl
phen	1,10-phenanthroline
pin	pinacol
PLDOS	projected local density of states
<i>p</i> -MBA	<i>para</i> -mercaptobenzoic acid
ppm	parts per million
prisman <sub>d</sub>	$\pi$ -prisman <sub>d</sub> , 4,10,15-(1,4)tribenzena-1,7-diazabicyclo[5.5.5]heptadecaphane
PSEPT	polyhedral skeleton electron pair theory
PXRD	powder X-ray diffraction
py	pyridine
QC	quasicrystal
sep	skeleton electron pair
SORI-CAD	sustained off-resonance irradiation collision-activated dissociation
SQUID	superconducting quantum interference device
<sup>t</sup> Bu	<i>tert</i> -butyl
THF	tetrahydrofuran
TIP	temperature independent paramagnetism
TM	transition metal atom
TOF	time of flight
VE	valence electron
VEC	valence electron concentration
XANES	X-ray absorption near edge structure
XPS	X-ray photoelectron spectroscopy
XRD	X-ray diffraction

# 1 MOTIVATION

From times immemorial, metal alloys, like the prototypical bronze or brass, have been used for decorative and functional purposes. Their oftentimes superior properties with regards to the pure metals originate from synergistic effects between their constituents, resulting in extraordinary physical, but also chemical properties which can be largely altered by fine-tuning of the delicate interplay of their underlying chemical composition, stoichiometry, and structure.<sup>1-3</sup> Taking into consideration the pre-dominant abundance of metallic elements in the periodic table, and the resulting manifold combinations thereof, we as coordination and organometallic molecular chemists cannot help but simply stand in awe of the unprecedented physical and chemical diversity of accessible alloy phases and distinct intermetallic compounds whose compositional and structural complexity is almost impossible to grasp on the basis of our own concepts of chemical bonding largely confined to the molecular space. However, if we do not allow ourselves to be overwhelmed by the vastness of this unacquainted discipline but rather understand it as an incentive, the aesthetic beauty of the underlying atomic lattices and their conceptual description as entangled polyhedral structures may at least serve as an heuristic source of inspiration for the molecular scientist. Given that many of the polyhedral structural motifs of intermetallics are reminiscent of the deltahedral arrangements frequently observed in molecular, atom-precise cluster chemistry, *why should it not be possible to transfer the riches of this intermetallic solid-state chemistry onto the molecular level? And which novel phenomena might we observe upon doing so?*

This general, motivational concept of (inter)metallic phase-inspired molecular chemistry is certainly not unheard-of, and precedence for the overall feasibility of this venture, meaning the stabilization of structural motifs from extended solid phases in discrete molecules, is provided by the exemplary chemistry of Zintl ions which are directly extracted "top-down" from binary Zintl phases *via* their dissolution in suitable solvents, like liquid ammonia, ethylenediamine or N,N-dimethylformamide.<sup>4</sup> Likewise, first steps approaching the extended metallic state from a "bottom-up" perspective have been undertaken with the soft, wet-chemical syntheses of increasingly large, atom-precise metalloid clusters from organometallic precursors. With regards to intermetallic phases, such as the brass-like Hume-Rothery phases, however, the discrepancy between heterometallic, molecular complexes, and the extended solid state is large, and very little is known on the space "in between". The just emerging field of ligand-stabilized intermetalloid clusters  $[M^1_a M^2_b \dots](L)_n$  ( $a + b + \dots \gg n$ ) that teeter on the brink of classical molecular chemistry and nanomaterials is, as we will see later, largely restricted to systems of the noble metals, whereas "molecular alloying" of increasingly dissimilar metals is much less investigated, if not unknown for many metal combinations. Inspiring representatives demonstrating the generally feasible synthetic access towards ligand-stabilized assemblies of homometallic non-noble, earth-abundant metals include an impressive array of large metalloid aluminium and gallium clusters reported by Schnöckel, Schnepf and co-workers.<sup>5, 6</sup> Only recently, Fischer *et al.* added zinc to the family of base metals forming such metalloid cluster compounds, when they succeeded in the isolation of



atom-precise organometallic Zn clusters  $[\text{Zn}_a](\text{L})_n$  ( $a = 8-10$ ,  $\text{L} = \text{Cp}^*$ ,  $\text{Me}$ ,  ${}^t\text{BuNC}$ ) whose chemistry was further connected to the goal of synthesizing Hume-Rothery-type  $[\text{Cu}_a\text{Zn}_b](\text{L})_n$  clusters, called "nanobrass".<sup>7</sup> A first success of the latter was reported in 2014 with the 8-electron closed-shell superatom complex  $[\text{Cu}_4\text{Zn}_4](\text{Cp}^*)_4(\text{CN}{}^t\text{Bu})_4$ , which features a star-tetrahedral  $\text{M}_8$  core mimicking a structural cut-out of  $\gamma$ -brass,  $\text{Cu}_5\text{Zn}_8$ .<sup>8</sup>

Motivated in this manner, the declared objective of this thesis was the exploration of novel synthetic pathways towards (ideally all-hydrocarbon) ligand-protected, atom-precise cluster compounds featuring combinations of d-block metals with the early p-block metals aluminium or gallium, as a means to transport the structural and compositional variety of extended Hume-Rothery intermetallics to the confined dimensions of the molecular level. Based on the reactivity and coordination chemistry of the carbenoid  $\text{ECp}^*$  ligand ( $\text{E} = \text{Al}$ ,  $\text{Ga}$ ,  $\text{Cp}^* = \text{pentamethylcyclopentadienyl}$ ), synthetic approaches and organo-transition metal building blocks were evaluated for the preparation of these novel molecular alloys. Herein, the overarching goal was the identification of repetitive patterns in their formation that can be merged into more generally applicable concepts for intermetalloid cluster synthesis. Thus obtained Hume-Rothery-type TM/E clusters of the general formula  $[\text{TM}_a\text{E}_b](\text{L})_n$  ( $\text{L} = \text{Cp}^*$ ,  $\text{H}$ ) were objected to a first assessment of structural characteristics and bonding situations with regards to their unique placing between molecular complexes and nanomaterials, as well as their potential role as well-defined molecular models of their macroscopic parent materials.

## References

1. R. Pöttgen, D. Johrendt, *Intermetallics - Synthesis, Structure, Function*, DeGruyter, Berlin/Boston, **2014**.
2. G. Sauthoff, *Intermetallics*, Wiley-VCH, Weinheim, **1995**.
3. R. Ferro, A. Saccone, *Intermetallic Chemistry*, Pergamon Materials Science, Elsevier, Amsterdam, **2008**.
4. S. Scharfe, F. Kraus, S. Stegmaier, A. Schier, T. F. Fässler, *Angew. Chem. Int. Ed.* **2011**, 50 (16), 3630-3670.
5. A. Schnepf, H. Schnöckel, *Angew. Chem. Int. Ed.* **2002**, 41 (19), 3532-3554.
6. H. Schnöckel, A. Schnepf. In *The Group 13 Metals Aluminium, Gallium, Indium and Thallium: Chemical Patterns and Peculiarities*; John Wiley & Sons, Ltd, **2011**, pp 402-487.
7. H. Banh, K. Dilchert, C. Schulz, C. Gemel, R. W. Seidel, R. Gautier, S. Kahlal, J.-Y. Saillard, R. A. Fischer, *Angew. Chem.* **2016**, 128 (10), 3344-3349.
8. K. Freitag, H. Banh, C. Gemel, R. W. Seidel, S. Kahlal, J.-Y. Saillard, R. A. Fischer, *Chem. Commun.* **2014**, 50 (63), 8681-8684.

## 2 SUMMARY

Motivated and inspired by the conceptual understanding of intermetallic group 13/transition metal clusters as replica of the structural and compositional diversity of Hume-Rothery phases within the confined dimensions of the molecular level, this thesis sought to identify and substantiate synthetic concepts for the formation of atom-precise TM/E cluster compounds approaching the (inter-)metalloid size regime. Herein, the multifunctional nature of organo group 13 species, particularly AlCp\* and GaCp\*, as versatile reducing agents, coordinating ligands for low-valent transition metal centres in complexes and clusters, and finally as a source for zero valent Al or Ga metal for cluster core formation, served altogether as a pivotal motif in the conceptual design of conceivable reaction pathways. While success or failure of the many explorative reactions investigated were largely unpredictable at the beginning of this venture, the results presented in this thesis substantiate first proof-of-concepts: The discussed compounds **1-15** (Figure 1-3; Table 1) represent an initial set of accordingly synthesized study cases, and include new and unprecedented metal-atom rich TM/E clusters as well as low-nuclearity coordination compounds as potential intermediates on the reaction pathway towards larger assemblies.

**Synthetic concepts and reaction pathways.** While the fundamental potential of the redox-active ECp\* ligand for the synthesis of novel intermetallic TM/E cluster compounds becomes particularly evident when taking into account the facile formation of related homometalloid clusters *via* reductive coupling of organometallic metal (pseudo)halide complexes in the presence of reducing agents, like potassium graphite or sodium borohydride, the synthetic access towards oligo- or polynuclear clusters  $[TM_aE_b](Cp^*)_n$  with  $a + b \gg n$  is still challenging and far from predictable. This is not only attributed to the plethora of competing reaction pathways commonly associated with cluster forming reactions, but also to the versatile, and thus difficult to steer, chemical nature of the ECp\* ligand. Within this regards, leading research questions include: *When does the group 13 organyl serve as a stabilizing ligand only? When does it act as a sacrificial reducing agent? How to assess its tendency to undergo Cp\* transfer reactions? Which factors promote insertion or bond activation reactions?* First insights contributing to an understanding of underlying, decisive factors are provided with the herein presented library of novel metal atom-rich cluster compounds  $[TM_aE_b](Cp^*)_n(H)_x$  with Cu/Al, Au/Al, Co/Ga and Ni/Ga combinations. Sparked by initial studies affording the archetypical Hume-Rothery-type cluster  $[Cu_6(AlCp^*)_6H_4]$  (**1**) and its closely related derivative  $[Cu_6(AlCp^*)_6(NCHPh)H_3]$  (**2**), which were denoted molecular models for  $\gamma$ -brass like intermetallics and their catalytically-relevant surface processes, respectively, the herein stipulated decisive role of ancillary hydride ligands was further confirmed by the isolation of  $[Au_a(AlCp^*)_6H_x]$  (**4**,  $a = 6$  or  $7$ ) and  $[Au_8(AlCp^*)_5(IMes)H_x]$  (**5**) from the reactions of  $[(NHC)AuH]$  (NHC = IPr, IMes) with AlCp\*, as well as the formation of  $[(Cp^*Co)_3Ga_6(Cp^*_3Co_3(\mu^3-CH))H_x]$  (**6**) upon treatment of  $[(P^iPr_3)_6Co_6H_8]$  with GaCp\*. In all cases, the isolobal phosphine and NHC ligands pave the way for intermetallic bond formation due to their ready displacement by the stronger ECp\* ligand, whereas the ancillary

hydrides act as redox non-innocent spectator ligands effecting the reduction of the resulting intermetallic core by partial elimination of hydrogen. Furthermore, in the formation of **4** and **5**, the active involvement of hydride ligands in hydride bridge-mediated cluster assembly processes appears conceivable given the mononuclear nature of the gold precursor.

Evidence for the beneficial influence of directed ligand exchange processes at pre-assembled  $[\text{TM}_a](\text{L})_n(\text{H})_x$  building blocks for selective product formation is provided by the almost quantitative syntheses of **1** and **6** in contrast to modest yields observed for **4** and **5**. Reminiscent of the concept of ligand exchange induced cluster growth reactions at metalloids gold and copper clusters,<sup>9, 10</sup> the reaction of  $\text{ECp}^*$  with the above defined, all-labile-bound organo-transition metal building units appears to allow for a preservation of the oligonuclear transition metal core, thus limiting the number of potential side reactions. In contrast, the direct assembly of TM/E clusters from low-nuclearity precursors, like  $[(\text{NHC})\text{AuH}]$ , seems to involve an array of difficult to control, competitive reaction pathways, eventually leading to undesirable complex product distributions with overall low yields and limited reproducibility. The resulting extraordinary susceptibility to smallest changes in factors like the chemical nature and purity of precursors, ancillary ligands, solvents, surface-to-volume ratio of reaction vessels, reaction times and temperature, is impressively illustrated by the vulnerable synthesis of the remarkable and truly intermetalloid CuAl cluster  $[\text{Cu}_{43}(\text{AlCp}^*)_{12}]$  (**3**) from  $[\text{CuMes}]_5$  and  $\text{AlCp}^*$ . Here, the absence of hydride ligands or further reductants requires the monovalent  $\text{AlCp}^*$  to serve as both, stabilizing ligand and reducing agent, as evident from the side formation of substantial amounts of  $[\text{Cp}^*\text{AlMes}_2]$ . The potential involvement of small, pre-formed TM/E building units as "seeds" for a stepwise alloying process is suggested by the synthesis of the NiGa cluster  $[\text{Ni}_8(\text{GaCp}^*)_6]$  (**8**) from  $[\text{Ni}(\text{cdt})]$  and  $\text{GaCp}^*$  which was found to proceed *via in situ* formed, but isolable  $[\text{Ni}(\text{cdt})(\text{GaCp}^*)]$  (**7**). The 1:1 adduct **7** is readily obtained from the stoichiometric reaction of  $[\text{Ni}(\text{cdt})]$  and  $\text{GaCp}^*$ , and undergoes further reaction to **8** upon thermal treatment with a surplus amount of the  $\text{GaCp}^*$ , triggering cleavage of the labile cdt ligand. Preliminary attempts to transfer the thus implied concept of ligand removal-initiated cluster growth reactions at accordingly designed all-labile mononuclear complexes  $[\text{TM}_1\text{E}_b(\text{Cp}^*)_n(\text{btsa})_m]$  (**9-13**;  $n, m = 1, 2$ ) failed to provide the targeted high-nuclearity TM/E cluster compounds, but indicate the facile formation of highly reactive, coordinatively unsaturated fragments which tend to undergo subsequent assembly processes.

**Structure and Bonding.** Following the identification and evaluation of first, successful synthetic routes towards the herein presented metalloids TM/E cluster compounds, a preliminary assessment of their underlying structural characteristics and bonding situations revealed distinct features correlating to both, heterometallic molecular complexes as well as intermetallic nanoalloys, thus disclosing their unique standing between classical coordination compounds and nanomaterials. With exception of **6** whose unprecedented, "inverse" core structure comprises a naked  $\text{Ga}_6$  kernel stabilized by peripheral  $[\text{CoCp}^*]$  units, the molecular

structures of the obtained clusters reveal core-shell arrangements of all-ECp\*-ligated transition metal cores, which can in parts be correlated to the nested polyhedra of closely-related intermetallics. For instance, the truly intermetalloid  $[\text{Cu}_{43}(\text{AlCp}^*)_{12}]$  (**3**) adopts a Mackay-type two shell icosahedral structure which is frequently found in quasicrystalline materials of related compositions, whereas the still not fully elucidated structure of  $[\text{Ni}_8(\text{GaCp}^*)_6]$  (**8**) is distantly reminiscent of related NiGa phases. In line with this, at first sight purely geometrical approximation of the extended (inter-)metallic state, the rationalization of the observed cluster skeletons on the basis of established electronic concepts provides evidence for the progressive involvement of the peripheral group 13 metal atoms in internal cluster bonding, and thus for the development of delocalized bonding situations beyond the homometallic transition metal cores. While the molecular structure of **1** is adequately described as  $[\text{Cu}_6(\text{AlCp}^*)_6\text{H}_4]$  with AlCp\* acting as an external two-electron donating ligand on the basis of cve counting principles, cluster **8** is presumably better described as  $[\text{Ni}_8\text{Ga}_6](\text{Cp}^*)_6$ . Likewise, the cobalt-gallium core of **6** can be understood on the basis of a central  $[\text{Ga}_6\text{Co}_3]$  cluster according to Wade-Mingos rules. Going one step further, quantum chemical investigations of the unique electronic structure of the paramagnetic  $[\text{Cu}_{43}(\text{AlCp}^*)_{12}]$  (**3**) on the DFT level of theory unambiguously reveal the full involvement of all twelve aluminium atoms in internal cluster core bonding, affording a 67 electron open-shell superatom configuration of the  $[\text{Cu}_{43}\text{Al}_{12}]^{12+}$  kernel, whose *a priori* polyradicalar reactivity seems to be contained by the steric protection of the spherical Cp\* ligand capsule, only. Here, the close proximity of the somewhat "entangled" set of 1H, 3S and 2D jellium levels hosting the HOMO and the lowest unoccupied levels even prefigures the formation of a conduction band which was confirmed by independent magnetic measurements. Consequently, particularly the Cu/Al intermetalloid  $\text{M}_{55}$  cluster **3** substantiates the initial vision of this thesis in bridging the gap between complexes, clusters and the more extended nanophases in an exceptional manner: A rational, bottom-up wet-chemical organometallic building-block synthesis of Hume-Rothery inspired larger group 13/transition metal clusters is possible.

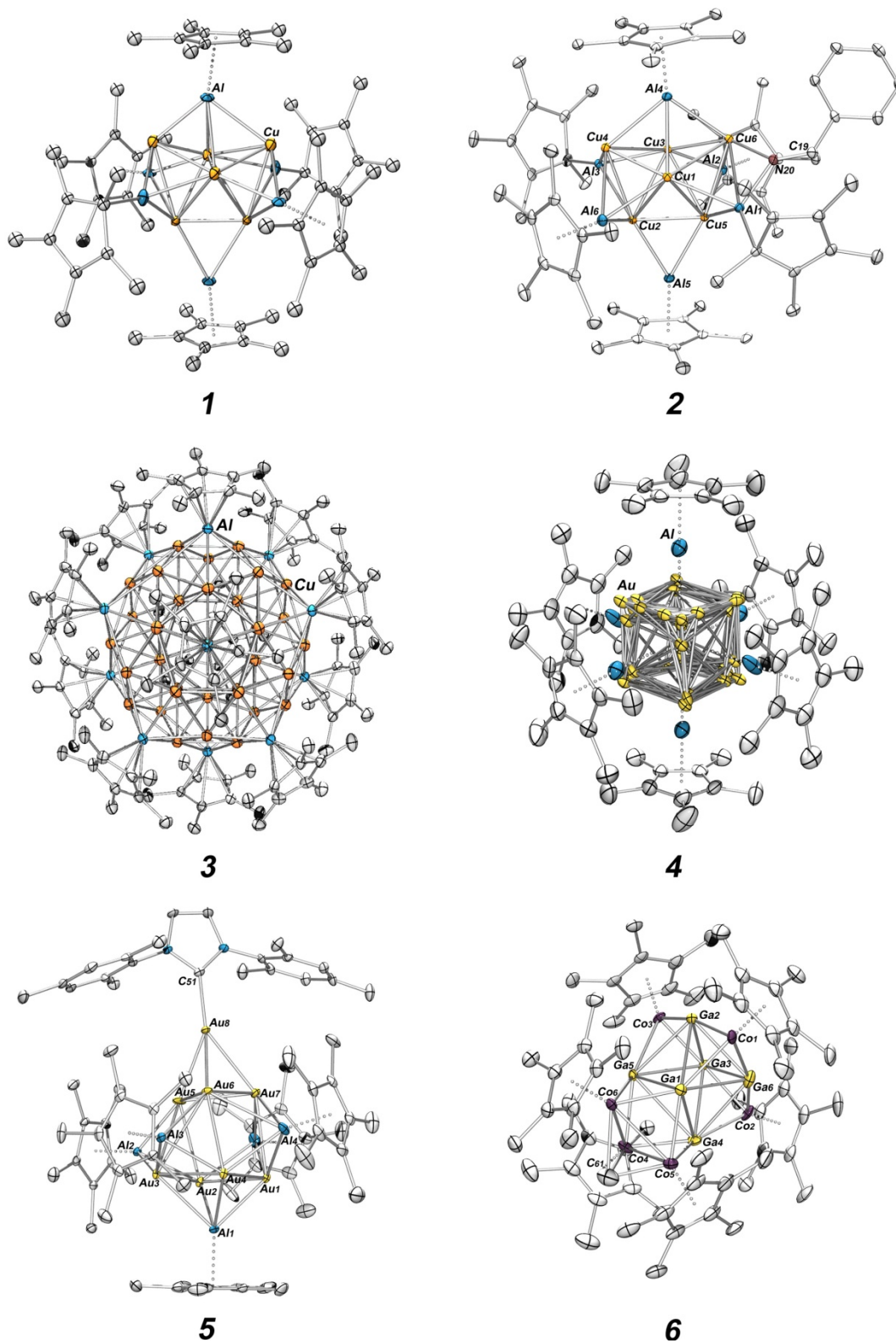


Figure 1. Overview of the synthesized compounds 1-6.

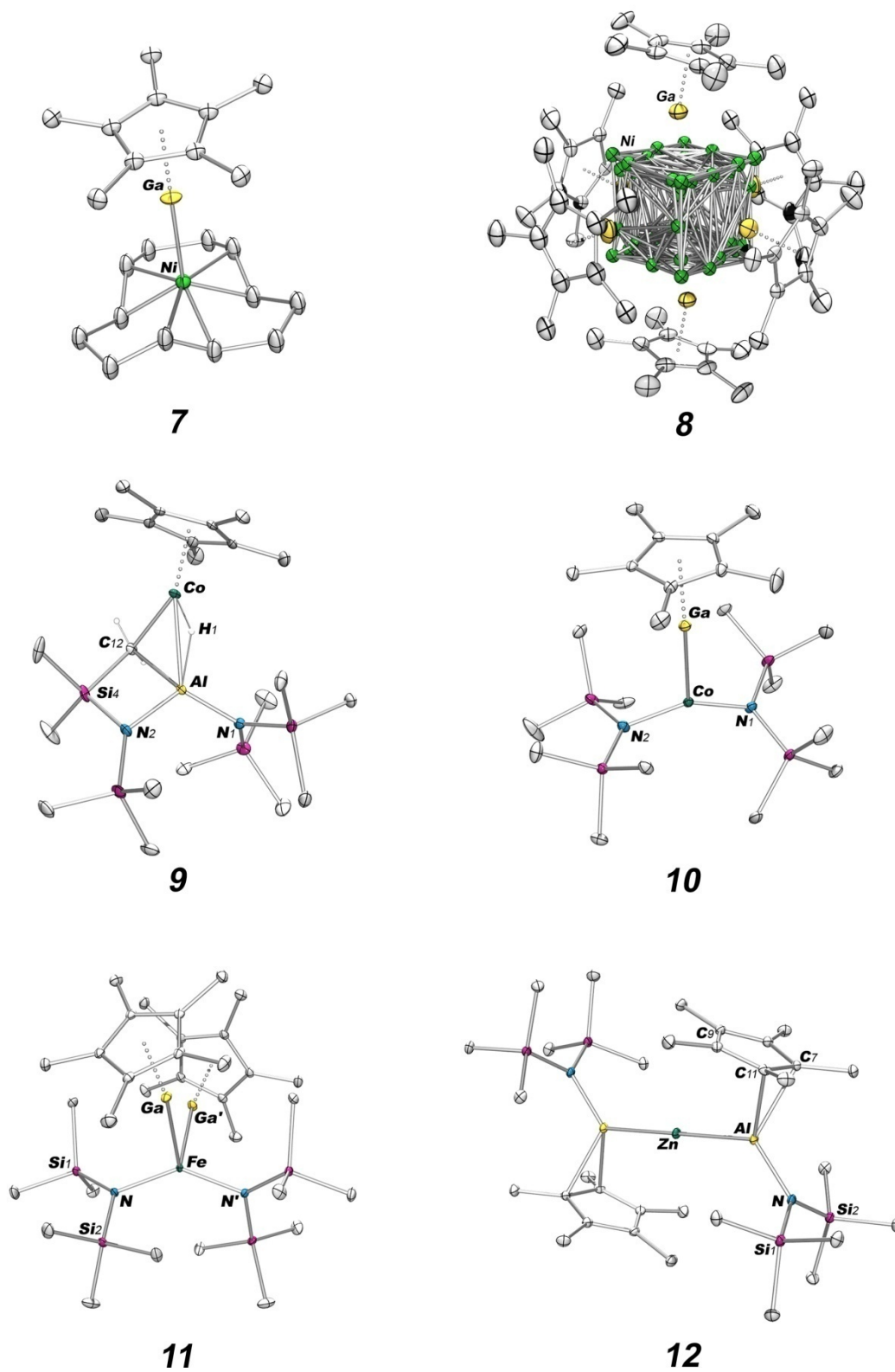


Figure 2. Overview of the synthesized compounds 7-12.

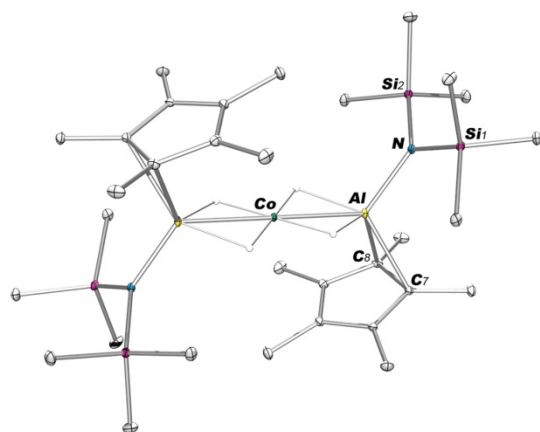
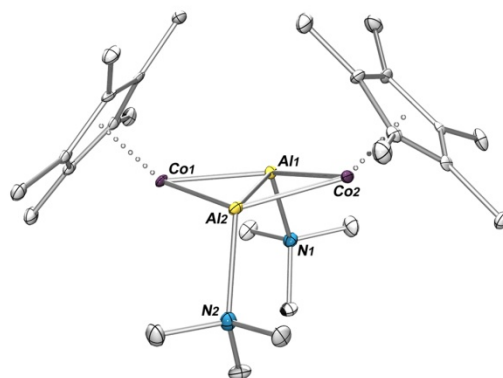
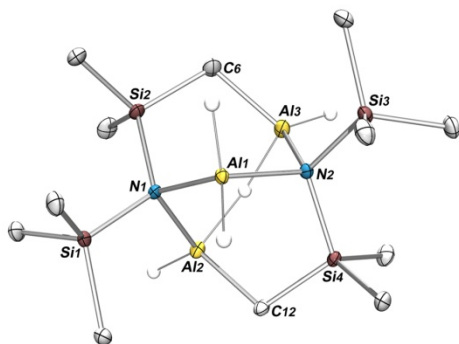
**13****14****15**

Figure 3. Overview of the synthesized compounds 13-15.



Table 1. Overview of the synthesized compounds **1-15** with classification and chapter.

No.	Compound	Classification	Ch.
1	$[\text{Cu}_6(\text{AlCp}^*)_6\text{H}_4]^{11}$	HR-type $[\text{Cu}_6\text{Al}_6]$ cluster	4.1
2	$[\text{Cu}_6(\text{AlCp}^*)_6(\text{N}=\text{CHPh})\text{H}_3]^{11}$	$[\text{Cu}_6\text{Al}_6]$ derivative, molecular semi-hydrogenation model	4.1
3	$[\text{Cu}_{43}(\text{AlCp}^*)_{12}]$	open-shell superatomic $[\text{Cu}_{43}\text{Al}_{12}]$ cluster with Mackay-type two-shell icosahedral structure	4.2
4	$[\text{Au}_a(\text{AlCp}^*)_6\text{H}_x]$	HR-type $[\text{Au}_a\text{Al}_6]$ cluster of unapparent nuclearity ( $a = 6$ or $7$ )	4.3
5	$[\text{Au}_8(\text{AlCp}^*)_5(\text{IMes})\text{H}_x]$	heteroleptic $[\text{Au}_8\text{Al}_6]$ cluster with ancillary NHC ligand, not fully characterized	4.3
6	$[(\text{Cp}^*\text{Co})_3\text{Ga}_6(\text{Cp}^*_3\text{Co}_3(\mu^3\text{-CH}))\text{H}_x]$	inverse HR-type $[\text{Co}_6\text{Ga}_6]$ cluster	4.4
7	$[\text{Ni}(\text{GaCp}^*)(\text{cdt})]$	1:1 $\text{GaCp}^*\text{-Ni}(\text{cdt})$ adduct	4.5
8	$[\text{Ni}_8(\text{GaCp}^*)_6]$	HR-type $[\text{Ni}_8\text{Ga}_6]$ cluster of unapparent core geometry	4.5
9	$[\text{Cp}^*\text{Co}(\mu\text{-H})(\text{Al}(\kappa^2\text{-(CH}_2\text{SiMe}_2)\text{NSiMe}_3)(\text{btsa}))]$	low-nuclearity $\text{CoAl}$ complex featuring $\text{Cp}^*$ transfer and $\text{btsa}$ activation	4.6
10	$[(\text{Cp}^*\text{Ga})\text{Co}(\text{btsa})_2]$	labile 1:1 $\text{GaCp}^*\text{-Co}(\text{btsa})_2$ adduct	4.6
11	$[(\text{Cp}^*\text{Ga})_2\text{Fe}(\text{btsa})_2]$	2:1 $\text{GaCp}^*\text{-Fe}(\text{btsa})_2$ adduct	4.6
12	$[(\text{Zn}(\text{Al}(\eta^2\text{-Cp}^*)(\text{btsa}))_2)]$	low-nuclearity $\text{ZnAl}_2$ complex with unsupported $\text{ZnAl}$ bonds	4.6
13	$[(\text{Co}(\mu\text{-H})_4(\text{Al}(\eta^2\text{-Cp}^*)(\text{btsa}))_2)]$	hydride-rich $\text{CoAl}_2$ insertion product	4.6
14	$[(\text{Cp}^*\text{Co})_2(\mu\text{-AlNMe}_3)_2\text{H}_4]$	butterfly- $\text{Co}_2\text{Al}_2$ cluster	4.6
15	$[\text{Al}_3\text{H}_4(\mu\text{-H})(\kappa^2\text{-(CH}_2\text{SiMe}_2)\text{NSiMe}_3)_2]$	trimeric alane side product, not fully characterized	4.6

## References

- R. Jin, C. Zeng, M. Zhou, Y. Chen, *Chem. Rev.* **2016**, 116 (18), 10346-10413.
- T.-A. D. Nguyen, Z. R. Jones, D. F. Leto, G. Wu, S. L. Scott, T. W. Hayton, *Chem. Mater.* **2016**, 28 (22), 8385-8390.
- C. Ganesamoorthy, J. Weßing, C. Kroll, R. W. Seidel, C. Gemel, R. A. Fischer, *Angew. Chem. Int. Ed.* **2014**, 53 (30), 7943-7947.

# 3 INTERMETALLIC PHASES AND CLUSTERS

Inspiration across the Disciplines

## 3.1 Intermetallic phases

### Classifications of intermetallic phases

Given the plethora of possible metal-metal combinations and the inherent combinatorial diversity of structural and electronic, physical and chemical properties, it is not surprising that a classification of intermetallic phases is non-trivial, and the lines between the different categories are, at best, blurry. Consequently, models to systematically describe, comprehend and predict the formation of solid-state intermetallics are manifold, and usually based on the correlation of a complex interplay of chosen factors such as composition, constitution, electronic configurations, bonding situations or structure-property relationships.<sup>1, 2, 12</sup> The probably most common approach is based on the systematization of metals with regards to their atomic scale parameters, i.e. the atomic radius, electronegativity and the valence electron concentration, which were found to be decisive factors for structure formation and alloying.<sup>3</sup> Accordingly, metals are divided into A- and B-metals (Figure 4); the former including alkaline and earth alkaline metals (A1) as well as transition metals with exception of group 12 (A2); the latter being further divided into post-transition metals including group 12 (B1), and semi-metals on the borderline to non-metals (B2). While A1 metals are characteristically considered as electropositive metals with comparably large atomic radii, A2 metals possess similar radii and electronegativities, but differ with regard to valence electron counts. In comparison, B1 metals display higher electronegativities and, resulting from their filled d-orbitals, clearly distinguishable structural and electronic properties from the transition metals. B2 metals partially behave as semi-conductors, and show a tendency for covalent interactions.

1 <b>H</b>																	2 <b>He</b>
3 <b>Li</b>	4 <b>Be</b>											5 <b>B</b>	6 <b>C</b>	7 <b>N</b>	8 <b>O</b>	9 <b>F</b>	10 <b>Ne</b>
11 <b>Na</b>	12 <b>Mg</b>											13 <b>Al</b>	14 <b>Si</b>	15 <b>P</b>	16 <b>S</b>	17 <b>Cl</b>	18 <b>Ar</b>
19 <b>K</b>	20 <b>Ca</b>	21 <b>Sc</b>	22 <b>Ti</b>	23 <b>V</b>	24 <b>Cr</b>	25 <b>Mn</b>	26 <b>Fe</b>	27 <b>Co</b>	28 <b>Ni</b>	29 <b>Cu</b>	30 <b>Zn</b>	31 <b>Ga</b>	32 <b>Ge</b>	33 <b>As</b>	34 <b>Se</b>	35 <b>Br</b>	36 <b>Kr</b>
37 <b>Rb</b>	38 <b>Sr</b>	39 <b>Y</b>	40 <b>Zr</b>	41 <b>Nb</b>	42 <b>Mo</b>	43 <b>Tc</b>	44 <b>Ru</b>	45 <b>Rh</b>	46 <b>Pd</b>	47 <b>Ag</b>	48 <b>Cd</b>	49 <b>In</b>	50 <b>Sn</b>	51 <b>Sb</b>	52 <b>Te</b>	53 <b>I</b>	54 <b>Xe</b>
55 <b>Cs</b>	56 <b>Ba</b>	57-71 *	72 <b>Hf</b>	73 <b>Ta</b>	74 <b>W</b>	75 <b>Re</b>	76 <b>Os</b>	77 <b>Ir</b>	78 <b>Pt</b>	79 <b>Au</b>	80 <b>Hg</b>	81 <b>Tl</b>	82 <b>Pb</b>	83 <b>Bi</b>	84 <b>Po</b>	85 <b>At</b>	86 <b>Rn</b>
87 <b>Fr</b>	88 <b>Ra</b>	89-103 **	104 <b>Rf</b>	105 <b>Db</b>	106 <b>Sg</b>	107 <b>Bh</b>	108 <b>Hs</b>	109 <b>Mt</b>	110 <b>Uun</b>	111 <b>Uuu</b>	112 <b>Uub</b>		114 <b>Uuq</b>				

\* lanthanide series

\*\* actinide series

Figure 4. Periodic table depicting the classification of metals into alkaline and earth alkaline metals (A1, green), transition metals (A2, violet), post-transition metals (B1, pink) and semi-metals (B2, blue).

	A1	A2	B1	B2
A1	<b>solid solutions</b> <b>Laves phases</b> <b>segregation</b>	<b>stoichiometric intermetallics</b>  <b>Laves phases</b>	<b>stoichiometric intermetallics,</b> <b>CsCl &amp; NaTi-type</b> <b>Laves phases,</b> <b>cluster-based intermetallics</b>	  <b>Zintl phases</b>
A2		<b>solid solutions with broad phase width, superlattices</b>	<b>Hume-Rothery phases</b>  <b>approximants,</b> <b>quasicrystals</b>	<b>stoichiometric intermetallics or small phase widths, e.g. NiAs-types</b>
B1			<b>solid solutions with covalent bond character</b>	<b>stoichiometric intermetallics with covalent bond character</b>
B2				<b>solid solutions with covalent bond character</b>

Figure 5. Classification of binary intermetallic systems based on the combination of A1, A2, B1, or B2 metals. While the formation of solid solutions is prevailing for closely related metal-metal combinations, more complex structures are found for metal combinations with increasingly different atomic radii, electronegativities or valence electron counts.

Following the categorization of metals, binary intermetallic phases can now be understood as the combination of different metal categories, and thus systematically assessed with regards to bonding types and structural motifs (Figure 5). While the formation of solid solutions with prevailing metallic or covalent bond character is reasonably foreseeable for closely related metals of the same, or neighbouring categories, a complex structural variety is observed for constituents with increasingly divergent atomic radii, electronegativities and/or electronic configurations. Amongst these, the salt-like Zintl phases, formed by combinations of A1 and B2 metals with largely different atomic radii and electronegativity, exhibit prevailing ionic bonding, whereas the bonding in Hume-Rothery phases (A2/B1 combinations) is essentially covalent. In contrast, Laves phases (mostly A/A combinations) primarily show metallic bonding character, thus representing the third border case with regards to the underlying, structure-determining bonding type. Here, the direct correlation of the classification of intermetallic phases on the basis of atomic scale factors to the *van-Arkel Ketelaar* triangle of chemical bonding becomes obvious (Figure 6). It goes without saying that the structural diversity of intermetallic phases goes well beyond the given limiting cases and a rich variety of phases that differ drastically with regard to bonding, structure and properties is found "in between". Stoichiometric intermetallic phases of particular, but recurring structural motifs,

e.g. of the CsCl, NaTl or NiAs-type, or cluster-based intermetallics, e.g. Frank-Kasper phases like the A15 family, represent only some of these, and a full account would be well beyond the scope of this work. However, chosen intermetallic phases will be introduced in more detail in the following sections.

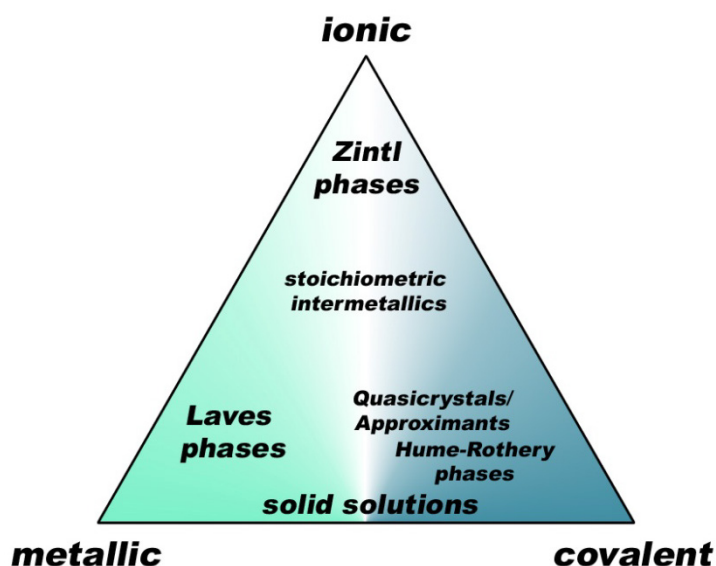


Figure 6. Adapted *van-Arken Ketelaar* triangle showing the correlation of chosen intermetallics with their inherent bond natures.

## Laves phases

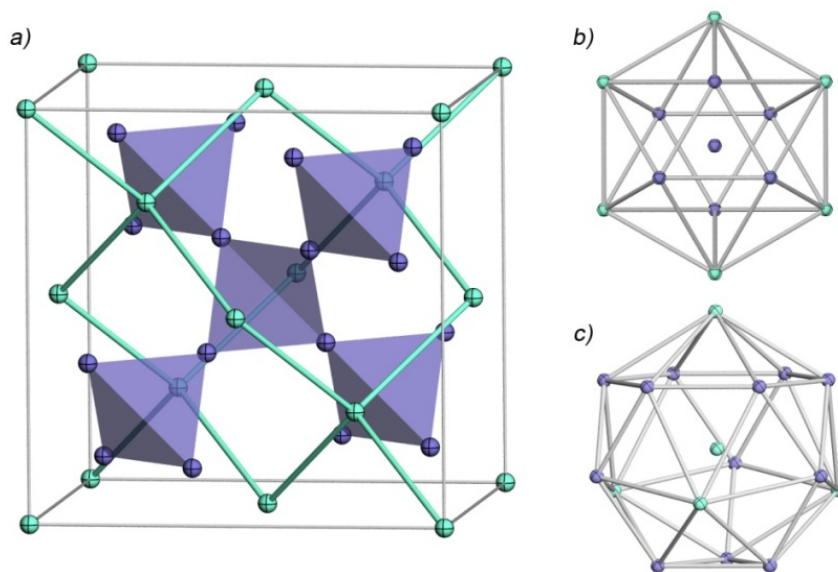
Named after the German mineralogist Fritz Laves,<sup>13, 14</sup> Laves phases are mainly binary intermetallics of an  $AB_2$  composition which belong to the family of Frank-Kasper phases, that is intermetallic phases with topologically close-packed structures featuring a closer packing of constituents of different atomic radii than homometallic f.c.c. or h.c.p. structures.<sup>1-3, 15</sup> Their structures are governed by atomic size factors rather than electronic rules, and are preferably formed for combinations of A1/A2 or A1/B1 metals with an  $r_{a/b}$  ratio close to the optimum value of 1.225.<sup>16, 17</sup> However, owing to the mainly geometrically driven selection rules and because the high stability is mainly a result of the increased coordination number with regards to the elemental components, examples across almost all possible combinations of metal categories are known with exception of B/B combinations (Table 2). In fact,  $r_{a/b}$  ratios were found to range between 1.05 and 1.68 with large deviations observed, amongst others, for Laves phases of the transition metals, e.g.  $ZrAl_2$ .<sup>18-20</sup> Here, the energy expense for structural adjustment is compensated by additional, attractive Coulomb interactions which stem from charge transfer phenomena from the second component to the transition metal to fill the incompletely filled inner shells.

Table 2. Examples of intermetallic compounds with Laves phase structures.<sup>15</sup>

	A1	A2	B1	B2
A1	CsNa <sub>2</sub> , CaLi <sub>2</sub> , SrMg <sub>2</sub>	MgNi <sub>2</sub> , MgCu <sub>2</sub>	CaAl <sub>2</sub> , CaCd <sub>2</sub> , MgZn <sub>2</sub>	KBi <sub>2</sub>
A2		TiCo <sub>2</sub> , ZrCr <sub>2</sub> , NbFe <sub>2</sub>	HfAl <sub>2</sub> , TaZn <sub>2</sub> , YAl <sub>2</sub>	BiAu <sub>2</sub>

Binary Laves phases adopt three different types of densely-packed structures: The hexagonal C14 structure, the cubic C15 structure, and the dihexagonal C36 structure, all of which feature the same structural motifs but obey different stacking rules.<sup>15</sup> Classic representatives are MgZn<sub>2</sub>,<sup>21</sup> MgCu<sub>2</sub><sup>22</sup> and MgNi<sub>2</sub>,<sup>23</sup> respectively. The most commonly occurring cubic MgCu<sub>2</sub> structure is composed of vertex-sharing Cu<sub>4</sub> tetrahedra which are formed by the ABCABC stacking of Cu Kagome networks (Figure 7a). The thus created tetrahedral voids are occupied by Mg atoms which are arranged in a diamond-type over-structure. Consequently, each Mg atom is located at the center of a CN16 Frank-Kasper coordination polyhedron composed of twelve neighbouring Cu atoms and four Mg atoms (Figure 7c). At the same time, each copper atom is surrounded by six Mg and six Cu atoms forming a CN12 coordination polyhedron (Figure 7b). Thus, the average coordination number adds up to 13.33, which applies for all three Laves structures and is an indication for the metallic bonding nature found within these intermetallics.

The closely related hexagonal MgZn<sub>2</sub> structure can be derived from the MgCu<sub>2</sub> structure by an ABAB stacking of Zn Kagome networks instead of the ABCABC stacking observed in MgCu<sub>2</sub>. As a consequence, linear arrangements of alternating vertex- and face-sharing Zn<sub>4</sub> tetrahedra are formed, which are likewise interpenetrated by a diamond-type arrangement of Mg atoms. The dihexagonal C36 structure of MgNi<sub>2</sub> features an ABAC stacking of Ni Kagome nets, with the overall structure featuring mixed stacking motifs of the MgCu<sub>2</sub> and MgZn<sub>2</sub> structures. Notably, even though the overall formation of Laves phases is almost explicitly determined by the proper ratio of atomic radii of the components, their exact structural features were found to obey the valence electron concentration (VEC). For the quasibinary section MgCu<sub>2</sub> - MgZn<sub>2</sub>, the MgCu<sub>2</sub>-type was found to be stable up to VEC  $\approx$  1.75, whereas the MgNi<sub>2</sub>-type is found around VEC  $\approx$  1.8. For higher VEC shortly below 2.0, the MgZn<sub>2</sub> type is predominant.<sup>17</sup> However, owing to their close structural resemblance, transformations between the three structures types are energetically accessible, and can be induced by thermal treatment or mechanical stress as observed for some Laves phases, e.g. for NbCo<sub>2</sub> or ZrFe<sub>2</sub>.<sup>2, 24, 25</sup>



**Figure 7.** a) Crystal structure of the Laves phase MgCu<sub>2</sub> (ICSD-reference no. 46007). Magnesium and copper atoms are depicted as green and violet ellipsoids, respectively. The copper Kagome nets are arranged in an ABCABC stacking resulting in the formation of vertex-sharing Cu<sub>4</sub> tetrahedra which are interpenetrated by a diamond-type arrangement of Mg atoms. b) and c) Frank Kasper polyhedra in MgCu<sub>2</sub>. Each copper center is located at the core of a CN12 polyhedron of six copper and six magnesium atoms; each Magnesium atom is embedded in a CN16 polyhedron of four magnesium and twelve copper atoms.

## Zintl phases

Alloying of the electropositive A1 metals, namely alkali, earth alkali and, in parts rare earth metals, with B1 or B2 metals close to the Zintl border results in the formation of intermetallic phases displaying a pronounced heteropolar, or ionic, intermetallic bonding nature.<sup>1-3, 26-29</sup> These so-called Zintl phases feature stoichiometrically precise compositions with salt-like structures that can be understood on the basis of the Zintl-Klemm-Busmann concept.<sup>30</sup> The latter formally divides the constituents into a cationic and an anionic fragment, in which the A1 metal transfers electrons to the more electronegative B metal. The consequently formed anionic substructures show internal covalent bonding, and obey the (8-N) rule in terms of connectivity, with N being the number of valence electrons of the p-block constituent. Often these structures are isostructural to the solid-state structures formed by isoelectronic elements, as for example in the prototypical NaTl, which is in fact the first Zintl phase reported by Zintl himself in 1939.<sup>31</sup> Taking the electron transfer from sodium to thallium into consideration, it can be formally regarded as (Na<sup>+</sup>)(Tl<sup>-</sup>), in which thallium has four valence electrons. In agreement with the (8-N) rule, the Tl atoms are arranged in a network with 4-fold connectivity which is isostructural with the diamond-network (Figure 8). The overall charge of the anionic partial structure is compensated by the small Na<sup>+</sup> ions that occupy the diamond-net's voids.



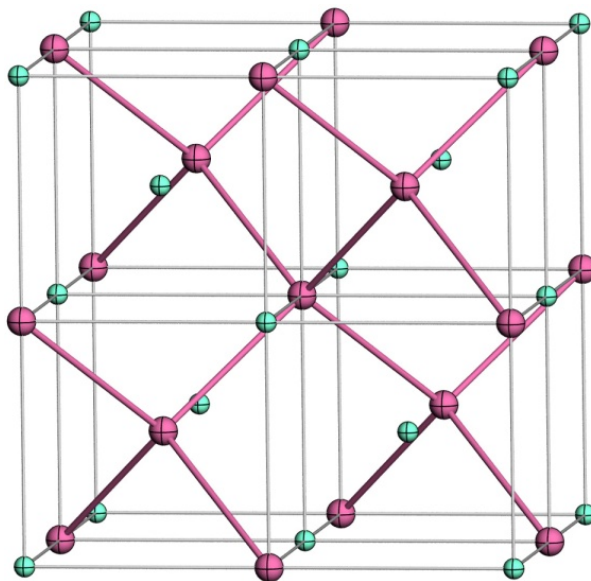


**Figure 8.** Crystal structure of the prototypical Zintl phase NaTl (ICSD-reference no. 105169). Thallium and sodium atoms are depicted as pink and green ellipsoids, respectively. The anionic thallium substructure resembles the diamond structure of isoelectronic carbon.

More complex Zintl phases are formed for compositions which do not feature homogeneous connectivity patterns, either because they contain two or more different anions, or because anions of different connectivities combine to form a polyanionic fragment. Typical examples are found amongst the silicides, for instance in the barium-silicon system. For  $\text{Ba}_5\text{Si}_3$ , electron transfer of two electrons per barium to the silicon atoms gives two types of anions, namely isolated  $\text{Si}^{4-}$  anions and  $[\text{Si}_2]^{6-}$  dumbbells with a connectivity of one.<sup>32</sup>  $[\text{Si}_4]^{6-}$  butterflies and  $[\text{Si}_{10}]^{20-}$  hexagons bearing four additional terminal silicon atoms are found in the solid-state structures of  $\text{Ba}_3\text{Si}_4$  or  $\text{SrSi}$ , respectively.<sup>33, 34</sup> In logic consequence, the structural diversity displayed by ternary and quaternary Zintl-phases containing two or more B metals is unequalled amongst intermetallic phases, albeit still explainable on the basis of the Zintl-Klemm-Busmann concept in many cases.<sup>27</sup> Depending on the electronegativities of the incorporated B metals, ternary structures tend to be isosteric to elemental phases and thus comparable to binary Zintl phases ( $\Delta \text{EN}$  is small), or display heteropolyanionic substructures which somewhat resemble the complex anions of the silicides ( $\Delta \text{EN}$  is big). For instance, in  $\text{LiGaGe}$ , or  $(\text{Li}^+)(\text{GaGe}^-)$ , the difference in electronegativities of gallium and germanium is small.<sup>35</sup> The electron provided by lithium is formally ascribed to the gallium atom to give  $\text{Ga}^-$  which is in turn isoelectronic to germanium and consequently allows for the formation of a wurtzite-like tetrahedral GaGe network. Quite differently,  $\text{Na}_7\text{In}_3\text{Se}_8$  contains linear chains of vertices- and edge-sharing  $\text{InSe}_4$  tetrahedra which contain  $\text{In}^-$  centers with four-fold connectivities, and  $\text{Se}^0$  and  $\text{Se}^-$  centers of two- and one-fold bonding, respectively.<sup>36</sup> Note that both, the Zintl-Klemm-Busmann concept and the (8-N) rule do apply.



A special type of Zintl phases occurs for combinations of A1 metals with B metals on, or left of the Zintl border, and is particularly common for the lewis-acidic B1 metals of group 13.<sup>26</sup> Here, the formation of anionic substructures of interconnected or isolated deltahedral polyanions with delocalized bonding situations is observed, that can no longer be understood on the basis of the Zintl-Klemm-Busmann concept, only. Instead, the Wade rules apply which have originally been developed for the well-established borane cage structures, but can be equally well consulted for the description of naked main group clusters, like those found in Zintl phases of the type  $A_4B_9$  (A = alkali metal, B = group 14 metal). A typical example is  $K_4Sn_9$ , in which isolated  $Sn_9^{4-}$  clusters are arranged in distorted hexagonally close-packed layers with an ABAB stacking (Figure 9a).<sup>37</sup> In accordance with the Wade rules, the  $Sn_9^{4-}$  clusters form monocapped square antiprisms, which match the expected form of an electron-precise nido-cluster with 22 CVE. Comparable structures are observed for Zintl phases of all group 14 (semi-)metals, with exception of silicon for which  $Si_9^{4-}$  has only been observed in the solid state in combination with the tetrahedral species  $Si_4^{4-}$ , e.g. in  $A_{12}Si_{17}$  (A = K, Rb, Cs).<sup>38, 39</sup> A larger and more diverse collection of polyanionic clusters in Zintl phases is found for group 13 metals. On the one hand, these form "Zintl-like" phases with isolated deltahedral polyanions, such as the electronically mismatched  $A_8B_{11}$  featuring pentacapped trigonal prismatic  $B_{11}^{7-}$  clusters, e.g. in  $K_8In_{11}$ .<sup>40</sup> On the other hand, a variety of Zintl-phases with interconnected networks of clusters is observed particularly for the earlier group 13 metals, in which delocalized bonding motifs within the clusters are accompanied by localized bonds between them. Accordingly, intermetallic compounds like  $KGa_3$ ,<sup>41</sup> can only be understood on the basis of a combination of both, the Wade-rules and the Zintl-Klemm-Busmann concept. For the given example of  $KGa_3$ , its gallium network is composed of highly interconnected 8-atom clusters, with each gallium atom forming an exo-bond to either a neighbouring cluster or to one of the isolated 4-bonded gallium atoms that are present in an equimolar ratio (Figure 9b). The clusters adopt a trigondodecahedral structure, which is a closo-type structure that requires  $2n + 2 = 18$  electrons according to Wade's rules. The additional eight exo-bonds are of a covalent and thus electron-precise nature, which requires another 8 electrons to be provided by each  $Ga_8$  cluster. Since the gallium atoms contribute  $8 \times 3 = 24$  electrons, the central  $Ga_8$  building block needs to carry a formal twofold negative charge. The additionally present 4-bonded gallium atoms account as  $Ga^-$  in agreement with the Zintl-Klemm-Busmann concept. As a result, per nine gallium atoms, a total negative charge of three needs to be counterbalanced, which is exactly the amount of potassium cations present according to the overall composition of  $KGa_3$  (or  $K_3Ga_9$ ). This way,  $KGa_3$  can be described as an electronically precise, true Zintl-phase, and the same principles apply for a number of comparable compounds, such as  $K_3Ga_{13}$  or  $Rb_2In_3$ .<sup>42, 43</sup>

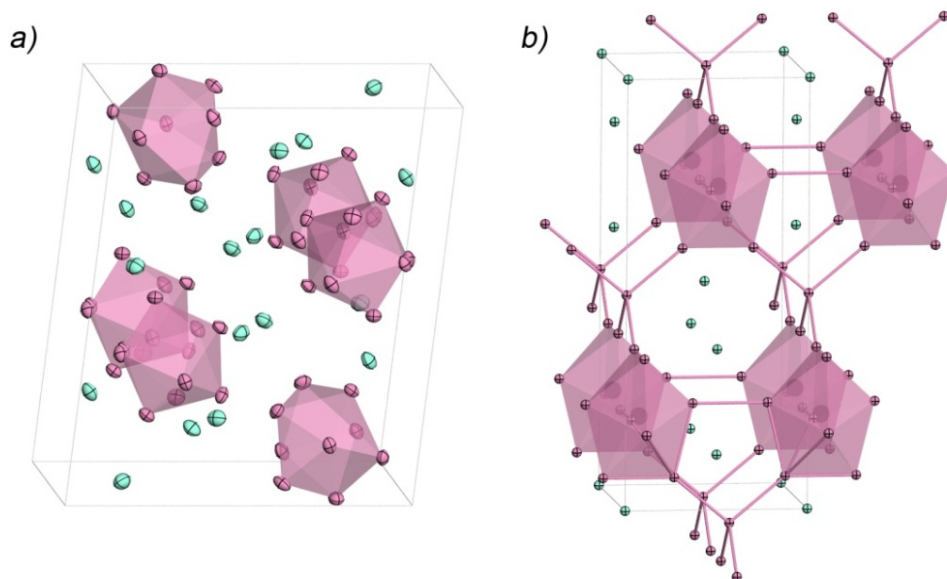


**Figure 9.** Crystal structures of the Zintl phases  $K_4Sn_9$  and  $KGa_3$  (ICSD-reference no. 240048 and 20664). a)  $K_4Sn_9$  contains isolated polyanionic  $Sn_9^{4-}$  clusters, whereas b)  $KGa_3$  forms a highly interconnected anionic net of 8-atom gallium clusters.

## Hume-Rothery phases

Hume-Rothery phases are representatives of a large class of intermetallic phases of the A2 and B1 metals, whose structures are primarily determined by the valence electron concentration  $e/a$ , rather than their composition.<sup>1-3</sup> As early as 1926, William Hume Rothery observed the systematic and successive occurrence of particular phase structures in various intermetallic compounds of different metal combinations, and suggested a dependence of the stability of such structures on atomic scale parameters.<sup>44</sup> On the basis of these findings, the so-called Hume-Rothery rules, a simplified set of rules correlating the stability of solid-state structures to the decisive atomic properties of atomic radii, electronegativities and valence electron concentrations, were developed.<sup>17, 45-47</sup> These apply for solid solutions in general, but are also valid for Hume-Rothery phases with a particular emphasis on the valence electron concentration. The most pertinent three factors include:

**The atomic size factor.**<sup>45-48</sup> According to the atomic size factor effect, favourable alloying occurs only for constituents whose atomic radii differ no more than 15%, or as alternatively defined on the basis of Goldschmidt radii, for  $r_{a/b}$  ratios in a range between 0.8 and 1.2. Notably, this concept is not only empirical, but has also been confirmed quantitatively by the evaluation of the elastic energy of solid solutions in dependence of the atomic radii of their constituents.

**The electronegativity difference  $\Delta EN$ .**<sup>45-47, 49</sup> For elements with similar electronegativities, alloy formation in the sense of solid solutions is likely to occur, whereas those with largely different electronegativities will rather form intermetallic compounds featuring directed bonding. A quantification of this concept is at least controversial, however, a rough critical value for intermetallic alloying of  $\Delta EN = 0.5$  on the Pauling electronegativity scale has been suggested by Darken and Gurry, and may serve as a first indicator.

**The electron concentration  $e/a$ .**<sup>45-47, 50, 51</sup> The valence electron concentration is defined as the average number of valence electrons per atom, and is calculated on the basis of the following valences: 0 for transition metals with open d-shells, 1 for group 11 metals, 2 for group 12 metals, and, along this line, 3 to 5 for group 13 to 15 metals, respectively. According to the electron concentration concept, specific structures are favoured for defined  $e/a$  ratios. This effect is most pronounced, and thus traceable, for intermetallic phases in which the size factor and the electronegativity effect are of minor importance. Such phases are called electron compounds, and the Hume-Rothery phases are a principal example.

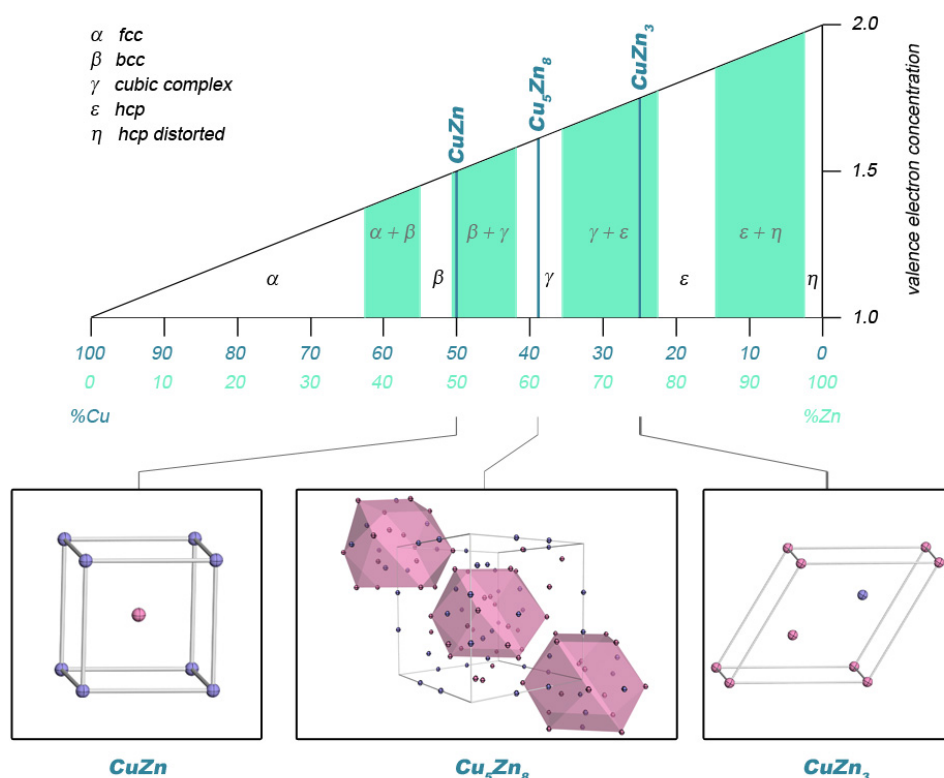


**Figure 10.** Phase sequences as observed in the copper-zinc system at room temperature with biphasic areas shaded in green colour, adapted from *Intermetallics - Synthesis, Structure, Function*.<sup>1</sup> The solid state-structures of the representative  $\beta$ -phase CuZn (ICSD-reference no. 56276), the  $\gamma$ -phase Cu<sub>5</sub>Zn<sub>8</sub> (ICSD-reference no. 103158) and the  $\epsilon$ -phase CuZn<sub>3</sub> (ICSD-reference no. 103153) are depicted in the lower boxes, whereat copper and zinc atoms are shown as violet and pink ellipsoids, respectively.

A suitable example illustrating how the structures of Hume-Rothery phases are governed by the electron concentration  $e/a$  is the phase sequence observed in the copper-zinc (brass) system at room temperature (Figure 10).<sup>1, 52, 53</sup> Starting from f.c.c. structured pure copper with a valence electron concentration of one, progressive alloying of zinc results in an increase of the  $e/a$  ratio, entailing successive structure transformations in favour of more stable arrangements. While the initial f.c.c. structure is retained for zinc contents up to 38 %, further substitution of copper sites leads to the formation of the  $\beta$  phase with a b.c.c.-type structure. The representative CuZn, with a valence electron concentration of 1.5 (21/14), adopts a disordered b.c.c. structure (W-type) at high temperatures, and the ordered CsCl-structure for temperatures below 740 K. Compositions close to the atom-precise Cu<sub>5</sub>Zn<sub>8</sub> ( $\gamma$ -brass,  $e/a = 21/13$ ) form  $\gamma$ -phases which can be described as complex defect-variants of the b.c.c. structure. They contain large cubic unit cells with recurring motifs of nested polyhedra. Finally, in the increasingly zinc-rich regime, first the  $\epsilon$  phase is observed for contents around 78- 86 % Zn, followed by the distorted h.c.p.-type  $\eta$  phase in a very narrow margin of only 2% Cu in Zn. CuZn<sub>3</sub>, as an example of the  $\epsilon$  phase, has a valence electron concentration of 21/12 and adopts a h.c.p. structure with statistical distribution of its components throughout the crystal structure.

The phase sequences observed in the copper-zinc systems are exemplary for Hume-Rothery phases, and also observed in the phase diagrams of other intermetallic systems, such as Cu-Sn, Cu-Al, Ag-Al, or Au-Zn.<sup>54-56</sup> In this context, particular emphasis is laid on the  $e/a$  ratio as the decisive structure determining factor, as impressively demonstrated by the series of  $\gamma$  brasses Cu<sub>5</sub>Zn<sub>8</sub>, Cu<sub>4</sub>Al<sub>9</sub> and Cu<sub>31</sub>Sn<sub>8</sub> which display largely different solute concentrations but a common  $e/a$  ratio of 21/13.<sup>57</sup> Accordingly, the origin of the particular stability of the observed structures must be of a purely electronic nature, and has been subject of theoretical approaches since the early 1930s.<sup>47</sup>

### Excursus: Stability concepts of Hume-Rothery phases

With the aim of finding a theoretical rationale for the electron concentration effect observed in Hume-Rothery phases, the Mott-Jones model was developed in the early 1930s, explaining the stability of certain phases on the basis of Fermi surface-Brillouin zone interactions.<sup>58, 59</sup> In this context, the Fermi surface describes an abstract sphere of constant energy in the reciprocal space that separates occupied from unoccupied electron states at zero temperature.<sup>60</sup> The Brillouin zone<sup>61</sup> is a symmetric polyhedron in the reciprocal space which is determined by the geometry of the crystal lattice in the real space, and can be understood as the unit cell of the reciprocal lattice. According to the Mott-Jones model, the particular stabilization of certain solid-state structures is traced back to energy gains that occur when the Fermi surface approaches or interacts with the first (or a higher) Brillouin zone.<sup>59</sup> What does

this mean? To understand the basic principles of the Mott-Jones model, it is necessary to go back to the basics of metallic bonding. For an extended metallic solid, the free electron approximations assumes electrons to be completely detached from the crystal lattice, forming a free electron gas.<sup>62, 63</sup> However, in a more realistic scenario, interaction with the periodically ordered metal cations, and the resulting ordered array of ionic potentials, will cause mixing and splitting of electronic states as a direct consequence of interference of the individual electron wave functions. Consequently, states with electron density residing near the ions, and states with electron density residing between the ions will be formed. This is called the "nearly free electron model" which forms the basis for the Mott-Jones model.<sup>62, 64</sup> At the same time, the separation of the electronic states creates pseudo energy gaps within the electron band structure. Metallic solids with a Fermi energy close to such a pseudo gap, experience a gain in kinetic energy as electrons from the depleted region around the pseudo gap are redistributed into the energetically more favourable lower lying DOS.<sup>62, 65</sup> Coming back to the Mott-Jones model, it has to be understood that the geometric form of the Brillouin zone correlates with the location of energy gaps in the electron band structure. In a simplified view, this is because both, the free electron plane waves described above, and the diffraction plane waves during X-ray scattering interfere with the ordered crystal lattice of the compound with comparable conditions for constructive and destructive interference (Figure 11).<sup>65</sup> While the former form the basis of the electron band structure, the latter cause the diffraction pattern on which basis, amongst others, the Brillouin zone is constructed.

Accordingly, a growing Fermi surface approaching the geometrical outline of the Brillouin zone can be understood in terms of filling the electronic states with valence electrons until the Fermi level (indicated by the Fermi surface in the reciprocal space) comes close to an energy gap in the electron band structure. Structures displaying this characteristic experience an electronic stabilization that provides enough energy to stabilize a phase relative to a competing one. Likewise, if the Fermi surface crosses the borders of the Brillouin zone, and electrons fill up the bands beyond the pseudo-gap, this is energetically highly unfavourable and eventually will lead to a phase transformation in favour of a structure of lower symmetry with a larger Brillouin zone. This is often referred to as the Hume-Rothery stabilization mechanism or the Hume-Rothery matching condition.<sup>47</sup> Critical  $e/a$  values for spherical Fermi surfaces touching the Brillouin zones have been calculated to 1.362 for the f.c.c. lattice, 1.480 for the b.c.c. lattice, and 1.538 for the  $\gamma$ -brass structure, and are in reasonably well agreement with the empirical data.<sup>47, 59</sup> Although the underlying theoretical approaches for the quantification of this early proposed model have been critically assessed in subsequent studies, its basic principles have repeatedly been affirmed and still form a valid basis for successive models.<sup>47, 65</sup>

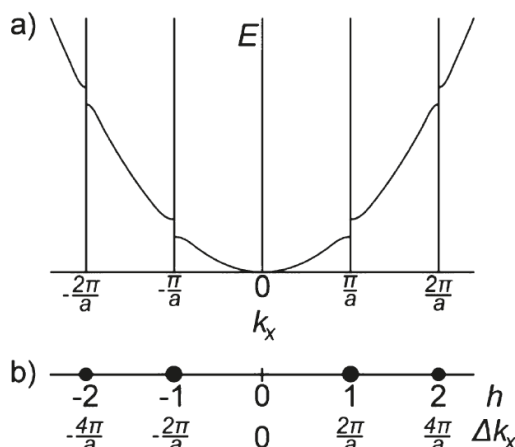


Figure 11. (a) The extended zone scheme of the electron band structure of a one-dimensional chain of atoms. Energy gaps stemming from the mixing and splitting of electronic states are observed at  $k_x = \pm\pi/a$ . (b) The corresponding X-ray diffraction pattern shows diffraction peaks correlating to the positions of energy gaps. Reprinted with permission from R. F. Berger, P. L. Walters, S. Lee, R. Hoffmann, *Chem. Rev.* 2011, 111 (8), 4522-4545. Copyright 2011 American Chemical Society.

## Complex metallic alloys (CMAs) - Quasicrystalline phases and approximants

A fundamental breach of established crystallographic concepts of that time, and in particular of the most fundamental assumption that all crystals consist of repeating periodic patterns, occurred in the aftermath of Dan Shechtman's discovery of the crystal structure of a rapidly solidified MnAl phase exhibiting a "forbidden" fivefold symmetry in 1982.<sup>66, 67</sup> With this, the era of quasicrystalline materials was heralded, bringing about the new definition of a crystal as a material that is no longer defined by its internal translational periodicity, but rather on the basis of its "essentially discrete diffraction pattern".<sup>68</sup>

Quasicrystalline intermetallics are formed for a wide variety of binary, ternary or quaternary metal combinations with a particular emphasis on combinations of A1 or A2 metals with B1 metals.<sup>69-72</sup> Two predominant groups are materials based on transition metal aluminides, and Mg-Zn based phases. Their structures possess no translational periodicity, however, this does not mean that they don't possess structural order. In fact, quasicrystalline phases can be understood on the basis of three-dimensional tilings with two or more so-called unit tiles that resemble unit cells in conventional crystal lattices.<sup>69-73</sup> Quite comparable to the two-dimensional Penrose tilings<sup>74</sup> (Figure 12) which were already published in the 1970s, these unit tiles are arranged following specific construction rules, eventually resulting in the formation of a non-repetitive, but ordered crystal structure whose dimensions are only limited by the crystal grain size. In contrast, the structurally closely related approximants exhibit

translationally periodic structures with extraordinary large unit cells and, in parts, local deviations from the average structure.<sup>69, 71, 75</sup>

Resulting from their complex interiors, the full structural analysis of quasicrystalline long- and short-range order, that is the quasilattice as such and the way the unit tiles are decorated by atoms, is non-trivial, and mainly based on the combinatorial approach of experimental methods, like X-ray diffraction and high-resolution imaging techniques, along with higher-dimensional theoretical modelling.<sup>76, 77</sup> Actual quasicrystalline structures unravelled up to now can then be classified with respect to their overall symmetry (N-gonal vs. icosahedral), the underlying quasilattice, and the atomic clusters building up their structures. In this context, N-gonal quasicrystals are mainly decagonal quasicrystals (DQCs), and only some metastable octagonal or dodecagonal representatives have been found.<sup>70, 78</sup> Based on the number of atomic layers per translation period along the tenfold axis, they are further divided into two-layer periodicity (*d*-Al-Co-Ni and *d*-Zn-Mg-Dy type), six-layer periodicity (*d*-Al-Mn-Pd type) and eight-layer periodicity (*d*-Al-Os-Pd type), whereas icosahedral quasicrystals (IQCs) are mainly classified according to the three prototypes *i*-Al-Mn-Pd, *i*-Zn-Mg-Ho, and *i*-Cd-Yb.<sup>70, 79</sup> The latter all relate to classical three-dimensional, cluster-decorated Penrose tilings but differ regarding the type of atomic clusters employed. The three fundamental atomic cluster types known to occur in QCs, namely the Mackay cluster,<sup>80, 81</sup> the Bergman or Samson cluster,<sup>82</sup> and the Tsai cluster,<sup>83, 84</sup> are depicted in Figure 13.

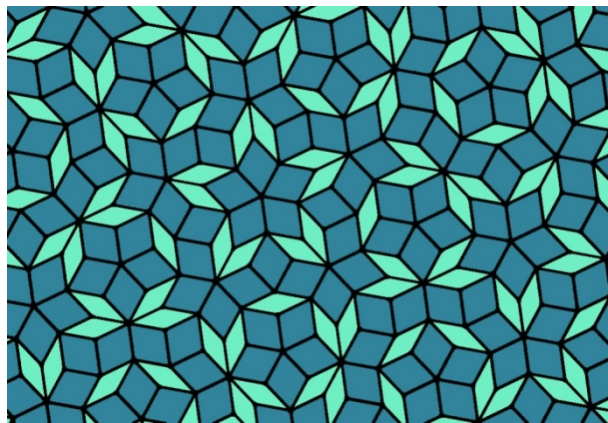
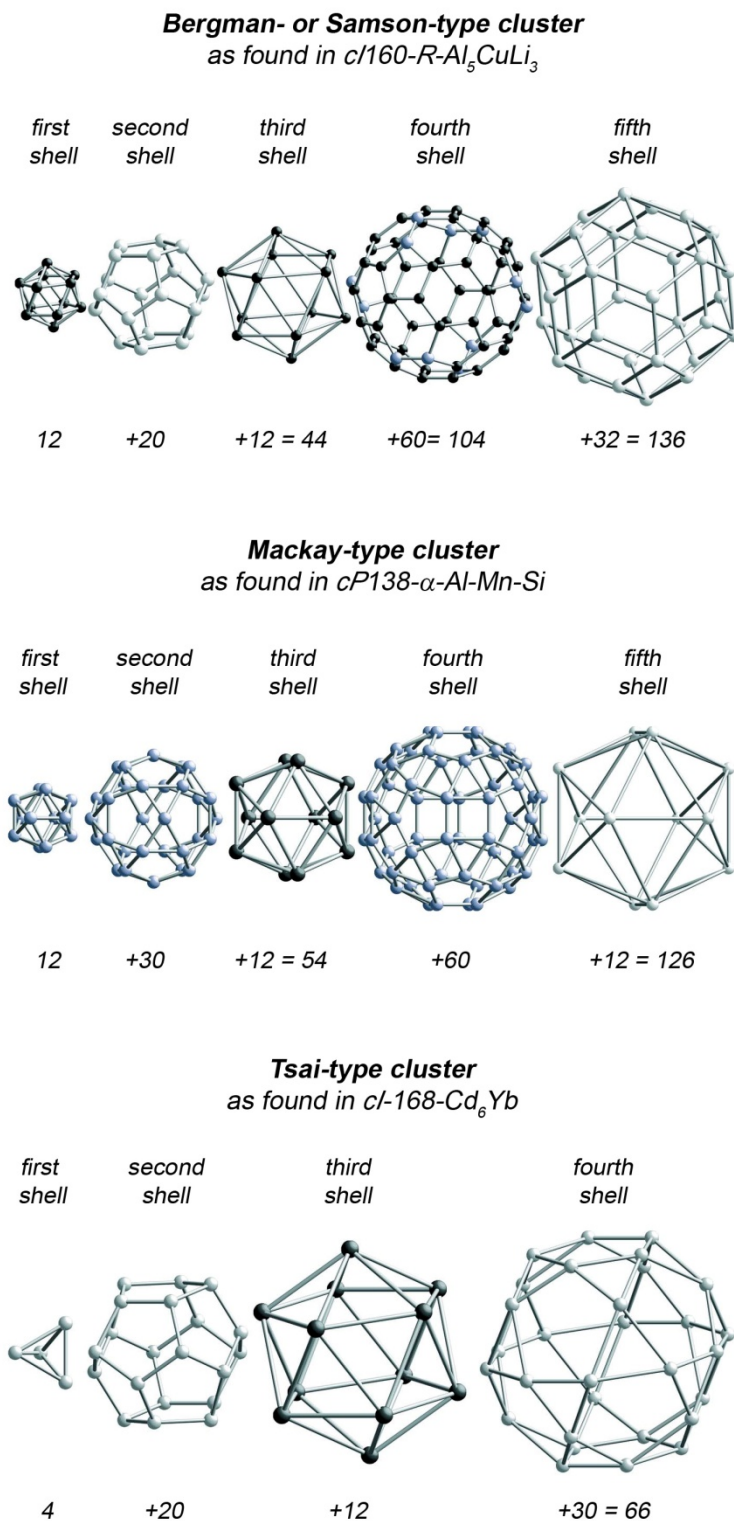


Figure 12. Penrose tiling composed of a narrow and a wide diamond tile. The resulting pattern shows no translational periodicity but exhibits a long-range order with five-fold symmetry.





**Figure 13.** Successive shell structures of atoms in the atomic clusters found in rhombic triacontahedral-type, Mackay icosahedral-type, and Tsai-type quasicrystals and their approximants, e.g. in  $cI160-R-Al_5CuLi_3$ ,  $cP138-\alpha-Al-Mn-Si$ , or  $cI168-Cd_6Yb$ , as indicated. The atom counts are given below the respective atom shell. Reprinted and adapted with permission of W. Steurer, S. Deloudi, *Acta Crystallogr., Sect. A* 2008, 64 (1), 1-11. Reproduced with permission of the International Union of Crystallography.<sup>70</sup>



Albeit they represent a comparably young class of intermetallic phases, the stability of quasicrystalline structures has been assessed on the basis of empirical observations, and first principle band calculations for closely related approximant systems. Interestingly, quasicrystals were reported to be strict electron compounds, just like Hume-Rothery phases, forming at specific valence electron concentrations.<sup>47, 85</sup> According to Tsai, stable IQCs of the *i*-Al-Mn-Pd type form for the homologous series  $Al_{63}Cu_{25}M_{12}$  (with  $M = Fe, Ru, Os$ ) and  $Al_{70}Pd_{20}M_{10}$  ( $M = Mn, Tc, Re$ ), featuring a common  $e/a$  ratio of  $\sim 1.75$ . For the *i*-Zn-Mg-Ho and the *i*-Cd-Yb class, a more flexible range between 2.0 and 2.15 was determined.<sup>85-87</sup> Following this approach, stable IQCs could even be derived following the  $e/a$  guiding principle, e.g. by replacement of divalent cadmium in  $Cd_{84}Yb_{16}$  or  $Cd_{84}Ca_{16}$  by a mixture of trivalent indium and monovalent silver to give stable  $In_{42}Ag_{42}Yb_{16}$  and  $In_{42}Ag_{42}Ca_{16}$ , respectively.<sup>88</sup> Note, that in this context, the valences of the transition metals with open d-shells were calculated on the basis of the proposed values of Raynor who in turn derived them from the analysis of  $e/a$  ratios of Al-TM intermetallics in 1949.<sup>89</sup> While the occurrence of homologous series of stable quasicrystalline structures and the successful synthesis of specifically targeted phases such as  $In_{42}Ag_{42}M_{16}$  ( $M = Yb, Ca$ ) indeed provide hard evidence for the applicability of Hume-Rothery rules, the quantification according to the presented principles is at best controversial, and the negative valencies for transition metals proposed by Raynor not very plausible. More recent  $e/a$  values derived from the Hume-Rothery plots of a number of alloys, including  $\gamma$ -brasses and approximants, are listed in table 3. The Fermi radii  $k_f$  calculated for different complex metallic alloys and approximants on the basis of these values were found to fulfill the Hume-Rothery matching condition  $K_p = 2k_f$  ( $K_p =$  diameter of the Brillouin zone), which is considered a first indication for the plausibility of the given numbers.<sup>47, 90</sup>

Table 3. Valencies for some first row transition metals, as determined by a) Raynor<sup>89</sup> and b) Mizutani *et al.*<sup>90</sup>

	Cr	Mn	Fe	Co	Ni
a)	-4.66	-3.66	-2.66	-1.61	-0.71
b)	-	0.46	0.7 0.68	0.26	0.15 0.53

Additional evidence for the applicability of the valence electron concentration concept was provided by first-principle band calculations. Indications for depletions of the band structure of quasicrystalline materials close to the Fermi level had already been found early, e.g. in X-ray diffraction patterns and X-ray photoemission spectra of the Al-Mn quasicrystalline phase.<sup>91</sup> However, first principle band calculations were considered beyond practical

computational capacities owing to the infinitely large unit cells. Later on, it was found that these calculations can be performed on structurally closely related approximants instead, and first principle band calculations performed on the closely related Al-Mn approximant confirmed a deep depression in its DOS close to the Fermi level.<sup>92</sup> Meanwhile these findings were found true for a number of approximants, including representatives from the Al-Mg-Zn, Al-Li-Cu, Al-Cu-TM-Si, and Al-Pd-Mn systems.<sup>47, 93</sup> The origin of the observed pseudo-gaps is often considered a combination of FsBz interactions and additional factors, e.g. orbital hybridization effects as observed in MI-type Al-Cu-Ru-Si approximant.<sup>47</sup> Nonetheless, the matching conditions for the Hume-Rothery stabilization mechanism are still valid, making these compounds true electron compounds.

## 3.2 Top-Down! From solid-state phases to molecular clusters

### Zintl ions as a most remarkable study case

Classical top-down approaches in the synthesis of metalloid clusters from solid-state materials include physical methods like supersonic jet expansion, magnetron sputtering or laser ablation of metallic specimen in ultra high vacuum to create charged or neutral nanoclusters and/or -particles in the gas phase.<sup>94-96</sup> These methods usually produce naked metal clusters of a broad size distribution, but allow for the investigation of size-selected nanoclusters of defined stoichiometries when coupled with a downstream mass analyzer. This way, the size-dependency of chemical and physical properties can be investigated on an atom-precise scale. However, the employed conditions and the lacking stabilization of the metalloid particles are far from an experimental set-up under realistic conditions. Likewise, these methods are restricted to non-preparative scales.

The wet-chemical synthesis of metal clusters starting from the solid state is less common, and only few examples are known. Amongst these, the rich chemistry of the Zintl ions is certainly the most striking one.<sup>4, 97-99</sup> Zintl ions are soluble, ligand-free polyanions of group 14 and 15 metals which are readily obtained *via* dissolution of suitable binary Zintl phases in liquid ammonia, ethylenediamine or *N,N*-dimethylformamide. The most prominent examples include the deltahedral  $[\text{E}_9]^{n-}$  ( $\text{E} = \text{Ge}, \text{Sn}, \text{Pb}$ ) and the heptapnicantortricyclane anions  $[\text{Pn}_7]^{3-}$  ( $\text{Pn} = \text{P}, \text{As}, \text{Sb}$ ).<sup>4, 100</sup> However, many more representatives are known, ranging from the smallest group 15 element polyanion, the dumbbell-shaped  $[\text{Bi}_2]^{2-}$  to the largest homoatomic group 14 element polyanion  $[\text{Pb}_{10}]^{2-}$ .<sup>101, 102</sup> Although their immense structural variety is certainly remarkable, the deep fascination for these compounds stems from the rich synthetic potential they exhibit in solution chemistry after being extracted from the solid state (Figure 14).<sup>4, 98</sup> These post-synthetic chemical transformations are largely connected to the controlled oxidation of the highly reduced polyanionic Zintl species, which was long thought to irrevocably effect cluster decomposition to form the elemental metal. Instead, oxidative coupling reactions take place in the presence of mild oxidizing agents, such as triphenylphosphine or -arsine, yielding oligo- and polymers of interconnected Zintl anions with exo-bonds that often appear to participate in the extended delocalized bonding comprising the entire anion. Typical examples include small dimeric units, like  $[\text{Ge}_9\text{-Ge}_9]^{6-}$  or  $[\text{P}_{11}\text{-P}_{11}]^{4-}$ , as well as oligomeric representatives as  $[\text{P}_7\text{-P}_7\text{-P}_7]^{3-}$  or  $[\text{Ge}_9=\text{Ge}_9=\text{Ge}_9=\text{Ge}_9]^{8-}$ , and polymeric  $[-(\text{Ge}_9^{2-})]_{\infty}$ .<sup>103-107</sup> For reactions with the heavier homologues  $\text{SbPh}_3$  and  $\text{BiPh}_3$ , functionalization of  $[\text{Ge}_9]^{4-}$  forming the disubstituted  $[\text{Ph}_2\text{E-Ge}_9\text{-EPh}_2]^{2-}$  ( $\text{E} = \text{Sb}, \text{Bi}$ ) is observed.<sup>108</sup> Likewise, procedures for the functionalization with common main group fragments, such as alkyl, silyl, stannyl, or germanyl groups have been established.<sup>4</sup>

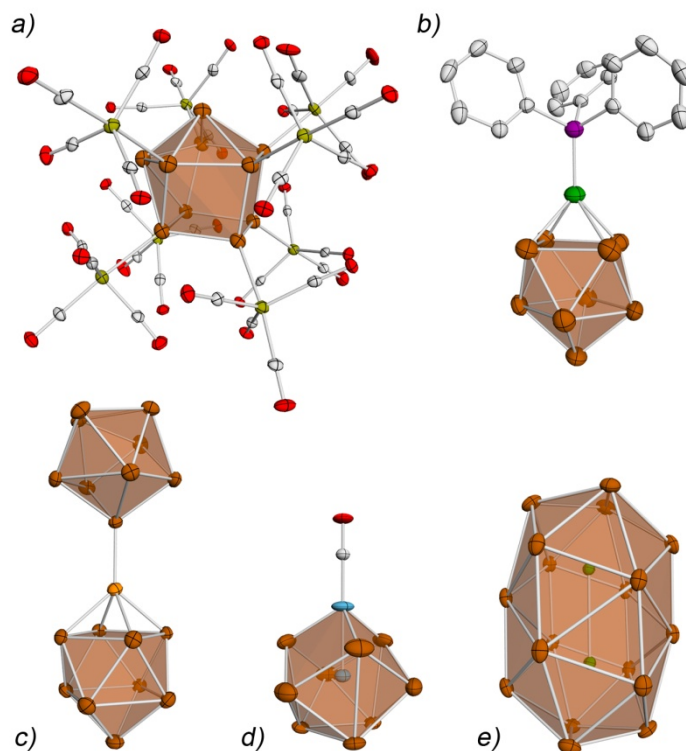


**Figure 14.** Molecular structures of exemplary intermetallic germanium clusters demonstrating the rich coordination chemistry of Zintl ions towards transition metals centers. a) Ligand-stabilized  $[\text{Ge}_{10}(\text{Fe}(\text{CO})_4)_8]^{6-}$ .<sup>109</sup> b)  $[\text{Ge}_9\text{Pd}(\text{PPh}_3)]^{3-}$  featuring the  $\eta^4$ -coordination of a  $\text{Ge}_9$  cluster to a  $\text{Pd}(\text{PPh}_3)$  fragment.<sup>110</sup> c) Stabilization of a ligand-free copper atom in  $[(\eta^4\text{-Ge}_9)\text{Cu}(\eta^1\text{-Ge}_9)]^{7-}$ .<sup>111</sup> d) Endohedrally filled  $[\text{Ni}@(\text{Ge}_9\text{Ni-CO})]^{2-}$  with an additional capping  $\text{Ni}(\text{CO})$  fragment.<sup>112</sup> e) The largest known endohedral Zintl ion  $[\text{Pd}_2@\text{Ge}_{18}]^{4-}$ .<sup>113</sup>

The ability of Zintl anions to serve as ligands for transition metal centers was first demonstrated in simple ligand exchange reactions at transition metal fragments  $\text{TM}(\text{CO})_3$  ( $\text{TM} = \text{Cr}, \text{Mo}, \text{W}$ ) in which labile  $\eta^6$ -arenes were replaced by the polyanionic tetrel clusters  $[\text{E}_9]^{4-}$  ( $\text{E} = \text{Sn}, \text{Pb}$ ) forming  $[\text{E}_9\text{TM}(\text{CO})_3]^{4-}$ .<sup>114-117</sup> Meanwhile, a huge variety of transition metal complexes featuring polytetrel and -pnictide ligands are known, which are mainly obtained from the solutions of Zintl phases and transition metal precursors in the presence of suitable cation-sequestering agents, e.g. cryptands or crown ethers. Typical examples include  $[(\text{ETM}(\text{CO})_5)_6]^{2-}$  ( $\text{E} = \text{Ge}, \text{Sn}; \text{M} = \text{Cr}, \text{Mo}, \text{W}$ ),<sup>118, 119</sup>  $[(\text{MesCu})_2\text{Si}_4]^{4-}$ ,<sup>120</sup>  $[\text{E}_9\text{ZnPh}]$  ( $\text{E} = \text{Si-Pb}$ ),<sup>121</sup> or  $[\text{Ni}(\text{Pn}_7)(\text{CO})]^{3-}$  ( $\text{Pn} = \text{P}, \text{Sb}$ ),<sup>122, 123</sup> and have been comprehensively reviewed in the literature.<sup>4</sup>

Most notably, coordination compounds of ligand-free transition metal centers are equally accessible. Infinite chains of  $[-(\text{HgGe}_9^{2-})]_\infty$  are obtained from the reaction of  $\text{K}_4\text{Ge}_9$  with elemental mercury in ethylenediamine or *N,N*-dimethylformamide,<sup>124, 125</sup> whereas the reaction of  $\text{K}_4\text{Ge}_9$  with the organometallic precursors  $[\text{PPh}_3\text{AuCl}]$  and  $[\text{Cd}(\text{mes})_2]$  yields  $[(\text{Ge}_9)\text{Au}_3(\text{Ge}_9)]^{5-}$  and  $[(\text{Pb}_9)\text{Cd-Cd}(\text{Pb}_9)]^{6-}$ , respectively, each featuring interconnected  $\text{E}_9$

fragments with bridging transition metal centers.<sup>126, 127</sup> In the reaction of ethylenediamine solutions of  $K_4Pb_9$  with  $[Ni(cod)_2]$  or  $[M(PPh_3)_4]$  ( $M = Pd, Pt$ ), the transition metal center is not only entirely stripped of its ligands, but also intercalated into the stabilizing shell of the Zintl anion to form  $[Ni@Pb_{10}]^{2-}$  or  $[M@Pb_{12}]^{2-}$ ,<sup>128, 129</sup> which are amongst the early prototypes of endohedral Zintl ions. While the cage structures of non-filled Zintl anions of group 14 elements are restricted to a maximum of ten skeleton atoms, e.g. in  $[Pb_{10}]^{2-}$ , the additional stabilization stemming from the incorporation of transition metals as central templates for the electron-precise clusters grants access to larger systems, like the above mentioned  $[M@Pb_{12}]^{2-}$ , or even  $[Pd_2@E_{18}]$  ( $E = Ge, Sn$ ).<sup>113, 130</sup> Furthermore, unusual vertex-fused clusters like  $[(Ni@Ge_9)Ni(Ni@Ge_9)]^{4-}$  can be synthesized, the latter being formed in the reaction of  $K_4Ge_9$  with an excess of  $[Ni(cod)_2]$ , presumably *via* a complex reaction cascade involving the ligand substitution of a labile ligand L at the *in situ* formed  $[Ni@(Ge_9Ni-L)]$  by a Ni-centered cluster  $[Ni@Ge_9]$ .<sup>131</sup> These and other impressive examples, like the complex  $[Ni_6Ge_{13}(CO)_5]^{4-}$  or group 15-based representatives as  $[As@Ni_{12}@As_{20}]^{3-}$  or  $[Zn@Zn_8Bi_4@Bi_7]^{5-}$ ,<sup>132-134</sup> can be regarded as "molecular alloys", that is heterometallic molecular compounds which are related to solid state materials in terms of composition, and might even show topological resemblance with regards to their structural motifs. In analogy to Schnöckel's terminology of metalloid clusters (compare section 1.3), they are also referred to as intermetalloid clusters.<sup>97</sup>

## 3.3 Metal cluster compounds

### Cobblestones on the road to solid-state materials

Generally speaking, metal cluster compounds are definite assemblies of metal atoms which are, at least to a substantial degree, stabilized by direct metal-metal interactions and exhibit structural, physical, and chemical properties somewhat in-between those of molecular coordination compounds and the solid state.<sup>135</sup> Against the long-held belief that a direct bonding between two metal atoms is unlikely, if not impossible, first examples of metal-metal bonds were reported in the early 1960s, triggering a fundamental rethinking, and an upsurge in the consequently established field of inorganic cluster chemistry.<sup>136, 137</sup> An initial, albeit very broad definition was set by Cotton in 1966, and describes metal cluster compounds as *"those containing a finite group of metal atoms which are held together entirely, mainly, or at least to a significant extent, by bonds directly between the metal atoms even though some non-metal atoms may be associated intimately with the cluster"*.<sup>137</sup> In principle, this definition comprises both, naked gas phase clusters and soluble, ligand-stabilized clusters. Owing to the wet-chemical synthetic focus of the presented work, however, the following sections will be confined to an introduction of the latter and undeservedly neglect the more physico-chemically oriented branch of the chemistry of metal cluster compounds.

### Ligand-stabilized metal clusters

Based on Cotton's definition (compare previous section), the most primitive model of a ligand-stabilized metal cluster  $[M_nL_m]^{x+/}$  is of binuclear nature and contains one homoatomic metal-metal bond, only. In fact, most of the early compounds featuring direct metal-metal bonding were restricted to comparably small homometallic clusters ( $n = 2-4$ ), with  $[Re_2X_8]^{2-}$  ( $X = Cl, Br$ ),  $[Cp_3Ni_3(CO)_2]$  or  $[Co_4(CO)_{12}]$  being typical examples, whereas oligonuclear clusters, like  $[Nb_6Cl_{12}]^{3+}$  or  $[Rh_6(CO)_{16}]$  posed rare exceptions.<sup>136-140</sup> Irrespective of their sizes, the oxidation states of the comprised metal atoms, or the type of stabilizing ligand, all of these compounds feature a common characteristic, which is the engagement of every metal atom in metal-ligand bonding. Consequently, the properties of these clusters are largely dominated by the presence of the mostly organic ligands and their chemical nature. With increasing size and nuclearity, non-ligand bound, or *naked*, metal atoms are incorporated into the central core (Figure 15), thus diminishing the chemical influence of the stabilizing ligand and contributing to an increasingly metallic behaviour of the compound.<sup>135</sup> In other words: The higher the nuclearity of a metallic cluster, the closer its connection to the extended solid state, and the more likely it is found to mimic certain properties of solid state chemistry.

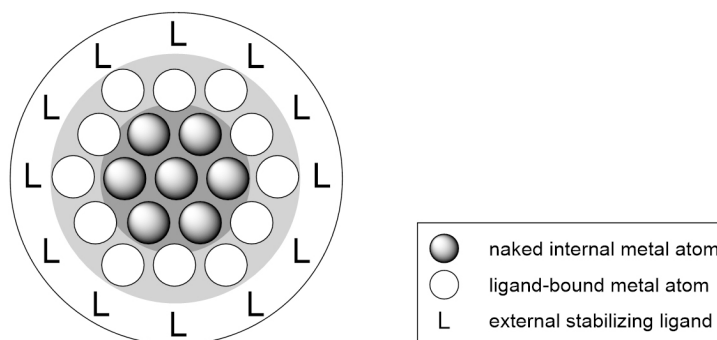
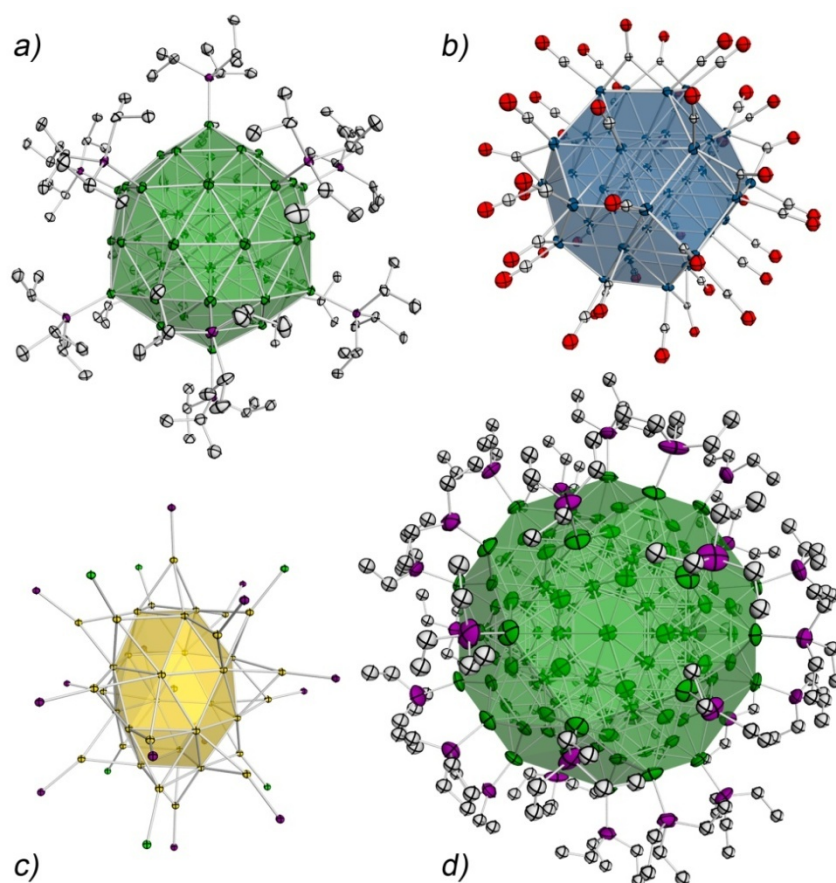


Figure 15. Schematic presentation of a conventionalized spherical ligand-stabilized cluster consisting of an outer ligand shell enwrapping the inner metal core of naked internal, and ligand-stabilized outer metal atoms. Adapted from *Molecular Clusters - A Bridge to Solid State Chemistry*.<sup>135</sup>

Ligand-stabilized metal cluster compounds containing metal atoms which are exclusively engaged in metal-metal bonding, and in which the amount of direct metal-metal contacts outnumbers the amount of metal-ligand bonds, are commonly referred to as "metalloid clusters"; a term that was coined no earlier than 1999 by Schnöckel in order to distinguish this fascinating class of inorganic compounds from the extensive group of metal clusters as defined by Cotton.<sup>141, 142</sup> Stemming from the greek word εἶδος (ideal, prototype), this terminology already seeks to imply the correlation of the topology of the metallic cluster core with the optimized structure of the respective solid state material. Albeit never fully structurally characterized and controversially discussed for years, the monometallic Au cluster  $[\text{Au}_{55}(\text{PPh}_3)_{12}\text{Cl}_6]$  nowadays acts as the undisputed prototype of this family of cluster compounds.<sup>143, 144</sup> It is readily and reproducibly obtained from the reduction of  $[\text{PPh}_3\text{AuCl}]$  with diborane in toluene, and believed to have a closed shell Mackay-type structure as indicated, amongst others, by HR-TEM investigations. Owing to their chemical robustness towards air and moisture, and the resulting relative synthetic ease with which this and other noble metal clusters can be handled, it is not surprising that first representatives of metalloid clusters were largely restricted to group 10 and 11 elements.<sup>9, 145, 146</sup> Amongst those, crystallographically characterized clusters are of particular significance for modern material sciences and nanochemistry, as they allow for a detailed insight into the topology and bonding situation of the metalloid core, and thus may contribute to an in-depth understanding of the formation and nature of the metallic bond. While the extended solid phases of group 10 and 11 elements feature fcc structures, the encapsulation of metallic cores into ligand shells in the "cluster size regime" results in an unprecedented structural diversity which may diverge from the parent material and exhibit closed-packed structures equally well as their combinations, or variations like pentagonal or icosahedral packing motifs. For instance,  $[\text{Au}_{39}(\text{PPh}_3)\text{Cl}_6]$  (hcp-structured metal core, Figure 16c),<sup>147</sup>  $[\text{Ni}_{38}\text{Pt}_6(\text{CO})_{48}\text{H}_{(6-n)}]^{n-}$  ( $n = 3-6$ , ccp-structured metal core),<sup>148</sup> or  $[\text{Pt}_{38}(\text{CO})_{44}\text{H}_m]^{2-}$  (fcc-structured metal core, Figure 16b)<sup>149</sup> all



exhibit polynuclear metal cores derived from closed-packed structural motifs, whereas the central cores of the more recent  $[\text{Pd}_{55}(\text{P}^i\text{Pr}_3)_{12}(\text{CO})_{20}]$  (Figure 16a),<sup>150</sup> or the cluster giants  $[\text{Pd}_{145}(\text{CO})_x(\text{PEt}_3)_{30}]$  ( $x \approx 60$ , Figure 16d)<sup>151</sup> and  $[(\mu_{12}\text{-Pt})\text{Pd}_{(164-x)}\text{Pt}_x(\text{CO})_{72}(\text{PPh}_3)_{20}]$  ( $x \approx 7$ )<sup>152</sup> show complex multi-shell structures based on icosahedral packing motifs. Note that these are just few selected representatives of a growing library of transition metal clusters, which were chosen on behalf of their dense core structures with metal atoms of low valencies, and the neutral ligands they are bearing. Likewise, impressive arrays of coinage metal clusters stabilized by thiolate ligands, such as the fully structurally characterized  $[\text{Au}_{102}(\text{SC}_6\text{H}_4\text{-COOH})_{44}]$  and  $[\text{Au}_{133}(\text{SCH}_2\text{CH}_2\text{Ph})_{60}]$ ,<sup>153, 154</sup> or giant salt-like structures of chalcogen-bridged systems, like  $[\text{Ag}_{320}(\text{S}^t\text{Bu})_{60}\text{S}_{130}(\text{dppe})_{12}]$ <sup>155</sup> have also been reported. However, a full account would be well beyond the scope of the presented work.



**Figure 16.** Molecular structures of exemplary metalloid transition metal clusters illustrate the aesthetic beauty and structural diversity of this class of compounds. a)  $[\text{Pd}_{55}(\text{P}^i\text{Pr}_3)_{12}(\text{CO})_{20}]$  (CO ligands omitted for clarity).<sup>150</sup> The central  $\text{Pd}_{55}$  core forms an icosahedral, two-shell Mackay cluster. b) The metallic core of  $[\text{Pt}_{38}(\text{CO})_{44}]^{2-}$  features a layered fcc structure.<sup>149</sup> c)  $[\text{Au}_{39}(\text{PPh}_3)_{14}\text{Cl}_6]^{2+}$  (phenyl groups of the  $\text{PPh}_3$  ligands omitted for clarity) comprises a central  $\text{Au}_{39}$  moiety with a layered hcp-type structure.<sup>147</sup> d) The giant  $[\text{Pd}_{145}(\text{CO})_x(\text{PEt}_3)_{30}]$  ( $x \approx 60$ ) possesses a capped three-shell  $\text{Pd}_{145}$  core geometry of pseudo-icosahedral symmetry.<sup>151</sup>



While transition metal clusters as described above are usually obtained bottom-up *via* the controlled reduction of suitable organometallic precursors in solution, the access towards comparable main group metal compounds is less intuitive, and synthetically highly demanding. In a variation of conventional metal atom vapor deposition techniques, the *co-condensation technique*, low-valent gaseous group 13 monohalides are prepared at high temperatures from the respective hydrogen halide gas and the elemental metal, to be subsequently trapped in metastable solutions *via* the co-condensation with a suitable solvent containing an additional, stabilizing donor component, such as  $\text{NEt}_3$  or  $\text{Et}_2\text{O}$ .<sup>5, 6</sup> Upon controlled warming of these solutions in the presence of suitable metalated ligands, a delicate balance between metathesis reaction and disproportionation of the group 13 subhalide is established, which eventually results in selective core growth termination. Following this procedure, the growth of the resulting metalloid cluster is largely determined by the disproportionation rate of the particular subhalide which in turn is directly dependent on the applied temperature, as nicely illustrated by the successive series of metalloid aluminium clusters obtained from the stepwise warming of an  $\text{AlCl}$  solution in the presence of lithium bis(trimethylsilyl)amide. Here, the cluster size progresses from  $[\text{Al}_7\text{R}_6]^-$  at  $-7^\circ\text{C}$  to  $[\text{Al}_{12}\text{R}_6]^-$  at room temperature, and finally culminates in  $[\text{Al}_{69}\text{R}_{18}]^{3-}$  at  $60^\circ\text{C}$  ( $\text{R} = -\text{N}(\text{SiMe}_3)_2$ ).<sup>141, 156, 157</sup> Further variations of the starting group 13 monohalide solution, the employed ligand-transfer reagent, or the reaction conditions give rise to a small, but exquisite library of homoleptic, metalloid aluminium and gallium clusters, like  $[\text{Al}_{77}\text{R}_{20}]^{2-}$ ,<sup>158</sup>  $[\text{Al}_{50}\text{Cp}^*_{12}]$ ,<sup>159</sup> or  $[\text{Ga}_{84}\text{R}_{20}]^{4-}$  ( $\text{R} = -\text{N}(\text{SiMe}_3)_2$ ; Figure 17).<sup>160</sup> Likewise, metalloid germanium clusters were shown to be accessible *via* the co-condensation method,<sup>161, 162</sup> as demonstrated with the more recent synthesis of  $[\text{Ge}_8\text{R}_6]$  ( $\text{R} = -\text{N}(\text{SiMe}_3)_2$ )<sup>163</sup> or  $[\text{Ge}_9\text{R}_3]^-$  ( $\text{R} = \text{Si}(\text{SiMe}_3)_3$ )<sup>164</sup> from the reactions of metastable  $\text{GeBr}$  solutions with the respective lithiated ligands.

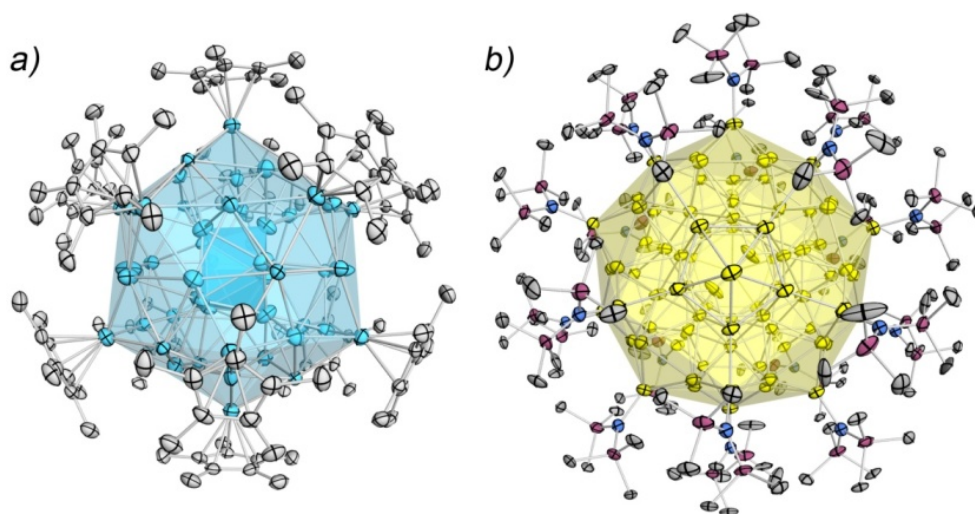


Figure 17. Molecular structures of the metalloid group 13 clusters  $[\text{Al}_{50}\text{Cp}^*_{12}]^{165}$  (a) and  $[\text{Ga}_{84}(\text{N}(\text{SiMe}_3)_2)_{20}]^{4+}$  (b), the largest structurally characterized Ga cluster.<sup>160</sup>

## Rationalizing high-nuclearity metal clusters:

### Models for cluster bonding

Rationalizing the complex structures and bonding situations of metallic, or even metalloid clusters is far from trivial as these compounds are ascribed to a certain transient state between molecular species and the extended solid-state. Consequently, established concepts applying for one or the other might also hold true for metallic clusters, or might equally well fail completely. Given the rich variety of elemental compositions, the broad size regime, the varying degree of metallic character, and the influence of the ligand shell, the assumption of a common concept being able to grasp metallic cluster bonding in its entity is, beyond doubt, illusive. However, certain commonalities of structure and bonding as observed amongst different cluster types can indeed be generalized and translated into reliable concepts.

### Cluster valence electron (CVE) counts

The rationalization of the molecular structures of cluster compounds on the basis of cve counting principles is based on the empirical correlation of recurring structural motifs with common cve counts which was later attributed to the preferred spatial distributions of cluster valence orbitals of n-atomic assemblies as a function of their energy level pattern, and consequently their bonding/non-bonding character, in quantum chemical calculations.<sup>135, 166-168</sup> Based on the 18 electron rule, the cve count includes all valence electrons provided, including the d-electrons of transition metals, without a specification of their contributions to cluster bonding. Accordingly, the number of cluster valence electrons is calculated as the sum of metal valence electrons, additionally provided electrons from the ligands, and the cluster charge. A brief overview of characteristic counts for certain core geometries is given below (Table 4).

While this concept provides a sufficient basis for the accurate description of small, mainly two- and three-connected cluster compounds, increasingly large systems of high nuclearity and connectivity often provide complex geometries and bonding situations which fail to comply with the underlying principles of the cve count. With regards to metalloid clusters, factors like the diminishing HOMO-LUMO gap translating into a higher variety of accessible structures, the electronic and steric influence of the ligand shell, or the incorporation of internal metal atoms and even larger interstitial fragments have to be considered. However, this does not render the cve count useless, and helpful generalizations for large transition metal cluster systems are forthcoming which make use of well-established concepts, like the condensation rules including the capping principle,<sup>169, 170</sup> polyhedral fusion<sup>171</sup> and polyhedral inclusion.<sup>172, 173</sup>

## 3 INTERMETALLIC PHASES AND CLUSTERS

Table 4. Cve counts for representative metal cluster geometries.

geometry	no. of atoms	cve count
dimer	2	34
trimer	3	48
tetrahedron	4	60
butterfly	4	62
square pyramid	4	64
trigonal bipyramid	5	72
square pyramid	5	74
octahedron	6	86
pentagonal pyramid	6	88
trigonal prism	6	90

For simplicity, two limiting cases of large metal atom assemblies are considered. On the one hand, clusters whose bonding is preliminary relying on radial interactions are envisioned as arrangements of naked polyhedral metal cores surrounded by a shell of "metal fragment ligands".<sup>135, 166, 174</sup> A suitable example is  $[\text{Ni}_{38}\text{Pt}_6(\text{CO})_{48}\text{H}_{(6-n)}]^{n-}$  with an observed cve count of 542 ( $44 \cdot 10 + 48 \cdot 2 + 6 = 542$ , for  $n = 0$ ).<sup>148</sup> Its structure can be considered to derive from multiple capping of a central octahedron of six central platinum atoms with 38 additional metal fragments. Under the assumption of radial cluster bonding alone, the expected cve count is then calculated from the optimized cve of an octahedron (86 cve) plus 12 electrons per capping ( $12 \cdot 38$  cve), and sums up to 542 cve. On the other hand, metalloids clusters exhibiting a substantial degree of tangential and radial bonding are considered as fully bonded outer clusters comprising interstitial metal clusters which serve as electron-donating templates, only.<sup>135, 166</sup> Here, the electron count is solely dependent on the electronic requirements of the outer shell as exemplary illustrated for  $[\text{Rh}_{13}(\text{CO})_{24}\text{H}_5]$ .<sup>175</sup> Its structure features a truncated hexagonal pyramid with an interstitial Rh atom. As shown by Lauher, the expected cve count for this shape is 170 which is in accordance with the observed number of cluster valence electrons ( $12 \cdot 9 + 24 \cdot 2 + 9 + 5 = 170$ ).

For more complex arrangements, dissection of the cluster structure into smaller fragments which in turn can be rationalized in a combined approach of limiting models and/or fusion principles may be useful. In this manner, the ellipsoidal-shaped  $\text{Pd}_{59}$  core of  $[\text{Pd}_{59}(\text{CO})_{32}(\text{PMe}_3)_{21}]$  can be treated as a fused dimer of two  $\text{Pd}_{31}$  fragments, each comprising a multiply capped  $\text{Pd}_4$  tetrahedron in an outer  $\text{Pd}_{27}$  "metal ligand" shell (Figure 18).<sup>176</sup> Under the assumption of a polyhedron-centered metal cluster with prevailing radial bonding, the expected cve per fragment sums up to  $60 + 12 \cdot 27 = 384$  cve. Fusion *via* a common  $\text{Pd}_6$  triangle ( $-(48 + 3 \cdot 14) = 90$  cve), and capping of the resulting  $\text{Pd}_{56}$  dimer with the remaining three Pd atoms as apical atoms of three dimer-bridging square pyramids ( $+3 \cdot 74$  cve) whose

basal atoms are shared pairwise with the respective Pd<sub>31</sub> halves ( $-3 \cdot (2 \cdot 34)$  cve) gives a total expected count of 696 cve, in agreement with the observed cve ( $59 \cdot 10 + 32 \cdot 2 + 21 \cdot 2 = 696$ ).

Likewise, the shell structures of metalloid clusters could, in principle, be handled as nested polyhedra of varying degree of radial and/or tangential bonding. However, it ought to be borne in mind that, with increasing cluster size, the diminishing resemblance of a molecular system, and the progressive assimilation of solid state-related properties render electron-counting rules as introduced above more and more questionable.

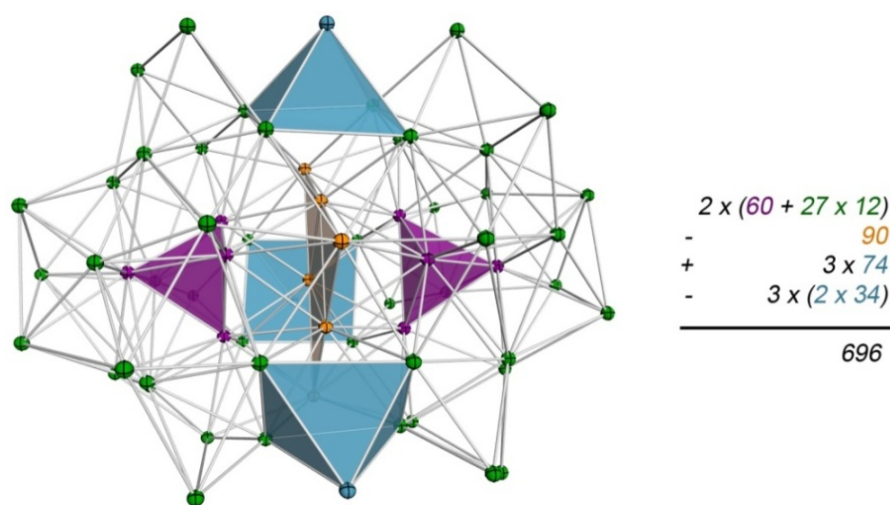


**Figure 18.** Schematic presentation of the Pd<sub>59</sub> core of  $[\text{Pd}_{59}(\text{CO})_{32}(\text{PMe}_3)_{21}]^{176}$  with highlighted relevant polyhedra for the cluster valence electron counting rules as implicated above. The metallic core is rationalized as a dimer of Pd<sub>31</sub> fragments with central Pd<sub>4</sub> cores (violet) inside a shell of 27 Pd atoms (green), which are fused *via* a common Pd<sub>6</sub> triangle (orange). Additional capping with three Pd atoms (blue) as apical atoms of fused square pyramids with edge sharing pairs of basal atoms gives a total cve of 696.

### Polyhedral skeleton electron pair theory (PSEPT) or extended Wade-Mingos rules

Initially developed for electron-deficient boranes and carboranes, the polyhedral skeleton electron pair theory (PSEPT), which is also referred to as the (extended) Wade-Mingos rules, correlates the geometry of a polyhedral cluster skeleton with the number of available skeleton electron pairs (sep).<sup>177</sup> In contrast to the cve count, this alternative concept distinguishes between cluster bonding and non-bonding valence electrons, assuming that internal bonding orbitals can be treated independently of those that are engaged in external cluster framework, or ligand, bonding.<sup>135, 166, 174</sup> Following this approach, ligand contributions can be largely disregarded, which greatly simplifies the correlation between cluster geometry and electron count. For increasingly complex systems however, an explicit assignment of the exact contribution of orbitals and electrons in cluster bonding is difficult and not always feasible.

Furthermore, mixing of bonding and non-bonding orbitals can occur, thus violating the underlying criterion for a valid sep count.

The PSEP-theory is particularly suitable for clusters that exhibit delocalized cluster bonding which is implemented in approximately spherical, deltahedral structures with a maximum number of neighbouring atoms. For polyhedral boranes following the general formula  $B_nH_m^{x-}$ , the resulting structures can be rationalized by increasingly open deltahedra with  $n$  vertices, whereat each BH vertex contributes two electrons to skeletal cluster bonding, while one electron provided by the boron atom is engaged in the external B-H bond. The empirically established correlations given in table 5 are largely supported by molecular orbital analysis deriving a total of  $2n+1$  bonding molecular orbitals, including  $n$  B-H bonds and  $n+1$  skeletal bonding molecular orbitals.<sup>178</sup> Analysis of the latter based on frontier orbital combinations of the involved BH units revealed a combination of radial and tangential interactions with one single bonding radial MO deriving from the in-phase combination of all sp-hybridized orbitals, and a set of bonding and non-bonding tangential MOs stemming from the combination of the perpendicular p-orbitals of the BH fragment.<sup>168, 179</sup>

**Table 5.** Correlation of sep counts and deltahedral structures of electron-deficient main group and transition metal clusters according to Wade-Mingos rules.

name	sep count	structure
closo	$n + 1$	polyhedron with $n$ occupied vertices
nido	$n + 2$	$(n+1)$ polyhedron with $n$ occupied vertices
arachno	$n + 3$	$(n+2)$ polyhedron with $n$ occupied vertices
hypso	$n + 4$	$(n+3)$ polyhedron with $n$ occupied vertices

Upon realization of the comparable cluster bonding requirements of certain organic and organometallic fragments, such as BH,  $CH^+$  or  $M(CO)_3$ , an extension of the PSEP-theory to include a rational approach on the cluster geometries of other main group elements and transition metals was developed, based on the isolobal principle.<sup>180, 181</sup> Formally defined as isolobal if "*the number, symmetry properties, approximate energy and shape of their frontier orbitals as well as the number of electrons occupying them are similar*", two such fragments exhibit similar bonding characteristics and thus can be described on common electronic grounds. Consequently, the isolobal principle provides a helpful simplification for the identification of orbitals that efficiently contribute to cluster bonding, and allows for the rationalization of cluster structures of other main group elements and even the transition metals using the extended Wade-Mingos rules. Following this principle, transition metal clusters can be correlated to polyhedral borane structures, as illustrated by the simple example of  $[Ru_6(CO)_{18}]^{2-}$ .<sup>182</sup> Owing to the isolobal analogy of  $M(CO)_3$  and BH fragments, each

$\text{Ru}(\text{CO})_3$  unit contributes two electrons to the internal skeletal cluster bonding. An additional two electrons stem from the overall charge of the molecule, thus giving a total sep count of  $\frac{1}{2} \cdot (6 \cdot 2 + 2) = 7$ , or  $n + 1$ , which satisfies the criterion of a *closo* cluster and matches the observed octahedral geometry. Likewise, the PSEP-theory can be consulted for a satisfactory rationalization of the deltahedral structures of post-transition metal cluster, such as the Zintl ions (compare section 1.2).<sup>4</sup> In the structures of anionic polytetrel clusters, each vertex is occupied by a bare group 14 element which, being isolobal to BH, provides two electrons for skeletal bonding. The remaining two electrons stay unavailable for cluster bonding as an external lone pair. Quite similarly, the bare group 15 atoms forming the vertices of the polypnictides are isolobal to C-H fragments, as e.g. found in carboranes, and provide three electrons for cluster bonding. In the exemplary case of  $[\text{E}_9]^{4-}$ , the resulting sep count of  $\frac{1}{2} \cdot (9 \cdot 2 + 4) = 11$ , or  $n + 2$ , indicates a *nido* cluster that is derived from an  $n + 1$  vertex *closo* polyhedron by removal of the vertex of highest connectivity. The expected geometry of a monocapped square antiprism, as derived from the *closo* bicapped square antiprism, indeed coincides with the observed structure.

While a broad range of particularly small and medium-sized metal clusters can be rationalized on the basis of the extended Wade-Mingos rules, larger assemblies often fail to meet their requirements. One of the rare examples to be adequately described is the metalloid group 13 cluster  $[\text{Ga}_{22}(\text{Si}^t\text{Bu}_3)_8]$ , whose structure comprises an octacapped, centered cuboctahedron with one triangular face replaced by a quadrilateral face (Figure 19).<sup>183</sup> If each  $\text{Ga}(\text{Si}^t\text{Bu}_3)$  unit contributes two electrons to internal cluster bonding, and each naked gallium atom provides one further electron while keeping two electrons as an external lone pair, the sep count is calculated as  $\frac{1}{2} \cdot (8 \cdot 2 + 14 \cdot 1) = 15$ . Considering that the sep counts associated with capped clusters are identical to those of their primary geometries, this correlates with  $n + 1$  for an eightfold capped *closo* 14-vertex polyhedron and renders a suitable description for the given structure, provided that the centered  $\text{Ga}_{14}$  core can be regarded a *closo* cluster for  $n = 14$ .



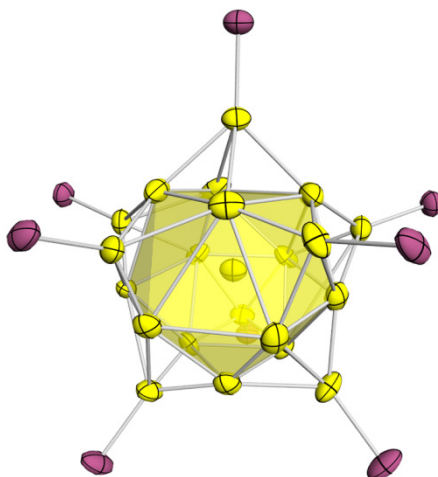


Figure 19. Central structural motif of the molecular structure of  $[\text{Ga}_{22}(\text{Si}^t\text{Bu}_3)_8]$  (carbon and hydrogen atoms omitted for clarity).<sup>183</sup> The  $\text{Ga}_{22}$  core contains 14 naked gallium atoms forming a centered, cuboctahedron-derived structure, and 8 ligated GaR fragments capping the quadrilateral faces. Based on the extended Wade-Mingos rules, its geometry can be rationalized as an eightfold capped closo  $\text{Ga}_{14}$  polyhedron.

### Jellium model and the superatom concept

In analogy to the atomic theory defining particularly stable electronic noble gas configurations for filled atomic orbitals following the Madelung or Klechkovskii rule, "magic numbers" of closed electronic shell configurations can be identified for the molecular orbitals of metallic clusters on the basis of the jellium model.<sup>184, 185</sup> The resulting "superatom electronic theory" provides a means to assess the stability and chemical nature of metal clusters and nanoparticles, and has been equally successfully applied for the description of bare gaseous metal clusters, gas-phase metal clusters bearing few simple ligands, and ligand-protected metalloid clusters, like gold thiolate or group 13 clusters.<sup>186</sup>

Initiated by the recognition of the mass abundances of bare alkali metal clusters produced by supersonic expansion in molecular beams during mass spectrometric experiments, the jellium model was developed in an approach to model the electronic structure of medium and large metal atom assemblies.<sup>187, 188</sup> In its simplest variation, the metallic cluster core is described on the basis of a delocalized electron cloud that interacts with the spherical Coulomb potential of a homogeneous positive background charge generated by the collective treatment of the cluster metal ions. On this basis, the one-electron energy eigenvalues of the cluster's molecular orbitals can be calculated providing discrete electronic energy levels with a shell-like structure.<sup>185</sup> Albeit overall comparable to the atomic levels in a free atom, the ordering of the electronic states of the delocalized "superatomic orbitals" is different and follows the sequence

$$1S^2 | 1P^6 | 1D^{10} | 2S^2 1F^{14} | 2P^6 1G^{18} | 2D^{10} 3S^2 1H^{22} | 2F^{14} 3P^6 1I^{26} | \dots$$

with strong shell closures observed for  $n = 2, 8, 18, 34, 58, 92, 138, \dots$  electrons.<sup>184, 185</sup> It is of note that depending on the underlying details of the applied mean field potential, shell closures for  $n = 20, 40, 68$  or  $70$  are equally reasonable, and stable clusters of this configuration have been reported.

For bare gas-phase metal clusters  $(A_N)^z$ , their relative stability can be predicted by simple correlation of the required shell-closing electron count  $n$  with the sum of the number  $N$  of core metal atoms  $A$  times their atomic valence  $v_A$ , if applicable under consideration of the overall charge  $z$ . A prototypical example featuring full shell closure is  $Al_{13}^-$  with an electron count of  $13 \cdot 3 + 1 = 40$ .<sup>189</sup> For ligand-stabilized metallic clusters, however, estimation of the delocalized cluster valence electrons is less trivial and dependent on the electronic influence of the ligand shell. Thus, for the description of a ligand-stabilized superatom complex  $(L_s \cdot A_N X_M)^z$  in which the central metallic core is stabilized by additional electron-withdrawing ligands  $X$ , and weakly bound ligands  $L_s$  with non-electron-withdrawing, dative bonding only, the electron count is defined as

$$n = N \cdot v_A - M \cdot v_X - z$$

with  $M$  being the amount of electron withdrawing ligands, and  $v_X$  quantifying the amount of electrons withdrawn.<sup>190, 191</sup> It goes without saying that this approach demands for a full understanding of the precise composition on the one hand, but on the other hand also requires knowledge on the nature of the surface chemical bond, both prerequisites which have greatly hampered the extension of the superatom concept to this class of ligand-stabilized compounds as they are largely dependent on a full structural characterization. This is impressively illustrated by the example of  $[Au_{102}(p\text{-MBA})_{44}]$  ( $p\text{-MBA} = para\text{-mercaptobenzoic acid } SC_7O_2H_5$ ), which can be understood as a 58-electron closed shell superatom.<sup>153, 191</sup> Following the "divide-and-protect" structural concept commonly applied for Au thiolate clusters, its molecular structure is more accurately described as  $[Au_{79}(Au_{23}(p\text{-MBA})_{44})]$  as it contains a central non-ligated  $Au_{79}$  core of  $D_{5h}$  symmetry which is protected by a gold-thiolate layer of 21  $RS\text{-}(AuSR)_x$  units ( $x = 1, 2$ ; Figure 20). Under the assumption that the latter act as one-electron withdrawing ligands, the electron count of  $n = 79 \cdot 1 - 21 \cdot 1 = 58$  is obtained which corresponds to a full shell closure with  $1G^{18}$  configuration for the highest occupied set of molecular orbitals. Notably, this correlation only becomes evident as a consequence of the full structural characterization of the metalloid cluster revealing its core-shell geometry and the involvement of 23 gold atoms in external ligand bonding forming 21 electron-localizing units.



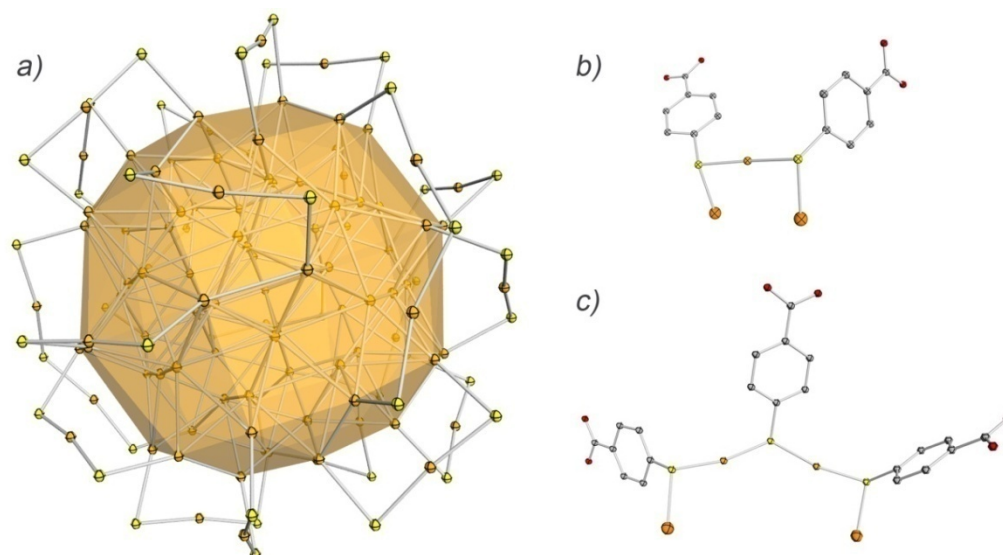


**Figure 20.** Molecular structure of  $[\text{Au}_{102}(\text{p-MBA})_{44}]$  ( $\text{p-MBA} = \textit{para}$ -mercaptobenzoic acid,  $\text{SC}_7\text{O}_2\text{H}_5$ ).<sup>153</sup> a) Core-shell geometry of the Au thiolate cluster (organic ligands with exception of the sulfur linkages omitted for clarity, Au orange, S yellow). The bare  $\text{Au}_{79}$  core is embedded in a passivating  $\text{Au}_{23}(\text{p-MBA})_{44}$  mantle which is composed of b) nineteen  $\text{RS}-(\text{AuSR})$  and c) two  $\text{RS}_2-(\text{AuSR})_2$  units (core gold atoms are depicted as larger, dark orange ellipsoids for b and c).

Quite similarly, the topologies of a handful of metalloids group 13 clusters can be rationalized on the basis of the superatom concept, although an extension of the jellium model to divalent and trivalent metals can be difficult as the free-electron approximation is most compatible with the actual electronic situation in the monovalent alkali metals.<sup>185, 192</sup> Furthermore, accommodating more valence electrons will increase the orbital energy of the metal atom which in turn enhances splitting of spherical symmetry degeneracies. In other words, the more valence electrons the system contains, the more pronounced its deviation from the assumed uniformly distributed, spherical background potential due to a higher impact of the effectively non-uniform distribution of nuclei in the cluster core.<sup>193, 194</sup> Irrespective of these constraints, the stability of a handful of representatives, like the metalloids gallium clusters  $[\text{Ga}_{22}(\text{N}(\text{SiMe}_3)_2)_8]$ ,  $[\text{Ga}_{22}(\text{N}(\text{SiMe}_3)_2)_{10}]^{2-}$  or  $[\text{Ga}_{23}(\text{N}(\text{SiMe}_3)_2)_{11}]$  can be rationalized on the basis of the jellium model, with the given examples resembling closed shell superatom clusters with 58-valence electrons.<sup>195</sup> For the corresponding electron counts, the bistrimethylsilylamide ligand is treated as a one-electron-withdrawing ligand which gives a count of  $22 \cdot 3 - 8 = 58$ ,  $22 \cdot 3 - 10 + 2 = 58$ , and  $23 \cdot 3 - 11 = 58$ , respectively. Likewise, closing of the manifold of  $2\text{F}^{14}\text{P}^6\text{I}^{26}$  is observed in Schnöckel's famous metalloids aluminium cluster  $[\text{Al}_{50}\text{Cp}^*_{12}]$ , for which a magic number electron count of  $n = 138$  is calculated ( $50 \cdot 3 - 12 = 138$ ).<sup>196</sup> The result of the simple electron count is supported by quantum mechanical analysis of the electronic structure providing a showcase example of the superatomic orbital filling sequence with significant energy gaps between the designated

electronic shells (Figure 21). Particular emphasis is laid on the appreciable HOMO-LUMO gap (0.9 eV) which is considered an indicator for the presence of closed electronic shell structures, and has also been observed for other jellium clusters, such as the 14-electron cluster  $[\text{Au}_{38}(\text{SPh-}^t\text{Bu})_{24}]^{197}$  or the above mentioned  $[\text{Au}_{102}(p\text{-MBA})_{44}]^{191}$ . In line with the high electronic stability of these superatomic species, physico-chemical properties like a comparably high chemical stability, a high ionization potential and a comparably low electron affinity are usually observed.

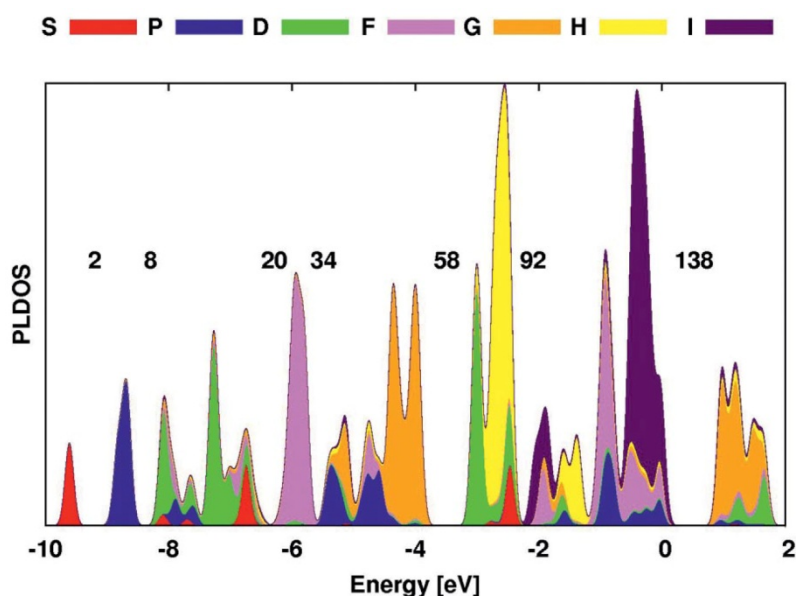


**Figure 21.** Projected local density of states (PLDOS) for  $[\text{Al}_{50}\text{Cp}^*_{12}]$  as a showcase example of the superatomic orbital filling sequence with significant energy gaps following electronic shell closures for the magic numbers  $n = 2, 8, 20, 34, 58, 92, 138$ . Reprinted with permission of P. A. Clayborne, O. Lopez-Acevedo, R. L. Whetten, H. Grönbeck, H. Häkkinen, *Eur. J. Inorg. Chem.* 2011, 2011 (17), 2649-2652. Copyright 2011 Wiley-VCH Verlag GmbH & Co. KGaA, Weinheim.

### Excursus: Closed shell geometries, or magic numbers of sphere packings

While the definition of closed-shell metal clusters on the basis of the jellium model and the herein rooted superatom concept refers to the electronic structure of these compounds featuring particularly stable, "magic" cluster electron counts which correlate to strong electronic shell closures, the same terminology is often used for clusters whose core geometries comprise successive, concentric shells of metal atoms. Corresponding "magic" atom number clusters can be traced back to 1962, when a thought-experiment was published by Mackay in which he derived a closed multiple-shell structure of icosahedral geometry from the dense non-crystallographic packing of equal spheres, and predicted its natural occurrence,

albeit admitting that "there are several reasons which make it unlikely that large numbers of atoms might be found arranged this way".<sup>80</sup> Almost twenty years later, initial experimental evidence pointing at a *de facto* preferred formation of such geometrically closed shell structures was provided by the observance of mass abundances of gaseous magic number-sized Xenon clusters in mass spectrometric experiments.<sup>198</sup> Meanwhile, magic number clusters with 13, 55, 147, 309, 561, ... atoms are recurring motifs in experimental and theoretical studies of naked elemental clusters and ligand-stabilized metal clusters alike; their stunning stability across the periodic table being attributed to their high sphericity and the inherent minimization of surface energies following classical Wulff construction principles.<sup>199</sup> The significant importance of Mackay's concept with regards to the structures of intermetallic compounds, *i.e.* complex metallic alloys and quasicrystalline phases (also see section 1.1) has been summarized elsewhere.<sup>81</sup> Herein, a certain emphasis is laid on the more recent discovery of according motifs in the crystallographically elucidated molecular structures of metalloidal clusters, like  $[\text{Pd}_{55}(\text{P}^i\text{Pr}_3)_{12}(\mu_3\text{-CO})_{20}]$ ,<sup>150</sup>  $[\text{Pd}_{145}(\text{CO})_{72}(\text{PEt}_3)_{30}]$ ,<sup>151</sup>  $[(\mu_{12}\text{-Pt})\text{Pd}_{164-x}\text{Pt}_x(\text{CO})_{72}(\text{PPh}_3)_{20}]$ <sup>152</sup> and  $[\text{Au}_{133}(\text{SC}_6\text{H}_4\text{-p-}^t\text{Bu})_{52}]$ ,<sup>154</sup> all of which feature (interior) icosahedral Mackay-type shell geometries.

### Metal aromaticity

The concept of aromaticity dates back to 1865, when the German chemist Friedrich August Kekulé coined the term to classify a particularly unreactive group of benzenoid hydrocarbons, with the actual nomenclature being inspired by the characteristic odour those compounds possessed.<sup>200, 201</sup> Albeit initially considered a purely "organic" concept applicable for mono- or polycyclic planar conjugate hydrocarbons, down to the present day numerous extensions were developed to include heterocyclic compounds, be they of organic or inorganic nature, three-dimensional transition metal sandwich compounds (e.g. ferrocenes), boron-based clusters, fullerenes, organometallic complexes, and even purely inorganic metal clusters as observed in the gaseous phase or the solid state.<sup>202-205</sup> Despite its vibrant use in all disciplines of chemistry, the overall concept of aromaticity constitutes one of the most diffuse chemical concepts lacking a universally valid definition, and can hardly be expressed in terms of measureable quantities. There is, however, a toolbox of criteria that have emerged as reliable indicators for aromaticity, including structural equalization and chemical inertness, magnetic properties, like "London diamagnetism", diatropic ring currents or nucleus independent chemical shifts (NICS), and characteristic electronic features such as the molecular orbital pattern or a high degree of electron delocalization.<sup>206, 207</sup>

Metalloaromaticity in the sense of all-metal aromaticity was first observed in the triangular cyclogallene dianion  $\text{Na}_2[(\text{Mes}_2\text{C}_6\text{H}_3)\text{Ga}]_3$  reported by Robinson *et al* (Figure 23).<sup>208</sup> Its molecular structure depicts the equilateral triangular arrangement of three  $\text{Ga}(\text{Mes}_2\text{C}_6\text{H}_3)$

units with the resulting  $\text{Ga}_3$  triangle being capped by two sodium atoms in perfectly central positions. Like its organic analogue  $\text{C}_3\text{H}_3^+$ , the compound can be described as a  $4n + 2$  Hückel  $\pi$ -aromatic system bearing two delocalized electrons in a  $3c2e$ -bond, whereat the electrons involved stem from electron donation from the alkali metals and are localized in the otherwise empty p-orbitals of the three gallium atoms. Note that the latter exhibit an overall  $sp^2$  hybridization, each of them being engaged in bonding to one *m*-terphenyl ligand and the two remaining gallium atoms. Quite similarly, the triangular heteroleptic  $\text{Pd}_3$  cluster  $[\text{Pd}_3(\mu\text{-SPh})_3(\text{PPh}_3)_3]^+$  represents the first transition metal analogue of  $\text{C}_3\text{H}_3^+$  (Figure 23).<sup>209</sup> Here, molecular orbital analysis revealed the formation of a set of occupied MOs arising from atomic d-orbital contributions which effectively contribute to delocalized metal-metal bonding involving all three Pd atoms, and exhibit  $\sigma$ -,  $\pi$ - and  $\delta$ -symmetry, respectively (Figure 22). In both cases, further typical indicators supportive of the proposed aromatic character of the system were observed, like negative values of computed NICS, or experimentally observed upfield shifts of NMR spectroscopic signals of atoms located perpendicular to the respective  $\text{M}_3$  triangle.

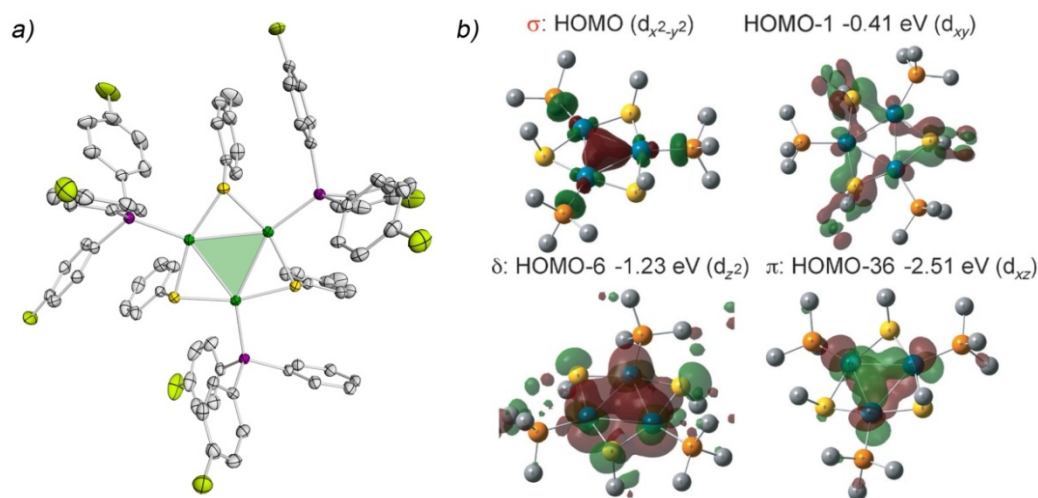


**Figure 22.** a) Molecular structure of  $[\text{Pd}_3(\mu\text{-SPh})_3(\text{PPh}_3)_3]^+$  in the solid state (H atoms omitted for clarity, Pd, S, P, C, F depicted as dark green, yellow, purple, grey, and light green ellipsoids at 30% probability). b) Selected molecular orbitals of  $[\text{Pd}_3(\mu\text{-SPh})_3(\text{PPh}_3)_3]^+$  which were found to contribute to delocalized  $3c2e$ -bonding between the three Pd atoms. Energies are given relative to the HOMO and atomic orbital contributions are given in brackets. Adapted from and reprinted with permission of S. Blanchard, L. Fensterbank, G. Gontard, E. Lacôte, G. Maestri, M. Malacria, *Angew. Chem. Int. Ed.* **2014**, 53 (7), 1987-1991. Copyright 2014 Wiley-VCH Verlag GmbH & Co. KGaA, Weinheim.

While the above mentioned examples constitute analogues of  $\pi$ -aromatic  $C_3H_3^+$ , rare isolobal analogues of triatomic hydrogen ion  $[H_3]^+$ , the prototypical example of a  $\sigma$ -aromatic molecule with delocalized 3c2e-bonding, have also been reported with  $[(LAu)_3]^+$  ( $L = 1,3$ -bis(2,6-diisopropylphenyl)imidazol-2-ylidene),<sup>210</sup>  $[(Cp^*Zn)_3]^+$  and  $[Zn_2CuCp^*_3]$ .<sup>211</sup> For  $[(LAu)_3]^+$  (Figure 23), a striking resemblance to  $[H_3]^+$  with regards to the electronic structure of their frontier orbitals has been reported. These are composed of two doubly degenerate LUMOs build with predominant p-AO contribution and a  $\sigma$ -type HOMO which mainly results from the in-phase combination of s-type atomic orbitals and is delocalized over the entire  $Au_3$  unit. On this basis, and taken into consideration complementary factors like the isolobal analogy of  $[LAu]^+$  and  $[H]^+$ , the high symmetry of the compound and its large HOMO-LUMO gap, the  $\sigma$ -aromaticity of  $[(LAu)_3]^+$  was proposed. The *de facto*  $\sigma$ -aromatic character of bare and ligand-stabilized  $[Au_3]^+$  clusters was later on confirmed by independent theoretical studies including the calculations of valuable indicators, like NICS, diatropic ring current density plots, and resonance energies.<sup>212</sup> Accordingly, the  $\sigma$ -aromaticity of  $[(LAu)_3]^+$  can be traced back to a bonding situation that is dominated by 6s orbital contributions of Au, whereas contributions from the d-orbitals are negligible owing to a full occupation of bonding and antibonding MOs with d-orbital contribution. With two 6s-electrons available, the  $4n + 2$  Hückel rule for aromatic systems is fulfilled for  $n = 0$ .

A high degree of  $\sigma$ -aromaticity was also observed for the recently reported  $[(Cp^*Zn)_3]^+$  (Figure 23) and  $[Zn_2CuCp^*_3]$ , whose bonding situations were investigated in detail by energy decomposition analysis.<sup>211</sup> In both cases, the major contribution was found to arise from  $\sigma$ -donation  $[Zn_2Cp^*_2] \rightarrow [MCp^*]^{n+}$  ( $n = 0, 1$  for  $M = Cu, Zn$ ) into the formally empty 4s orbital, a situation which can also be understood as a "side-on" coordinated  $Zn_2Cp^*_2$  complex to an electron-deficient  $MCp^*$  fragment, in analogy to side-on coordinated dihydrogen complexes of coordinatively unsaturated transition metal centers  $[L_nM(\eta^2-H_2)]$ .

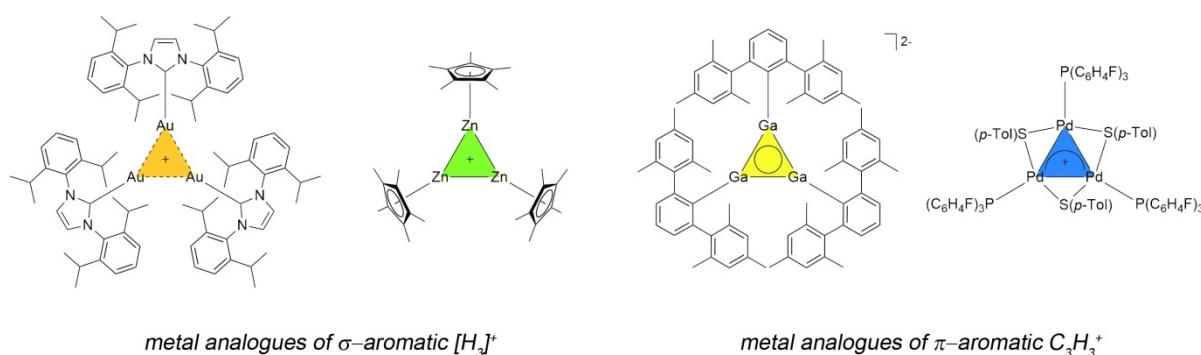


Figure 23. Selected examples of metal analogues of  $\sigma$ -aromatic  $[H_3]^+$  and  $\pi$ -aromatic  $C_3H_3^+$ .<sup>208-211</sup>

Although the manifestation of metalloaromaticity in organometallic coordination compounds is largely restricted to small metallacycles of three to four metal atoms, its potential significance for a conceptual understanding of larger assemblies should not be underestimated. Reasoning that the three-dimensional polyhedral geometries of large metal clusters are constructed from tightly bound triangular and quadrilateral building blocks, one might argue that metalloaromatic contributions to cluster stabilization are conceivable. In fact, recent results reporting on the isolation of the stable  $[\text{K}([2.2.2]\text{crypt})]^+$  salt of a  $[\text{Au}_2\text{Sb}_{16}]^{4-}$  polyanion possessing two all-metal  $\sigma$ -aromatic  $\text{AuSb}_4$  fragments provide strong evidence for this thesis.<sup>213</sup> The rod-like  $\text{Sb}_{16}$  cage represents the largest unfragmented antimony polyanion isolated to date, and its stability is believed to originate from substantial contributions from the verifiable  $\sigma$ -aromaticity of the two embedded  $\text{AuSb}_4$  units. Additionally, the rich structural variety of all-metal aromatic clusters studied in the gas phase or as components of solid-state materials goes well beyond small three- and four-membered ring systems and further implies a potential verification of aromatic stabilization in three-dimensional ligand-stabilized clusters in due course.<sup>203-205</sup> Intermetallic phases like the ternary  $\text{Na}_8\text{BaPb}_6$  and  $\text{Na}_8\text{BaSn}_6$ , or amalgam ( $\text{Na}_3\text{Hg}_2$ ), were found to comprise planar,  $\pi$ -aromatic  $\text{Pb}_5^{6-}/\text{Sn}_5^{6-}$  rings, or multiply aromatic square  $\text{Hg}_4^{6-}$  units, respectively as building blocks.<sup>214, 215</sup> With regards to the latter, multiple aromaticity refers to the simultaneous observance of  $\sigma$ - and  $\pi$ -aromaticity stemming from the occupation of delocalized, bonding  $\sigma$ - and  $\pi$ -molecular orbitals, alike. Based on model calculations of its molecular orbital pattern,  $\text{Hg}_4^{6-}$  was described as isoelectronic to the gaseous prototypical example of  $\text{Al}_4^{2-}$ .

*Note: In analogy to multiple aromaticity, conflicting aromaticity in terms of contradicting contributions of aromatic and antiaromatic character might equally well occur, as for example observed in the most remarkable  $\text{K}_2[\text{Ga}_4(\text{C}_6\text{H}_3\text{-}2,6\text{-Trip}_2)_2]$  ( $\text{Trip} = \text{C}_6\text{H}_2\text{-}2,4,6\text{-}^i\text{Pr}_3$ ) reported by Power et al.<sup>216, 217</sup> The central square  $\text{Ga}_4$  unit possesses two delocalized  $\pi$ -electrons, formally making it  $\pi$ -aromatic. At the same time, only six electrons are available for  $\sigma$ -bond formation amongst the four gallium atoms, which according to simple electron-counting rules, invokes  $\sigma$ -antiaromaticity and would, in principle, favour a rhombohedral structure. The nonetheless observed almost perfectly square planar geometry of the  $\text{Ga}_4$  core originates from contributions of the hybridization of the two ligand-bound gallium atoms which, by coincidence, annuls the rhombus distortion.*

Experimental studies on gaseous metal clusters prepared by laser vaporization already transferred the concept of metalloaromaticity into the third dimension. First bimetallic systems exhibiting three-dimensional all-metal aromaticity were reported with the prototypical mixed-metal clusters  $\text{MAl}_6^-$  ( $\text{M} = \text{Li}, \text{Na}, \text{K}, \text{Cu}, \text{Au}$ ) in a combined

photoelectron spectroscopic and ab-initio study.<sup>218</sup> The inherent  $Al_6^{2-}$  anion was shown to possess an octahedral  $O_h$  ground state which can be understood as the fusion of two aromatic  $Al_3^-$  units, whose aromatic character is retained upon combination, thus rendering three-dimensional  $\sigma$ - and  $\pi$ -aromaticity for the resulting  $Al_6^{2-}$  unit. Analysis of its electronic configuration revealed the full occupation of six low lying molecular orbitals that were localized into six lone pairs residing at the aluminium atoms, along with eight electrons occupying strongly delocalized orbitals stretching the entire cluster. These satisfy the  $2(n+1)^2$  counting rule for spherical aromaticity as originally introduced for the description of fullerenes.<sup>202</sup> Spherical aromaticity was also reported for the tetrahedral gold cluster  $Au_{20}$  which is accessible by laser vaporization of a pure Au target with a helium carrier gas.<sup>219</sup> Here, negative NICS values and the analysis of the molecular orbital pattern speak in favour of an aromatic stabilization. However, considering that an electron count of  $n = 20$  electrons in tetrahedral systems also fulfils the criterion of the superatom concept which is likewise based on a delocalized electron distribution, care ought to be taken with regards to rash classification of large systems as aromatic, and a categorization primarily based on the basis of negative NICS values is to be considered with caution. As initially introduced, aromaticity itself is a diffuse concept that demands for an extensive analysis in terms of multiple measures. This holds particularly true for large metal clusters, as the inherent delocalized metal bonding provides a conceptually different setting for aromaticity probes when compared to organic systems, and established procedures have to be carefully re-evaluated with regards to their suitability. Against this backdrop, early assessments of some Zintl ions as spherically aromatic systems mainly on the basis of negative NICS values have to be critically revisited.<sup>220</sup> It is of note that current reviews on all-metal aromaticity fail to include these reports. Instead, more recent accounts reporting on two intriguing metal clusters incorporated in the extended metal-organic frameworks of  $[Mn^I_8Mn^{II}_3(H_2O)_6(HL)_{12}](OH)_2 \cdot 17H_2O)_n$  and  $Na_{2.6}K_{1.4}([Na(DMF)]_8[Zn^I_8(HL)_4(L)_8]) \cdot 8H_2O \cdot 2HL \cdot DMF$  ( $L =$  tetrazole dianion) are highlighted.<sup>221, 222</sup> In both cases, unusual cubic  $M_8$  units ( $M = Mn, Zn$ ) with multicentered M-M bonding and extensive electron delocalization over the  $[M_8]$  cube are observed, which are described as the first representatives of "cubic" aromaticity on the basis of complementary experimental and theoretical studies. Using the example of  $[Zn_8]$  (Figure 24), analysis of its bonding pattern revealed the formation of eight delocalized molecular orbitals stemming from combinations of the underlying s-AOs with slight mixing from Zn  $4p$  and  $3d$  contributions.<sup>222</sup> Amongst these, four bonding orbitals are fully occupied resulting in electron delocalization over the entire cube. The actual aromatic character of the perfectly symmetric  $[Zn_8]$  unit is further supported by an unusual chemical robustness, and an array of theoretical analyses including electron localization function (ELF) calculations, determination of the considerably negative NICS indices at cubic-, face- and bond-centres, and the calculation of an unexpectedly large resonance energy.



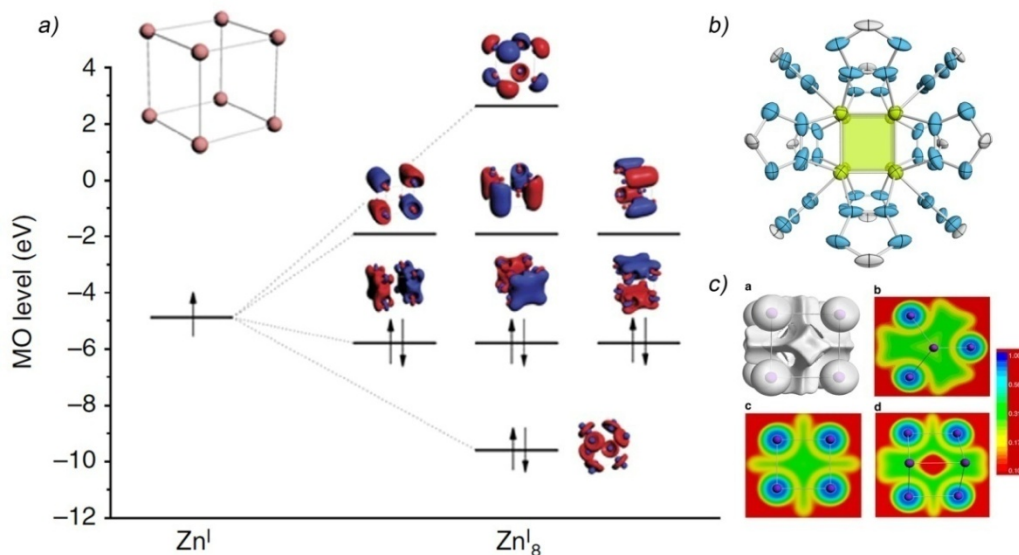


**Figure 24.** a) Molecular orbital pattern of  $Zn_8^I$  as derived from s-atom orbital contributions. Eight delocalized MOs are formed, whereat the four bonding MOs with  $a_{1g}$  and  $t_{1u}$  symmetry are fully occupied. b) Molecular structure of the cluster  $(Zn_8(HL)_4(L_8))^{12-}$  (H atoms omitted for clarity, Zn, N, C depicted as green, blue and grey ellipsoids at 30 % probability, respectively). The unique tetragonally distorted  $Zn_8^I$  cube features direct multi-centred Zn-Zn bonding with a high degree of electron delocalization. c) Electron localization function (ELF) calculations performed for  $Zn_8^I$  with depiction of the isosurface of the cube (a), and top views of the triangular (b), square (c) and diagonal rectangular (d) surfaces. ELF contours show significant electron-pair density along the Zn-Zn vertices in favour of direct Zn-Zn bonding. Adapted and reprinted by permission from Macmillan Publishers Limited: Springer Nature, Nature Communication "A multicentre-bonded  $[ZnI]_8$  cluster with cubic aromaticity" by P. Cui, H.-S. Hu, B. Zhao, J. T. Miller, P. Cheng, J. Li, 2015.



## 3.4 Bottom-up! From a molecular view to the solid state

### "What we can learn from metalloid clusters"

Although a systematic investigation of structure and property relationships amongst the just introduced family of metalloid cluster compounds, and a comprehensive correlation to solid state materials is still hindered by the limited abundance of suitable model systems, fascinating findings already imply the suitability of these compounds as potential model systems for extended solid phases with regards to topological, physical and chemical properties.<sup>5, 6, 9, 135, 146, 161, 162, 223</sup> From a generally accepted point of view, metalloid clusters are regarded as snapshots on the way from single metal atoms to the metallic phase, and are considered to provide fundamental insights into elementary processes governing metal formation and dissolution. Staying with the examples of metalloid clusters of the p-block and transition metal elements, Schnöckel's prototypical metalloid group 13 clusters are, beyond doubt, the most thoroughly studied metal atom assemblies in this size regime.<sup>5, 6, 223</sup> Insights into the stepwise growth of such aluminium and gallium clusters during co-condensation experiments were obtained by careful adjustment of reaction conditions, and the exemplary successive sequence of  $\text{Al}_7\text{R}_6^- \rightarrow \text{Al}_{12}\text{R}_8^- \rightarrow \text{Al}_{69}\text{R}_{18}^{3-}$  has already been addressed in section 1.3. Furthermore, MALDI mass spectrometric experiments on the behaviour of  $[\text{AlCp}^*]_4$  upon laser irradiation revealed the formation of a metalloid cluster cation  $[\text{Al}_8\text{Cp}^*_4]^{n+}$ , which is assumed to stem from multiple coordination of monomeric  $\text{AlCp}^*$  units to undissociated  $[\text{AlCp}^*]_4$  with subsequent elimination of  $\text{AlCp}^*_3$ .<sup>224</sup> On this basis and further supported by DFT calculations, a similar mechanism was proposed for the experimentally observed formation of  $[\text{Al}_{20}\text{Cp}^*_8\text{X}_{10}]$  ( $\text{X} = \text{Cl}, \text{Br}$ )<sup>225</sup> and  $[\text{Al}_{50}\text{Cp}^*_{12}]$ <sup>159</sup> upon thermal treatment of  $[\text{AlCp}^*]_4$  in the presence of aluminium halides, thus shedding light on potential decomposition pathways of organometallic compounds (Figure 25).<sup>226</sup> Likewise, conclusions on potential pathways in the dissociation of bulk metals could be drawn from fragmentation patterns and threshold dissociation energies derived from sustained off-resonance irradiation collision-activated dissociation studies (SORI-CAD) on  $[\text{Ga}_{19}(\text{C}(\text{SiMe}_3)_3)_6]$ .<sup>227</sup> Here, preferential dissociation of  $\text{Ga}(\text{C}(\text{SiMe}_3)_3)$  fragments rather than a release of the organic ligand did not only contribute to a better understanding of metalloid clusters of this kind as core-shell like structures  $[\text{Ga}_n(\text{GaR})_x]$ , but also led the authors to propose a hypothetical mechanism of metal dissociation, e.g. in oxidation processes. Based on the successive oxidation of surface gallium atoms, they assumed a weakening of their internal Ga-Ga bonding which consequently would allow for the separation of  $\text{GaR}$ , or optionally further oxidized  $\text{GaR}_3$ , from the bulk metal.

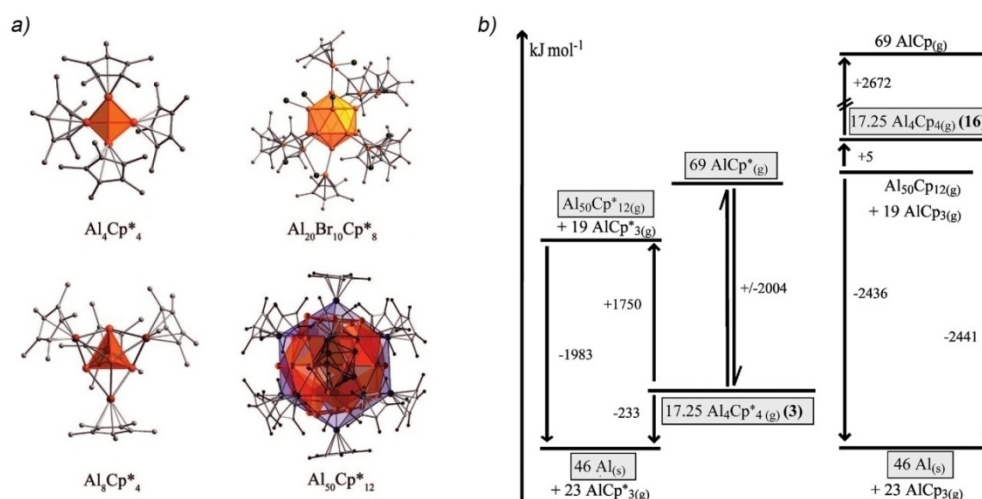


**Figure 25.** a) Molecular structures of  $[AlCp^*]_4$ ,  $[Al_{20}Cp^*_8Br_{10}]$  and  $[Al_{50}Cp^*_{12}]$ , and optimized structure of  $[Al_8Cp^*_4]$ . The higher nuclearity Al clusters are believed to be formed by addition of monomeric  $AlCp^*$  fragments to undissociated  $[AlCp^*]_4$  with subsequent elimination of  $AlCp^*_3$  fragments. b) Exemplary calculated energy diagram ( $kJ\ mol^{-1}$ ) for the disproportionation of  $[AlR]_4$  ( $R = Cp, Cp^*$ ) to elemental Al and  $AlR_3$  via intermediate formation of  $[Al_{50}R_{12}]$ . The high energetic barrier for the formation of  $[Al_{50}Cp^*_{12}]$  from  $[AlCp^*]_4$  can easily be bridged by repetitive addition of monomeric  $AlCp^*$  and elimination of  $AlCp^*_3$ . Adapted from and reprinted with permission of M. Huber, P. Henke, H. Schnöckel, *Chem. Eur. J.* **2009**, 15 (45), 12180-12183. Copyright 2011 Wiley-VCH Verlag GmbH & Co. KGaA, Weinheim.

The internal topologies of metalloid clusters of this kind often correlate to structural motifs found in related solid state phases. This is particularly true for Zintl ions whose structures are essentially retained upon extraction from the respective Zintl phases, but also applies for ligand-stabilized metalloid clusters obtained from wet-chemical, bottom-up synthetic procedures. As mentioned earlier, nature's tendency to form densely packed structures for increasingly large metal atom assemblies is reflected in the exemplary molecular structures of  $[Au_{39}(PPh_3)_{14}Cl_6]^{2+}$  or  $[Pt_{38}(CO)_{44}]^{2-}$ .<sup>147, 149</sup> Structural motifs corresponding to cut-outs of fcc-structured aluminium or the more complex  $\beta$ -modification of gallium are found for  $[Al_{12}(N(SiMe_3)_2)_6]^-$  or  $[Ga_{18}(Si^tBu_3)_8]$ .<sup>156, 183</sup> Likewise, the conceptually different bonding situation of metal atoms in molecularly defined metalloid clusters in comparison to the bulk metal, along with the electronic and steric influence of the stabilizing ligand shell, can allow for an unusually broad variety of accessible geometries. Consequently, metalloid clusters may equally well feature uncommon or even novel topologies, thus inspiring modern material chemists in their search for hitherto unknown element modifications. This is nicely exemplified by the successful isolation of the highly sensitive  $[Al_{22}Br_{20} \cdot 12\ THF]$  which hints at the existence of a hypothetical  $\beta$ -Al modification.<sup>228</sup> Its structure comprises a naked  $Al_{12}$  icosahedron whose basal vertices are connected to ten  $AlBr_2(THF)$  fragments, with the overall motif reminding of the bonding situation in  $\beta$ -rhombohedral boron.

Provided a certain resemblance to extended solid-state materials, e.g. in terms of composition and topology, metalloids clusters might additionally serve as well-defined, spatially confined model systems unravelling fundamental structure  $\leftrightarrow$  property relationships. With regards to metal doping, detailed analyses of the bonding situations in heteroatom-doped metalloids clusters, like the Si-doped aluminium clusters  $[\text{SiAl}_{14}\text{Cp}^*_6]^{229, 230}$  and  $[\text{SiAl}_{56}(\text{N}(\text{SiMe}_3)\text{Dipp})_{12}]$  (Dipp =  $\text{C}_6\text{H}_3\text{-2,6-}^i\text{Pr}_2$ ),<sup>231</sup> or the heterometallic transition metal-doped gold clusters  $[(\text{M}(\text{AuPMe}_3)_{11}(\text{AuCl}))[\text{GaCl}_4]_3]$  (M = Ni, Pd, Pt),<sup>232</sup> might provide valuable insights into local electronic structures and contribute to a deeper understanding of doping effects. Moreover, the underlying mechanistic of physical phenomena, i.e. transport phenomena, might be re-assessed on a molecular level. For instance, the Se-functionalized gallium cluster  $[\text{Ga}_{24}\text{Br}_{18}\text{Se}_2] \cdot 12 \text{ THF}$  which is obtained from the reaction of GaBr with  $\text{Se}(\text{SiMe}_3)_2$  was put forward as a model for the photoconductivity of crystalline GaSe.<sup>233</sup> In the crystalline state, these  $\text{Ga}_{24}$  clusters are arranged in an almost perfect dense packing with one-dimensional linkage of the individual clusters *via* weak Se-Se interactions. The resulting chains of  $\text{Ga}_{24}$  superatoms bear striking topological resemblance to the lattice structure of photoconducting GaSe. However, even though first indications pointing at their model character for solid GaSe were provided by complementary spectroscopic and energetic findings, a more detailed inquiry was not pursued. In a quite comparable case of cluster-cluster interactions in the crystalline state invoking remarkable transport phenomena, highly ordered  $[\text{Ga}_{84}(\text{N}(\text{SiMe}_3)_2)_{20}]^{4+}$  was reported to show electrical- and superconducting behaviour for temperatures below  $T_c \approx 7\text{K}$ .<sup>234, 235</sup> Even though electric charge transfer mechanisms within this nanomaterial could not be fully elucidated, the perfect tubular arrangement of  $\text{Ga}_{84}$  clusters and solvent molecules in the crystalline state was reported to be an essential prerequisite for electric conductivity, most likely *via* electronic coupling between the individual clusters.

The ability of metalloids clusters to serve as molecular models for chemical reactions at catalytically active (nano-)materials is generally accepted, and particularly well-established for bare metal clusters, either in the gas phase or on a solid support.<sup>236, 237</sup> For ligand-stabilized metalloids clusters, recent advances in the wet-chemical synthetic access towards atomically precise nanoclusters nowadays allow for the systematic correlation of catalytic properties with structure and composition.<sup>9, 146</sup> Consequently, these compounds are not only considered to be of interest as catalysts themselves, but provide the opportunity to comprehensively elucidate fundamental concepts like molecular activation, active centers or catalytic mechanisms. Furthermore, and in contrast to the vast majority of ill-defined heterogeneous nanoparticulate catalysts, metalloids clusters are amenable to complementary treatment with high-level density functional theory methods. In this regards, atom-precise metalloids clusters of the noble metals, particularly of gold, are of significant importance owing to their mature synthesis and comparably high stability. For instance, extensive investigations on the catalytic activity of  $[\text{Au}_{25}(\text{SR})_{18}]$  have shown its potential in various

catalytic processes (including hydrogenation, redox-active and C-C coupling reactions, equally well as electro- or photocatalysis), and contributed to an understanding of ligand effects, preferred adsorption sites, and activation mechanisms, e.g. with the concept of charge-state mediated reactivity.<sup>145</sup>

## 3.5 Hume-Rothery phase inspired molecular chemistry

### Coordination chemistry of ECp\* (E = Al, Ga)

As evident from the short overview presented above, the wet-chemical synthesis of ligand-stabilized metalloid clusters is mainly dominated by the formation of homometallic metal atom assemblies and comparably few examples of bimetallic nature are known, many of which are restricted to doped metal clusters containing only a small fraction of heteroatoms. Examples of truly intermetallic, structurally elucidated clusters in this size regime are found amongst the heterometallic carbonyls, e.g.  $[\text{Ru}_6\text{Pd}_6(\text{CO})_{24}]^{2-}$ ,  $[\text{Ag}_{16}\text{Ni}_{24}(\text{CO})_{40}]^{4-}$  or  $[\text{Pd}_{33}\text{Ni}_9(\text{CO})_{41}(\text{PPh}_3)]^{4-}$ ,<sup>238-240</sup> and amongst mixed coinage metal clusters, like the giant AuAg cluster  $[\text{Au}_{80}\text{Ag}_{30}(\text{C}\equiv\text{CPh})_{24}\text{Cl}_9]^+$  or the very recent example of  $[\text{Au}_{19}\text{Cu}_{30}(\text{C}\equiv\text{CR})_{22}(\text{PPh}_3)_6\text{Cl}_2]^{3+}$ , both with only partial  $\text{M}^0$  character.<sup>241, 242</sup> Intermetalloid clusters featuring the combination of transition metals (A2 metals) with metals from the p-block (B1/B2 metals) are exceedingly rare, with the Chevrel-phase related  $[\text{Pd}_6(\mu_3\text{-Te})_8]^{4-}$  being an exceptional example with A2-B2 metal combination.<sup>243</sup>

Considering metal combinations reminiscent of Hume-Rothery phases, that is transition metal/p-block metal (A2/B1) combinations left of the Zintl-border, a systematic access towards related intermetallic molecular compounds is provided by the coordination chemistry of monovalent group 13 organyls  $\text{E}^1\text{R}$  (E = Al, Ga, R = organic rest) as exotic ligands towards transition metal centers. Within this context, the sterically shielded ECp\* ligand (Cp\* = 1,2,3,4,5-pentamethylcyclopentadienyl) has emerged as a particularly versatile ligand owing to the flexible binding mode of the Cp\* unit, and its ability to serve as a removable protecting group. Being isolobal to the CO ligand, the coordination chemistry of the two-electron donating ECp\* is largely dominated by its strong  $\sigma$ -donating and moderate to weak  $\pi$ -accepting properties. Consequently, and in close resemblance of the  $\pi$ -acidic CO and phosphine ligands, a tendency for the stabilization of low-valent metal centers of middle to late transition metals is observed, whereat manifold synthetic strategies have been developed including the substitution of labile ligands,<sup>244-246</sup> addition reactions at electronically unsaturated metal fragments,<sup>247</sup> redox-reactions of trivalent precursors  $[\text{X}_2\text{ECp}^*]$  (X = e.g. Cl, Br)<sup>248</sup> and insertion reactions into polarized TM-L bonds (L = Cl, Br, N(SiMe<sub>3</sub>)<sub>2</sub>).<sup>249, 250</sup> The coordination chemistry of thus formed homo- and heteroleptic ECp\*-coordinated transition metal complexes  $[\text{TM}_a(\text{ECp}^*)_n]$  or  $[\text{TM}_a(\text{ECp}^*)_n(\text{L})_m]$  of usually low nuclearity ( $a \ll n, m$ ;  $a = 1, 2, 3$ ) is well-established meanwhile, and the reviews cited below are recommended for a comprehensive overview.<sup>251-255</sup>

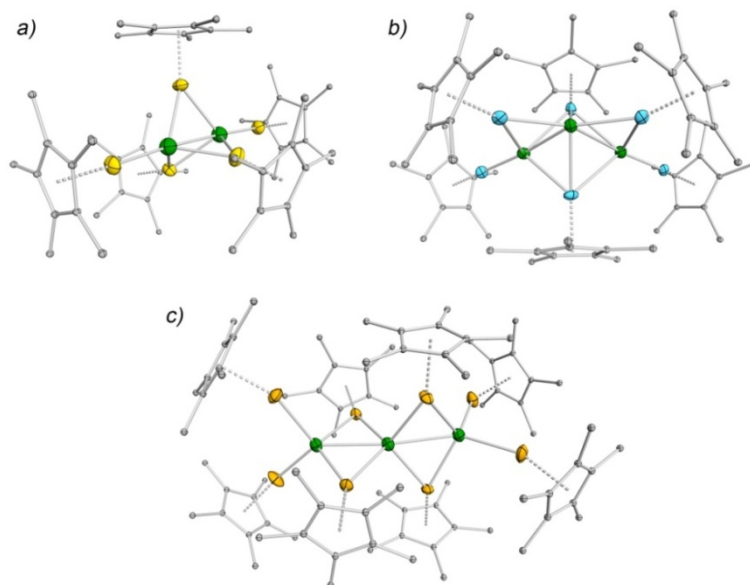


**Figure 26.** Molecular structures of the homoleptic, ECp\*-stabilized palladium clusters a)  $[\text{Pd}_2(\text{GaCp}^*)_5]$ , b)  $[\text{Pd}_3(\text{AlCp}^*)_6]$  and c)  $[\text{Pd}_3(\text{InCp}^*)_8]$  as representative clusters  $[\text{TM}_a(\text{ECp}^*)_b]$  of low nuclearity ( $a < b$ ).<sup>256, 257</sup> While a) and c) feature linear arrangements of the central Pd atoms bridged by ECp\* ligands, the more compact structure of b) comprises a triangular arrangement of palladium atoms with AlCp\* ligands in terminal, bridging and capping positions.

Despite the overall well understood reactivity of the ECp\* ligand, the access towards intermetallic clusters of higher nuclearity is still limited, and the synthesis of homoleptic metalloids clusters  $[\text{TM}_a(\text{ECp}^*)_n]$  with  $a > b$  remains challenging. While initial, albeit rare examples of GaCp\*-substituted transition metal carbonyl clusters, like  $[\text{Ni}_4(\mu\text{-GaCp}^*)_4(\text{CO})_6]$  and  $[\text{Rh}_6(\mu_3\text{-CO})_{4-x}(\mu_3\text{-GaCp}^*)_x(\text{CO})_{12}]$  represent strict analogues of their fully CO-ligated counterparts,<sup>244, 258</sup> first evidence for the accessibility of novel structural motifs was provided by the successful isolation of a series of unprecedented homoleptic GaCp\*-stabilized platinum and palladium clusters.<sup>246, 256, 257, 259</sup> The prototypical dinuclear  $[\text{TM}_2(\text{GaCp}^*)_5]$  (TM = Pd, Pt)<sup>246, 257, 260</sup> and trinuclear  $[\text{Pd}_3(\text{ECp}^*)_n]$  ( $n = 6$  for E = Al,  $n = 8$  for E = Ga, In; Figure 26)<sup>256, 257</sup> feature metallic cores of ECp\*-bridged transition metal centers with comparably weak polarized TM-E bonding in comparison to their mononuclear equivalents, and only weak interactions between the  $d^{10}$  metals, as indicated by quantum chemical analysis of the Pt-Pt bond in  $[\text{Pt}_2(\text{GaCp}^*)_5]$  with the help of natural bond orbital (NBO) and atoms-in-molecules (AIM) methods.<sup>260</sup> Although only a handful of these compounds are known, their discovery was pathbreaking in many respects. Comparative studies did not only relate the restricted synthetic access to delicate reaction kinetics influenced by factors like the remarkably high TM-E bond energies favouring mononuclear complexes  $[\text{TM}(\text{ECp}^*)_n]$ , competing side reactions and/or the association/dissociation equilibrium of ECp\*, but even culminated in a mechanistic rationale for ligand exchange reactions and fluxional processes in solution.<sup>257, 259</sup> Furthermore, with the discovery of the unique coordination chemistry of the

ECp\* ligand, more fundamental questions were raised addressing its overall bonding situation, and its potential participation in cluster bonding in particular. This is illustrated by the exemplary case of  $[\text{Pd}_3(\text{AlCp}^*)_6]$  (Figure 27).<sup>257</sup> Intuitively, its structure is described as a  $\text{Pd}_3$  triangle with two perpendicularly arranged  $\mu_3$ -bridging, and four equatorial  $\text{AlCp}^*$  ligands, two of which adopt  $\mu_2$ -bridging, and two of which terminal positions. Alternatively, its structure could be understood in terms of a  $\text{Pd}_3\text{Al}_2$  cluster with two Cp\* ligands in axial positions and an additional four  $\text{AlCp}^*$  ligands coordinated to the  $\text{Pd}_3$  triangle. At least formally one might even imagine the addition of a reactive  $[\text{Pd}(\text{AlCp}^*)]$  fragment to a yet unknown intermediate species  $[\text{Pd}_2(\text{AlCp}^*)_5]$ , in analogy to  $[\text{TM}_2(\text{GaCp}^*)_5]$ . Albeit no detailed quantum chemical analysis of the bonding situation has been performed, simple electron counting principles provide a strong indication for the actual involvement of the two axial Al atoms in cluster bonding: While the actual cluster valence electron count for a triangular  $\text{Pd}_3$  cluster with six  $\text{AlCp}^*$  ligands is  $3 \cdot 10 + 6 \cdot 2 = 42$  cve, and thus well below the expected 48 cve, the combined approach treating two aluminium atoms as part of a  $\text{Pd}_3\text{Al}_2$  cluster gives an actual cve count of 74 with  $3 \cdot 10 + 2 \cdot 13 = 56$  cluster valence electrons from the palladium and aluminium centers, and an additional  $2 \cdot 5 + 4 \cdot 2 = 18$  electrons donated by the Cp\* and  $\text{AlCp}^*$  ligands, respectively. The accordingly expected square pyramidal geometry is indeed observed for  $[\text{Pd}_3(\text{AlCp}^*)_6]$ . Similar considerations can be made for the other representatives of reported low-nuclearity clusters  $[\text{TM}_a(\text{ECp}^*)_b]$ . For instance, the closely related structures of  $[\text{Pd}_3(\text{ECp}^*)_8]$  (E = Ga, In),<sup>256, 257</sup> can be reasonably well rationalized as corner-sharing squares with the observed  $3 \cdot 10 + 4 \cdot 13 + 4 \cdot 5 + 4 \cdot 2 = 110$  cve meeting the calculated count of  $2 \cdot 64 - 18 = 110$  electrons, as obtained from the addition of two squares minus one common vertice.

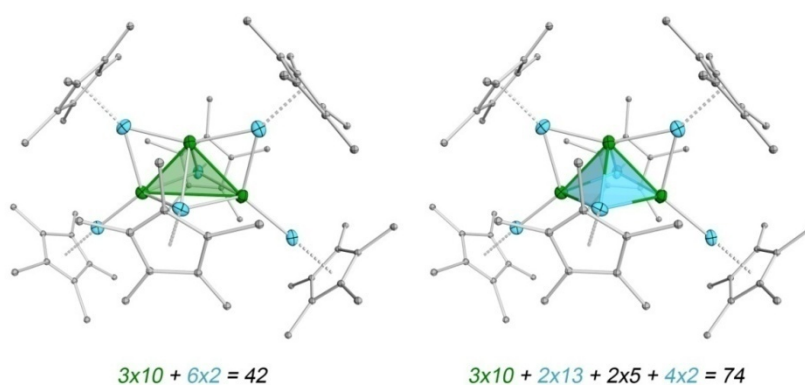


**Figure 27.** Comparative illustration of two alternative ways to rationalize the structure of  $[\text{Pd}_3(\text{AlCp}^*)_6]$  (Pd, Al, C depicted in green, blue and grey, respectively).<sup>257</sup> The PdAl cluster can either be assessed as a  $\text{Pd}_3$  triangle bearing six  $\text{AlCp}^*$  ligands (left) or as a  $\text{Pd}_3\text{Al}_2$  cluster with two Cp\* and four  $\text{AlCp}^*$  ligands (right). While the observed cluster valence electron count for the triangular geometry is well below the expected 48 cve, the actual cve of 74 for the  $\text{Pd}_3\text{Al}_2$  variant is in accordance with the expected count for the observed square pyramidal arrangement.



## Organozinc-rich complexes and clusters - chemistry of the closely related ligand ZnR

Although the presented work focuses on the synthetic access on Hume-Rothery type clusters with transition metal/group 13 combinations, recent inspiring advances in the synthesis of the closely related organozinc-rich coordination compounds of transition metals unambiguously support the overarching concept of a correlation of molecular TM/E model compounds with the respective solid-phases, and thus must not be neglected here. While the access towards high-nuclearity intermetallic clusters  $[TM_a(ECp^*)_b]$  ( $E = Al, Ga$ ) still remains challenging, a reliable strategy for the synthesis of organozinc-rich coordination compounds has been developed based on selective Ga/Zn transmetallation reactions at GaCp\*-coordinated TM complexes.<sup>261-266</sup> Resulting from their direct neighbourhood in the periodic system, gallium and zinc possess comparable atomic radii and electronegativities (1.8 and 1.7 for Ga and Zn, respectively on the Allred-Rochow scale), which allow for a certain exchangeability of the elements as observed in ternary M/Ga/Zn intermetallic phases.<sup>267, 268</sup> Additionally, regarding GaCp\* as a simple  $2e^-$ -donor ligand, one GaCp\* fragment may be replaced by two one-electron donating ZnR units. Accordingly, a library of highly-coordinated pseudo-homoleptic organozinc-rich coordination compounds  $[M(ZnR)_n]$  ( $M = Mo, Ni, Pd, Pt; n > 8$ ; Figure 28) was obtained by the reaction of appropriate all-gallium coordinated transition metal precursors  $[Mo(GaCp^*)_6]$ ,  $[Ru_2(Ga)(GaCp^*)_7H_3]$  or  $[Ru(GaCp^*)_6Cl_2]$ ,  $[(GaCp^*)_4RhGa(\eta^1-Cp^*)Me]$  and  $[M(GaCp^*)_4]$  ( $M = Ni, Pd, Pt$ ) with an excess of  $ZnMe_2$  or  $ZnEt_2$ .<sup>262</sup> These reactions were found to proceed via redox-active ligand substitutions involving the reduction of  $Zn^{II}$  to  $Zn^I$  along with the concomitant oxidation of GaCp\* to  $Cp^*_xGaMe_{3-x}$  and the formation of decamethylfulvalene (as observed by NMR spectroscopy), thus suggesting a radical mechanism. The resulting compounds strictly follow the 18 VE rule and exhibit typical regular polyhedral structures around the central transition metal atom which are related to structural motifs found in respective M/Zn intermetallics (Figure 28). However, while on the first glance a certain correlation to endohedral Zintl ions such as  $Pt@Pb_{12}^{2-}$  appears to be reasonable, quantum chemical calculations suggest a unique nontrivial bonding situation, featuring multi-centred electron-deficient M-Zn bonds along with weak tangential Zn-Zn interactions. For  $[Mo(ZnMe)_9(ZnCp^*)_3]$ , this is best described as a perfectly  $sd^5$ -hybridized Mo atom, engaging six 3-center-2-electron Zn-Mo-Zn electron-sharing bonds across the diagonals of the  $MoZn_{12}$  core.<sup>261</sup> The residual six electrons are delocalized over the Zn cage, evoking weak Zn-Zn interactions. Consequently, these compounds build a bridge from classical coordination compounds to clusters with regards to classical bonding situations.



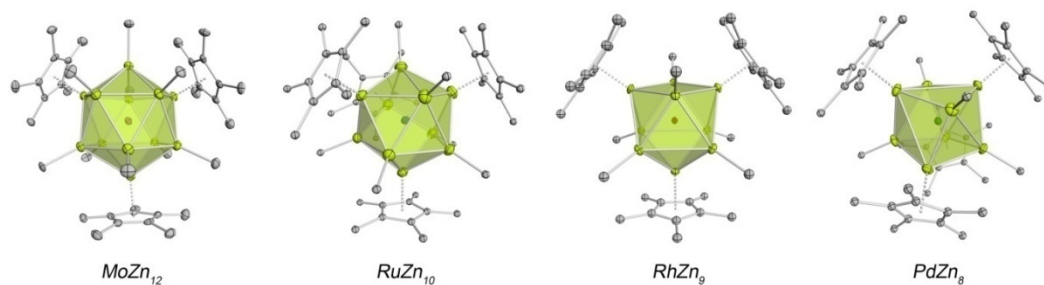


**Figure 28.** Molecular structures of  $[\text{Mo}(\text{ZnCp}^*)_3(\text{ZnMe})_9]$  ( $\text{MoZn}_{12}$ ),  $[\text{Ru}(\text{ZnCp}^*)_4(\text{ZnMe})_6]$  ( $\text{RuZn}_{10}$ ),  $[\text{Rh}(\text{ZnCp}^*)_3(\text{ZnMe})_6]$  ( $\text{RhZn}_9$ ) and  $[\text{Pd}(\text{ZnCp}^*)_4(\text{ZnMe})_4]$  ( $\text{PdZn}_8$ ; Mo, Ru, Rh, Pd, Zn, C depicted in purple, blue, red, dark green and light green, respectively) with highlighted  $\text{Zn}_n$  coordination polyhedra around the central transition metal. All compounds strictly follow the 18VE rule.<sup>262</sup>

Notably, in the reactions of homoleptic  $\text{GaCp}^*$ -ligated precursors, Ga/Zn mixed-shell compounds of the general formula  $[\text{M}(\text{GaR})_n(\text{ZnR})_m]$  ( $\text{R} = \text{Me}, \text{Cp}^*$ ) were also obtained. By reducing the excess of  $\text{ZnMe}_2$  in the reaction of  $[\text{Mo}(\text{GaCp}^*)_6]$ , the two Zn/Ga mixed ligand complexes  $[\text{Mo}(\text{GaMe})_4(\text{ZnCp}^*)_4]$  and  $[\text{Mo}(\text{GaMe})_2(\text{ZnCp}^*)_4(\text{ZnMe})_4]$  were isolated as intermediates in the formation of  $[\text{Mo}(\text{ZnMe})_9(\text{ZnCp}^*)_3]$ .<sup>261, 262</sup> The latter features a deca-coordinated centaur polyhedron, a 10-vertex body obtained from fusion of a cube and an icosahedron, which was related to the  $\text{VGa}_{10}$  polyhedra found in the binary  $\text{V}_8\text{Ga}_{41}$  phase.

To date, the concept of selective Ga/Zn transmetalation reactions at  $\text{GaCp}^*$ -ligated TM centres could not be extended towards the synthesis of molecular congeners of one of the most famous Hume-Rothery phases, brass. However, with the synthesis of “Carmona’s reagent”  $[\text{Zn}_2\text{Cp}^*_2]$  a versatile tool for controlled M-Zn bond formation was found, finally facilitating the synthesis of the first atom-precise molecular Cu/Zn clusters  $[(\text{CuCN}^t\text{Bu})_4(\text{ZnCp}^*)_3(\text{ZnR})]$  ( $\text{R} = \text{Cp}, \text{Cp}^*$ ) *via* treatment of  $[\text{CpCuCN}^t\text{Bu}]$  with  $[\text{Zn}_2\text{Cp}^*_2]$ .<sup>8</sup> These isostructural compounds comprise a  $T_d$ -symmetric central  $\text{Cu}_4$  tetrahedron which is embedded in the tetrahedral arrangement of four face-capping  $\text{ZnR}$  fragments. A related, inverse structural motif of intersecting  $\text{Cu}_4$  and  $\text{Zn}_4$  tetrahedra is also found in the nested polyhedra of the solid state structure of  $\gamma$ -brass  $\text{Cu}_5\text{Zn}_8$ , in which an inner  $\text{Zn}_4$  core is surrounded by an outer tetrahedron of Cu atoms (Figure 29). Notably, both compounds can be rationalized with the unified superatom concept, according to which strong electronic shell closure is expected for spherical clusters with eight cluster valence electrons, like  $[(\text{CuCN}^t\text{Bu})_4(\text{ZnCp}^*)_3(\text{ZnR})]$  ( $n = N \cdot v_A - M \cdot v_x - z = (4 \cdot 1 + 4 \cdot 2) - 4 \cdot 1 - 0 = 8$ ). This is further supported by the  $a_1^2 t_2^6$  electronic configuration derived from DFT calculations, which relates to the consecutive closing of the  $1S^2 1P^6$  electronic states as predicted by the superatom concept.

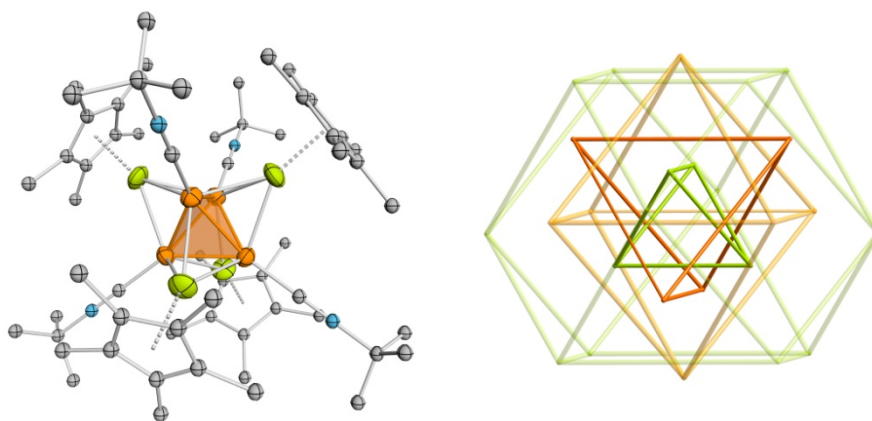


Figure 29. Molecular structure of  $[(\text{CuCN}^t\text{Bu})_4(\text{ZnCp}^*)_4]$  (left; Cu, Zn depicted in orange, green; disorder sites omitted for clarity) and nested polyhedra of  $\gamma$ -brass. The central structural motif of two interpenetrating tetrahedra of the  $\text{Cu}_4\text{Zn}_4$  metal core of  $[(\text{CuCN}^t\text{Bu})_4(\text{ZnCp}^*)_4]$  is also found in the  $\text{Cu}_{10}\text{Zn}_{16}$  clusters of  $\gamma$ -brass, albeit with an inverse Cu/Zn distribution.<sup>8</sup>

## From molecular coordination chemistry to nanomaterials - catalytic potential of Hume-Rothery nanophases

The flexible binding properties of Cp\*, its facile release, and its role as a sterically demanding protection group are important aspects within the concepts of cluster growth and the utilization of ECp\* compounds as precursors for nanomaterials. In fact, intermetallic TM/E nanoparticles are readily accessible by co-hydrogenolysis of substitution labile, ideally all-hydrocarbon ligated, transition metal precursors and ECp\* in the presence of suitable hydrocarbon surfactants as capping ligands, whereat metallic E is released from ECp\* upon hydrogen treatment *via* reductive elimination of Cp\*H from presumably *in situ* generated  $[\text{Cp}^*\text{E}(\text{H})_x]$ .<sup>251, 269-273</sup> Following this approach, colloidal Al nanoparticles are obtained from the reaction of  $[\text{AlCp}^*]_4$  under 3 bar hydrogen pressure in mesitylene at 150 °C.<sup>272</sup> Bimetallic CuAl nanoparticles of the  $\theta$ -CuAl<sub>2</sub> phase are formed *via* soft co-hydrogenolysis of  $[\text{AlCp}^*]_4$  with  $[\text{CpCu}(\text{PMe}_3)]$  in a 2:1 ratio in mesitylene at 150 °C.<sup>272</sup> Likewise, treatment of  $[\text{Co}(\eta^4\text{-C}_8\text{H}_{12})(\eta^3\text{-C}_8\text{H}_{13})]$  or  $[\text{Ni}(\text{cod})_2]$  with one equivalent of AlCp\* under mild hydrogenolytic conditions results in the formation of  $\beta$ -CoAl and  $\beta$ -NiAl alloy nanoparticles, respectively.<sup>270, 271</sup>

A more complex situation is faced when AlCp\* is replaced by GaCp\* as the surprisingly low reactivity of GaCp\* towards H<sub>2</sub> in combination with the low TM-Ga bond dissociation energy demands for harsher conditions and longer reaction times to furnish bimetallic TM/E nanoparticles. For instance, colloidal Ni/Ga nanoalloys of the overall compositions NiGa, Ni<sub>2</sub>Ga<sub>3</sub> and Ni<sub>3</sub>Ga can be synthesized by co-hydrogenolysis of  $[\text{Ni}(\text{cod})_2]$  and GaCp\* in non-aqueous media under 4 bar of hydrogen pressure at high temperatures, however with lower control of composition and phase purity.<sup>273</sup> A more selective access seems to be provided with

the transfer of this precursor chemistry to ionic liquids as the reaction medium. The microwave-induced thermal decomposition of  $[\text{Ni}(\text{cod})_2]$  and  $\text{GaCp}^*$  in  $[\text{BMIM}][\text{BF}_4]$  selectively yields non-agglomerated, highly crystalline  $\text{NiGa}$  and  $\text{Ni}_3\text{Ga}$  nanoparticles, even in the absence of surfactant additives. These display high catalytic activity in selective semihydrogenation reactions, a feature which has already been reported for related Hume-Rothery nanophases such as  $\text{PdGa}$ ,  $\text{Pd}_3\text{Ga}_7$  or  $\text{Fe}_4\text{Al}_{13}$ .<sup>274, 275</sup>

Aiming at the identification of early intermediates in the wet-chemical bottom-up preparation of TM/E nanophases, the hydrogenolysis of the all-labile ruthenium complex  $[\text{Ru}(\eta^4\text{-cod})(\eta^3\text{-C}_4\text{H}_7)_2]$  ( $\text{C}_4\text{H}_7 = 2\text{-methylallyl}$ ) in the presence of  $\text{GaCp}^*$  was investigated.<sup>276</sup> While slow formation of  $\text{RuGa}$  and  $\text{RuGa}_2$  particles was observed for prolonged reaction times under harsh hydrogenolytic conditions ( $150^\circ\text{C}$ , 3 bar  $\text{H}_2$ , 7 days), the well-defined, neutral complex  $[(\text{GaCp}^*)_4(\text{H})\text{Ru}(\mu\text{-Ga})\text{Ru}(\text{H})_2(\text{GaCp}^*)_3]$  was selectively obtained upon early interruption of the reaction at lower temperatures ( $60^\circ\text{C}$ , 3 bar  $\text{H}_2$ , 1h; Figure 30). Its remarkable structure features two  $[\text{Ru}(\text{GaCp}^*)_{5-x}(\text{H})_x]$  fragments bridged by a "naked" Ga atom which is presumably formed by selective hydrogenolytic cleavage of a  $\text{Cp}^*$  ligand from coordinated  $\text{GaCp}^*$ . Potential mechanistic pathways substantiated by DFT calculations suggest the formation of a  $\text{GaCp}^*$ -rich key intermediate  $[\text{Ru}(\text{GaCp}^*)_4\text{H}_2]$  which undergoes loss of  $\text{Cp}^*\text{H}$  to form the pentacoordinate  $[\text{Ru}(\text{GaCp}^*)_3(\text{H})(\text{Ga})]$ . Subsequent association/dissociation equilibria of  $\text{GaCp}^*$  from these intermediates eventually facilitates dimerization to form  $[(\text{GaCp}^*)_4(\text{H})\text{Ru}(\mu\text{-Ga})\text{Ru}(\text{H})_2(\text{GaCp}^*)_3]$ . The resultant unusual motif of a naked, bridging Ga atom can be understood as an early stage intermediate in alloy formation processes facilitated by selective cleavage of  $\text{Cp}^*\text{H}$ .

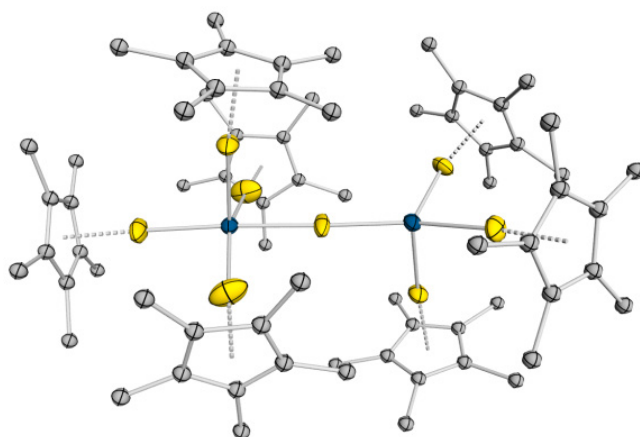


**Figure 30.** Molecular structure of  $[(\text{GaCp}^*)_4(\text{H})\text{Ru}(\mu\text{-Ga})\text{Ru}(\text{H})_2(\text{GaCp}^*)_3]$  as obtained from mild hydrogenolysis of all-labile Ru complexes  $[\text{Ru}(\eta^4\text{-cod})(\eta^3\text{-C}_4\text{H}_7)_2]$  or  $[\text{Ru}(\eta^4\text{-cod})(\eta^6\text{-cot})]$  in the presence of  $\text{GaCp}^*$ . The unusual structural motif of a naked, bridging Ga atom can be understood as an early stage intermediate in alloy formation processes facilitated by selective cleavage of  $\text{Cp}^*\text{H}$ .<sup>276</sup>

## References

1. R. Pöttgen, D. Johrendt, *Intermetallics - Synthesis, Structure, Function*, DeGruyter, Berlin/Boston, **2014**.
2. G. Sauthoff, *Intermetallics*, Wiley-VCH, Weinheim, **1995**.
3. R. Ferro, A. Saccone, *Intermetallic Chemistry*, Pergamon Materials Science, Elsevier, Amsterdam, **2008**.
4. S. Scharfe, F. Kraus, S. Stegmaier, A. Schier, T. F. Fässler, *Angew. Chem. Int. Ed.* **2011**, 50 (16), 3630-3670.
5. A. Schnepf, H. Schnöckel, *Angew. Chem. Int. Ed.* **2002**, 41 (19), 3532-3554.
6. H. Schnöckel, A. Schnepf. In *The Group 13 Metals Aluminium, Gallium, Indium and Thallium: Chemical Patterns and Peculiarities*; John Wiley & Sons, Ltd, **2011**, pp 402-487.
8. K. Freitag, H. Banh, C. Gemel, R. W. Seidel, S. Kahlal, J.-Y. Saillard, R. A. Fischer, *Chem. Commun.* **2014**, 50 (63), 8681-8684.
9. R. Jin, C. Zeng, M. Zhou, Y. Chen, *Chem. Rev.* **2016**, 116 (18), 10346-10413.
12. R. Nesper, *Angew. Chem.* **1991**, 103 (7), 805-834.
13. E. Parthé, *Z. Kristallogr.* **2006**, 221 (5-7), 301.
14. W. Fischer, *Z. Kristallogr.* **2006**, 221 (5-7), 305.
15. R. L. Johnston, R. Hoffmann, *Z. Anorg. Allg. Chem.* **1992**, 616 (10), 105-120.
16. F. J. Laves, H. Witte, *Metallwirtsch.* **1936**, 15,
17. M. Ellner, B. Predel. In *Intermetallic compounds - principles and practice*, J. H. Westbrook, R. L. Fleischer, Ed.; John Wiley & Sons Ltd, Chichester, **1994**, Chpt. 5, Vol. 1, pp 91-125.
18. M. V. Nevitt, *Electronic structure and alloy chemistry of transition elements*, Interscience, New York, **1963**.
19. J. K. A. Gschneidner, K. Pecharsky Vitalij, *Z. Kristallogr.* **2006**, 221 (5-7), 375.
20. E. Teatum, K. Gschneidner, J. Waber, Report LA-2345, US Dept of Commerce, Washington, DC, **1960**.
21. J. B. Friauf, *Phys. Rev.* **1927**, 29 (1), 34-40.
22. J. B. Friauf, *J. Am. Chem. Soc.* **1927**, 49 (12), 3107-3114.
23. F. Laves, H. Witte, *Metallwirtsch.* **1935**, 14, 645-649.
24. Y. Liu, J. D. Livingston, S. M. Allen, *Metal. Trans. A* **1992**, 23 (12), 3303-3308.
25. A. Von Keitz, G. Sauthoff, *Intermetallics* **2002**, 10 (5), 497-510.
26. S. C. Sevov. In *Intermetallic Compounds - Principles and Practice*; John Wiley & Sons, Ltd, **2002**, Chpt. 6, Vol. 3, pp 113-132.
27. T. F. Fässler, *Zintl phases: principles and recent developments*, Springer, Heidelberg, **2011**.
28. J. D. Corbett, *Angew. Chem. Int. Ed.* **2000**, 39 (4), 670-690.
29. J. D. Corbett, *Inorg. Chem.* **2010**, 49 (1), 13-28.
30. W. Klemm, E. Busmann, *Z. Anorg. Allg. Chem.* **1963**, 319 (5-6), 297-311.
31. E. Zintl, *Angew. Chem.* **1939**, 52 (1), 1-6.
32. K. Janzon, H. Schäfer, A. Weiss, *Z. Naturforsch. B* **1966**, 21 (3), 287.
33. U. Aydemir, A. Ormeci, H. Borrmann, B. Böhme, F. Zürcher, B. Uslu, T. Goebel, W. Schnelle, P. Simon, W. Carrillo-Cabrera, F. Haarmann, M. Baitinger, R. Nesper, H. G. von Schnering, Y. Grin, *Z. Anorg. Allg. Chem.* **2008**, 634 (10), 1651-1661.
34. G. Rocktäschel, A. Weiss, *Z. Anorg. Allg. Chem.* **1962**, 316 (3-4), 231-236.
35. W. Bockelmann, H. Jacobs, H. U. Schuster, *Z. Naturforsch. B* **1970**, 25 (11), 1305.
36. B. Eisenmann, A. Hofmann, *Z. Kristallogr.* **1991**, 197 (1-4), 159.
37. C. Hoch, M. Wendorff, C. Rohr, *Acta Crystallogr., Sect. C* **2002**, 58 (4), i45-i46.
38. V. Quéneau, E. Todorov, S. C. Sevov, *J. Am. Chem. Soc.* **1998**, 120 (13), 3263-3264.

39. C. Hoch, M. Wendorff, C. Röhr, *J. Alloys Compd.* **2003**, 361 (1), 206-221.
40. S. C. Sevov, J. D. Corbett, *Inorg. Chem.* **1991**, 30 (26), 4875-4877.
41. R. G. Ling, C. Belin, *C. R. Acad. Sci. Paris* **1982**, 294, 1083.
42. C. Belin, *Acta Crystallogr., Sect. B* **1980**, 36 (6), 1339-1343.
43. C. Slavi Sevov, J. D. Corbett, *Z. Anorg. Allg. Chem.* **1993**, 619 (1), 128-132.
44. W. Hume-Rothery, *J. Inst. Met.* **1926**, 35, 307.
45. W. Hume-Rothery. In *Phase Stability in Metals and Alloys*, P. S. Rudman, J. Stringer, R. I. Jaffee, Ed.; MacGraw Hill, New York, **1967**, pp 3-23.
46. T. B. Massalski. In *The Science of Alloys for the 21st Century: A Hume-Rothery Symposium Celebration*; TMS, Warrendale, **2000**, pp 55-70.
47. U. Mizutani, *Hume-Rothery Rules for Structurally Complex Alloy Phases*, CRC Press, **2011**.
48. W. Hume-Rothery, G. W. Mabbott, K. M. C. Evans, *Philos. Trans. R. Soc. London, Ser. A* **1934**, 233 (721-730), 1-97.
49. L. S. Darken, R. W. Gurry, *Physical Chemistry of Metals*, McGraw-Hill Book Co., New York, **1953**.
50. L. M. Hoistad, S. Lee, *J. Am. Chem. Soc.* **1991**, 113 (22), 8216-8220.
51. G. P. Tiwari, R. V. Ramanujan, *J. Mater. Sci.* **2001**, 36 (2), 271-283.
52. B. Predel. In *Cr-Cs – Cu-Zr*, O. Madelung, Ed.; Springer Berlin Heidelberg, Berlin, Heidelberg, **1994**, pp 1-11.
53. W. Hume-Rothery, R. E. Smallman, C. W. Haworth, *The Structure of Metals and Alloys*, 5th ed.; Metals & Metallurgy Trust, London, **1969**.
54. A. Westgren, G. Phragmén, *Lond. Edinb. Dubl. Phil. Mag.* **1925**, 50 (295), 311-341.
55. A. Westgren, G. Phragmén, *Z. Metallkunde* **1926**, 18, 279.
56. A. Westgren, G. Phragmén, *Z. Anorg. Allg. Chem.* **1928**, 175 (1), 80-89.
57. A. F. Westgren, G. Phragmen, *Trans. Faraday Soc.* **1929**, 25 (0), 379-385.
58. H. Jones, *Proc. R. Soc. London, Ser. A* **1934**, 144 (851), 225-234.
59. N. F. Mott, H. Jones, *The theory of the properties of metals and alloys*, Clarendon Press, Oxford, **1936**.
60. S. B. Dugdale, *Phys. Scr.* **2016**, 91 (5), 053009.
61. L. Brillouin, *J. Phys. Radium* **1930**, 1 (11), 377-400.
62. C. Kittel, *Introduction to Solid State Physics*, John Wiley & Sons, New York, **2005**.
63. A. Sommerfeld, *Naturwissenschaften* **1928**, 16 (21), 374-381.
64. F. Bloch, *Z. Phys.* **1929**, 52 (7), 555-600.
65. R. F. Berger, P. L. Walters, S. Lee, R. Hoffmann, *Chem. Rev.* **2011**, 111 (8), 4522-4545.
66. D. Shechtman, I. Blech, D. Gratias, J. W. Cahn, *Phys. Rev. Lett.* **1984**, 53 (20), 1951-1953.
67. D. Shechtman, I. A. Blech, *Metall. Trans. A* **1985**, 16A, 1005-12.
68. IUCr, *Acta Crystallogr., Sect. A* **1992**, 48 (6), 922-946.
69. J. M. Dubois, *Useful quasicrystals*, World Scientific, Singapore, **2005**.
70. W. Steurer, S. Deloudi, *Acta Crystallogr., Sect. A* **2008**, 64 (1), 1-11.
71. J.-M. Dubois, *Chem. Soc. Rev.* **2012**, 41 (20), 6760-6777.
72. D. V. Louzguine-Luzgin, A. Inoue, *Annu. Rev. Mater. Res.* **2008**, 38 (1), 403-423.
73. E. A. Lord, *Curr. Sci.* **1991**, 61 (5), 313-319.
74. R. Penrose, *Bull. Inst. Math. Appl.* **1974**, 10, 266-271.
75. A. I. Goldman, R. F. Kelton, *Rev. Mod. Phys.* **1993**, 65 (1), 213-230.
76. T. Haibach, A. Cervellino, M. A. Estermann, W. Steurer, *Z. Kristallogr.* **2000**, 215 (10), 569.
77. W. Steurer, *J. Non-Cryst. Solids* **2004**, 334-335 (Supplement C), 137-142.
78. W. Steurer, *Z. Kristallogr.* **2004**, 219 (7), 391.

79. A. Yamamoto, H. Takakura, *Ferroelectrics* **2004**, 305 (1), 223-227.
80. A. Mackay, *Acta Crystallogr.* **1962**, 15 (9), 916-918.
81. K. H. Kuo, *Struct. Chem.* **2002**, 13 (3), 221-230.
82. G. Bergman, J. L. T. Waugh, L. Pauling, *Acta Crystallogr.* **1957**, 10 (4), 254-259.
83. A. Palenzona, *J. Less. Common. Met.* **1971**, 25 (4), 367-372.
84. R. Maezawa, S. Kashimoto, T. Ishimasa, *Philos. Mag. Lett.* **2004**, 84 (4), 215-223.
85. A.-P. Tsai, *Chem. Soc. Rev.* **2013**, 42 (12), 5352-5365.
86. A. P. Tsai, *J. Non-Cryst. Solids* **2004**, 334-335 (Supplement C), 317-322.
87. A. P. Tsai, *Sci. Technol. Adv. Mater.* **2008**, 9 (1), 013008.
88. J. Q. Guo, E. Abe, A. P. Tsai, *Philos. Mag. Lett.* **2002**, 82 (1), 27-35.
89. G. V. Raynor, *Prog. Metal Phys.* **1949**, 1 (Supplement C), 1-76.
90. U. Mizutani, R. Asahi, T. Takeuchi, H. Sato, O. Kontsevoi, A. J. Freeman, *Z. Kristallogr.* **2009**, 224 (1-2), 17.
91. A. Traverse, L. Dumoulin, E. Belin, C. S  nemaud. In *Quasicrystalline Materials*, C. Janot, J. M. Dubois, Ed.; World Scientific, Singapore, **1988**, pp 399-408.
92. T. Fujiwara, *Phys. Rev. B* **1989**, 40 (2), 942-946.
93. G. Trambly de Laissardi  re, D. Nguyen-Manh, D. Mayou, *Prog. Mater Sci.* **2005**, 50 (6), 679-788.
94. W. A. de Heer, *Rev. Mod. Phys.* **1993**, 65 (3), 611-676.
95. H. Pauly, *Atom, Molecule, and Cluster Beams I and II*, Springer, Berlin **2000**.
96. P. Milani, S. Iannotta, *Cluster Beam Synthesis of Nanostructured Materials*, Springer, Berlin, **1999**.
97. T. F. F  ssler, S. D. Hoffmann, *Angew. Chem. Int. Ed.* **2004**, 43 (46), 6242-6247.
98. S. C. Sevov, J. M. Goicoechea, *Organometallics* **2006**, 25 (24), 5678-5692.
99. J. D. Corbett, *Chem. Rev.* **1985**, 85 (5), 383-397.
100. T. F. F  ssler, *Coord. Chem. Rev.* **2001**, 215 (1), 347-377.
101. L. Xu, S. Bobev, J. El-Bahraoui, S. C. Sevov, *J. Am. Chem. Soc.* **2000**, 122 (8), 1838-1839.
102. A. Spiekermann, S. D. Hoffmann, T. F. F  ssler, *Angew. Chem. Int. Ed.* **2006**, 45 (21), 3459-3462.
103. A. Nienhaus, S. D. Hoffmann, T. F. F  ssler, *Z. Anorg. Allg. Chem.* **2006**, 632 (10-11), 1752-1758.
104. N. Korber, *Phosphorus Sulfur Silicon Relat. Elem.* **1997**, 124 (1), 339-346.
105. G. Fritz, H.-W. Schneider, W. H  nle, H. G. von Schnering, *Z. Naturforsch. B* **1988**, 43 (5), 561.
106. A. Ugrinov, S. C. Sevov, *Inorg. Chem.* **2003**, 42 (19), 5789-5791.
107. C. Downie, Z. Tang, A. M. Guloy, *Angew. Chem. Int. Ed.* **2000**, 39 (2), 337-340.
108. A. Ugrinov, S. C. Sevov, *J. Am. Chem. Soc.* **2002**, 124 (11), 2442-2443.
109. A. Schnepf, C. Schenk, *Angew. Chem. Int. Ed.* **2006**, 45 (32), 5373-5376.
110. Z.-M. Sun, Y.-F. Zhao, J. Li, L.-S. Wang, *J. Clust. Sci.* **2009**, 20 (3), 601-609.
111. S. Scharfe, T. F. F  ssler, *Eur. J. Inorg. Chem.* **2010**, 2010 (8), 1207-1213.
112. J. M. Goicoechea, S. C. Sevov, *J. Am. Chem. Soc.* **2006**, 128 (12), 4155-4161.
113. J. M. Goicoechea, S. C. Sevov, *J. Am. Chem. Soc.* **2005**, 127 (21), 7676-7677.
114. B. W. Eichhorn, R. C. Haushalter, *J. Am. Chem. Soc.* **1988**, 110, 8704-8706.
115. J. Campbell, H. P. A. Mercier, H. Franke, D. P. Santry, D. A. Dixon, G. J. Schrobilgen, *Inorg. Chem.* **2002**, 41 (1), 86-107.
116. B. W. Eichhorn, R. C. Haushalter, *J. Chem. Soc., Chem. Commun.* **1990**, (13), 937-938.
117. B. Kesanli, J. Fettinger, B. Eichhorn, *Chem. Eur. J.* **2001**, 7 (24), 5277-5285.
118. P. Kircher, G. Huttner, K. Heinze, G. Renner, *Angew. Chem. Int. Ed.* **1998**, 37 (12), 1664-1666.

119. G. Renner, P. Kircher, G. Huttner, P. Rutsch, K. Heinze, *Eur. J. Inorg. Chem.* **2001**, 2001 (4), 973-980.
120. M. Waibel, F. Kraus, S. Scharfe, B. Wahl, T. F. Fässler, *Angew. Chem. Int. Ed.* **2010**, 49 (37), 6611-6615.
121. J. M. Goicoechea, S. C. Sevov, *Organometallics* **2006**, 25 (19), 4530-4536.
122. S. Charles, B. W. Eichhorn, S. G. Bott, *J. Am. Chem. Soc.* **1993**, 115 (13), 5837-5838.
123. S. Charles, J. C. Fettinger, S. G. Bott, B. W. Eichhorn, *J. Am. Chem. Soc.* **1996**, 118 (19), 4713-4714.
124. A. Nienhaus, R. Hauptmann, T. F. Fässler, *Angew. Chem. Int. Ed.* **2002**, 41 (17), 3213-3215.
125. M. B. Boeddinghaus, S. D. Hoffmann, T. F. Fässler, *Z. Anorg. Allg. Chem.* **2007**, 633 (13-14), 2338-2341.
126. A. Spiekermann, S. D. Hoffmann, F. Kraus, T. F. Fässler, *Angew. Chem. Int. Ed.* **2007**, 46 (10), 1638-1640.
127. B. Zhou, M. S. Denning, T. A. D. Chapman, J. E. McGrady, J. M. Goicoechea, *Chem. Commun.* **2009**, (46), 7221-7223.
128. E. N. Esenturk, J. Fettinger, B. Eichhorn, *Chem. Commun.* **2005**, (2), 247-249.
129. E. N. Esenturk, J. Fettinger, B. Eichhorn, *J. Am. Chem. Soc.* **2006**, 128 (28), 9178-9186.
130. Z.-M. Sun, H. Xiao, J. Li, L.-S. Wang, *J. Am. Chem. Soc.* **2007**, 129 (31), 9560-9561.
131. J. M. Goicoechea, S. C. Sevov, *Angew. Chem. Int. Ed.* **2005**, 44 (26), 4026-4028.
132. E. N. Esenturk, J. Fettinger, B. Eichhorn, *Polyhedron* **2006**, 25 (2), 521-529.
133. M. J. Moses, J. C. Fettinger, B. W. Eichhorn, *Science* **2003**, 300 (5620), 778-780.
134. J. M. Goicoechea, S. C. Sevov, *Angew. Chem. Int. Ed.* **2006**, 45 (31), 5147-5150.
135. T. P. Fehlner, J.-F. Halet, J.-Y. Saillard, *Molecular Clusters - A Bridge to Solid State Chemistry*, Cambridge University Press, Cambridge, **2007**.
136. J. Lewis, *Pure Appl. Chem.* **1965**, 10 (1), 11.
137. F. A. Cotton, *Q. Rev. Chem. Soc.* **1966**, 20 (3), 389-401.
138. H. Schäfer, H. G. Schnering, *Angew. Chem.* **1964**, 76 (20), 833-849.
139. E. R. Corey, L. F. Dahl, W. Beck, *J. Am. Chem. Soc.* **1963**, 85 (8), 1202-1203.
140. P. Corradini, *J. Chem. Phys.* **1959**, 31 (6), 1676-1677.
141. A. Purath, R. Köppe, H. Schnöckel, *Angew. Chem. Int. Ed.* **1999**, 38 (19), 2926-2928.
142. A. Schnepf, G. Stösser, H. Schnöckel, *J. Am. Chem. Soc.* **2000**, 122 (38), 9178-9181.
143. G. Schmid, R. Pfeil, R. Boese, F. Bandermann, S. Meyer, G. H. M. Calis, J. W. A. van der Velden, *Chem. Ber.* **1981**, 114 (11), 3634-3642.
144. G. Schmid, *Chem. Soc. Rev.* **2008**, 37 (9), 1909-1930.
145. G. Li, R. Jin, *Acc. Chem. Res.* **2013**, 46 (8), 1749-1758.
146. I. Chakraborty, T. Pradeep, *Chem. Rev.* **2017**, 117 (12), 8208-8271.
147. B. K. Teo, X. Shi, H. Zhang, *J. Am. Chem. Soc.* **1992**, 114 (7), 2743-2745.
148. A. Ceriotti, F. Demartin, G. Longoni, M. Manassero, M. Marchionna, G. Piva, M. Sansoni, *Angew. Chem.* **1985**, 97 (8), 708-710.
149. A. Ceriotti, N. Masciocchi, P. Macchi, G. Longoni, *Angew. Chem.* **1999**, 111 (24), 3941-3944.
150. J. D. Erickson, E. G. Mednikov, S. A. Ivanov, L. F. Dahl, *J. Am. Chem. Soc.* **2016**, 138 (5), 1502-1505.
151. N. T. Tran, D. R. Powell, L. F. Dahl, *Angew. Chem. Int. Ed.* **2000**, 39 (22), 4121-4125.
152. E. G. Mednikov, M. C. Jewell, L. F. Dahl, *J. Am. Chem. Soc.* **2007**, 129 (37), 11619-11630.
153. P. D. Jadzinsky, G. Calero, C. J. Ackerson, D. A. Bushnell, R. D. Kornberg, *Science* **2007**, 318 (5849), 430-433.



154. A. Dass, S. Theivendran, P. R. Nimmala, C. Kumara, V. R. Jupally, A. Fortunelli, L. Sementa, G. Barcaro, X. Zuo, B. C. Noll, *J. Am. Chem. Soc.* **2015**, 137 (14), 4610-4613.
155. C. E. Anson, A. Eichhöfer, I. Issac, D. Fenske, O. Fuhr, P. Sevillano, C. Persau, D. Stalke, J. Zhang, *Angew. Chem. Int. Ed.* **2008**, 47 (7), 1326-1331.
156. A. Purath, R. Koppe, H. Schnöckel, *Chem. Commun.* **1999**, (19), 1933-1934.
157. H. Köhnlein, A. Purath, C. Klemp, E. Baum, I. Krossing, G. Stösser, H. Schnöckel, *Inorg. Chem.* **2001**, 40 (19), 4830-4838.
158. A. Ecker, E. Weckert, H. Schnöckel, *Nature* **1997**, 387, 379.
159. J. Vollet, J. R. Hartig, H. Schnöckel, *Angew. Chem. Int. Ed.* **2004**, 43 (24), 3186-3189.
160. A. Schnepf, H. Schnöckel, *Angew. Chem. Int. Ed.* **2001**, 40 (4), 711-715.
161. A. Schnepf, *Chem. Soc. Rev.* **2007**, 36 (5), 745-758.
162. A. Schnepf, *New J. Chem.* **2010**, 34 (10), 2079-2092.
163. A. Schnepf, R. Köppe, *Angew. Chem. Int. Ed.* **2003**, 42 (8), 911-913.
164. A. Schnepf, *Angew. Chem. Int. Ed.* **2003**, 42 (23), 2624-2625.
165. H.-J. Himmel, J. Vollet, *Organometallics* **2002**, 21 (26), 5972-5977.
166. D. Michael, P. Mingos, R. L. Johnston. In *Theoretical Approaches*; Springer Berlin Heidelberg, **1987**, pp 29-87.
167. J. W. Lauher, *J. Am. Chem. Soc.* **1978**, 100 (17), 5305-5315.
168. A. J. Stone, *Inorg. Chem.* **1981**, 20 (2), 563-571.
169. D. M. P. Mingos, *Nat. Phys. Sci.* **1972**, 236, 99.
170. D. M. P. Mingos, M. I. Forsyth, *J. Chem. Soc., Dalton Trans.* **1977**, (6), 610-616.
171. D. M. P. Mingos, *J. Chem. Soc., Chem. Commun.* **1983**, (12), 706-708.
172. D. M. P. Mingos, *Chem. Soc. Rev.* **1986**, 15 (1), 31-61.
173. D. M. P. Mingos, *J. Chem. Soc., Chem. Commun.* **1985**, (19), 1352-1354.
174. B. K. Teo, H. Zhang, *Polyhedron* **1990**, 9 (15), 1985-1999.
175. V. G. Albano, A. Ceriotti, P. Chini, G. Ciani, S. Martinengo, W. M. Anker, *J. Chem. Soc., Chem. Commun.* **1975**, (20), 859-860.
176. N. T. Tran, M. Kawano, D. R. Powell, L. F. Dahl, *J. Am. Chem. Soc.* **1998**, 120 (42), 10986-10987.
177. D. M. P. Mingos, *Acc. Chem. Res.* **1984**, 17 (9), 311-319.
178. K. Wade, *Electron-deficient compounds*, Nelson, London, **1971**.
179. P. Brint, J. P. Cronin, E. Seward, T. Whelan, *J. Chem. Soc., Dalton Trans.* **1983**, (5), 975-980.
180. M. Elian, M. M. L. Chen, R. Hoffmann, D. M. P. Mingos, *Inorg. Chem.* **1976**, 15 (5), 1148-1155.
181. R. Hoffmann, *Angew. Chem. Int. Ed. Engl.* **1982**, 21 (10), 711-724.
182. C. R. Eady, B. F. G. Johnson, J. Lewis, M. C. Malatesta, P. Machin, M. McPartlin, *J. Chem. Soc., Chem. Commun.* **1976**, (22), 945-946.
183. A. Donchev, A. Schnepf, G. Stößer, E. Baum, H. Schnöckel, T. Blank, N. Wiberg, *Chem. Eur. J.* **2001**, 7 (15), 3348-3353.
184. D. J. Wales. In *Encyclopedia of Inorganic Chemistry*, R. B. King, Ed.; John Wiley & Sons, Chichester, **2005**, Vol. III, pp 1506-1525.
185. M. Brack, *Rev. Mod. Phys.* **1993**, 65 (3), 677-732.
186. Z. Luo, A. W. Castleman, *Acc. Chem. Res.* **2014**, 47 (10), 2931-2940.
187. W. D. Knight, K. Clemenger, W. A. de Heer, W. A. Saunders, M. Y. Chou, M. L. Cohen, *Phys. Rev. Lett.* **1984**, 52 (24), 2141-2143.
188. W. D. Knight, W. A. de Heer, K. Clemenger, W. A. Saunders, *Solid State Commun.* **1985**, 53 (5), 445-446.
189. R. E. Leuchtner, A. C. Harms, A. W. C. Jr., *J. Chem. Phys.* **1989**, 91 (4), 2753-2754.
190. H. Hakkinen, *Chem. Soc. Rev.* **2008**, 37 (9), 1847-1859.



191. M. Walter, J. Akola, O. Lopez-Acevedo, P. D. Jadzinsky, G. Calero, C. J. Ackerson, R. L. Whetten, H. Grönbeck, H. Häkkinen, *PNAS* **2008**, 105 (27), 9157-9162.
192. N. W. Ashcroft, N. Mermin, *Solid State Physics*, Saunders College Publishing, New York **1976**.
193. K. E. Schriver, J. L. Persson, E. C. Honea, R. L. Whetten, *Phys. Rev. Lett.* **1990**, 64 (21), 2539-2542.
194. J. L. Persson, R. L. Whetten, H.-P. Cheng, R. S. Berry, *Chem. Phys. Lett.* **1991**, 186 (2), 215-222.
195. J. Hartig, A. Stoesser, P. Hauser, H. Schnöckel, *Angew. Chem. Int. Ed.* **2007**, 46, 1658-62.
196. P. A. Clayborne, O. Lopez-Acevedo, R. L. Whetten, H. Grönbeck, H. Häkkinen, *Eur. J. Inorg. Chem.* **2011**, 2011 (17), 2649-2652.
197. C. Zeng, H. Qian, T. Li, G. Li, N. L. Rosi, B. Yoon, R. N. Barnett, R. L. Whetten, U. Landman, R. Jin, *Angew. Chem. Int. Ed.* **2012**, 51 (52), 13114-13118.
198. O. Echt, K. Sattler, E. Recknagel, *Phys. Rev. Lett.* **1981**, 47 (16), 1121-1124.
199. M. v. Laue, *Z. Kristallogr.* **1943**, 105 (1-6), 124.
200. A. Kekulé, *Bull. Soc. Chim. Fr.* **1865**, 3, 98-110.
201. D. H. Wilcox, F. R. Greenbaum, *J. Chem. Educ.* **1965**, 42 (5), 266.
202. Z. Chen, R. B. King, *Chem. Rev.* **2005**, 105 (10), 3613-3642.
203. A. I. Boldyrev, L.-S. Wang, *Chem. Rev.* **2005**, 105 (10), 3716-3757.
204. J. M. Mercero, A. I. Boldyrev, G. Merino, J. M. Ugalde, *Chem. Soc. Rev.* **2015**, 44 (18), 6519-6534.
205. A. I. Boldyrev, L.-S. Wang, *PCCP* **2016**, 18 (17), 11589-11605.
206. V. I. Minkin, M. N. Glukhovtsev, B. Y. Simkin, *Aromaticity and Antiaromaticity: Electronic and Structural Aspects*, J. Wiley & Sons, New York, **1994**.
207. C. A. Tsipis, *Coord. Chem. Rev.* **2005**, 249 (24), 2740-2762.
208. X.-W. Li, W. T. Pennington, G. H. Robinson, *J. Am. Chem. Soc.* **1995**, 117 (28), 7578-7579.
209. S. Blanchard, L. Fensterbank, G. Gontard, E. Lacôte, G. Maestri, M. Malacria, *Angew. Chem. Int. Ed.* **2014**, 53 (7), 1987-1991.
210. T. J. Robilotto, J. Bacsá, T. G. Gray, J. P. Sadighi, *Angew. Chem. Int. Ed.* **2012**, 51 (48), 12077-12080.
211. K. Freitag, C. Gemel, P. Jerabek, I. M. Oppel, R. W. Seidel, G. Frenking, H. Banh, K. Dilchert, R. A. Fischer, *Angew. Chem. Int. Ed.* **2015**, 54 (14), 4370-4374.
212. S. Pan, R. Saha, S. Mandal, P. K. Chattaraj, *PCCP* **2016**, 18 (17), 11661-11676.
213. I. A. Popov, F.-X. Pan, X.-R. You, L.-J. Li, E. Matito, C. Liu, H.-J. Zhai, Z.-M. Sun, A. I. Boldyrev, *Angew. Chem. Int. Ed.* **2016**, 55 (49), 15344-15346.
214. I. Todorov, S. C. Sevov, *Inorg. Chem.* **2004**, 43 (20), 6490-6494.
215. A. E. Kuznetsov, J. D. Corbett, L.-S. Wang, A. I. Boldyrev, *Angew. Chem. Int. Ed.* **2001**, 40 (18), 3369-3372.
216. B. Twamley, P. P. Power, *Angew. Chem. Int. Ed.* **2000**, 39 (19), 3500-3503.
217. A. D. Phillips, P. P. Power, *J. Clust. Sci.* **2002**, 13 (4), 569-586.
218. A. E. Kuznetsov, A. I. Boldyrev, H.-J. Zhai, X. Li, L.-S. Wang, *J. Am. Chem. Soc.* **2002**, 124 (39), 11791-11801.
219. R. B. King, Z. Chen, P. v. R. Schleyer, *Inorg. Chem.* **2004**, 43 (15), 4564-4566.
220. A. Hirsch, Z. Chen, H. Jiao, *Angew. Chem. Int. Ed.* **2001**, 40 (15), 2834-2838.
221. H.-C. Hu, H.-S. Hu, B. Zhao, P. Cui, P. Cheng, J. Li, *Angew. Chem. Int. Ed.* **2015**, 54 (40), 11681-11685.
222. P. Cui, H.-S. Hu, B. Zhao, J. T. Miller, P. Cheng, J. Li, *Nat. Commun.* **2015**, 6, 6331.
223. H. Schnöckel, *Chem. Rev.* **2010**, 110 (7), 4125-4163.

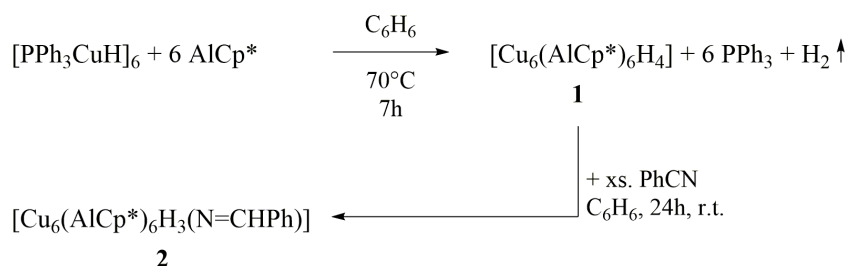
224. K. Koch, R. Burgert, G. Stösser, H. Schnöckel, *Eur. J. Mass Spectrom.* **2005**, 11 (5), 469-474.
225. J. Vollet, R. Burgert, H. Schnöckel, *Angew. Chem. Int. Ed.* **2005**, 44 (42), 6956-6960.
226. M. Huber, P. Henke, H. Schnöckel, *Chem. Eur. J.* **2009**, 15 (45), 12180-12183.
227. K. Weiß, H. Schnöckel, *Z. Anorg. Allg. Chem.* **2003**, 629 (7-8), 1175-1183.
228. C. Klemp, R. Köppe, E. Weckert, H. Schnöckel, *Angew. Chem. Int. Ed.* **1999**, 38 (12), 1739-1743.
229. A. Purath, C. Dohmeier, A. Ecker, R. Köppe, H. Krautscheid, H. Schnöckel, R. Ahlrichs, C. Stoermer, J. Friedrich, P. Jutzi, *J. Am. Chem. Soc.* **2000**, 122 (29), 6955-6959.
230. M. Huber, J. Hartig, K. Koch, H. Schnöckel, *Z. Anorg. Allg. Chem.* **2009**, 635 (3), 423-430.
231. M. Huber, A. Schnepf, C. E. Anson, H. Schnöckel, *Angew. Chem. Int. Ed.* **2008**, 47 (43), 8201-8206.
232. A. Puls, P. Jerabek, W. Kurashige, M. Förster, M. Molon, T. Bollermann, M. Winter, C. Gemel, Y. Negishi, G. Frenking, R. A. Fischer, *Angew. Chem. Int. Ed.* **2014**, 53 (17), 4327-4331.
233. J. Hartig, F. Klöwer, J. Rinck, A.-N. Unterreiner, H. Schnöckel, *Angew. Chem. Int. Ed.* **2007**, 46 (34), 6549-6552.
234. J. Hagel, M. T. Kelemen, G. Fischer, B. Pilawa, J. Wosnitza, E. Dormann, H. v. Löhneysen, A. Schnepf, H. Schnöckel, U. Neisel, J. Beck, *J. Low Temp. Phys.* **2002**, 129 (3), 133-142.
235. J. Hartig, A. Schnepf, L. J. de Jongh, D. Bono, H. Schnöckel, *Z. Anorg. Allg. Chem.* **2007**, 633 (1), 63-76.
236. E. C. Tyo, S. Vajda, *Nat. Nanotechnol.* **2015**, 10 (7), 577-588.
237. R. Ferrando, J. Jellinek, R. L. Johnston, *Chem. Rev.* **2008**, 108 (3), 845-910.
238. R. Raja, S. Hermans, D. S. Shephard, B. F. G. Johnson, R. Raja, G. Sankar, S. Bromley, J. Meurig Thomas, *Chem. Commun.* **1999**, (16), 1571-1572.
239. J. Zhang, L. F. Dahl, *J. Chem. Soc., Dalton Trans.* **2002**, (7), 1269-1274.
240. M. Kawano, J. W. Bacon, C. F. Campana, B. E. Winger, J. D. Dudek, S. A. Sirchio, S. L. Scruggs, U. Geiser, L. F. Dahl, *Inorg. Chem.* **2001**, 40 (11), 2554-2569.
241. J.-L. Zeng, Z.-J. Guan, Y. Du, Z.-A. Nan, Y.-M. Lin, Q.-M. Wang, *J. Am. Chem. Soc.* **2016**, 138 (25), 7848-7851.
242. X.-K. Wan, X.-L. Cheng, Q. Tang, Y.-Z. Han, G. Hu, D.-e. Jiang, Q.-M. Wang, *J. Am. Chem. Soc.* **2017**, 139 (28), 9451-9454.
243. G. Thiele, Z. You, S. Dehnen, *Inorg. Chem.* **2015**, 54 (6), 2491-2493.
244. P. Jutzi, B. Neumann, G. Reumann, H.-G. Stammler, *Organometallics* **1998**, 17 (7), 1305-1314.
245. P. Jutzi, B. Neumann, L. O. Schebaum, A. Stammler, H.-G. Stammler, *Organometallics* **1999**, 18 (21), 4462-4464.
246. C. Gemel, T. Steinke, D. Weiss, M. Cokoja, M. Winter, R. A. Fischer, *Organometallics* **2003**, 22 (13), 2705-2710.
247. M. Cokoja, T. Steinke, C. Gemel, T. Welzel, M. Winter, K. Merz, R. A. Fischer, *J. Organomet. Chem.* **2003**, 684 (1-2), 277-286.
248. J. Weiss, D. Stetzkamp, B. Nuber, R. A. Fischer, C. Boehme, G. Frenking, *Angew. Chem. Int. Ed. Engl.* **1997**, 36 (1-2), 70-72.
249. P. Jutzi, B. Neumann, L. O. Schebaum, A. Stammler, H.-G. Stammler, *Organometallics* **2000**, 19 (7), 1445-1447.
250. J. Weßing, C. Göbel, B. Weber, C. Gemel, R. A. Fischer, *Inorg. Chem.* **2017**, 56 (6), 3517-3525.

251. S. González-Gallardo, T. Bollermann, R. A. Fischer, R. Murugavel, *Chem. Rev.* **2012**, 112 (6), 3136-3170.
252. C. Gemel, T. Steinke, M. Cokoja, A. Kempter, Roland A. Fischer, *Eur. J. Inorg. Chem.* **2004**, 4161-4176.
253. P. W. Roesky, *Dalton Trans.* **2009**, (11), 1887-1893.
254. S. Gonzalez-Gallardo, G. Prabusankar, T. Cadenbach, C. Gemel, M. von Hopffgarten, G. Frenking, R. A. Fischer. In *Metal-Metal Bonding*, G. Parkin, Ed.; Springer Berlin Heidelberg, **2010**, pp 147-188.
255. G. Linti, H. Schnöckel, *Coord. Chem. Rev.* **2000**, 206–207, 285-319.
256. T. Steinke, C. Gemel, M. Winter, R. A. Fischer, *Angew. Chem. Int. Ed.* **2002**, 41 (24), 4761-4763.
257. T. Steinke, C. Gemel, M. Winter, R. A. Fischer, *Chem. Eur. J.* **2005**, 11 (5), 1636-1646.
258. E. V. Grachova, P. Jutzi, B. Neumann, L. O. Schebaum, H.-G. Stammer, S. P. Tunik, *J. Chem. Soc., Dalton Trans.* **2002**, (3), 302-304.
259. B. Buchin, C. Gemel, T. Cadenbach, R. A. Fischer, *Inorg. Chem.* **2006**, 45 (4), 1789-1794.
260. Wei, M. Winter, R. A. Fischer, C. Yu, K. Wichmann, G. Frenking, *Chem. Commun.* **2000**, (24), 2495-2496.
261. T. Cadenbach, T. Bollermann, C. Gemel, I. Fernandez, M. von Hopffgarten, G. Frenking, R. A. Fischer, *Angew. Chem. Int. Ed.* **2008**, 47 (47), 9150-9154.
262. T. Cadenbach, T. Bollermann, C. Gemel, M. Tombul, I. Fernandez, M. v. Hopffgarten, G. Frenking, R. A. Fischer, *J. Am. Chem. Soc.* **2009**, 131 (44), 16063-16077.
263. M. Molon, K. Dilchert, C. Gemel, R. W. Seidel, J. Schaumann, R. A. Fischer, *Inorg. Chem.* **2013**, 52 (24), 14275-14283.
264. M. Molon, C. Gemel, P. Jerabek, L. Trombach, G. Frenking, R. A. Fischer, *Inorg. Chem.* **2014**, 53 (19), 10403-10411.
265. M. Molon, C. Gemel, R. A. Fischer, *Dalton Trans.* **2014**, 43 (8), 3114-3120.
266. M. Molon, C. Gemel, R. A. Fischer, *Eur. J. Inorg. Chem.* **2013**, 2013 (21), 3616-3622.
267. U. Häussermann, P. Viklund, C. Svensson, S. Eriksson, P. Berastegui, S. Lidin, *Angew. Chem. Int. Ed.* **1999**, 38 (4), 488-492.
268. P. Viklund, C. Svensson, S. Hull, S. I. Simak, P. Berastegui, U. Häußermann, *Chem. Eur. J.* **2001**, 7 (23), 5143-5152.
269. M. Cokoja, B. R. Jagirdar, H. Parala, A. Birkner, R. A. Fischer, *Eur. J. Inorg. Chem.* **2008**, 2008 (21), 3330-3339.
270. M. Cokoja, H. Parala, A. Birkner, R. A. Fischer, O. Margeat, D. Ciuculescu, C. Amiens, B. Chaudret, A. Falqui, P. Lecante, *Eur. J. Inorg. Chem.* **2010**, 2010 (11), 1599-1603.
271. M. Cokoja, H. Parala, A. Birkner, O. Shekhah, M. W. E. van den Berg, R. A. Fischer, *Chem. Mater.* **2007**, 19 (23), 5721-5733.
272. M. Cokoja, H. Parala, M.-K. Schröter, A. Birkner, M. W. E. van den Berg, W. Grünert, R. A. Fischer, *Chem. Mater.* **2006**, 18 (6), 1634-1642.
273. K. Schutte, A. Doddi, C. Kroll, H. Meyer, C. Wiktor, C. Gemel, G. van Tendeloo, R. A. Fischer, C. Janiak, *Nanoscale* **2014**, 6 (10), 5532-5544.
274. M. Armbrüster, K. Kovnir, M. Behrens, D. Teschner, Y. Grin, R. Schlögl, *J. Am. Chem. Soc.* **2010**, 132 (42), 14745-14747.
275. M. Armbrüster, K. Kovnir, M. Friedrich, D. Teschner, G. Wowsnick, M. Hahne, P. Gille, L. Szentmiklósi, M. Feuerbacher, M. Heggen, F. Girgsdies, D. Rosenthal, R. Schlögl, Y. Grin, *Nat. Mater.* **2012**, 11, 690.
276. T. Cadenbach, C. Gemel, R. Schmid, M. Halbherr, K. Yussenko, M. Cokoja, R. A. Fischer, *Angew. Chem. Int. Ed.* **2009**, 48 (21), 3872-3876.

## 4 RESULTS AND DISCUSSION

## 4.1 Laying the groundwork - $[\text{Cu}_6(\text{AlCp}^*)_6\text{H}_4]$ as an archetypical metalloid TM/E cluster

The results presented in the following chapter laid the foundations for the PhD thesis at hand and consequently ought to be thoroughly reviewed and completed herein. Initially discovered by Dr. C. Ganesamoorthy at our chair, the recapitulation of the synthesis of the intermetalloid Cu/Al cluster  $[\text{Cu}_6(\text{AlCp}^*)_6\text{H}_4]$  (**1**) and its derivative  $[\text{Cu}_6(\text{AlCp}^*)_6\text{H}_3(\text{N}=\text{CHPh})]$  (**2**), along with their extensive characterization were already pursued as part of my Master thesis in 2013 and finalized in the course of the first months of my PhD thesis. Compound **1** represents the first example of a remarkable intermetallic cluster left of the Zintl border which is exclusively stabilized by a hydrocarbon shell of Cp\* ligands and hydrides. A comprehensive report has been published in the following reference.<sup>11</sup>



**Scheme 1.** Synthesis of  $[\text{Cu}_6(\text{AlCp}^*)_6\text{H}_4]$  (**1**) and  $[\text{Cu}_6(\text{AlCp}^*)_6\text{H}_3(\text{N}=\text{CHPh})]$  (**2**). **1** is selectively obtained from  $[\text{PPh}_3\text{CuH}]_6$  and AlCp\* by ligand substitution of the labile phosphine ligand with concurrent, partial reduction of the Cu centers *via* elimination of hydrogen. Subsequent reaction with an excess of benzonitrile affords the stoichiometric insertion product **2** featuring reduction of the nitrile group by hydride transfer from the CuAl cluster to the nitrilic carbon.

The unprecedented intermetallic hydrido cluster  $[\text{Cu}_6(\text{AlCp}^*)_6\text{H}_4]$  (**1**) is selectively obtained from the stoichiometric reaction of Stryker's reagent  $[\text{PPh}_3\text{CuH}]_6$  with six equivalents of AlCp\* at 70°C in benzene (Scheme 1). The composition of the highly air- and moisture sensitive compound was confirmed by means of NMR and IR spectroscopic analysis, liquid injection field desorption ionisation (LIFDI)-mass spectrometry, elemental analysis and single crystal X-ray diffraction analysis. Its molecular structure comprises a bicapped tetrahedral  $\text{Cu}_6$  unit which is incorporated into the octahedral arrangement of six AlCp\* ligands, with the resultant intermetallic  $\text{Cu}_6\text{Al}_6$  core geometry correlating to structural motifs found amongst the nested polyhedra of common Hume-Rothery phases, like  $\gamma$ -brass or the structurally related  $\text{Cu}_4\text{Al}_9$  (Figure 31).

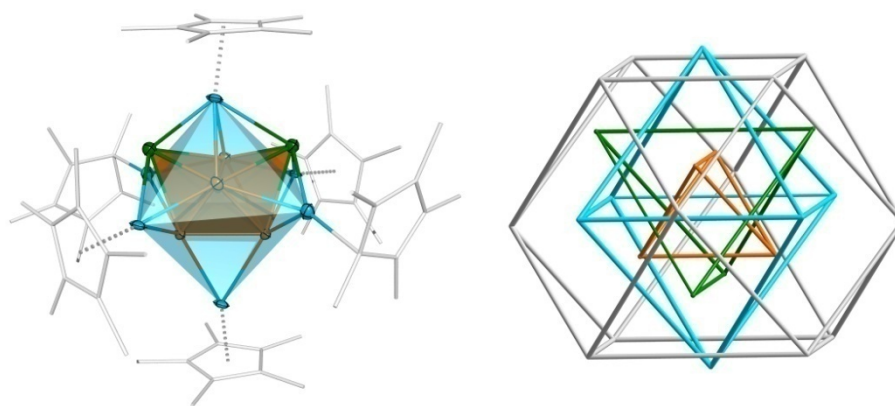


**Figure 31.** One disorder site of the molecular structure of **1** (left; hydrogen atoms omitted for clarity, thermal ellipsoids shown at the 30% probability level, Cu, Al depicted in orange and green, blue, respectively). The intermetallic  $\text{Cu}_6\text{Al}_6$  core comprises a bicapped tetrahedral  $\text{Cu}_6$  unit inside an octahedral  $\text{Al}_6$  arrangement. The overall structural motif correlates to nested polyhedra found in the solid state structures of  $\gamma$ -brass and related phases, like  $\text{Cu}_4\text{Al}_9$  (left). Reprinted with permission of C. Ganesamoorthy, J. Weßing, C. Kroll, R. W. Seidel, C. Gemel, R. A. Fischer, *Angew. Chem. Int. Ed.* **2014**, 53 (30), 7943-7947. Copyright 2014 Wiley-VCH Verlag GmbH & Co. KGaA, Weinheim.

Most notably, compound **1** is formed by ligand substitution of the labile phosphine ligands at the copper hydride precursor with concurrent elimination of hydrogen resulting in the partial reduction of the central copper atoms. The former is a commonly employed strategy in the formation of TM-E bonds, usually giving mononuclear complexes of the overall formula  $[\text{TM}(\text{PR}_3)_n(\text{ECp}^*)_m]$  instead of compounds of higher nuclearity.<sup>251, 277, 278</sup> Consequently, in the formation of **1**, the additionally observed elimination of hydrogen as an innocent leaving group was assigned a crucial role for the formation of the oligonuclear copper core with partial  $\text{Cu}^0$  character. However, triggered by the discovery of the related CoGa cluster  $[(\text{Cp}^*\text{Co})_3\text{Ga}_6(\text{Cp}^*_3\text{Co}_3(\mu^3\text{-CH}))\text{H}_x]$  (**6**) (compare chapter 4.4), an alternative theory arose assuming that ligand substitution at a preformed metal core, as provided by the hexameric  $[\text{PPh}_3\text{CuH}]_6$ <sup>279</sup> in the given case, might allow for the retention of the cluster core's nuclearity and invoke structural rearrangement, only. First indications thereof are provided by *in situ*  $^1\text{H}$  NMR spectroscopic measurements of the reaction mixture of  $[\text{PPh}_3\text{CuH}]_6$  and  $\text{AlCp}^*$  in  $\text{C}_6\text{D}_6$  at  $70^\circ\text{C}$ . These reveal the formation of coalescent, featureless signals corresponding to either fluctuating or chemically closely related  $\text{PPh}_3$  moieties in the aromatic region, instead of simultaneously de-/increasing signals of the starting reagent  $[\text{PPh}_3\text{CuH}]$  (7.61, 6.96 and 6.81 ppm) and the liberated  $\text{PPh}_3$  ligand (7.39 and 7.06 ppm; Figure 32). At the same time, a broad underlying signal is observed around 2.10 ppm which might indicate the formation of only partially substituted species  $[\text{Cu}_6(\text{PPh}_3)_{6-b}(\text{AlCp}^*)_b\text{H}_x]$ . Attempts to resolve such species in *in situ*  $^{31}\text{P}$  NMR spectroscopic measurements remained inconclusive.

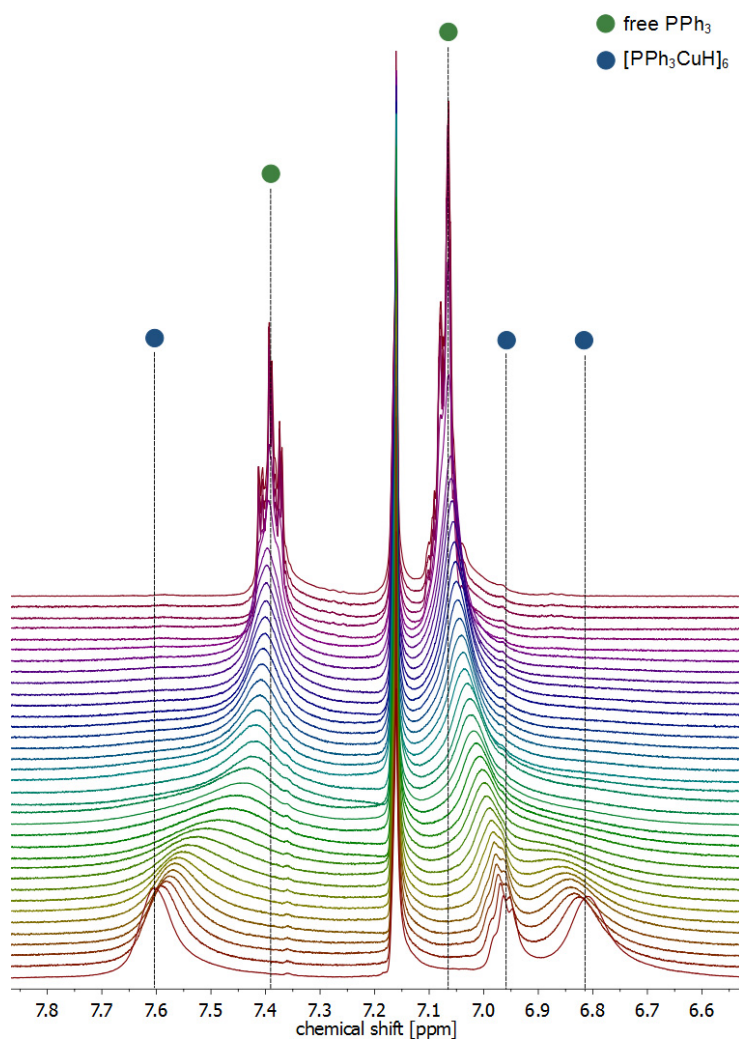


**Figure 32.** Detailed view on the development of the aromatic PPh<sub>3</sub> signals during *in situ* <sup>1</sup>H NMR spectroscopic measurements of the reaction mixture of [PPh<sub>3</sub>CuH]<sub>6</sub> and AlCp\* in C<sub>6</sub>D<sub>6</sub> at 70 °C over the course of 4h. Coalescent, featureless signals rather than simultaneously de-/increasing signals of [PPh<sub>3</sub>CuH] and the free PPh<sub>3</sub> ligand are observed, which might indicate the formation of only partially substituted species [Cu<sub>6</sub>(PPh<sub>3</sub>)<sub>6-b</sub>(AlCp\*)<sub>b</sub>H<sub>x</sub>].

Note that a closely related behaviour has actually been reported for gold thiolate clusters which undergo ligand exchange induced structural transformations upon heating in the presence of an alternative thiolate ligand.<sup>9</sup> For instance, thermal treatment of a solution of [Au<sub>38</sub>(SCH<sub>2</sub>CH<sub>2</sub>Ph)<sub>24</sub>] with an excess of 4-*t*-butylthiolphenol results in the selective formation of the smaller Au cluster [Au<sub>36</sub>(SC<sub>6</sub>H<sub>4</sub>-4-<sup>t</sup>Bu)<sub>24</sub>].<sup>197</sup> Likewise, ligand exchange induced growth was reported for the reaction of [Cu<sub>25</sub>H<sub>22</sub>(PPh<sub>3</sub>)<sub>12</sub>]Cl with an excess of 4,7-diphenyl-1,10-phenanthroline at room temperature.<sup>10</sup> Here, the atomically precise [Cu<sub>29</sub>Cl<sub>4</sub>H<sub>22</sub>(Ph<sub>2</sub>phen)<sub>12</sub>]Cl was obtained in almost quantitative yields.

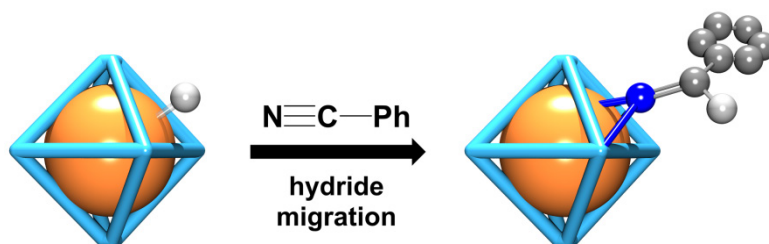


**Figure 33.** Conceptual scheme of the hydride transfer reaction occurring upon coordination of one molecule of benzonitrile. The overall reactivity reminds of hydrogenation reactions occurring at catalytically active Hume-Rothery nanophases, thus rendering **2** a first molecular model for potential surface intermediates of such reactions. Reprinted with permission of C. Ganesamoorthy, J. Weßing, C. Kroll, R. W. Seidel, C. Gemel, R. A. Fischer, *Angew. Chem. Int. Ed.* **2014**, 53 (30), 7943-7947. Copyright 2014 Wiley-VCH Verlag GmbH & Co. KGaA, Weinheim.

Bearing in mind the high catalytic activity of Hume-Rothery nanophases in hydrogenation reactions, **1** was treated with various organic substrates bearing unsaturated functionalities in an attempt to study the availability of the remaining cluster-bound hydrides for hydride transfer reactions, and the stability of **1** in the presence of such small organic molecules. It was reasoned that, provided an isolation of reaction intermediates and/or products, such homogeneous hydrogenation reactions might add to the conceptual understanding of related reactions at catalytically active Hume-Rothery nanophases and the synergistic effects contributing to their exceptional catalytic performance. In the reaction of **1** with an excess of benzonitrile at room temperature for 24h (Scheme 1), the selective formation of the 1:1 insertion product  $[\text{Cu}_6(\text{AlCp}^*)_6\text{H}_3(\text{N}=\text{CHPh})]$  (**2**) is observed. **2** features the coordination of one molecule of benzonitrile with concomitant reduction of the nitrile functionality by hydride transfer from the  $[\text{Cu}_6\text{Al}_6\text{H}_4]$  cluster core to the nitrilic carbon. The resultant iminate species remains coordinated to the cluster surface in a CuAl bridging position. With regards to catalytic hydrogenation reactions at Hume-Rothery nanophases, such as  $\text{Fe}_3\text{Al}_{14}$  or  $\text{PdGa}$ ,<sup>274, 275</sup> the insertion of benzonitrile into a metal-hydride bond of **1** was suggested as a first molecular study case for potential reaction intermediates at the respective interfaces (Figure 33). Furthermore, the resulting CuAl bridging bonding mode was regarded an indication for potential cooperative interaction between the distinct metal sites.

#### 4.1.1 Excursus: Electron counting for the model compounds **1** and **2** - An effective tool to assess observed reactivities

As introduced earlier, simple electron counting principles can be employed to rationalize complex structures and even assess the reaction behaviour of coordination compounds. Regarding the synthesis of **1**, formation of the unprecedented CuAl cluster is suggested to occur by ligand substitution at a pre-assembled  $\text{Cu}_6$  core which undergoes structure



transformation upon progressive replacement of phosphine ligands by AlCp\*. Based on the analysis of cluster valence electron counts, this appears to be a reasonable scenario. In the solid state, the reactant [PPh<sub>3</sub>CuH]<sub>6</sub> features a central octahedral Cu<sub>6</sub> core with each Cu vertex bearing a terminally bound phosphine ligand.<sup>279</sup> However, the observed count of  $6 \cdot 11 + 6 \cdot 2 + 6 \cdot 1 = 84$  cluster valence electrons does not match the expected 86 cve, but rather suggests a bicapped tetrahedron as the most stable geometry. Considering the high steric demand and the preferential terminal coordination of the PPh<sub>3</sub> ligand, the diverging structure is most likely a result of ligand effects. Upon progressive substitution of phosphine ligands by the isolobal two electron-donor AlCp\*, steric strain is reduced. Furthermore, the more versatile AlCp\* ligand is able to adopt bridging positions, thus allowing for structure transformation of the central Cu<sub>6</sub> unit towards a bicapped tetrahedron.

Notably, the concomitant elimination of hydrogen lowers the eventual cluster valence count of **1** to 82 cve, instead of the expected 84 cve. The resulting mismatch may actually provide an explanation for the selective formation of **2** in the presence of an excess of benzonitrile, albeit the steric hindrance of the almost spherical hydrocarbon shell of six Cp\* ligands must certainly not be neglected. Irrespective thereof, the coordination of exactly one molecule of benzonitrile and its reduction to an iminate species *via* hydride transfer furnishes the two additional electrons required to match the expected value of 84 cve ( $6 \cdot 11 + 6 \cdot 2 + 3 \cdot 1 + 1 \cdot 3$ ).

#### 4.1.2 Identifying new routines - Assessing the suitability of XPS as a classical solid-state characterization technique for the characterization of **1**

*The experimental XPS spectra discussed in the following paragraph were measured by the group of Prof. Dr. Sebastian Günther, particularly involving M.Sc. Tim Kratky, Technical University of Munich, Germany.*

Approaching the size regime of metalloid clusters [TM<sub>a</sub>(ECp\*)<sub>b</sub>], increasing difficulties arise with regards to the characterization of such cluster compounds due to their diminished solubility in common organic solvents. Consequently, techniques employed in the characterization of classical complexes and small clusters, like solution-phase NMR spectroscopy or mass spectrometry are no longer applicable, and alternative techniques have to be consulted for a comprehensive analysis. Conceivable methods commonly employed for the characterization of materials include solid state magic angle spinning (MAS) NMR spectroscopy, powder X-ray diffraction (PXRD), X-ray photoelectron spectroscopy (XPS), and X-ray absorption spectroscopic (XAS) measurements, like extended X-ray absorption fine structure (EXAFS) or X-ray absorption near edge structure spectroscopy (XANES). However,

owing to the high air and moisture sensibility of the samples, new routines have to be established for sample preparation and data acquisition. Likewise, the lack of suitable reference data and experience with such compounds hamper an accurate evaluation of compiled data.

Using the well defined and extensively characterized model system  $[\text{Cu}_6(\text{AlCp}^*)_6\text{H}_4]$  (**1**), the applicability of established solid state characterization techniques for this particular, and related intermetallic clusters  $[\text{TM}_a(\text{ECp}^*)_b]$  can be assessed and adapted accordingly. For the exemplary case of XPS, recent investigations on the copper hydride nanoclusters  $[\text{Cu}_{25}\text{H}_{22}(\text{PPh}_3)_{12}]\text{Cl}$  and  $[\text{Cu}_{29}\text{Cl}_4\text{H}_{22}(\text{Ph}_2\text{phen})_{12}]\text{Cl}$  demonstrate the method's potential in the elucidation of cluster composition, and the oxidation states of central metal atoms.<sup>10, 280</sup> In another example, the  $\text{Au}4f_{7/2}$  and  $\text{Cu}2p_{3/2}$  binding energies of the bimetallic  $\text{Au}_{19}\text{Cu}_{30}$  nanoclusters  $[\text{Au}_{19}\text{Cu}_{30}(\text{C}\equiv\text{CR})_{22}(\text{PPh}_3)_6\text{Cl}_2](\text{NO}_3)_3$  ( $\text{R}$  = thiophen-3-yl, phenyl) were found to correlate reasonably well with the reduced oxidation states of the central Au and Cu atoms.<sup>242</sup>

The XPS survey spectrum of **1** (Figure 34) shows photoelectron signals corresponding to the binding energies of carbon ( $\text{C}1s$ ), copper ( $\text{Cu}2p$ ,  $\text{Cu}3s$ ,  $\text{Cu}3p$ ) and aluminium ( $\text{Al}2s$ ,  $\text{Al}2p$ ), along with the  $\text{C}KVV$  and  $\text{Cu}LMM$  Auger peaks.<sup>281</sup> Additionally, photoelectron peaks attributed to oxygen ( $\text{O}1s$ ) and silicon ( $\text{Si}2s$ ,  $\text{Si}2p$ ), and the Auger peak of oxygen ( $\text{O}KLL$ ) are observed, which are believed to stem from negligible amounts of residual grease, and potentially air.

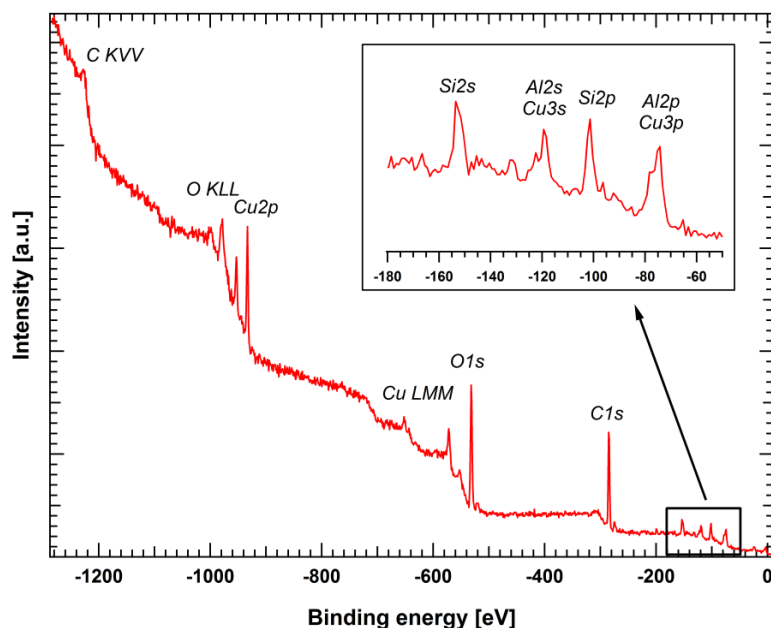


**Figure 34.** XPS survey spectrum of  $[\text{Cu}_6(\text{AlCp}^*)_6\text{H}_4]$  (**1**) showing the photoelectron peaks of Cu, Al and C, along with the Auger peaks of C and Cu. Additional signals (O, Si) originate from negligible impurities, i.e. grease, and potentially air contact upon sample transfer to the analytical set-up.

Owing to considerable sample charging effects in the range of 3-4 eV, as indicated by notably higher binding energies than provided by literature-known reference data, binding energies were calibrated using the C1s peak at 284.6 eV. The corrected Cu2p<sub>3/2</sub> and Al2s binding energies were determined to be 933.0 and 119.1 eV, respectively. While reference data of molecular Al cluster compounds is scarce, the determined Cu2p<sub>3/2</sub> binding energy is indicative of low valent copper centers with an oxidation state between 0 and +I as it is only slightly higher than those observed for elemental copper foil (932.4 eV)<sup>282</sup> or the mixed-valency Cu<sup>I</sup>/Cu<sup>0</sup> centers of [Au<sub>19</sub>Cu<sub>30</sub>(C≡CR)<sub>22</sub>(PPh<sub>3</sub>)<sub>6</sub>Cl<sub>2</sub>](NO<sub>3</sub>)<sub>3</sub> (932.9 eV).<sup>242</sup> This is further supported by the shape of the Cu2p peak which lacks the otherwise observed Cu<sup>2+</sup> satellite features (Figure 35b). The Auger parameter of 1848.2 eV, calculated from the Cu2p<sub>3/2</sub> and the Cu L<sub>3</sub>M<sub>45</sub>M<sub>45</sub> peaks, is lower than the value observed for bulk Cu (1851.2 eV), but lies in a comparable range as those reported for oligonuclear Cu(I) clusters (1848.6 eV for [HCu(PPh<sub>3</sub>)<sub>6</sub>]; 1847.4 eV for [ClCu(PPh<sub>3</sub>)<sub>4</sub>], or larger copper clusters with partial Cu(0) character, like [Cu<sub>25</sub>H<sub>22</sub>(PPh<sub>3</sub>)<sub>12</sub>]Cl (1849.1 eV) or [Cu<sub>29</sub>Cl<sub>4</sub>H<sub>22</sub>(Ph<sub>2</sub>phen)<sub>12</sub>]Cl (1848.9 eV; Table 6).<sup>280</sup> The thus indicated substantial Cu(I) character is in good agreement with the composition of **1**, particularly with regards to four residual hydride ligands at the intermetallic Cu/Al cluster core. Note that partial Cu(0) character can neither be reliably confirmed, nor excluded.

*Comment: In this context, it should be noted that the formalisms of valence or oxidation states for coordination compounds with complex core compositions are ambiguous, albeit frequently used. Consequently, XPS should be considered as a means to directly assess the unique chemical state of elements, rather than a tool for the classification in terms of discrete oxidation states or valencies.*

Based on the deconvolution of the overlapping Al2s and Cu3s photoelectron peaks, the Al:Cu ratio was estimated to 2.2:1 which deviates considerably from the expected ratio of 1:1 (Figure 35c). This is ascribed to the spherical molecular structure of **1** with an arrangement that is reminiscent of core-shell systems. Given the surface-sensitive nature of XPS with signals that originate from few nanometers only, a diminished escape probability of photoelectrons of the less exposed elements is conceivable. In addition, photoelectrons excited from such central species are more likely to interact with the surrounding sample after their emission, thus being effectively more shielded. A comparable effect has been observed in the determination of relative atomic abundances for [Cu<sub>25</sub>H<sub>22</sub>(PPh<sub>3</sub>)<sub>12</sub>]Cl and [Cu<sub>29</sub>Cl<sub>4</sub>H<sub>22</sub>(Ph<sub>2</sub>phen)<sub>12</sub>]Cl based on XPS results.<sup>10, 280</sup> While the experimentally determined atomic ratios of the innermost components (Cu:P or Cu:N) were in good agreement with the calculated ones, drastically enhanced values were reported for the relative abundances of carbon forming the outermost ligand shell.

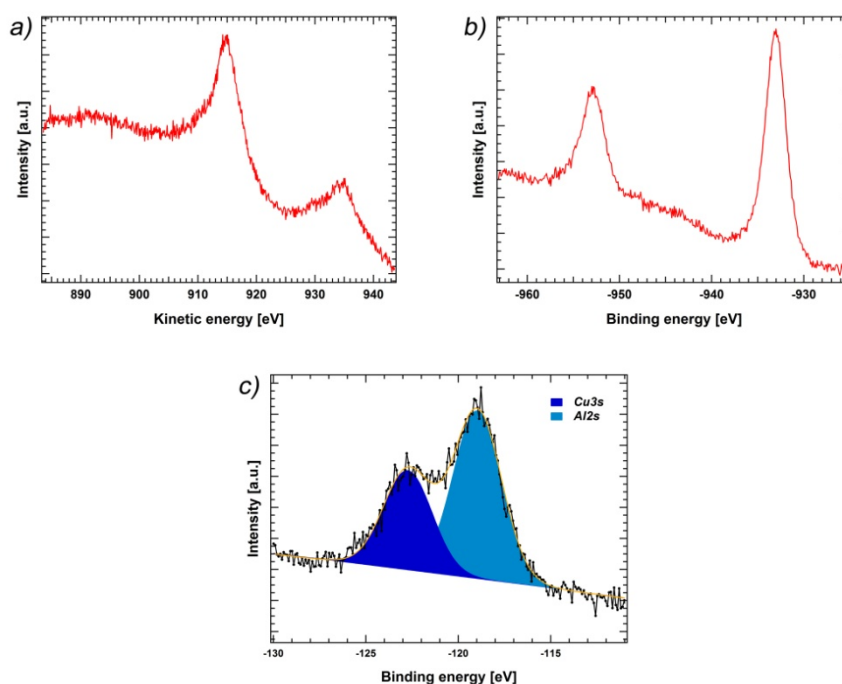


**Figure 35.** High resolution scans of a) the Cu Auger peaks  $L_3M_{45}M_{45}$  and  $L_2M_{45}M_{45}$ , and b) the Cu2p photoelectron peaks of  $[Cu_6(AlCp^*)_6H_4]$  (**1**). Based on the chemical shift and shape of the latter, and the Auger parameter (1848.2 eV), copper was assigned a low oxidation state with substantiate Cu(I) character. Partial Cu(0) character can neither be reliably confirmed, nor excluded. c) High resolution scan of the overlapping Cu3s and Al2s region. The elemental ratio is determined to Cu:Al  $\approx$  1:2.2.

**Table 6.** Auger parameters of **1**, and selected Cu(0) and Cu(I) compounds.<sup>280</sup> The determined value of 1848.2 eV is indicative of Cu species with substantiate Cu(I) character. However, partial Cu(0) character cannot be entirely excluded.

Sample	Auger parameter [eV]
$[Cu_6(AlCp^*)_6H_4]$ ( <b>1</b> )	<b>1848.2</b>
$[ClCu(PPh_3)]_4$	1847.4
$[HCu(PPh_3)]_6$	1848.6
$[Cu_{29}Cl_4H_{22}(Ph_2phen)_{12}]Cl$	1848.9
$[Cu_{25}H_{22}(PPh_3)_{12}]Cl$	1849.1
Cu foil	1851.2

### 4.1.3 Concluding remarks

The archetypical, intermetallic CuAl cluster  $[\text{Cu}_6(\text{AlCp}^*)_6\text{H}_4]$  (**1**) and its closely related derivative  $[\text{Cu}_6(\text{AlCp}^*)_6(\text{N}=\text{CHPh})\text{H}_3]$  (**2**) do not only provide a first proof-of-principle for the accessibility of all-AlCp\*-ligated transition metal atom assemblies approaching the metalloid cluster size regime, but rather provide us with a fully elucidated, and well-accessible model case system for follow-up investigation of TM/E nanoclusters. On the one hand, a deeper understanding of the formation mechanism of **1** will eventually contribute to the rational development of reliable synthetic strategies of related compounds; on the other hand, **1** can be used as a reference system to test and develop new routines in the characterization of such systems, e.g. XPS, EXAFS, XANES or pair distribution function (PDF) analysis. Given the classification of **1** and **2** as molecular models for the substructures of bulk intermetallics, and catalytic processes at their surfaces, relevant insights can be expected from a thorough investigation of the follow-up chemistry of **1**. Furthermore, an elucidation of the electronic situation of **1** might shed some light on the bonding situation in mixed-metal TM/E cluster compounds and nanomaterials, and the effect of p-metal doping in noble metal assemblies. Note in this regards, that  $[\text{Cu}_6(\text{AlCp}^*)_6\text{H}_4]$  can potentially be understood as a two-electron superatom.

## 4.2 The intermetalloid CuAl cluster $[\text{Cu}_{43}(\text{AlCp}^*)_{12}]$ (**3**), a rare example of a heterometallic open-shell superatom with a Mackay-type $\text{M}_{55}$ two-shell icosahedral structure

*The work presented in the following chapter is rooted in initial studies conducted by Dr. C. Ganesamoorthy during his research stay as a post-doctoral researcher at the Chair of Inorganic Chemistry II, Ruhr-University Bochum, under the guidance of Prof. Dr. Roland A. Fischer. In his work, Dr. C. Ganesamoorthy discovered the synthesis of  $[\text{Cu}_{43}(\text{AlCp}^*)_{12}]$  from  $[\text{Cu}(\text{Mes})]_5$  or the pre-assembled  $[\text{Cu}_6(\text{AlCp}^*)_6\text{H}_4]$  (**1**), respectively, and performed preliminary characterizations. The recapitulation and optimization of the synthesis of  $[\text{Cu}_{43}(\text{AlCp}^*)_{12}]$  (**3**) as well as its comprehensive characterization were started in my Master thesis in 2013 and followed-up during the course of this PhD thesis.*

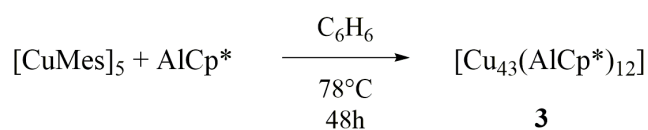
### 4.2.1 Introductory remarks

In 1981, the discovery of Schmid's famous gold cluster compound “[ $\text{Au}_{55}(\text{PPh}_3)_{12}\text{Cl}_6$ ]” opened the field of metalloid clusters as an intermediate state of matter between molecular complexes, clusters and bulk metals, and ever since stimulated research on structure and bonding in such systems.<sup>143, 144</sup> Meanwhile, a handful of structurally characterized metalloid clusters of this size regime have emerged, i.e. Schnöckel's  $[\text{Al}_{50}\text{Cp}^*_{12}]$  or the very recent heterometallic AuCu cluster compound  $[\text{Au}_{19}\text{Cu}_{30}(\text{C}\equiv\text{CR})_{22}(\text{PPh}_3)_6\text{Cl}_2]$ .<sup>159, 242</sup> A first unambiguous proof of the proposed  $\text{M}_{55}$  magic atom number structure in ligand-stabilized homometallic transition metal clusters was reported in 2016 by Dahl *et al.* with the Mackay-type two-shell icosahedral palladium cluster  $[\text{Pd}_{55}(\text{P}^i\text{Pr}_3)_{12}(\text{CO})_{20}]$ .<sup>150</sup>

Thus inspired, the prospect of expanding the chemistry of Hume-Rothery type coordination compounds into the field of (inter-)metalloid clusters has always been a fascinating research enterprise. Considering Schnöckel's  $[\text{Al}_{50}\text{Cp}^*_{12}]$  which can alternatively be written as  $[\text{Al}_{38}(\text{AlCp}^*)_{12}]$ , a stabilization of naked metalloid kernels using the  $\text{ECp}^*$  ligand seems feasible, and examples of all- $\text{ECp}^*$ -ligated transition metal clusters approaching the classification as intermetalloid are presented in other chapters of this thesis. In the following, the synthesis and characterization of the truly intermetalloid cluster  $[\text{Cu}_{43}(\text{AlCp}^*)_{12}]$ , also written as  $[\text{Cu}_{43}\text{Al}_{12}](\text{Cp}^*)_{12}$  (**3**) is discussed, which provides a first proof-of-principle of the capability of  $\text{AlCp}^*$  to effectively stabilize polynuclear, heterometal cluster cores. Compound **3** represents the first ligated intermetallic  $\text{M}_{55}$  magic atom number cluster with a fully elucidated Mackay-type two-shell icosahedral structure. DFT-based theoretical analysis of its electronic situation support the description of **3** as a 67 electron open-shell superatom, being composed of a  $[\text{Cu}_{43}\text{Al}_{12}]^{12+}$  kernel protected by twelve anionic  $\text{Cp}^*$  ligands.

### 4.2.2 Synthesis of $[\text{Cu}_{43}(\text{AlCp}^*)_{12}]$ (**3**)

The non-stoichiometric reaction of  $[\text{Cu}(\text{Mes})]_5$  and  $\text{AlCp}^*$  in benzene at elevated temperatures yields a black crystalline solid which was identified as  $[\text{Cu}_{43}(\text{AlCp}^*)_{12}]$  (**3**) by means of single crystal X-ray diffraction analysis, solid-state MAS NMR spectroscopy, IR spectroscopy, as well as elemental analysis and atom absorption spectroscopy. Concluding from *in situ*  $^1\text{H}$  NMR spectroscopic measurements, the synthesis of **3** is accompanied by the formation of significant amounts of  $[\text{Cp}^*\text{Al}(\text{Mes})_2]$ . Taking the dark red coloration of the resulting reaction mixture into consideration, the additional formation of yet unidentified, NMR-silent or lowly concentrated metal-atom rich coordination compounds is postulated.



**Scheme 2.** Synthesis of  $[\text{Cu}_{43}(\text{AlCp}^*)_{12}]$  (**3**) from  $[\text{Cu}(\text{Mes})]_5$  and  $\text{AlCp}^*$ . The non-stoichiometric reaction is accompanied by the formation of significant amounts of  $[\text{Cp}^*\text{Al}(\text{Mes})_2]$ , as indicated by *in situ*  $^1\text{H}$  NMR spectroscopic studies. Besides **3**, the formation of yet unidentified metal atom-rich coordination compounds in the reaction mixture is postulated based on the dark red benzene solutions obtained after isolation of the product.

Compound **3** is highly air and moisture sensitive, and burns upon exposure to air. Following its precipitation, **3** is insoluble in common organic solvents and can neither be purified nor characterized by conventional wet-chemical techniques. Consequently, meaningful data, e.g. from mass spectrometric measurements, remains inaccessible for a comprehensive characterization which in turn is largely reliant on single crystal X-ray diffraction analysis. Irrespective of its overall insolubility, suitable crystals of **3** for X-ray diffraction studies could be obtained by careful adjustment of the reaction conditions which allowed for the slow crystallization of the compound directly from the reaction mixture.

*Note:* The formation of **3** was found to be highly responsive to variations of the reaction conditions, whereat even smallest changes in the experimental procedure or the chemical nature of starting reagents and reaction medium were found to be detrimental to the reaction outcome. This is mainly attributed to the exceedingly flat potential energy surfaces usually associated with increasingly large atom assemblies, like **3**, and the resultant abundance of energetically accessible structures. As a consequence, the formation of **3** is prone to kinetic influences which is why upscaling from NMR scale reactions demanded for a most sensitive

*adjustment of reaction conditions with regards to temperature and time, concentration, and even the surface to volume ratio of the reaction vessel. A detailed description of the final, reproducible synthetic procedure is given in the experimental section.*

### 4.2.3 Structural analysis of $[\text{Cu}_{43}(\text{AlCp}^*)_{12}]$ (**3**)

Compound **3** crystallizes as black cubes in the cubic space group *Im-3* with two molecules per unit cell and co-crystallization of twelve additional molecules of benzene. Its highly symmetric molecular structure comprises an intermetallic  $\text{Cu}_{43}\text{Al}_{12}$  kernel which is embedded into the all-enclosing spherical capsule of twelve  $\text{Cp}^*$  ligands (Figure 36). Herein, the "magic number"  $\text{M}_{55}$  core adopts a multiple-shell Mackay-type icosahedron<sup>80</sup> which can be alternatively written as  $\text{Cu}@\text{Cu}_{12}@(\text{Cu}_{30}@\text{Al}_{12})$ , and is closely related to the geometries of recently reported, crystallographically characterized (inter-)metalloid clusters, like  $[\text{Pd}_{55}(\text{P}^i\text{Pr}_3)_{12}(\mu_3\text{-CO})_{20}]^{150}$  or  $[\text{Au}_{19}\text{Cu}_{30}(\text{C}\equiv\text{CR})_{22}(\text{PPh}_3)_6\text{Cl}_2]^{3+}$ .<sup>242</sup> Essentially isostructural arrangements are also found in the interior geometries of giant, multi-shell transition metal cluster compounds, such as  $[\text{Pd}_{145}(\text{CO})_{72}(\text{PEt}_3)_{30}]$ ,<sup>151</sup>  $[(\mu_{12}\text{-Pt})\text{Pd}_{164-x}\text{Pt}_x(\text{CO})_{72}(\text{PPh}_3)_{20}]^{152}$  or  $[\text{Au}_{133}(\text{SC}_6\text{H}_4\text{-p-}^t\text{Bu})_{52}]$ .<sup>154</sup>

In line with the description of a classical two-shell Mackay cluster, the intermetallic  $\text{Cu}_{43}\text{Al}_{12}$  kernel is composed of a body-centered  $\text{Cu}_{12}$  icosahedron inside a  $\text{Cu}_{30}$  icosidodecahedron. The remaining aluminium atoms are located in capping positions above the twelve pentagonal  $\text{Cu}_5$  faces of the latter, thus forming the icosahedral vertices of the second Mackay-type shell. Dissection of the resulting structure into identical face-sharing distorted tetrahedra gives twenty tetrahedral 10-atom units whose vertices are occupied by the central Cu atom and three neighbouring Al atoms, respectively. The observed distortion (approx. 5.3%) of radial Cu-Al edges (5.006 Å) with regards to tangential Al-Al distances (5.270 Å) is in good agreement with the 5% distortion predicted by Mackay on the basis of angular strain considerations,<sup>80</sup> and has also been observed in the molecular structure of  $[\text{Pd}_{55}(\text{P}^i\text{Pr}_3)_{12}(\mu_3\text{-CO})_{20}]$ .<sup>150</sup> Further small deviations of tetrahedral angles and edge ratios from the predicted values are anticipated to result from the packing of distinguishable spheres with differing atomic radii (Cu 140 ppm, Al 184 ppm).<sup>283, 284</sup>



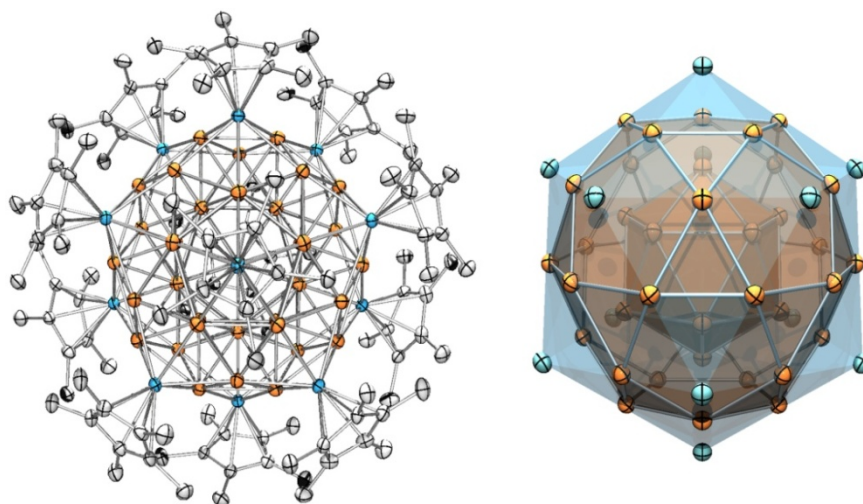


**Figure 36.** Molecular structure of  $[\text{Cu}_{43}(\text{AlCp}^*)_{12}]$  (**3**) in the solid state (left) and multiple-shell structure of the intermetallic  $\text{Cu}_{43}\text{Al}_{12}$  kernel of **3**, with Cu, Al, C depicted in orange, blue and grey, respectively. Thermal ellipsoids are shown at the 30 % probability level, hydrogen atoms and co-crystallized solvent molecules are omitted for clarity. Selected interatomic distances (Å) and angles (deg):  $\text{Cu}_{\text{centr.}}-\text{Cu}_{12}$  2.441(2),  $\text{Cu}_{12}-\text{Cu}_{12}$  2.566(2),  $\text{Cu}_{12}-\text{Cu}_{30}$  2.425(2)-2.432(2),  $\text{Cu}_{30}-\text{Cu}_{30}$  2.557(2)-2.566(2),  $\text{Cu}_{12}-\text{Al}$  2.565(3),  $\text{Cu}_{30}-\text{Al}$  2.626(3)-2.653(3),  $\text{Al}-\text{Cp}^*_{\text{centr.}}$  1.953,  $\text{Cu}_{12}-\text{Cu}_{\text{centr.}}-\text{Cu}_{12}$  av. 63.44,  $\text{Al}-\text{Cu}_{\text{centr.}}-\text{Al}$  av. 63.43,  $\text{Cu}_{12}-\text{Cu}_{12}-\text{Cu}_{12}$  av. 59.99,  $\text{Al}-\text{Al}-\text{Al}$  av. 60.02,  $\text{Cu}-\text{Al}-\text{Cp}^*_{\text{centr.}}$  179.49.

The Cu-Cu bonds within **3** range from 2.425(2) to 2.566(2) Å with slightly shorter radial (2.425(2)-2.441(2) Å) than tangential (2.557(2)-2.566(2) Å) copper distances, in accordance with the strain-induced compression discussed above. They are considerably shorter than the sum of the *van der Waals* radii (2.80 Å),<sup>283</sup> and comparable to elemental copper (2.55 Å)<sup>285</sup> or the closely related, intermetallic CuAl cluster  $[\text{Cu}_6(\text{AlCp}^*)_6(\text{N}=\text{CHPh})\text{H}_3]$  (2.328(1)-2.702(1) Å, av. 2.536 Å).<sup>11</sup> Rare examples of other ligand-stabilized Cu-nanoclusters with at least partial  $\text{Cu}^0$  character usually exhibit distinctly longer Cu-Cu bonds, like in  $[\text{Cu}_{25}(\text{PPh}_3)_{12}\text{H}_{22}]\text{Cl}$  (av. 2.635 Å),<sup>280</sup>  $[\text{Cu}_{29}\text{Cl}_4\text{H}_{22}(\text{Ph}_2\text{phen})_{12}]\text{Cl}$  (av. 2.65 Å)<sup>10</sup> or  $[\text{Au}_{19}\text{Cu}_{30}(\text{C}\equiv\text{CR})_{22}(\text{PPh}_3)_6\text{Cl}_2]^{3+}$  (2.917 Å).<sup>242</sup>

The coordination of twelve AlCp\* ligands occurs *via* the pentagonal faces of the  $\text{Cu}_{30}$  icosidodecahedron, with each aluminium atom being located at the tip of a compressed pentagonal bipyramid. The Cu-Al distances of 2.565(3) to 2.653(3) Å are elongated with regards to  $[\text{Cu}_6(\text{AlCp}^*)_6(\text{N}=\text{CHPh})\text{H}_3]$  (**2**) (av. 2.503 Å),<sup>11</sup> but still in a comparable range to those of intermetallic CuAl phases, like  $\text{CuAl}_2$  (2.587(7) Å)<sup>286</sup> or  $\text{Cu}_9\text{Al}_4$  (2.479(3)-2.775(5) Å).<sup>287</sup> The radial Cu-Al-Cp\*<sub>centr.</sub> angle of 179.49° is almost linear, and the Al-Cp\*<sub>centr.</sub> distance of 1.953 Å is only slightly longer than in  $[\text{Cu}_6(\text{AlCp}^*)_6(\text{N}=\text{CHPh})\text{H}_3]$ , probably due to the higher steric crowding at the metal cluster surface.

Note that, although the location of aluminium atoms at the cluster surface of **3** is preliminary anticipated to result from the preservation of the Al-Cp\* bond upon ligation, a general preference of Al for positions at the outermost surface shell was also revealed in quantum chemical investigations of ligand-free 55- and 561-atom CuAl nanoclusters. Here, the lower surface energy of Al with regards to Cu was found to be decisive.<sup>288</sup>

#### 4.2.4 Spectroscopic characterization of [Cu<sub>43</sub>(AlCp\*)<sub>12</sub>] (**3**)

The composition of the bulk material as analytically pure [Cu<sub>43</sub>(AlCp\*)<sub>12</sub>] (**3**) was confirmed by solid state MAS NMR and IR spectroscopy, as well as elemental analysis and AAS. Regarding the latter, significant deviations of the experimentally determined elemental composition from the calculated values are ascribed to residual amounts of co-crystallized benzene. Inclusion of three molecules of benzene to formally give [Cu<sub>43</sub>(AlCp\*)<sub>12</sub>] · 3C<sub>6</sub>H<sub>6</sub> matches the observed high C/H and low metal contents, thus providing consistent theoretical and experimental values. This is further supported by single crystal X-ray diffraction analysis, and MAS NMR data.

In accordance with its highly symmetric molecular structure, <sup>1</sup>H MAS NMR spectroscopic measurements of **3** give rise to one broad singlet at 1.72 ppm corresponding to the twelve chemically equivalent AlCp\* ligands. An additional signal is observed at 6.95 ppm which is attributed to the presence of co-crystallized benzene. Likewise, the <sup>13</sup>C MAS NMR spectrum of **3** shows the expected peaks at 117.94 and 14.27 ppm stemming from the sp<sup>2</sup> and sp<sup>3</sup> hybridized carbon atoms of the Cp\* ligands along with a benzene signal at 129.12 ppm. Notably, splitting of the latter is observed upon variation of the pulse program or scan parameters, like the prescan delay intervals, which is ascribed to a non-symmetrical distribution of benzene molecules throughout the crystalline sample. Attempts to reproduce an earlier obtained <sup>27</sup>Al MAS NMR spectrum<sup>289</sup> revealing an exceedingly broad signal of low resolution at -97.25 ppm failed. Provided the latter originates from the compound itself rather than from impurities or background signals of the set-up, this position would indeed be close to the chemical shift reported for neat [AlCp\*]<sub>4</sub> in the solid state (-90 ppm), but distinctly lower than the value reported for the AlCp\* ligands of [Al<sub>38</sub>(AlCp\*)<sub>12</sub>] (200 ppm).<sup>290</sup>

Complementary IR spectroscopic measurements of **3** reveal characteristic vibrational bands of the Cp\* ligands including the ν<sub>C-H</sub> and ν<sub>C-C</sub> vibrational modes at 2872 and 2818 cm<sup>-1</sup>, and 1412 and 1358 cm<sup>-1</sup>, respectively. Furthermore, the strong symmetric Al-C stretching vibration is observed around 391 cm<sup>-1</sup>, in analogy to the experimentally and theoretically found Al-C absorptions of matrix-isolated monomeric AlCp\*.<sup>165</sup>

### 4.2.5 Theoretical investigations of $[\text{Cu}_{43}(\text{AlCp}^*)_{12}]$ (**3**)

*The results presented in the following paragraph are based on the work of the group of Prof. Dr. Jean-Yves Saillard, particularly involving Dr. Rémi Marchal and Dr. Samia Kahlal, Institut des Sciences Chimiques de Rennes, France.*

As it turns out, a rationalization of  $[\text{Cu}_{43}(\text{AlCp}^*)_{12}]$  (**3**) on the basis of the initially introduced, established electron counting concepts is non-trivial and fails to provide a simplistic view on its electronic nature. Considering the peripheral AlCp\* units as neutral two electron ligands, the  $\text{Cu}_{43}$  superatomic core exhibits an electron count of 43 cve which fails to comply with the stable electron counts proposed by the superatom concept. Likewise, inclusion of aluminum as part of the cluster core with Cp\* acting as a one-electron withdrawing ligand gives an actual count of 67 cve ( $43 \cdot 1 + 12 \cdot 3 - 12 \cdot 1$ ) which, albeit close to the "magic" count of 68, seems counterintuitive given that, in a first approximation, only one orbital per atom (one 4s(Cu) and one sp(Al) hybrid AO) is expected to effectively contribute to the formation of jellium-type orbitals. For thus derived 55 combinations, distribution of 67 cluster electrons would clearly result in the occupation of antibonding states.

Thus motivated, DFT calculations were performed on the model compound  $[\text{Cu}_{43}(\text{AlCp})_{12}]$  (**3'**) at the BP86/TZP level of theory in order to elucidate the electronic structure of **3**. These reveal open-shell ground states for **3'** (3 unpaired electrons of  $(t_{2u})^2(a_g)^1$  configuration in  $I_h$  symmetry), as well as its even-electron ions  $[\mathbf{3}']^+$  and  $[\mathbf{3}']^-$ . In contrast, closed-shell configurations were found for  $[\mathbf{3}']^{3+}$  and the highly charged  $[\mathbf{3}']^{9+}$  cation, with large HOMO-LUMO gaps of 0.41 and 0.80 eV, respectively. This is in line with classical cluster valence electron counts: Considering AlCp as a "mere" two-electron ligand which is not involved in cluster bonding, the actual cve count of a central  $[\text{Cu}_{43}]^{3+}$  or  $[\text{Cu}_{43}]^{9+}$  core matches the "magic" counts of 40 or 34, respectively. Likewise,  $[\text{Cu}_{43}\text{Al}_{12}]^{9+}$  features a "magic" electron count of 58. At first sight, both configurations appear conceivable when assuming that **3** was bearing three, or even nine additional hydride ligands. However, this possibility was tested by DFT calculations and did not provide any closed-shell situation for any of the tested models. Furthermore, no experimental evidence for additional hydride ligands was found.

Figure 37 shows a comparative illustration of the Kohn-Sham orbital diagrams of  $[\mathbf{3}']^{3+}$  and its naked  $[\text{Cu}_{43}]^{3+}$  kernel in  $I_h$  symmetry, respectively. While strongly related electronic structures were to be expected in case of the appropriate description of  $[\mathbf{3}']^{3+}$  as an all-AlCp ligated  $[\text{Cu}_{43}]^{3+}$  superatomic core, significant differences with regards to the energetic order of superatom orbitals and their occupation can be noticed. In particular, the  $g_g$  and  $h_g$  LUMOs of  $[\text{Cu}_{43}]^{3+}$ , which correspond to the splitted 1G jellium level in  $I_h$  symmetry, correlate with occupied states in  $[\mathbf{3}']^{3+}$ . Likewise, the  $t_{1u}$  highest occupied orbitals of  $[\text{Cu}_{43}]^{3+}$  and  $[\mathbf{3}']^{3+}$  derive from different atomic contributions, and are assigned to the 2P and 1H jellium-type

levels, respectively. Overall, the clearly distinct superatom electron configuration of  $[\mathbf{3}']^{3+}$  ( $1S^2 1P^6 1D^{10} 2S^2 1F^{14} 2P^6 1G^{18}$  (HOMO- $t_{1u}$ )<sup>6</sup>; 58 + 6 electrons) with regards to  $[\text{Cu}_{43}]^{3+}$  ( $1S^2 1P^6 1D^{10} 2S^2 1F^{14} 2P^6$ ; 40 electrons) clearly indicates an involvement of all aluminum atoms in cluster bonding.

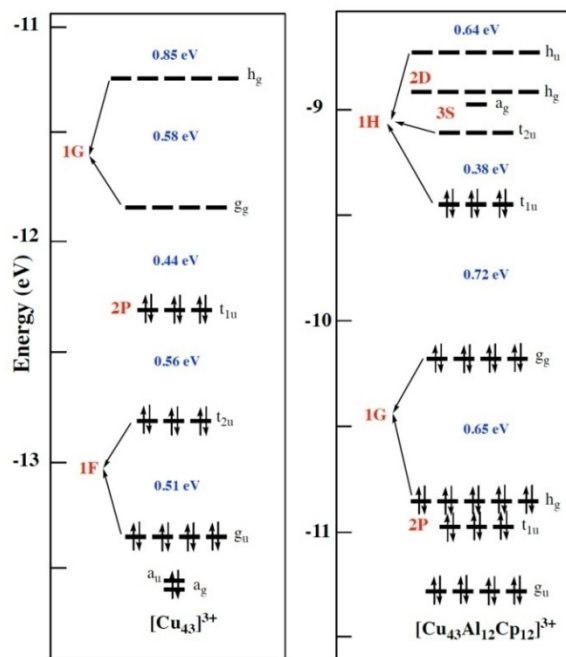


Figure 37. Kohn-Sham orbital diagrams of  $[\text{Cu}_{43}]^{3+}$  (left) and  $[\text{Cu}_{43}\text{Al}_{12}\text{Cp}_{12}]^{3+}$  (right) in  $I_h$  symmetry. Jellium levels (1F, 2P, 1G, 1H, 2D, 3S) were indexed from their atom contributions.

For a neutral cluster  $\mathbf{3}'$ , three additional unpaired electrons are distributed into the energetically closest  $t_{2u}$  and  $a_g$  states, which are assigned to the 1H ( $t_{2u}$ ) and 3S ( $a_g$ ) jellium levels. Herein, the close proximity ( $\sim 0.7$  eV) of the somewhat "entangled" set of 1H ( $t_{1u} + t_{2u} + h_u$ ), 3S ( $a_g$ ) and 2D ( $h_g$ ) jellium levels hosting the  $t_{1u}$  HOMO and the lowest unoccupied levels of  $[\mathbf{3}']^{3+}$  (or  $\mathbf{3}'$ ) is distantly reminiscent of the formation of a conduction band. Their *a priori* expected antibonding nature is tempered by the stabilizing participation of 4p(Cu) orbitals.

Based on these results, the exceptional electronic situation of  $\mathbf{3}'$ , or  $\mathbf{3}$ , can be described as a novel open-shell superatom with metallic-type electronic configuration which is composed of a  $[\text{Cu}_{43}\text{Al}_{12}]^{12+}$  jellium-type core, embedded into the stabilizing hydrocarbon shell of twelve  $\text{Cp}^-/\text{Cp}^*$  ligands. In this context, the significant polyradicalar reactivity commonly associated with such an open-shell superatom configuration appears to be completely annihilated by the steric protection of the spherical ligand capsule. The unusually large electron count of 67 cve is unprecedented amongst comparable Cu-based superatoms, like the recently reported  $[\text{Au}_{19}\text{Cu}_{30}(\text{CCR})_{22}(\text{PPh}_3)_6\text{Cl}_2]^{3-}$  (22 cve)<sup>242</sup> or homometallic representatives, such as  $[\text{Cu}_{13}(\text{S}_2\text{CN}^{\text{B}}\text{Bu}_2)_6(\text{acetylide})_4]^+$  (2 cve).<sup>291</sup>

### 4.2.6 Magnetic characterization of $[\text{Cu}_{43}(\text{AlCp}^*)_{12}]$ (**3**)

The results presented in the following paragraph are based on the work of the group of Prof. Dr. Birgit Weber, particularly including M.Sc. Christoph Göbel, University of Bayreuth, and the group of Prof. Dr. Olivier Cador, Institut des Sciences Chimiques de Rennes, respectively.

In initial measurements, the magnetic properties of **3** were assessed using temperature-dependent as well as field-dependent magnetic susceptibility measurements. Temperature-dependent magnetic susceptibility measurements were conducted in a temperature range from 2 to 300 K, revealing an overall paramagnetic behavior of the compound ( $\chi_M > 0$ ) with obvious deviations from classical Marie-Curie paramagnetism (Figure 38, left). For temperatures down to 50 K, the molar susceptibility  $\chi_M$  remains almost constant, and the  $1/\chi_M$  vs. T plot deviates considerably from the linear correlation expected for a Marie-Curie paramagnet in this temperature range. The thus indicated temperature independent paramagnetism (TIP) is confirmed by field-dependent measurements at 10, 50 and 200 K which reveal a linear dependency of the magnetization M and the applied magnetic field H (Figure 38, right). For temperatures below 50 K, a steep increase of the molar susceptibility indicates emerging contributions of a Marie-Curie-type paramagnetism. Accordingly, slight deviations from an ideal straight line are observed for field-dependent measurements at 10 K.

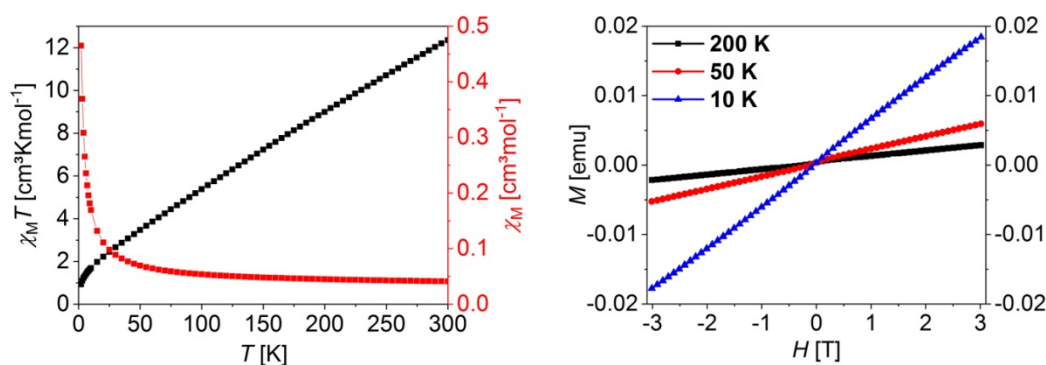


**Figure 38.** Temperature-dependent magnetic measurements of **3** given as  $\chi_M$  vs. T plot (red curve) and  $1/\chi_M$  vs. T plot (black curve; left). Down to  $T = 50$  K, the molar magnetic susceptibility  $\chi_M$  remains almost constant which indicates temperature independent paramagnetism. This is confirmed by the linear correlation of the magnetization M and the magnetic field during field-dependent magnetic susceptibility measurements at 10, 50 and 200 K (right). Below 50 K, contributions from Marie-Curie paramagnetism are observed.

At room temperature, the effective Bohr magneton number of **3** is determined to  $\mu_{\text{eff}} \approx 10$  which gives a total electron spin quantum number of  $S = 4.5$  according to the spin-only formula  $\mu_{\text{S}} = 2(S(S+1))^{1/2}$ . However, owing to the significant deviations from Marie-Curie paramagnetism which resembles the underlying criterion for the validity of the spin-only formula, this value can only serve as a rough estimate.

Based on these results, the magnetization process of the intermetalloid CuAl cluster **3** is probably most accurately described on the basis of two contributing paramagnetic effects, classical Marie-Curie paramagnetism and temperature-independent paramagnetism. The latter is, amongst others, characteristic for metals where it is ascribed to the energetic splitting of  $\alpha$ - and  $\beta$ -spin electrons of the conduction band in an external magnetic field which effects a weak net magnetic moment that is essentially independent of the measurement temperature but responsive to the magnetic field strength.<sup>292</sup> The former is classically expected for coordination compounds with isolated magnetic spin centers. While the exact origin of the observed unusual magnetization effects remains yet unclear, the overall magnetic behavior of **3** might superficially be understood as a combination of molecular and metallic magnetic properties, thus mirroring the exceptional chemical nature of **3** as a link between coordination chemistry and the extended solid state. In fact, anomalous magnetic behavior of nano-sized compounds and materials is observed frequently and has for instance been reported for naked and protected nano-sized noble metal assemblies which show unforeseen properties, like superdiamagnetism, superparamagnetism or ferromagnetism despite the diamagnetic nature of the respective bulk metals.<sup>293, 294</sup> These effects, which are commonly referred to as nanomagnetism, are believed to mainly result from factors like the broken translational symmetry as well as finite-size, surface and compositional effects.

Taking into consideration the results of DFT calculations on the electronic structure of **3** (see above), the degree of magnetization of the sample as observed in preliminary magnetic susceptibility measurements, and the thus derived effective Bohr magneton number  $\mu_{\text{eff}} \approx 10$  and molecular spin  $S = 9/2$  are unexpectedly high, and do not match the theoretical results indicating the presence of three unpaired electrons, only. Consequently, additional independent measurements were performed at variable magnetic field strengths in order to exclude the presence of ferromagnetic impurities. These cause a dependency of the magnetization on the external magnetic field which eventually allows for their quantification, and the accordant correction of the experimental data.<sup>295</sup> In fact, for **3**, approximately 20% of the detected signals are attributed to ferromagnetic contaminations in the microgram scale, e.g. stemming from abrasive material of metallic spatulas.



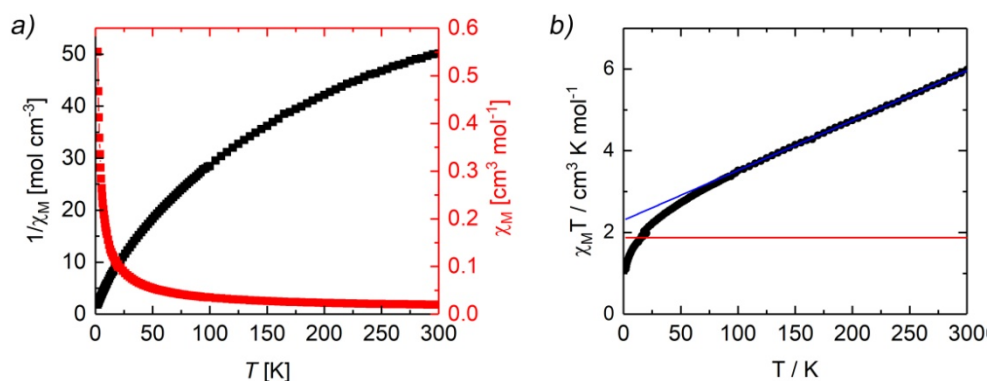


**Figure 39.** a) Temperature-dependent magnetic susceptibility measurements of **3** given as  $\chi_M$  vs.  $T$  plot (red curve) and  $1/\chi_M$  vs.  $T$  plot (black curve; left), corrected by contributions from ferromagnetic impurities (approx. 20%). b)  $\chi_M T$  vs.  $T$  plot with the calculated value for  $S = 3/2$  under assumption of  $g = 2$  (red curve). For low temperatures ( $T < 50$  K), good agreement of experimental and calculated data is found. For  $T > 50$  K, the experimental data can be linearly fitted for  $S = 3/2$  using a slightly modified Zeeman factor ( $g = 2.21$ ) and an additional factor for the influence of the TIP ( $0.0122 \text{ cm}^3 \text{ mol}^{-1}$ ).

Thus corrected results of temperature-dependent magnetic susceptibility measurements are shown in figure 39. These confirm the earlier discussed global magnetization behaviour of **3** as a combination of temperature-independent and Marie-Curie-type paramagnetism, but are in much better agreement with the results from theory. Although an exact quantification of the molecular spin is difficult owing to the complex electronic structure of the compound and resultant difficulties in assessing involved orbital contributions, strong indications are found for the presence of more than one and certainly less than the originally estimated nine unpaired electrons. At low temperatures ( $T < 50$  K), the experimental  $\chi_M T$  values are in good agreement with the expected values for  $S = 3/2$ , considering a Zeeman factor of  $g = 2$  (Figure 39b). Likewise, for  $T > 50$  K, the temperature-dependence of  $\chi_M T$  corresponds to a linear fit for  $S = 3/2$ , using a slightly modified Zeeman factor of  $g = 2.21$  and a TIP of  $0.0122 \text{ cm}^3 \text{ mol}^{-1}$ . The latter is anticipated to result from strong spin-orbit coupling and distortions. Furthermore, the presence of several low lying excited states (confirmed by DFT calculations) is anticipated to allow for second order Zeeman perturbation.

#### 4.2.7 Concluding remarks

The Hume-Rothery phase-inspired, paramagnetic CuAl cluster  $[\text{Cu}_{43}(\text{AlCp}^*)_{12}]$  (**3**), also written as  $[\text{Cu}_{43}\text{Al}_{12}](\text{Cp}^*)_{12}$ , is reproducibly obtained from the non-stoichiometric reaction of  $[\text{CuMes}]_5$  and  $\text{AlCp}^*$ . The all-hydrocarbon ligand-stabilized magic number  $M_{55}$  cluster features a Mackay-type two-shell icosahedral structure which can alternatively be written as  $\text{Cu}@\text{Cu}_{12}@(\text{Cu}_{30}@\text{Al}_{12})@\text{Cp}^*_{12}$ . Its unprecedented 67 electron open-shell superatom

configuration was confirmed by theoretical investigations at the DFT level of theory, revealing a superatomic configuration of  $1S^2 1P^6 1D^{10} 2S^2 1F^{14} 2P^6 1G^{18} 1H^9$  with three unpaired electrons in formally antibonding jellium states. Notably, the close proximity of the  $1H$  ( $t_{1u} + t_{2u} + h_u$ ),  $3S$  ( $a_g$ ) and  $2D$  ( $h_g$ ) jellium levels hosting the  $t_{1u}$  HOMO and the lowest unoccupied levels prefigures the formation of a conduction band, which is in accordance with magnetic measurements indicating substantial second order Zeeman perturbation caused by the presence of low lying excited states.

Earlier results from our chair show that an isostructural cluster  $[Cu_{43-x}Al_x(AlCp^*)_{12}]$  **3''** is obtained from the reaction of  $[Cu_6(AlCp^*)_6H_4]$  with  $[CuMes]_5$ , following the building-block principle.<sup>289</sup> **3''** features the statistical incorporation of  $x \leq 3$  aluminum atoms, as concluded from preliminary single-crystal X-ray diffraction studies and elemental analysis. Taking into consideration the unique electronic structure of **3**, aluminum doping of the naked  $Cu_{43}$  kernel should give rise to further open-shell superatoms with "non-magic" electron counts of 69, 71 or 73 electrons (for  $x = 1-3$ ) provided no hydrides are bound to the cluster surface. In case of the latter, closed-shell superatomic configurations are equally possible with 58, 68 or 70 electrons being the nearest "magic number" counts. Irrespective thereof, either scenario provides us with a fascinating study case for the influence of small compositional changes on the electronic structure of **3**, and might potentially contribute to a deeper understanding of its bonding situation.



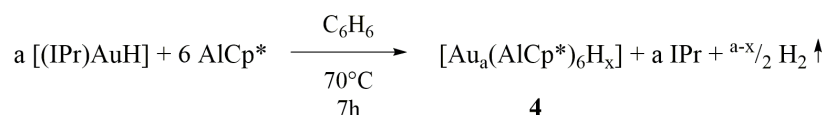
## 4.3 [Au<sub>a</sub>(AlCp\*)<sub>6</sub>H<sub>x</sub>] (**4**), an all-AlCp\* ligated Au cluster of unapparent nuclearity

### 4.3.1 Introductory remarks

Sparked by the synthesis of the prototypical [Cu<sub>6</sub>(AlCp\*)<sub>6</sub>H<sub>4</sub>] (**1**), the endeavour to broaden the just disclosed field of intermetalloid transition metal/group 13 metal cluster compounds led to the systematic and knowledge-based investigation of promising synthetic strategies. The anticipated crucial role of ancillary hydride ligands allowing for the reduction of the transition metal core by partial elimination of H<sub>2</sub> upon ligand exchange reactions at the TM center was investigated by variation of the precursor [(L)<sub>n</sub>TMH<sub>x</sub>]. In this regards, L resembles sterically demanding, 2e<sup>-</sup>-donating ligands, like phosphines or N-heterocyclic carbenes (NHCs), which are capable of stabilizing low-valent transition metal centers but readily replaceable by the isolobal ECp\*. While thus motivated reactions of [(PR<sub>3</sub>)<sub>n</sub>TMH<sub>x</sub>] (TM = Fe, Co; R = Ph, Me)<sup>296, 297</sup> with ECp\* remained largely inconclusive, the readily available Au-NHC complex [(IPr)AuH] (IPr = 1,3-bis(2,6-diisopropylphenyl)imidazol-2-ylidene)<sup>298</sup> provides access to the first bimetallic Au/Al cluster compound [Au<sub>a</sub>(AlCp\*)<sub>6</sub>H<sub>x</sub>] (**4**, a = 6 or 7). Furthermore, variation of the NHC ligand and/or the reaction stoichiometries appears to allow for the synthesis of heteroleptic Au/Al clusters of the general formula [Au<sub>a</sub>Al<sub>b</sub>](Cp\*)<sub>n</sub>(NHC)<sub>m</sub> with residual NHC ligands remaining at the intermetallic cluster core.

### 4.3.2 Synthesis of [Au<sub>a</sub>(AlCp\*)<sub>6</sub>H<sub>x</sub>] (**4**)

The reaction of [(IPr)AuH] with AlCp\* in a 4:3 stoichiometric ratio in benzene affords the Au/Al cluster compound [Au<sub>a</sub>(AlCp\*)<sub>6</sub>H<sub>x</sub>] (**4**, a = 6 or 7) as black crystals in yields of approx. 15 % (Scheme 3).



**Scheme 3.** Synthesis of [Au<sub>a</sub>(AlCp\*)<sub>6</sub>H<sub>x</sub>] (**4**, a = 6 or 7) from [(IPr)AuH] and AlCp\*. Comparable to the synthesis of [Cu<sub>6</sub>(AlCp\*)<sub>6</sub>H<sub>4</sub>] (**1**), the labile NHC ligand is readily replaced by the stronger AlCp\* ligand. Concomitant H<sub>2</sub> evolution effects the partial reduction of Au<sup>I</sup> furnishing a Au<sub>a</sub> kernel which is embedded into the stabilizing shell of six AlCp\* ligands.

Irrespective of the modest yield, *in situ*  $^1\text{H}$  NMR spectroscopic studies reveal the reaction to be surprisingly clean and proceed *via* well-defined, albeit yet to be elucidated, reaction pathways. Herein, the formation of an IPr-bearing intermediate ( $\delta_{\text{H}} = 7.18 \text{ t}, 7.07 \text{ d}, 2.83 \text{ sept}, 1.42 \text{ d}, 0.97 \text{ d}$ ) as well as progressive liberation of the IPr ligand and traces of  $\text{Cp}^*\text{H}$  are observed upon prolonged thermal treatment of the reaction mixture. The former seems to bear an additional  $\text{Cp}^*$  ligand, as deduced from a linearly responding signal at 1.90 ppm, thus indicating the formation of a low-nuclearity AuAl complex. Keeping in mind literature-known complexes, like  $[\text{Au}(\text{IPr})(\text{PR}_3)]^+$  ( $\text{R} = \text{}^t\text{Bu}, \text{}^n\text{Bu}, \text{Ph}$ ),<sup>299</sup> the formation of the hypothetical  $[(\text{IPr})\text{Au}(\text{AlCp}^*)\text{H}]$  appears conceivable and might facilitate subsequent cluster growth reactions, e.g. by elimination of the bulky NHC ligand to furnish unstable  $[\text{Cp}^*\text{AlAuH}]$  fragments which eventually assemble to give **4**. Note that the formation of simple side products stemming from the reaction of liberated IPr with  $\text{AlCp}^*$  was excluded by *in situ*  $^1\text{H}$  NMR control experiments. Similar to the synthesis of  $[\text{Cu}_6(\text{AlCp}^*)_6\text{H}_4]$  (**1**), the formation of **4** is accompanied by elimination of hydrogen, and thus at least partial reduction of the resulting gold core, as indicated by noticeable gas evolution during the reaction. However, IR spectroscopic characterization of the compound reveals remaining M-M bridging hydrides and confirms its overall composition as  $[\text{Au}_a(\text{AlCp}^*)_6\text{H}_x]$ .

The highly air- and moisture-sensitive **4** smoulders upon exposure to air, but can be stored under argon atmosphere at  $-30\text{ }^\circ\text{C}$  for weeks without signs of decomposition. Following its crystallization from the reaction mixture, compound **4** is barely soluble in conventional polar and unpolar solvents, like *n*-hexane, toluene or THF. Consequently, its characterization is largely dependent on analytical methods which are applicable to the solid state, such as MAS NMR spectroscopy, or elemental analysis and AAS. However, given the difficulties arising in reproducibly up-scaling the reaction from NMR to preparative scales, a comprehensive characterization of **4** still remains challenging.

### 4.3.3 Structural analysis of $[\text{Au}_a(\text{AlCp}^*)_6\text{H}_x]$ (**4**)

Suitable crystals of **4** for single crystal X-ray diffraction analysis were obtained directly from the reaction mixture, whereat higher quality crystals were obtained when performing the reaction in toluene instead of benzene. Compound **4** crystallizes in the monoclinic space group  $C2/m$  with two molecules per unit cell and inclusion of four disordered molecules of toluene. Its molecular structure comprises a highly disordered, naked  $\text{Au}_a$  kernel of unapparent nuclearity which is surrounded by the discrete octahedral shell of six  $\text{AlCp}^*$  ligands (Figure 40). In this regards, an obvious analogy can be drawn to the molecular structures of  $[\text{Cu}_6(\text{AlCp}^*)_6\text{H}_4]$  (**1**) and  $[\text{Ni}_8(\text{GaCp}^*)_6]$  (**8**) which likewise feature an unusually pronounced disorder of their central core geometries. For  $[\text{Ni}_8(\text{GaCp}^*)_6]$  (**8**), this was attributed to the almost spherical arrangement of its ligand shell which was suggested to be

capable of hosting variable core geometries without noteworthy perturbation. With the synthesis of **4**, a third specimen of a highly disordered nature was discovered, stressing the need for alternative characterization techniques to unravel the challenging (structural) phenomena observed for cluster compounds that teeter on the brink of classical molecular chemistry and nanomaterials.

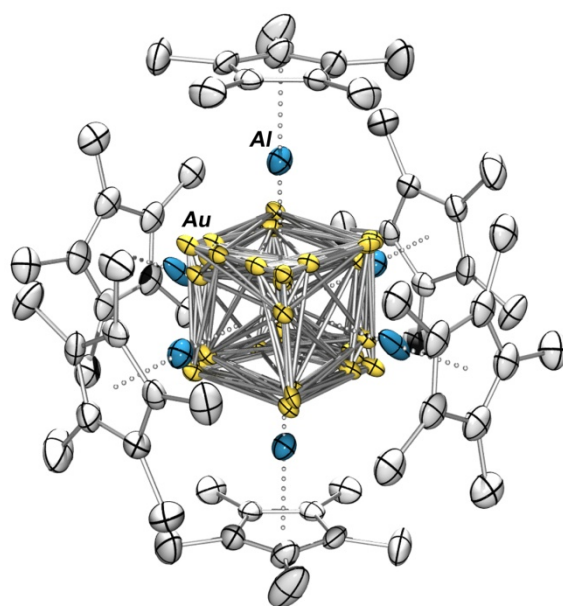


**Figure 40.** Severely disordered molecular structure of  $[\text{Au}_a(\text{AlCp}^*)_6\text{H}_x]$  (**4**;  $a = 6,7$ ) in the solid state (Au, Al, C depicted in yellow, blue and grey, respectively). Displacement ellipsoids are shown on the 30% probability level, hydrogen atoms, co-crystallized solvent molecules and the disorder sites of the Cp\* ligands are omitted for clarity. The unusually high degree of disorder of the central  $\text{Au}_a$  unit precludes the identification of its nuclearity and underlying core geometry. Likewise, geometrical parameters cannot be reliably determined.

Owing to the high degree of disorder of the central Au kernel which precludes a reliable identification of its underlying core geometry, refinement of all disordered Au sites was performed with individual occupation factors, analogous to common refinement strategies employed in the solution of substitutionally disordered or partially occupied crystallographic sites.<sup>300</sup> The thus derived approximate Au:Al ratio of 6.44 to 6 provides evidence for a nuclear core composition of  $\text{Au}_7\text{Al}_6$  or  $\text{Au}_6\text{Al}_6$ . However, this composition could neither be reliably confirmed nor excluded by complementary characterization of the bulk phase yet. Note that a quantitative analysis of geometrical parameters of the central  $\text{Au}_a$  core structure is impossible on the basis of the given molecular structure. As a rough estimate, the longest edges of the disordered cuboidal  $\text{Au}_a$  kernel were determined to vary between 2.802(4) and 2.875(3) Å. This is comparable to the Au-Au distances of elemental gold (2.884 Å)<sup>301</sup> and certainly

matches the unusually broad range of Au-Au bond lengths observed for oligonuclear Au<sub>a</sub> clusters.<sup>301, 302</sup>

The discrete ligand shell of six AlCp\* ligands is almost spherical, whereat the aluminium atoms form a regular octahedron with inner angles close to the optimum value of 90° and interatomic Al-Al distances of av. 4.428(5) Å. While the Au-Al distance cannot be reliably determined owing to the disordered nature of the Au<sub>a</sub> core (d<sub>Au-Al</sub> separations range from 2.297(4) to 2.749(4) Å), the average Al-Cp\*<sub>centr.</sub> distance of 1.932 Å lies in between those of comparable TM/Al clusters, like [Pd<sub>3</sub>(AlCp\*)<sub>8</sub>] (av. 1.953 Å)<sup>257</sup> or [Cu<sub>6</sub>(AlCp\*)<sub>6</sub>H<sub>4</sub>] (av. 1.904 Å),<sup>11</sup> and is noticeably shortened with regards to [AlCp\*]<sub>4</sub> (av. 2.015 Å).<sup>303</sup>

#### 4.3.4 Rationalizing potential core geometries of [Au<sub>a</sub>(AlCp\*)<sub>6</sub>H<sub>x</sub>] (**4**) - available means to assess unapparent molecular structures

A reasonable strategy to unravel the molecular structures of analytically challenging compounds like **4** includes the identification of conceivable compositions and geometries based on the available literature data, e.g. of comparable cluster compounds, and their evaluation against common stability concepts. Accordingly, Au<sub>a</sub> clusters of comparable sizes (a = 6-8) and at least partial Au<sup>0</sup> character were identified and analyzed with regards to the geometry of their cluster skeleton. Herein, particular emphasis was laid on Au-phosphine clusters owing to the isolobal analogy of the phosphine and the ECp\* ligand.<sup>302</sup> Note that gold-carbonyl clusters of comparable sizes are virtually unknown, with the heteroleptic Au<sub>6</sub> aggregate [PPh<sub>4</sub>]<sub>2</sub>[Au<sub>6</sub>(CF<sub>3</sub>)<sub>6</sub>Br<sub>2</sub>(CO)<sub>2</sub>]<sup>304</sup> being a sole example.

Thus collected, potential core geometries were compared with the cuboidal arrangement of Au disorder sites in the molecular structure of **4**, and analyzed with regards to their dimensions and sphericity, as well as the presence of suitable coordination sites allowing for the coordination of six, preferentially μ<sub>2</sub>- or μ<sub>3</sub>-bound AlCp\* ligands in an overall octahedral arrangement. Figure 41 shows the resultant selection of potential core geometries with suitable candidates highlighted in black. Surprisingly, no suitable skeleton was identified for a potential heptanuclear compound. Likewise, only a centered structure was found for a core composition of Au<sub>8</sub>. However, this does not render the nuclearities of a = 7 or 8 impossible. Reasonable, albeit not literature-reported structures include capped trigonal prismatic, tri- or tetracapped tetrahedral or cubic geometries.

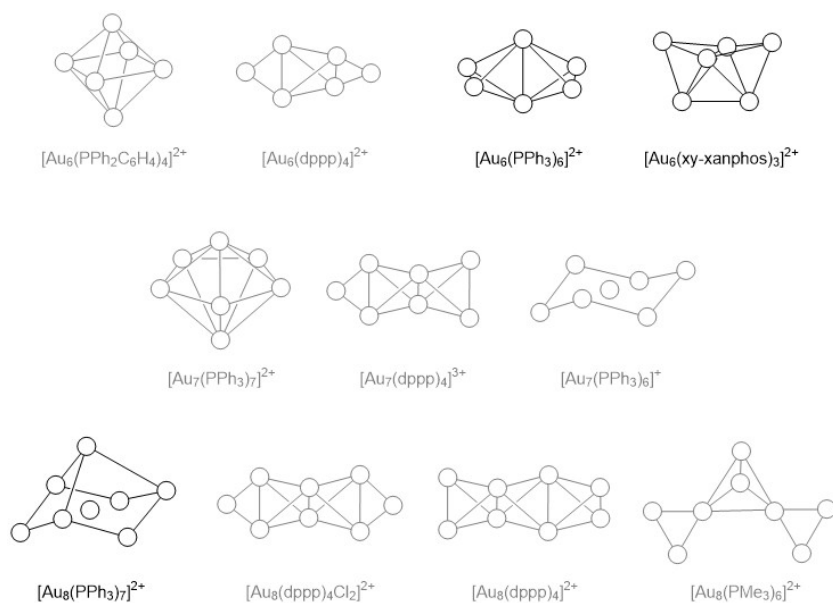


**Figure 41.** Core geometries of literature-reported hexa-, hepta- and octanuclear gold-phosphine cluster compounds with conceivable skeleton geometries for **4** marked in black. Structures that do not fulfil the structural requirements of **4** are marked in grey.

Unfortunately, further analysis of the thus derived geometries proved to be of little help in the structure elucidation of **4**, as the rich structural diversity of known Au clusters, along with their exceptional electronic situation which makes them difficult to rationalize on the basis of common electron counting paradigms hamper a straightforward prediction of conceivable geometries. The latter is rooted in the increasing separation between 3d and 4p orbital energies for late transition metals which effectively pushes tangential cluster orbitals to higher levels and makes them inaccessible for cluster bonding.<sup>135, 301, 305</sup> As a consequence, Au clusters are dominated by radial bonding which largely takes place through the s-functions, and do no longer obey conventional electron counting rules for transition metals.

More guidance can be expected from the superatom concept which was found to apply for a variety of ligand-protected Au clusters,<sup>191</sup> and likewise provides shell-closing electron counts for several conceivable compositions of **4**. Irrespective of the role of the AlCp\* ligand (external ligand or integral part of the cluster skeleton), stable counts of 2, 8 or 18 cve are obtained for the general formula  $[\text{Au}_a(\text{AlCp}^*)_6\text{H}_x]$  ( $a = 6-8$ ) with variable number  $x$  of electron-withdrawing hydride ligands (Table 7). In this regards, compositions with  $x = 0$  appear unlikely given the clear evidence for residual hydride ligands from IR spectroscopic analysis of **4**. Notably, for  $a = 6$ , the "magic" count of two cluster valence electrons is obtained for  $x = 4$  hydrides. The resultant, hypothetical composition  $[\text{Au}_6(\text{AlCp}^*)_6\text{H}_4]$  is strictly analogous to  $[\text{Cu}_6(\text{AlCp}^*)_6\text{H}_4]$  (**1**), which would render **4** a potential, isostructural homologue of **1**. In fact, the Au<sub>6</sub> core geometry of a bicapped tetrahedron has also been found amongst the conceivable geometries derived from Au-phosphine clusters.

**Table 7.** Shell-closing electron counts for  $[\text{Au}_a(\text{AlCp}^*)_6\text{H}_x]$  in dependency of  $a$  and  $x$ . Less likely compositions with  $x = 0$  are marked in grey.

	$[\text{Au}_6(\text{AlCp}^*)_6\text{H}_x]$	$[\text{Au}_7(\text{AlCp}^*)_6\text{H}_x]$	$[\text{Au}_8(\text{AlCp}^*)_6\text{H}_x]$
AlCp* as external	$6 \cdot 1 - x = \mathbf{2}$	$7 \cdot 1 - x = \mathbf{2}$	$8 \cdot 1 - x = \mathbf{8}$
ligand	$x = 4$	$x = 5$	$x = 0$ (or 6)
Al involved in	$6 \cdot 1 + 6 \cdot 2 - x = \mathbf{18}$	$7 \cdot 1 + 6 \cdot 2 - x = \mathbf{18}$	$8 \cdot 1 + 6 \cdot 2 - x = \mathbf{18}$
cluster bonding	$x = 0$	$x = 1$	$x = 2$

#### 4.3.5 Theoretical investigations of a hypothetical $[\text{Au}_7(\text{AlCp}^*)_6\text{H}_x]$

*The quantum chemical calculations presented in the following paragraph were performed by M.Sc. Julius Hornung, Chair of Inorganic and Metal-Organic Chemistry, TUM, and are part of his PhD studies.*

Taking into consideration the combined results of X-ray diffraction studies and conceptual conclusions of the previous sections, conceivable compositions  $[\text{Au}_a(\text{AlCp}^*)_6\text{H}_x]$  of **4** include  $a = 6-8$  gold atoms with a variable amount  $x$  of additional hydride ligands. Complementary results from solid-state MAS NMR spectroscopy, and elemental analysis and AAS (see below) point towards  $a = 6$  or  $7$ , and the presence of an asymmetric  $\text{Au}_a$  core geometry. However, while conceivable skeletons for  $a = 6$  could be identified from the analysis of structural motifs of Au phosphine cluster compounds, no corresponding structure was found for a hypothetical  $a = 7$ . Consequently, theoretical investigations were performed on the model compound  $[\text{Au}_7(\text{AlMe})_6\text{H}]$  (**4'**), in order to identify and evaluate potentially stable molecular structures against the experimental data of **4**. Herein, the sterically demanding Cp\* ligands were replaced by methyl groups to minimize computational costs. Geometry optimization of **4'** was performed at the BP86-D3/TZVPP level of theory, starting from the cuboidal skeleton of **4** whereat one Au vertex was replaced by a hydride ligand. The resulting molecular structure was confirmed as a local minimum by frequency calculations.

The optimized molecular structure of **4'** features a central  $\text{Au}_7$  core reminiscent of a strongly distorted cube lacking one vertex which is stabilized by the unsymmetrical arrangement of six AlMe ligands (Figure 42a). Of the latter, three are coordinated to the "intact" rectangular faces of the  $\text{Au}_7$  kernel while the remaining three AlMe ligands combine to form an equilateral, triangular  $[(\text{AlMe})_3(\mu_3\text{-H})]$  fragment which is located above the Au(5)-Au(6)-Au(7) triangular face. The resulting contorted ligand sphere diverges considerably from the experimentally observed almost perfect octahedral geometry of AlCp\* ligands in **4**. However, this discrepancy might stem from the distinctly lower steric bulk of the herein employed methyl group with regards to the Cp\* ligand. In this context, particularly the herein



observed  $[(\text{AlMe})_3(\mu_3\text{-H})]$  unit is expected to undergo considerable structural transformation upon increasing steric demand of the organic ligand. In addition, by replacing  $\text{Cp}^*$  by methyl ligands, the increasingly decisive, potential dispersion forces between the  $\text{Cp}^*$  ligands are not taken into consideration. Both factors would presumably contribute to a more spherical ligand sphere.

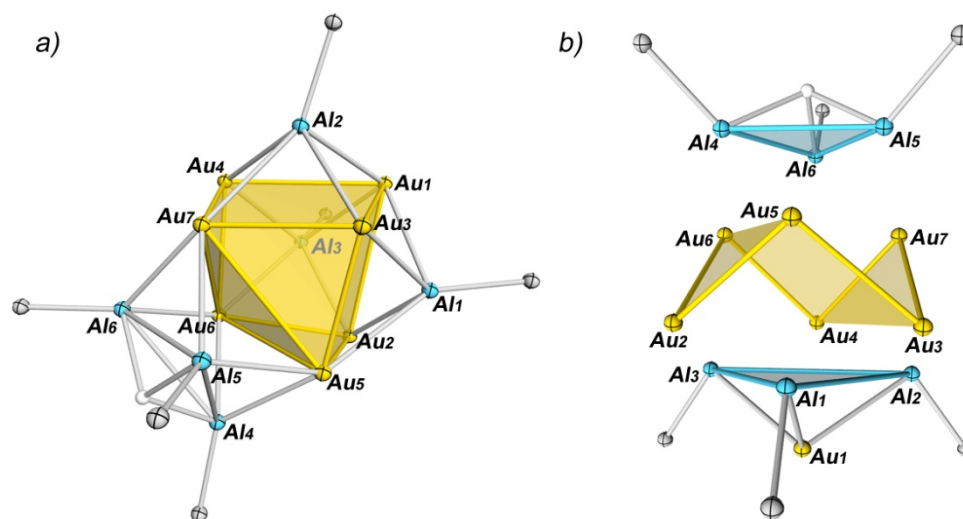


Figure 42. Different views on the optimized molecular structure of  $[\text{Au}_7(\text{AlMe}_6)\text{H}]$  (**4'**) as obtained from geometry optimization at the BP86-D3/TZVPP level of theory. The result was confirmed as a local minimum by frequency calculations.

Closer examination of the optimized molecular structure of **4'** reveals that its overall geometry can also be described as a spherical AuAl cluster comprising a hexagonal, puckered belt, i.e. a  $\text{Au}_6$  chair, which is capped by two  $\text{Al}_3\text{Me}_3$  fragments along either side of its three-fold symmetry axis (Figure 42b). The remaining Au(1) atom and the hydride ligand are located in a  $\mu_3$ -capping position above the respective  $\text{Al}_3$  triangles. Comparable, albeit centered, skeletal arrangements are frequently found amongst gold-phosphine cluster compounds, like  $[\text{Au}_{13}\text{Cl}_2(\text{PMe}_2\text{Ph})_{10}]$  or  $[\text{Au}_{11}\text{I}_3(\text{PPh}_3)_7]$ .<sup>306, 307</sup> These follow the  $12n+18$  cve rule,<sup>305</sup> which certainly does neither apply for **4'**, nor its experimentally determined parent compound **4**. For the latter, the observed cve count of  $185 + x$  ( $7 \cdot 11 + 6 \cdot 13 + 6 \cdot 5 + x$  hydrides) is well above the expected 174 cve. However, this does not render the proposed structure unlikely, as this deviation is likely to arise from the absence of the central Au atom which is usually observed for comparable, higher nuclearity Au clusters (compare also  $[\text{Au}_8(\text{PPh}_3)_7]^{2+}$ , Figure 41), and reinforces contributions from radial bonding. For non-centered structures, like **4'**, higher relative contributions from tangential interactions are to be expected, thus changing the underlying bonding situation and the electronic requirements it meets up with. Note that

the non-centered structure of the closely related  $[\text{Au}_7(\text{PR}_3)_7]^+$  has an oblate geometry which derives from a pentagonal bipyramid.<sup>308</sup>

In fact, the optimized  $\text{Au}_7$  structure of **4'** can be well envisioned inside the experimentally determined cuboidal, disordered  $\text{Au}_a$  kernel of **4** which exhibits edge lengths of approx. 2.8025 to 2.8753 Å. Au-Au bonds within the puckered  $\text{Au}_6$  belt of **4'** are in a narrow range of 2.7981 to 2.7992 Å, whereas the interatomic distances between Au(1) and its nearest neighbouring Au atoms Au(2), Au(3) and Au(4) are significantly elongated to av. 3.2759 Å. The Au-Al distances of the  $\text{Al}_3$  triangles to the respectively closest atoms of the  $\text{Au}_6$  ring vary between 2.5081 and 2.5445 Å, and the Au(1)-Al distances average to 2.6264 Å. All values are located within the experimentally observed ranges in the molecular structure of **4**. As pointed out earlier, large deviations are found for the overall arrangement of the AlR ligands, with short Al-Al distances within the hydride-bearing  $\text{Al}_3$  triangle (Al(4)-Al(5)-Al(6); av. 2.8646 Å) and long distances within the Au-capped  $\text{Al}_3$  fragment (Al(1)-Al(2)-Al(3); av. 3.9894 Å). This is significantly shorter than the Al-Al interatomic distances of **4** (4.429 Å). However, this might be due to the low steric demand of the herein employed methyl groups with regards to the "real"  $\text{Cp}^*$  ligands.

*Note: The theoretical investigations discussed herein are supposed to function as subsidiary but not at all decisive analytical means for the structure elucidation of **4**. While they are certainly able to disclose potential geometries of its molecular structure, an assignment of the compound's true chemical nature has to be based on the complex interplay of conceivable prospects and confirmative experimental evidence. In this regards, it should further be noticed that analogous structure optimization of the model compound  $[\text{Au}_8(\text{AlMe})_6]$  (**4''**) was performed at an early stage of this project but omitted in the current chapter owing to more recent experimental data pointing towards  $a = 6$  or  $7$ . Cartesian coordinates of the optimized structure as well as computational details are provided in the supplementary data (section 6.3.1).*

#### 4.3.6 Spectroscopic characterization of $[\text{Au}_a(\text{AlCp}^*)_6\text{H}_x]$ (**4**)

Solid-state  $^1\text{H}$  MAS NMR spectroscopic measurements of **4** give rise to three distinct signals at 7.44, 1.85 and 1.09 ppm. In line with the results of single-crystal X-ray diffraction analysis, the low-intensity peak at 7.44 ppm is attributed to co-crystallized benzene, whereas the signal at 1.85 ppm corresponds to the  $\text{Cp}^*$  ligands of **4**. The overall broadened shape of the latter, along with the presence of an additional, overlapping signal at 1.09 ppm is indicative of the presence of chemically distinct  $\text{Cp}^*$  ligands, which matches an anticipated unsymmetric  $\text{Au}_a$  core geometry. Although the presence of potential impurities causing the



observed additional signals cannot be entirely excluded at the current stage, a comparable effect is observed in the  $^{13}\text{C}$  MAS NMR spectrum of **4** which shows two signals at 14.42 and 11.88 ppm resembling the methyl groups of distinguishable Cp\* ligands. A corresponding set of signals is found at 137.63 and 134.61 ppm, and attributed to the inner carbon atoms of the respective Cp\* groups. The herein observed, slightly unusual shift to lower fields might stem from the *a priori* paramagnetic nature of the central Au core. Note that an additional signal of yet unclarified origin is found at 51.98 ppm, whereas no signal corresponding to the co-crystallized benzene molecules is observed. The latter might be hidden beneath the signals of the Cp\* ring or not fully resolved owing to its assumed low intensity.

IR spectroscopic measurements of **4** provide clear evidence for the formation of a homoleptic, all AlCp\*-ligated compound, thus supporting the preliminary formula of  $[\text{Au}_a(\text{AlCp}^*)_6\text{H}_x]$ . Besides the characteristic set of  $\nu_{\text{C-H}}$  (2962, 2903 and  $2847\text{ cm}^{-1}$ ) and  $\nu_{\text{C-C-Me}}$  vibrational modes ( $1426$  and  $1370\text{ cm}^{-1}$ ) commonly observed for Cp\* ligands, an intense absorption is observed at  $424\text{ cm}^{-1}$  which attributes to the Al-C stretching mode. In addition, a weak signal at  $1747\text{ cm}^{-1}$  provides evidence for hydride ligands remaining at the AuAl cluster core. The latter is in the range of terminal Al-hydride stretching modes reported in the literature ( $1700\text{-}1800\text{ cm}^{-1}$ ),<sup>165, 309-311</sup> and significantly red-shifted with regards to the terminal gold-hydride stretches found for gaseous AuH species<sup>312</sup> or the starting reagent  $[(\text{IPr})\text{AuH}]$  ( $1976\text{ cm}^{-1}$ ).<sup>298</sup> Reports on heterometallic Au complexes bearing bridging hydride ligands are scarce, and usually fail to provide conclusive IR data.

Characterization of **4** by means of elemental analysis and atom absorption spectroscopy supports a composition of  $[\text{Au}_a(\text{AlCp}^*)_6\text{H}_x]$  with  $a < 8$ , but certainly does not fit an anticipated  $[\text{Au}_7(\text{AlCp}^*)_6\text{H}_x]$ . Table 8 shows a comparison of the experimental data with the calculated values for  $[\text{Au}_a(\text{AlCp}^*)_6\text{H}_x]$  ( $a = 6\text{-}8$ ,  $x = 0$ ). In fact, the experimentally obtained molecular weight distribution fits best for  $a = 6$ . However, this does not take into consideration residual amounts of co-crystallized benzene. Furthermore, remaining unreacted AlCp\* would cause a shift of C, H and Al values to higher absolute numbers, along with a shift to lower values for Au. Consequently, contamination of a hypothetical  $[\text{Au}_7(\text{AlCp}^*)_6\text{H}_x]$  with one molecule of AlCp\* per molecule of **4** would give an identical calculated molecular weight distribution like  $[\text{Au}_6(\text{AlCp}^*)_6\text{H}_x]$ .

Table 8. Experimental and calculated molecular weight distributions for  $[\text{Au}_a(\text{AlCp}^*)_6\text{H}_x]$  (**4**) with  $a = 6\text{-}8$  and  $x = 0$ .

	C	H	Au	Al
experimental	32.47	4.59	54.16	7.43
calc. for $[\text{Au}_6(\text{AlCp}^*)_6]$	33.44	4.21	54.84	7.51
calc. for $[\text{Au}_7(\text{AlCp}^*)_6]$	30.64	3.86	58.62	6.88
calc. for $[\text{Au}_8(\text{AlCp}^*)_6]$	28.27	3.56	61.82	6.35

### 4.3.7 Concluding remarks

Following up on the synthetic rationale of  $[(L)_nTMH_x]$  precursors offering a potential starting point for the synthesis of TM/E cluster compounds upon selective exchange of the labile ligand L and reduction of the resulting TM core by elimination of  $H_2$  as an innocent leaving group, the reaction of  $[(IPr)AuH]$  with  $AlCp^*$  was found to yield the novel intermetallic cluster  $[Au_a(AlCp^*)_6H_x]$  (**4**) of yet unknown core composition. Based on experimental results from single-crystal X-ray diffraction studies and MAS-NMR spectroscopy along with elemental analysis and AAS, the number a of Au atoms forming the central  $Au_a$  kernel was determined to 6 or 7 with conceivable geometries including a  $Au_6$  bicapped tetrahedron or a  $Au_7$  monocapped, puckered  $Au_6$  ring. The latter was established by geometry optimization of the model compound  $[Au_7(AlMe)_6H]$  (**4'**). The presence of residual hydrides at the cluster surface of **4** is unambiguously clear from IR spectroscopic results. Depending on their exact number, "magic" counts of two or eighteen cluster electrons, corresponding to strong shell closures according to the superatom theory might be obtained.

Preliminary studies show that a variation of the NHC ligand may result in the formation of heteroleptic Au/Al clusters of the general formula  $[Au_aAl_b](Cp^*)_n(NHC)_m$ . In detail, low amounts of black crystals with a composition of  $[Au_8(AlCp^*)_5(IMes)H_x]$  (**5**) were isolated from the reaction of the closely related  $[(IMes)AuH]$  (IMes = 1,3-bis(2,4,6-trimethylphenyl)imidazol-2-ylidene) with  $AlCp^*$  at elevated temperatures in benzene (Figure 43). According to *in situ*  $^1H$  NMR spectroscopic measurements, the formation of **5** is accompanied by liberation of the IMes ligand without involvement of further traceable intermediates. Although these results could not be reproduced on a preparative scale yet, they certainly raise the question for the role of the ancillary NHC ligand in the formation mechanism, i.e. does a modification of the steric and electronic demand of the NHC ligand allow for the synthesis of a small library of structurally diverse AuAl cluster compounds?

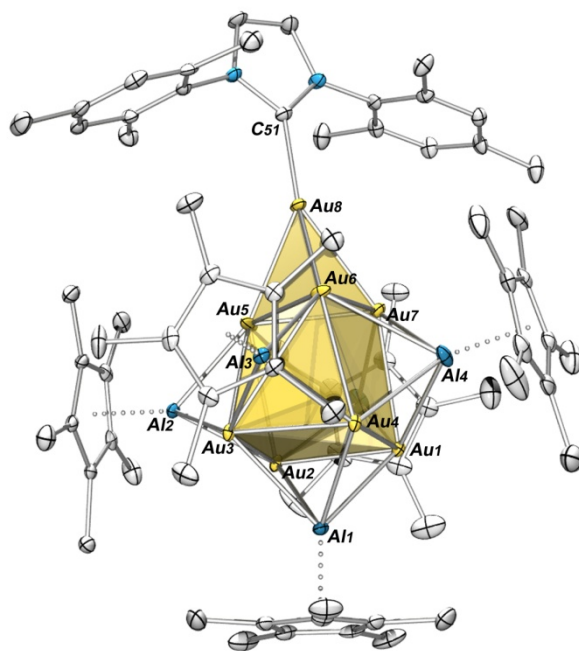


**Figure 43.** Molecular structure of  $[\text{Au}_8(\text{AlCp}^*)_5(\text{IMes})\text{H}_x]$  (**5**) in the solid state with Au, Al, C, N depicted as yellow, blue, grey, light blue, respectively. Thermal ellipsoids are drawn at the 30 % probability levels, hydrogen atoms and co-crystallized solvent molecules are omitted for clarity. The polyhedral  $\text{Au}_8$  skeleton is highlighted in yellow.

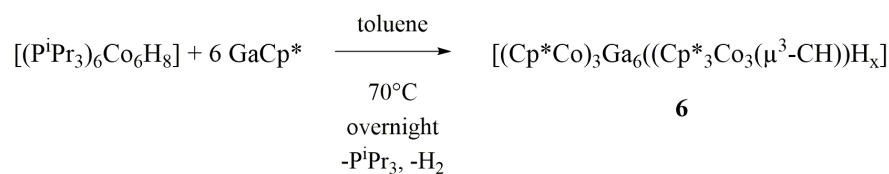
## 4.4 [(Cp\*Co)<sub>3</sub>Ga<sub>6</sub>(Cp\*<sub>3</sub>Co<sub>3</sub>(μ<sup>3</sup>-CH))H<sub>x</sub>] (6), an "inverse" TM/E cluster featuring a naked Ga<sub>6</sub> core inside a CoCp\* shell

### 4.4.1 Introductory remarks

Only recently, Nishiyama *et al.* published the synthesis of the hexanuclear cobalt hydride cluster [Co<sub>6</sub>H<sub>8</sub>(P<sup>i</sup>Pr<sub>3</sub>)<sub>6</sub>] *via* the reaction of [Co(btsa)<sub>2</sub>] with two equivalents of pinacolborane (HBpin) in the presence of tris-isopropylphosphine.<sup>313</sup> Herein, *in situ* formation of the, albeit not explicitly detected, Co complex [P<sup>i</sup>Pr<sub>3</sub>Co(btsa)<sub>2</sub>], in analogy to literature-known [PPh<sub>3</sub>Co(btsa)<sub>2</sub>]<sup>314</sup> followed by abstraction of the bulky btsa ligand with concomitant hydride transfer to the cobalt center was proposed to furnish low-coordinate cobalt-hydride species which would eventually undergo cluster assembly to give [Co<sub>6</sub>H<sub>8</sub>(P<sup>i</sup>Pr<sub>3</sub>)<sub>6</sub>]. Intrigued by the close resemblance to the hexameric [PPh<sub>3</sub>CuH]<sub>6</sub> which constituted the starting point for the synthesis of the archetypical CuAl cluster [Cu<sub>6</sub>(AlCp\*)<sub>6</sub>H<sub>4</sub>] (1), and keeping in mind the prospect of ligand substitutions at preformed transition metal cluster cores as a reliable gateway into the field of TM/E clusters, the reactivity of [Co<sub>6</sub>H<sub>8</sub>(P<sup>i</sup>Pr<sub>3</sub>)<sub>6</sub>] towards ECp\* was investigated. Not surprisingly, [Co<sub>6</sub>H<sub>8</sub>(P<sup>i</sup>Pr<sub>3</sub>)<sub>6</sub>] was found to undergo facile ligand exchange reactions with both, GaCp\* and AlCp\*, the results of which are summarized in the following chapter.

### 4.4.2 Synthesis of [(Cp\*Co)<sub>3</sub>Ga<sub>6</sub>(Cp\*<sub>3</sub>Co<sub>3</sub>(μ<sup>3</sup>-CH))H<sub>x</sub>] (6)

The reaction of [Co<sub>6</sub>(P<sup>i</sup>Pr<sub>3</sub>)<sub>6</sub>H<sub>8</sub>] with an excess of GaCp\* at 70°C in toluene yields the intermetallic CoGa cluster [(Cp\*Co)<sub>3</sub>Ga<sub>6</sub>(Cp\*<sub>3</sub>Co<sub>3</sub>(μ<sup>3</sup>-CH))H<sub>x</sub>] (6) in good, reproducible yields around 80 % (Scheme 4). 6 is formed by ligand substitution of the labile phosphine by the stronger GaCp\* ligand with concomitant Cp\* transfer to the cobalt centres evoking cluster rearrangement. The additionally observed partial elimination of hydrogen as an innocent leaving group results in the reduction of the thus formed naked gallium core atoms.



**Scheme 4.** Synthesis of [(Cp\*Co)<sub>3</sub>Ga<sub>6</sub>(Cp\*<sub>3</sub>Co<sub>3</sub>(μ<sup>3</sup>-CH))H<sub>x</sub>] (6) from [(P<sup>i</sup>Pr<sub>3</sub>)<sub>6</sub>Co<sub>6</sub>H<sub>8</sub>] and GaCp\*. The stronger GaCp\* ligand replaces the labile tris-isopropylphosphine. Concomitant Cp\* transfer reactions and reduction of the metallic cluster core by elimination of hydrogen affords a naked Ga<sub>6</sub> unit which is stabilized by six CoCp\* ligands.

Compound **6** is highly air and moisture sensitive, and smoulders upon exposure to air. It is moderately soluble in unpolar organic solvents, like mesitylene or toluene, and can be purified by crystallization from hot mesitylene solutions upon slow cooling.

#### 4.4.3 Structural characterization of $[(\text{Cp}^*\text{Co})_3\text{Ga}_6(\text{Cp}^*_3\text{Co}_3(\mu^3\text{-CH}))\text{H}_x]$ (**6**)

Compound **6** crystallizes as dark red plates in the monoclinic space group  $C2/c$  with one molecule of **6** and two co-crystallized molecules of toluene in the asymmetric unit. Its molecular structure contains a naked  $\text{Ga}_6$  core which is stabilized by formal coordination of six  $\text{CoCp}^*$  ligands, three of which form an unusual, methylidyne-bridged  $[(\text{Cp}^*\text{Co})_3(\mu^3\text{-CH})]$  unit (Figure 44). The disordered  $\text{Ga}_6$  core features a distorted octahedral geometry with a  $\text{Ga}(1)\text{-Ga}(2\text{A})\text{-Ga}(3\text{A})\text{-Ga}(4)$  trapezoid basal plane exhibiting one significantly elongated edge ( $d_{\text{Ga}1\text{-Ga}4}$  3.122(1) Å). Ga-Ga distances range from 2.723(4) to 3.122(1) Å (av. 2.8734 Å), and are distinctly shorter than the sum of the *van der Waals* radii (Ga 1.87 Å)<sup>284</sup> or the Ga-Ga distances in hexameric  $[\text{GaCp}^*]_6$  (4.073 and 4.173 Å),<sup>315</sup> thus indicating substantial metal-metal interactions. Their noticeable elongation with regards to Ga-Ga bonds in comparable octahedral  $\text{Ga}_6$  clusters, like  $[\text{Ga}_6(\text{Si}^t\text{Bu}_3)_4(\text{CH}_2\text{Ph}_2)_2]$  (av. 2.587 Å)<sup>316</sup> or  $[\text{Ga}_6(\text{Mes})_4(\text{C}^i\text{Pr})\text{NC}(\text{Me})_2]_2$  (av. 2.539 Å),<sup>317, 318</sup> is mainly attributed to the differing coordination modes of the respective ligands (terminal vs. bridging).

Stabilization of the naked gallium kernel is achieved by the coordination of three  $\mu_3$ -bound  $\text{CoCp}^*$  ligands and one face-capping  $[(\text{Cp}^*\text{Co})_3(\mu\text{-CH})]$  fragment which are located above alternating faces of the  $\text{Ga}_6$  octahedron. Herein, the cobalt atoms of the latter are coordinated in a  $\mu_2$ -bridging mode above the Ga-Ga edges, forming an almost ideal equilateral triangle which lies parallel to the capped  $\text{Ga}_3$  face, and coordinates an additional methylidyne ligand of yet unclarified origin (compare section 4.4.5). In an alternative view, the molecular structure of **6** can be described as composed of two fused, strongly distorted octahedra,  $\text{Co}_3\text{Ga}_3$  and  $\text{Ga}_6$ , sharing a common  $\text{Ga}_3$  plane with the latter being coordinated by three additional face-capping  $\text{CoCp}^*$  ligands. Either way, the significantly widened Ga-Ga bonds of the involved  $\text{Ga}_3$  triangle point towards the pronounced distortion of the  $\text{Ga}_6$  octahedron being caused by the coordination of the unusual  $[(\text{Cp}^*\text{Co})_3(\mu\text{-CH})]$  fragment.

The Ga-Co distances vary between 2.243(2) and 2.398(5) Å with shorter distances found for capping  $\text{CoCp}^*$  ligands (av. 2.300 Å) and longer Ga-Co spacings observed for the  $\mu_2$ -bridging cobalt atoms of the  $[(\text{Cp}^*\text{Co})_3(\mu\text{-CH})]$  unit (av. 2.379 Å). These are slightly elongated with regards to the literature-reported  $[\text{Cp}^*\text{Co}(\text{GaCp}^*)_3][\text{BAr}_4^{\text{F}}]_2$  (av. 2.297 Å)<sup>319</sup> featuring terminally bound  $\text{GaCp}^*$  ligands, but shorter than the Co-Ga bonds of the bridging  $\text{GaCp}^*$  ligands in  $[(\text{CO})_3\text{Co}(\mu\text{-GaCp}^*)_2\text{Co}(\text{CO})_3]$  (av. 2.389 Å).<sup>244</sup> Notably, the closely related intermetalloid CoGa cluster  $[\text{Ga}_{10}(\text{CoCp}^*)_6]$ <sup>320</sup> (compare section 6.3.3 for details on

synthesis and crystallographic data) has been discovered in our chair whose molecular structure comprises a central Ga<sub>10</sub> kernel being coordinated by six face-capping CoCp\* units, and is essentially isostructural to the homometallic Ga<sub>10</sub> cluster compounds [Ga<sub>10</sub>R<sub>6</sub>]<sup>x-</sup> (x = 0, 1 for R = Si(SiMe<sub>3</sub>)<sub>3</sub>, Si(CMe<sub>3</sub>)<sub>3</sub>) with regards to the central gallium core's geometry.<sup>321</sup> Here, Ga-Co distances range from 2.225(2) to 2.433(3) Å with an average of 2.315 Å which is consistent with the observed values for the molecular structure of **6**.

Note that hydrides could not be located on the differential Fourier maps, albeit their presence is unequivocally clear from the spectroscopic characterization of **6**.

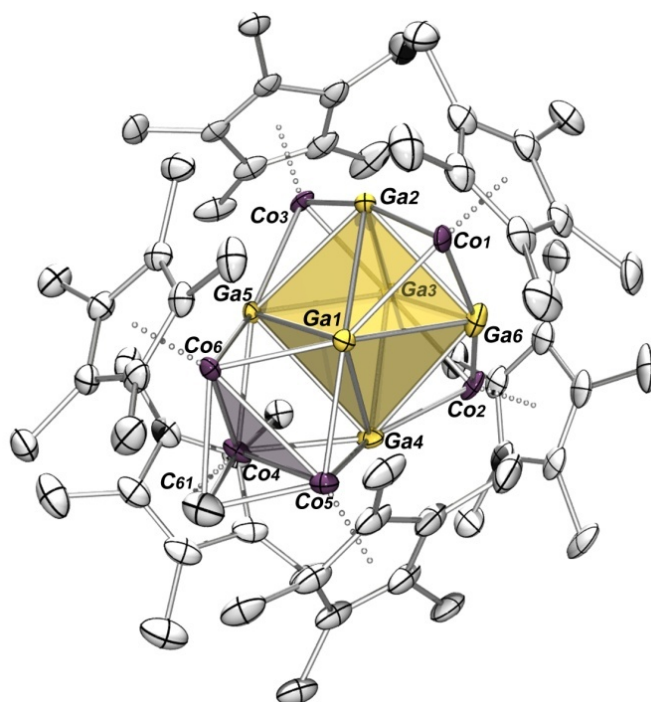


**Figure 44.** Molecular structure of [(Cp\*Co)<sub>3</sub>Ga<sub>6</sub>(Cp\*<sub>3</sub>Co<sub>3</sub>(μ<sup>3</sup>-CH))H<sub>x</sub>] (**6**) in the solid state with Ga, Co and C depicted in yellow, violet and grey, respectively. Displacement ellipsoids are shown on the 50 % probability level, hydrogen atoms, co-crystallized solvent molecules and disorder sites are omitted for clarity. Selected interatomic distances (Å) and angles (deg) of **6**: Ga(1)-Ga(2A) 2.793(1), Ga(1)-Ga(4) 3.122(1), Ga(1)-Ga(5) 3.006(1), Ga(1)-Ga(6A) 2.903(3), Ga(2A)-Ga(3A) 2.771(3), Ga(2A)-Ga(5) 2.847(1), Ga(2A)-Ga(6A) 2.751(4), Ga(3A)-Ga(4) 2.811(1), Ga(3A)-Ga(5) 2.878(1), Ga(3A)-Ga(6A) 2.723(4), Ga(4)-Ga(5) 3.003(1), Ga(4)-Ga(6A) 2.869(4), Ga-CoCp\* av. 2.300, Ga-Co av. 2.379, Co-Co av. 2.688, Co-Cp\*<sub>centr.</sub> 1.742, Co-C(61) av. 2.230, Ga(1)-Ga(2A)-Ga(3A) 94.2, Ga(2A)-Ga(3A)-Ga(4) 92.9, Ga(3A)-Ga(4)-Ga(1) 86.6, Ga(4)-Ga(1)-Ga(2A) 86.2, Ga(1)-Ga(5)-Ga(3A) 87.7, Ga(1)-Ga(6A)-Ga(2A) 92.2, Ga(4)-Ga(5)-Ga(2A) 87.5, Ga-(μ<sub>3</sub>-Co)-Ga 75.5, Ga-(μ<sub>2</sub>-Co)-Ga 79.6, Co-Co-Co 60.0, Co-C(61)-Co 74.1.

#### 4.4.4 Rationalizing the structure of $[(\text{Cp}^*\text{Co})_3\text{Ga}_6(\text{Cp}^*_3\text{Co}_3(\mu^3\text{-CH}))\text{H}_x]$ (**6**) on the basis of electron counting principles - a hypothetical excursus

Given the unprecedented molecular structure of **6**, how can it be rationalized on the basis of established electron counting principles? With regards to cluster valence electron counts, dissection of the  $\text{Co}_6\text{Ga}_6$  skeleton into several fragments appears plausible. Accordingly, **6** can be treated as two fused  $\text{Co}_3\text{Ga}_3$  and  $\text{Ga}_6$  octahedra sharing a common  $\text{Ga}_3$  face. The remaining three  $\text{CoCp}^*$  fragments can either be considered as integral parts of the metallic cluster core, or as external two-electron-donating ligands, according to the isolobal analogy of  $\text{Cp}^*\text{Co}$  and  $\text{BH}$ . For the latter case, the actual electron count is calculated as  $6 \cdot 13(\text{Ga}) + 3 \cdot 9(\text{Co}) + 3 \cdot 5(\text{Cp}^*) + 1 \cdot 3(\text{CH}) + 3 \cdot 2(\text{Cp}^*\text{Co}) = 129$  cve which is slightly above the expected 124 cve obtained from fusion of two octahedra ( $2 \cdot 86$  cve) minus the common triangular face (48 cve). Capping of the thus obtained structure with three additional vertices to include the remaining cobalt atoms in the internal cluster skeleton gives an expected count of 160 cve. Again, the actual electron count of **6** ( $6 \cdot 13(\text{Ga}) + 6 \cdot 9(\text{Co}) + 6 \cdot 5(\text{Cp}^*) + 3(\text{CH}) = 165$  cve) exceeds the expected value. In both cases, the presence of additional hydrides adding further electrons has been neglected.

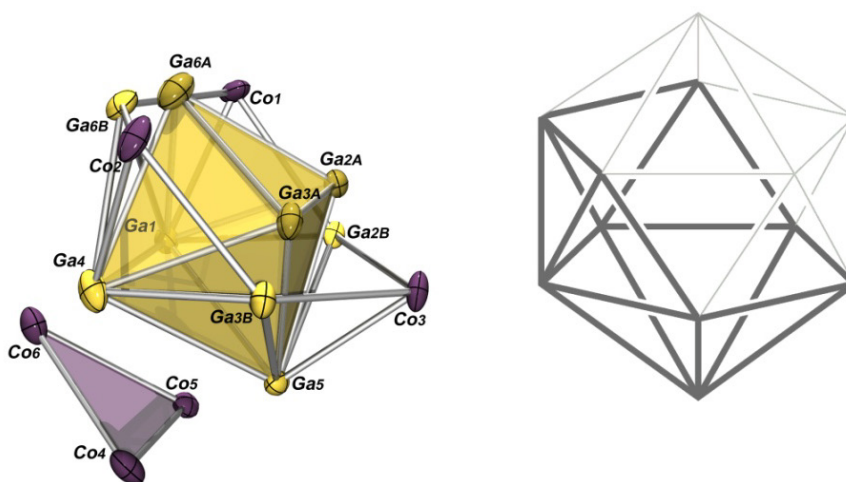


Figure 45. Comparison of the disordered  $[\text{Ga}_6\text{Co}_6]$  kernel of **6** with the nido-cluster structure expected according to Wade-Mingos rules.

Alternatively, the number of skeleton electron pairs of **6** can be calculated. Assuming that each gallium atom only contributes one electron to cluster bonding and keeps the remaining two electrons as an external lone pair, the actual number of skeleton electron pairs is determined to  $\frac{1}{2} \cdot [6 \cdot 1(\text{Ga}) + 6 \cdot 2(\text{CoCp}^*) + 1 \cdot 3(\text{CH})] = 10.5$  seps. Taking further into consideration the yet unclarified number of hydrides residing at the cluster surface, sep counts of 11, 12, or even 13 are obtained for one, three and five hydrides, respectively. For a nine-



vertex cluster, this would indicate a nido, arachno or hypho structure, respectively, all of which can be traced back to an icosahedron lacking the appropriate amount of vertices.<sup>166</sup> Comparison with the disordered cluster skeleton of **6** suggests that the  $\mu_3$ -capping  $\text{CoCp}^*$  fragments are actually involved in cluster bonding, whereas the triangular  $[\text{Cp}^*_3\text{Co}_3(\mu\text{-CH})]$  fragment is to be considered an external moiety (Figure 45).

Re-evaluation of the number of cluster valence electrons on the basis of these findings shows that the disordered structure of **6**, if derived from a distorted tricapped octahedron, should exhibit a cve count of 122. The actual count involving the three  $\text{CoCp}^*$  fragments as part of the internal cluster bonding is given as  $6 \cdot 13(\text{Ga}) + 3 \cdot 9(\text{Co}) + 3 \cdot 5(\text{Cp}^*) = 120$  cve plus additional electron contributions of the residual hydrides and the coordinated  $[\text{Cp}^*_3\text{Co}_3(\mu\text{-CH})]$  fragment. The latter itself features a cve count of 45 which is three lower than expected. Pushing these considerations a bit further, the molecular structure of **6** might, albeit only under the assumption of more than two residual hydride ligands, be understood on the basis of an electron-rich  $\text{Ga}_6\text{Co}_3$  cluster skeleton interacting with an electron-deficient  $\text{Co}_3$  fragment. In how far these hypothetical considerations can provide a glimpse on the actual electronic situation within **6** and what these results might imply for its formation mechanism needs to be evaluated by theoretical investigations.

#### 4.4.5 Spectroscopic characterization of $[(\text{Cp}^*\text{Co})_3\text{Ga}_6(\text{Cp}^*_3\text{Co}_3(\mu^3\text{-CH}))\text{H}_x]$ (**6**)

Complementary characterization of the bulk material of **6** was performed by means of NMR, IR and XPS spectroscopy, and LIFDI mass spectrometry. In addition, the molecular composition of **6** was confirmed by elemental analysis and atom absorption spectroscopy.

The  $^1\text{H}$  NMR spectrum of **6** shows coalescent signals between 2.20 and 2.04 ppm corresponding to the chemically distinguishable  $\text{Cp}^*$  ligands along with a low intensity singlet at -15.29 ppm which is indicative of residual hydride ligands at the intermetallic cluster core. Two additional signals at 1.23 and 0.88 ppm stem from residual *n*-hexane that could not be removed by drying *in vacuo* and is assumed to co-crystallize during washing steps. Notably, no signal corresponding to the  $\text{Co}_3$ -capping methylidyne group was found which is mainly attributed to the overall low solubility of the compound. Attempts to resolve the missing signal by recording spectra at elevated temperatures remained inconclusive. However, deconvolution of the initially coalescent  $\text{Cp}^*$  signals into three clearly distinguishable signals at 2.21, 2.15 and 2.10 ppm with an integral ratio of 2:3:1 was observed. Interestingly,  $^1\text{H}$  NMR spectra showing the clearly resolved  $\text{Cp}^*$  signals are also obtained after crystallization of **6** from mesitylene, albeit the signal at 2.15 ppm is superimposed by an intense singlet stemming from cocrystallized solvent molecules. The remaining signal of the aromatic



protons of mesitylene is observed at 6.71 ppm. Note that two additional signals of low intensity are observed at low fields with chemical shifts of 29.42 and 19.74 ppm, both of which lie in the expected range of a Co<sub>3</sub>-capping CH ligand. For comparison, the <sup>1</sup>H NMR signals of the closely-related CH groups of [Cp\*<sub>3</sub>Co<sub>3</sub>(μ-CH)<sub>2</sub>] were reported at 16.99 ppm in benzene-d<sub>6</sub> at room temperature.<sup>322</sup>

Apparently, the material re-crystallized from mesitylene exhibits a slightly higher solubility in benzene, thus facilitating <sup>13</sup>C NMR spectroscopic measurements. These give rise to three sets of signals at 93.01, 90.11 and 84.60 ppm, and 13.44, 13.16 and 13.10 ppm corresponding to the inner carbon atoms and the methyl groups of the Cp\* ligands, respectively. In analogy to the <sup>1</sup>H NMR spectrum, no signal stemming from the methylidyne group was observed whereas additional signals at 137.63, 127.38 and 21.33 ppm arise from residual amounts of mesitylene. The lack of observable signals in the <sup>31</sup>P NMR spectrum of isolated **6** clearly indicates the absence of residual tris-isopropylphosphine ligands.

Characteristic absorption bands of the Cp\* ligands are observed in the IR spectrum of **6** including the ν<sub>C-H</sub> stretching modes at 2964, 2886 and 2849 cm<sup>-1</sup>, and the ν<sub>C-C</sub> vibrations at 1454 cm<sup>-1</sup>. The most intense vibrational modes at 1371 and 1023 cm<sup>-1</sup> correlate to the symmetric CH<sub>3</sub> bending and the CH<sub>3</sub> rocking mode. Furthermore, evidence for an M-M bridging hydride species is provided by a broad absorption band at 1674 cm<sup>-1</sup>, in accordance with the frequently observed signal broadening of such vibrational modes and a shift to lower wave numbers in comparison to terminal ν<sub>M-H</sub> vibrations.<sup>323</sup> While terminal cobalt- or gallium hydride species were reported to produce distinct signals between 2000 and 1800 cm<sup>-1</sup>, the ν<sub>M-H</sub> vibrations of M-M bridging hydrides are usually found at distinctly lower values.<sup>323-326</sup> For example, the metal-hydride stretching of the μ<sub>3</sub>-capping hydride in [(Cp\*Co)<sub>3</sub>(μ<sub>3</sub>-CH)(μ-H)] is found at 1675 cm<sup>-1</sup>.<sup>322</sup>

Characterization of **6** by LIFDI mass spectrometry reveals the full molecular ion peak at *m/z* 1599.9 ([*MI*]<sup>+</sup>, calc. 1600.3 for x = 4) and confirms the overall constitution of **6** as [(Cp\*Co)<sub>3</sub>Ga<sub>6</sub>(Cp\*<sub>3</sub>Co<sub>3</sub>(μ<sup>3</sup>-CH))H<sub>x</sub>]. Note that the *m/z* value indicates the presence of four hydride ligands. The most intense signal at *m/z* 1583.9 results from loss of the methylidyne group ([*MI-CH*]<sup>+</sup>, calc. 1584.3 for x = 1), whereas additional weak peaks at *m/z* 1516.0 and 1447.7 are caused by subsequent cleavage of one gallium atom ([*MI-CH-Ga*]<sup>+</sup>, calc. 1514.6 for x = 1) and one Cp\* ligand ([*MI-CH-Cp\**]<sup>+</sup>, calc. 1448.1), respectively. In all cases, the calculated isotopic distribution patterns are in excellent agreement with the experimental data (Figure 46).

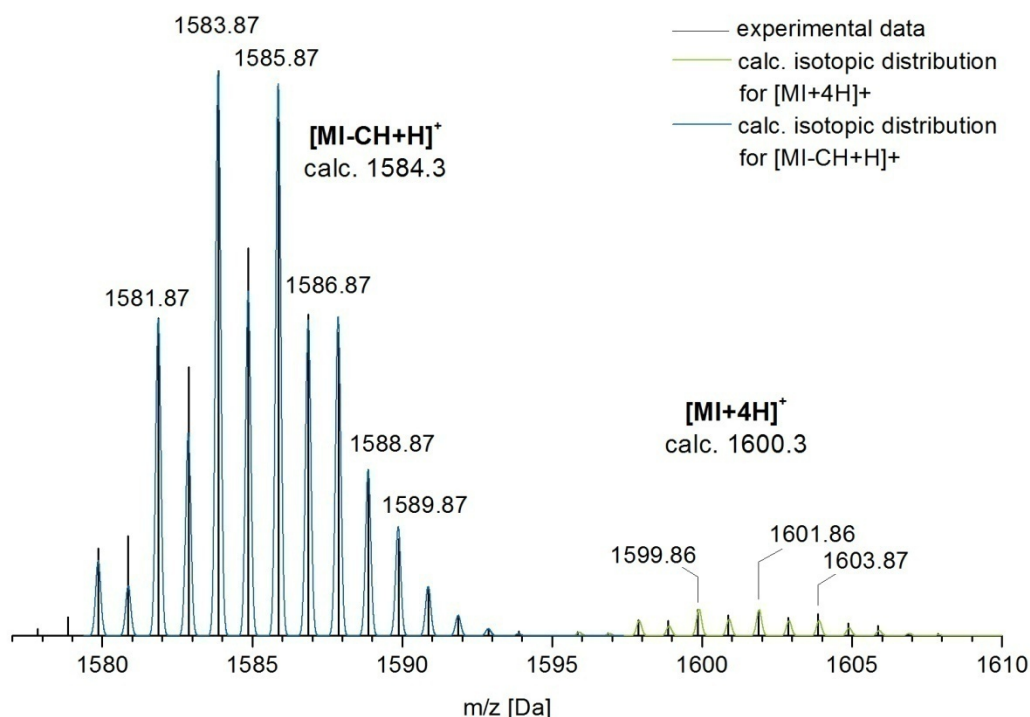


**Figure 46.** Experimental (black) and calculated isotopic distribution patterns of the molecular ion peak  $[MI]^+$  of  $[(Cp^*Co)_3Ga_6(Cp^*_3Co_3(\mu^3-CH))H_x]$  (**6**) at  $m/z$  1599.9 (calc. 1600.3 for  $x = 4$ ; green) and its fragment  $[MI-CH]^+$  at  $m/z$  1583.9 (calc. 1584.3 for  $x = 1$ ; blue) resulting from loss of the methylidyne ligand.

### On the origin of the methylidyne ligand of $[(Cp^*Co)_3Ga_6(Cp^*_3Co_3(\mu^3-CH))H_x]$ (**6**)

Interestingly, the molecular structure of **6** reveals a  $\mu^3$ -coordinated methylidyne group of yet unclarified origin at the peripheral  $Co_3$  triangle. While these findings could not be confirmed by  $^1H$  or  $^{13}C$  NMR spectroscopic analysis, additional evidence for a peripheral CH ligand is provided by LIFDI-mass spectrometric results showing the full molecular ion peak at  $m/z$  1599.9 ( $[MI]^+$ , calc. 1600.3) for an anticipated amount of four residual hydrides at the intermetallic cluster core. It is of note, that the likewise conceivable scenario of a hydroxy or oxo group coordinating to the CoGa cluster core did not go unnoticed, and an exposure of **6** to smallest traces of air or moisture cannot be entirely excluded. Related clusters, like  $[Cp^*_3Co_3(\mu^3-O)_2]$  or  $[Cp^*_4Co_4(\mu^3-OH)_4]$ ,<sup>327</sup> are indeed literature-known, and a hypothetical  $[(Cp^*Co)_3Ga_6(Cp^*_3Co_3(\mu^3-OH))H_x]$  (calc. 1600.3 for  $x = 0$ ) could certainly not be distinguished from the currently anticipated composition of **6** as  $[(Cp^*Co)_3Ga_6(Cp^*_3Co_3(\mu^3-CH))H_x]$  (calc. 1600.3 for  $x = 4$ ) by mass spectrometric measurements, owing to the essentially identical position and isotopic distribution pattern of the respective molecular ion peaks. However, metal fragment-bridging OH-groups are usually reported to evoke sharp and distinct  $\nu_{OH}$  stretching vibrations around  $3650\text{ cm}^{-1}$ , e.g. in the closely related heterocubane-type clusters  $[Cp^*_4Co_4(\mu^3-OH)_4]$  ( $3655\text{ cm}^{-1}$ ) and

$[(\text{Cp}^*_3\text{Co}_3(\mu^3\text{-OH})_4)_2\text{Co}]$  ( $3661\text{ cm}^{-1}$ ),<sup>327</sup> a characteristic which is not observed in the IR spectrum of **6**. Instead very weak absorptions are observed at  $832$  and  $795\text{ cm}^{-1}$ , which are in the range of the  $\delta_{\text{CH}}$  vibrational modes reported for  $[\text{HCCo}_3(\text{CO})_9]$  ( $850\text{ cm}^{-1}$ ).<sup>328</sup> In addition, single crystal X-ray diffraction data of **6** points towards the  $\mu^3$ -coordination of a methylidyne rather than a hydroxy or oxo ligand. Here, the replacement of the methylidyne carbon by oxygen leads to illegitimately large displacement parameters, and a noticeable increase of the  $R_{\text{gt}}$  index by  $0.2\%$ . Note in this regards, that a comparison of the Co-C(61) interatomic distance (av.  $2.230\text{ \AA}$ ) to literature-known bond lengths of either  $\text{Co}_3$ -bound functionality remained inconclusive. In all cases, distinctly shorter bond distances are reported, e.g. for  $[\text{Cp}^*_3\text{Co}_3(\mu^3\text{-O})_2]$  (av.  $1.914\text{ \AA}$ ),  $[\text{Cp}^*_4\text{Co}_4(\mu^3\text{-OH})_4]$  (av.  $2.09\text{ \AA}$ ) or  $[\text{Cp}^*_3\text{Co}_3(\mu^3\text{-CH})(\mu^3\text{-H})]$  ( $1.856(4)\text{ \AA}$ ),<sup>322, 327</sup> which is attributed to the likewise distinctly shorter edge lengths of their underlying  $\text{Co}_3$  triangles with regards to **6**.

The origin of the anticipated CH ligand still remains open for debate, however, conceivable scenarios include C-C bond activation of solvent and/or ligand molecules. While bond activations at Co complexes are certainly literature-known, these are mainly restricted to the "more facile" cleavage of C-H, C-O or even C-F bonds.<sup>329-331</sup> Reports on homogeneous cobalt-catalyzed C-C activations are scarce,<sup>332, 333</sup> and usually restricted to high-valent Co(III) species; whereas the majority of such functionalizations is associated with noble metal catalysts.<sup>334</sup> Nonetheless, cooperative effects between the cobalt and gallium centers facilitating such bond activations are indeed conceivable, and related C-C bond activation reactions were found to occur at  $\text{ECp}^*$  complexes of the heavier homologue rhodium.<sup>335, 336</sup>

In order to test a potential C-C bond activation of solvent molecules, i.e. toluene, the reaction of  $[(\text{P}^i\text{Pr}_3)_6\text{Co}_6\text{H}_8]$  with  $\text{GaCp}^*$  was performed in perdeuterated toluene. As in previous reactions, black crystals of **6'** were obtained which were subjected to  $^1\text{H}$ ,  $^2\text{H}$  and  $^{13}\text{C}$  NMR spectroscopic analysis - with inconclusive results. Likewise,  $^1\text{H}$  NMR spectroscopic analysis of the filtrate was performed which indeed gives rise to small additional signals in the aromatic region, in particular at  $7.17\text{ ppm}$  which corresponds to pentadeuterated benzene. However, the exact origin of these traces is unclear. IR spectroscopic results of **6'** are essentially identical to those of **6** with exception of one intense absorption at  $539\text{ cm}^{-1}$  which is significantly red-shifted with regards to **6** ( $724\text{ cm}^{-1}$ ). Both values are in good agreement with literature-data on out-of-plane C-H/C-D bending modes of toluene/toluene- $\text{d}_6$ .<sup>337</sup>

#### 4.4.6 XPS spectroscopic characterization of $[(\text{Cp}^*\text{Co})_3\text{Ga}_6(\text{Cp}^*_3\text{Co}_3(\mu^3\text{-CH}))\text{H}_x]$ (**6**)

The experimental XPS spectra discussed in the following paragraph were measured by the group of Prof. Dr. Sebastian Günther, particularly involving M.Sc. Tim Kratky, Technical University of Munich, Germany.

The XPS survey spectrum of **6** reveals the expected photoelectron peaks corresponding to gallium (Ga2p), cobalt (Co2p) and carbon (C1s) as well as the C *KVV* and Ga *LMM* Auger peaks (Figure 47).<sup>281</sup> Additionally, signals attributing to oxygen (O1s, O *KLL*) and silicon (Si2s, Si2p) are observed, the latter stemming from residual impurities.

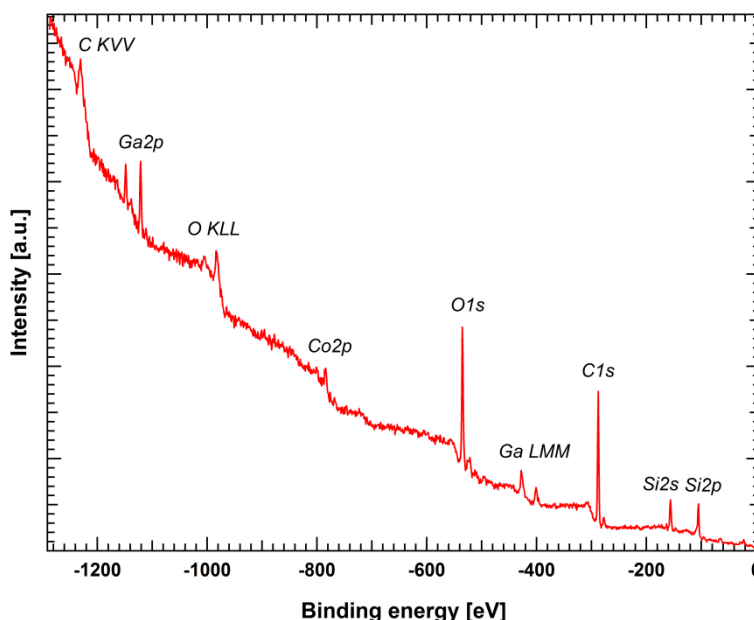
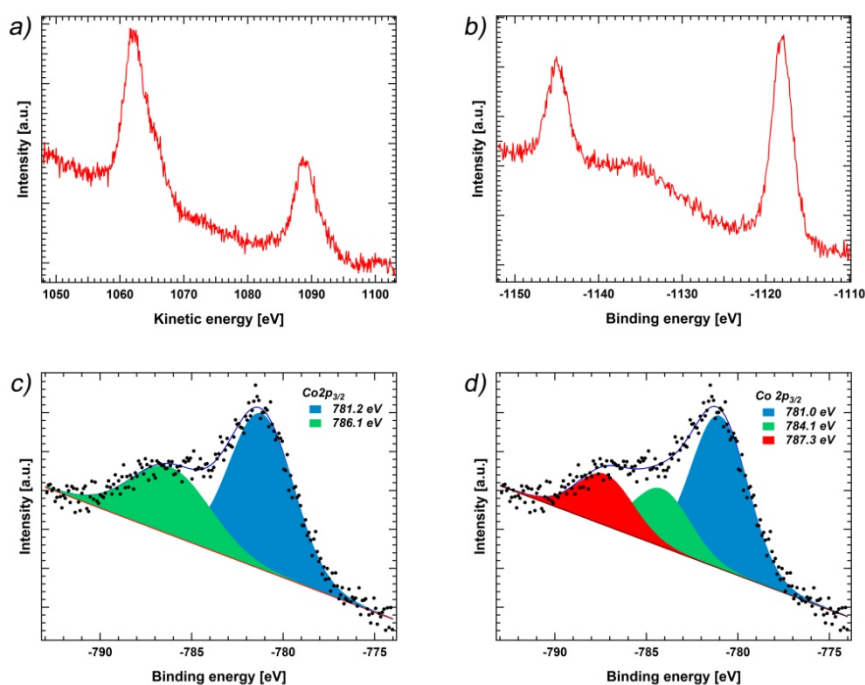


Figure 47. The XPS survey spectrum of  $[(\text{Cp}^*\text{Co})_3\text{Ga}_6(\text{Cp}^*_3\text{Co}_3(\mu^3\text{-CH}))\text{H}_x]$  (**6**) gives rise to photoelectron peaks of carbon (C1s), gallium (Ga2p) and cobalt (Co2p) as well as the C *KVV* and Ga *LMM* Auger peaks. Additional signals (O1s, Si2s, Si2p) stem from residual impurities.

Spectra were referenced by setting the C1s peak to 284.6 eV as an internal charge correction standard. The thus corrected, clearly resolved Ga2p<sub>1/2</sub> and Ga2p<sub>3/2</sub> signals are found at binding energies of 1144.9 and 1118.1 eV, respectively (Figure 48b). While the few reference data available suggests the shift in Auger and photoelectron energies to be of limited value as a measure for the chemical state of gallium, its Auger parameter was reported to be more decisive. For **6**, the Auger parameter of 2180.6 eV, as calculated from the Ga2p<sub>3/2</sub> and the Ga *L<sub>3</sub>M<sub>45</sub>M<sub>45</sub>* peaks, is clearly distinct from the significantly higher values found for bulk Ga<sup>0</sup> (2184.5 eV), but in a comparable range as those reported for molecular Ga

compounds with varying oxidation states from +I to +III (approx. 2180 eV).<sup>338</sup> For instance, the molecular Ga(I) complexes  $[\text{GaNacNac}^{\text{Dipp}}]$  (2179.6 eV) or  $[\text{Ga}(\text{prismand})][\text{OTf}]$  (2180.0 eV) possess almost identical Auger parameters to the Ga(III) compounds  $\text{GaCl}_3$  (2179.4 eV) or  $\text{GaCl}_2\text{Mes}$  (2180.3 eV). Consequently, even though the presence of low-valent gallium centers appears more reasonable with regards to the overall composition of **6**, this cannot be reliably confirmed on the basis of XPS.

The Co2p peak shows significantly split spin-orbit components with  $\text{Co}2p_{1/2}$  and  $\text{Co}2p_{3/2}$  binding energies at 796.2 and 781.2 eV, respectively. The additionally observed intense Co2p satellite peaks at 802.8 and 786.1 eV indicate substantial Co(II) character.<sup>281</sup> Deconvolution of the  $\text{Co}2p_{3/2}$  peak gives significantly broadened components with large full width at half maximum (FWHM) values  $> 4$  eV which might indicate the presence of chemically distinct but closely related species whose differences in core level binding energies fall below the intrinsic resolution limit of XPS (Figure 48c). Based on the integration of  $\text{Ga}2p_{3/2}$  and  $\text{Co}2p_{3/2}$  peaks, the Ga:Co ratio was estimated to 1:1.5 which does not reflect the actual atomic ratio, but is in a reasonable range when considering the spherical molecular structure of the cluster and the resultant attenuation effects commonly observed for the inner atoms of such assemblies (compare chapter 4.1.2).



**Figure 48.** High resolution scans of a) the Ga  $L_3M_{45}M_{45}$  Auger peak and b) the Ga2p photoelectron peaks of  $[(\text{Cp}^*\text{Co})_3\text{Ga}_6(\text{Cp}^*_3\text{Co}_3(\mu^3\text{-CH}))\text{H}_x]$  (**6**). The Auger parameter (2180.6 eV) is significantly lower than that of  $\text{Ga}^0$  (2184.5 eV) but comparable to those of molecular gallium compounds in various oxidation states between +I and +III. c) and d) High resolution scan of the deconvoluted  $\text{Co}2p_{3/2}$  peak with two and three components, respectively.

*Note: Deconvolution of the Co2p<sub>3/2</sub> peak into three or more components did provide reasonable mathematical fits but resulted in contributions of supposed cobalt species with unclarified origin and ratios. For example, deconvolution into three signals indicates contributions from two chemically distinct cobalt species (Co<sub>A</sub> 784.1 and Co<sub>B</sub> 781.0 eV) besides the characteristic Co(II) satellite feature (787.3 eV; Figure 48d). Irrespective of the partial contribution of the satellite peak, the Co<sub>A</sub>:Co<sub>B</sub> integral ratio is clearly in favour of Co<sub>B</sub> and cannot be correlated to the molecular structure of **6**. However, exposure of the sample to air during the transfer to the XPS spectrometer cannot be reliably excluded and might cause partial oxidation which would entail a shift to higher binding energies.*

#### 4.4.7 Reactivity of [Co<sub>6</sub>H<sub>8</sub>(P<sup>i</sup>Pr<sub>3</sub>)<sub>6</sub>] towards AlCp\*

While the reaction of [Co<sub>6</sub>H<sub>8</sub>(P<sup>i</sup>Pr<sub>3</sub>)<sub>6</sub>] with GaCp\* was found to almost quantitatively give the CoGa cluster compound [(Cp\*Co)<sub>3</sub>Ga<sub>6</sub>(Cp\*<sub>3</sub>Co<sub>3</sub>(μ<sup>3</sup>-CH))H<sub>x</sub>] (**6**), the analogous reaction with AlCp\* remains yet inconclusive. *In situ* NMR spectroscopic measurements tracing the progress of the reaction with six equivalents of AlCp\* upon mild thermal treatment at 60°C clearly indicate the substitution of the labile tris-isopropylphosphine ligand and gradual consumption of both educts. The former is concluded from increasing signals at 1.69 and 1.06 ppm in the <sup>1</sup>H NMR spectrum, as well as an eminent signal at 19.36 ppm in the <sup>31</sup>P NMR spectrum, indicating the liberation of substantial amounts of P<sup>i</sup>Pr<sub>3</sub>. Additional evidence for the formation of one or more paramagnetic compounds is provided by a variety of broad, and paramagnetically shifted signals.

Performing the reaction at preparative scales yields a black pyrophoric material of low solubility which evades characterization by means of NMR spectroscopy either because of insufficient solubility or because of a presumed paramagnetic nature. The IR spectrum reveals the characteristic set of ν<sub>C-H</sub> and ν<sub>C-C</sub> vibrational modes frequently observed for Cp\* ligands at 2958, 2896, 2851 and 1446 cm<sup>-1</sup>, respectively, along with the prominent CH<sub>3</sub> bending and rocking modes at 1372 and 1022 cm<sup>-1</sup>. Notably, the intense ν<sub>Al-C</sub> absorption is not observed, thus indicating Cp\* transfer reactions from AlCp\* to the cobalt centers, quite comparable to the Cp\* transfer in the synthesis of **6**.

Irrespective of the low solubility of the substance, complementary LIFDI-MS measurements give rise to several signals which largely correspond to pentamethylcyclopentadienyl cobalt clusters and/or fragments thereof. While the assumed molecular ion peak at *m/z* 838.9 could not be reliably identified, peaks at *m/z* 610.6, 597.8 and 584.8 correlate to fragments of the overall composition [Co<sub>3</sub>Cp\*<sub>3</sub>(CH)<sub>2</sub>]<sup>+</sup> (calc. 608.5), [Co<sub>3</sub>Cp\*<sub>3</sub>(CH)]<sup>+</sup> (calc. 595.5) and [Co<sub>3</sub>Cp\*<sub>3</sub>]<sup>+</sup> (calc. 582.5). In this context it is noteworthy, that the diamagnetic cobalt cluster [Co<sub>3</sub>Cp\*<sub>3</sub>(μ<sub>3</sub>-CH)<sub>2</sub>] has indeed been reported,<sup>322</sup> but can be

reliably excluded as the main product of the given reaction owing to its substantially different solubility in organic solvents and its facile characterization by  $^1\text{H}$  NMR spectroscopy. Consequently, the herein observed masses are assumed to resemble fragments stemming from one or more higher nuclearity  $\text{Co}_a$  cluster compounds. Given the variety of heteronuclear pentamethyl- and cyclopentadienylcobalt cluster compounds incorporating heteroatoms into their cluster skeleton,<sup>339-342</sup> the formation of a mixed CoAl cluster is equally conceivable. For instance, the cobaltaborane  $[(\mu_3\text{-H})_2(\text{CpCo})_4\text{B}_2\text{H}_2]$  was reported to form in the reaction of  $[\text{CpCo}(\text{PPh}_3)(\text{C}_2\text{Et}_2)]$  with  $\text{BH}_3\cdot\text{THF}$ .<sup>343</sup> In fact, the observed mass signal at  $m/z$  838.8 is in reasonable agreement with an analogous cluster of the hypothetical formula  $[(\text{Cp}^*\text{Co})_4\text{Al}_2\text{H}_x]$  (calc. 834.6 for  $x = 4$ ). Likewise, a compound/fragment of the formal composition  $[\text{Co}_5\text{Cp}^*_4]$  (calc. 835.6) appears possible.

#### 4.4.8 Concluding remarks

The almost quantitative synthesis of the intermetalloid CoGa cluster  $[(\text{Cp}^*\text{Co})_3\text{Ga}_6(\text{Cp}^*_3\text{Co}_3(\mu^3\text{-CH}))\text{H}_x]$  (**6**) from treatment of the pre-assembled cobalt hydride cluster  $[\text{Co}_6\text{H}_8(\text{P}^i\text{Pr}_3)_6]$  with  $\text{GaCp}^*$  provides additional evidence for the initially proposed theory of a facile access towards intermetalloid cluster compounds  $[\text{TM}_a\text{E}_b](\text{Cp}^*)_n$  *via* directed ligand exchange reactions at pre-assembled transition metal atom assemblies. Similar to the synthesis of  $[\text{Cu}_6(\text{AlCp}^*)_6\text{H}_4]$  (**1**), the phosphine ligand is readily replaced by the  $\text{ECp}^*$  ligand, whereat structural re-arrangement to form a naked  $\text{Ga}_6$  kernel stabilized by six  $\text{CoCp}^*$  units is presumably triggered by  $\text{Cp}^*$  transfer to the lewis-acidic cobalt centers. Comparable observations are made for the reaction with  $\text{AlCp}^*$  which is assumed to form homo- or heterometallic pentamethylcyclopentadienyl cobalt cluster compounds on the basis of preliminary mass spectrometric and IR spectroscopic results.

The unprecedented finding of a methylidyne ligand being coordinated to the peripheral  $[\text{Cp}^*_3\text{Co}_3]$  fragment of **6** hints at C-C bond activation reactions occurring during the formation of the compound. This observation discloses a potential reactivity of **6** in catalytically relevant transformations. In this regard, questions that need to be clarified are "What is the origin of the CH ligand (toluene,  $\text{Cp}^*$  ligand, etc.)?" and "Is it possible to avoid the coordination of this ligand, in order to create a vacant reaction site for comparable bond activation reactions?"

Furthermore, given the library of available, phosphine-stabilized metalloid transition metal clusters, subsequent efforts should now be extended towards further representatives of this class of compounds, like the pentanuclear  $[(\text{P}^i\text{Pr}_3)_5\text{Ni}_5\text{H}_6]$ .<sup>344</sup> Within this context, establishing means to control potential  $\text{Cp}^*$  transfer reactions might pave the way towards low-valent, truly mixed metal cores. As discussed in chapter 4.6, the tendency of  $\text{ECp}^*$  to undergo  $\text{Cp}^*$

transfer appears to be largely dependent on the lewis acidity of the transition metal involved, and can be influenced by the presence of electron-donating co-ligands, such as hydrides. Furthermore, large metal atom assemblies  $[TM_a](L)_n$  with  $a > n$ , could be expected to primarily undergo reconstruction of the outer coordination sphere leaving the central  $[TM_{a-n}]$  core unchanged.



## 4.5 The intermetalloid NiGa cluster $[\text{Ni}_8(\text{GaCp}^*)_6]$ (8) - a structural chameleon bearing resemblance to binary NiGa phases

*The results presented in the following chapter are based on initial studies of Dr. Tobias Steinke during his post-doctoral research stay with Prof. Fischer at the Chair of Inorganic Chemistry II, Ruhr-University Bochum. Their completion and re-evaluation in the following chapter is partially based on the work of M.Sc. Lena Staiger during her master studies, which she performed at the Chair of Inorganic and Metal-Organic Chemistry, TUM under my supervision. Accordingly, they are also part of her master thesis.*

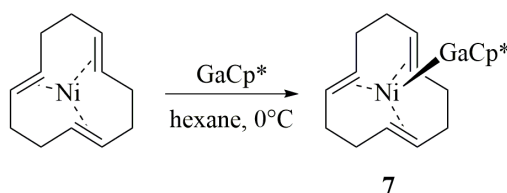
### 4.5.1 Introductory remarks

With regards to the available fundamental synthetic strategies for  $\text{TM}_a\text{E}_b$  cluster assembly, direct approaches tend to suffer from a substantiated lack of control owing to the multitude of energetically accessible reaction pathways and competing side reactions, consequently affording various reaction products with usually low selectivity. In contrast, the building block approach, should allow for a more directed and thus more comprehensible reaction outcome as it makes use of pre-assembled TM-E fragments and aims at the directed stimulation of cluster growth, e.g. *via* reaction with suitable organometallic precursors, controlled thermal decomposition, or the specific cleavage of labile ligands.

While the soft wet-chemical decomposition of suitable precursors or mixtures thereof is commonly employed in the synthesis of intermetallic nanoparticles, including examples with transition metal-group 13 metal combinations from our group,<sup>269-273</sup> the potential of such strategies for  $\text{TM}_a\text{E}_b$  cluster synthesis remains largely unexplored. First experiments at the protolytic cleavage of  $\text{Cp}^*\text{H}$  from coordinated  $\text{Ga}(\text{R})\text{Cp}^*$  ligands were performed with the reaction of  $[(\text{GaCp}^*)_4\text{Rh}(\text{Ga}(\text{Me})\text{Cp}^*)]$  with  $[\text{H}(\text{OEt}_2)_2][\text{BAr}_4^{\text{F}}]$  yielding the cationic complex  $[(\text{GaCp}^*)_4\text{Rh}(\text{GaMe})][\text{BAr}_4^{\text{F}}]$ .<sup>345</sup> Likewise, the oxidative cleavage of  $\text{Cp}^*$  ligands by treatment with  $[\text{FeCp}_2][\text{BAr}_4^{\text{F}}]$  was reported to be surprisingly selective. For instance, reaction of  $[\text{Ni}(\text{GaCp}^*)_4]$  with equimolar amounts of  $[\text{FeCp}_2][\text{BAr}_4^{\text{F}}]$  affords  $[\text{GaNi}(\text{GaCp}^*)_4]^+$ , whereas the analogous reaction of  $[\text{Pt}(\text{GaCp}^*)_4]$  with sub-stoichiometric amounts of  $[\text{FeCp}_2][\text{BAr}_4^{\text{F}}]$  effects cluster growth to give  $[(\mu_2\text{-Ga})\text{Pt}_3(\text{GaCp}^*)_6]^+$ .<sup>346</sup> A more recent showcase example impressively demonstrating the immense potential of oxidative  $\text{Cp}^*$  cleavage for cluster growth reactions was reported with the unusual zinc cluster  $[\text{Zn}_{10}\text{Cp}^*_6\text{Me}]^+$  which is obtained from the reaction of  $[\text{Zn}_2\text{Cp}^*_2]$  with  $[\text{FeCp}_2][\text{BAr}_4^{\text{F}}]$  in the presence of  $\text{ZnMe}_2$ .<sup>7</sup>

Following this line of thought, the synthesis of small TM-ECp\* complexes bearing readily cleavable, labile co-ligands and/or protection groups appears promising for subsequent cluster growth reactions. In the following chapter, the synthesis of  $[\text{Ni}(\text{cdt})(\text{GaCp}^*)]$  (**7**), a bimetallic NiGa complex bearing a labile cdt ligand, and its cluster growth reaction affording the intermetalloid NiGa cluster  $[\text{Ni}_8(\text{GaCp}^*)_6]$  (**8**) upon mild thermal treatment in the presence of an excess of GaCp\* are discussed. The latter features a highly unusual molecular structure which discloses new challenges arising when approaching the intermetalloid cluster size regime.

#### 4.5.2 Synthesis and characterization of $[\text{Ni}(\text{cdt})(\text{GaCp}^*)]$ (**7**)



Scheme 5. Synthesis of  $[\text{Ni}(\text{GaCp}^*)(\text{cdt})]$  (**7**) from  $[\text{Ni}(\text{cdt})]$  and GaCp\*.

Analogous to the formation of the stable 18 VE complexes  $[\text{Ni}(\text{cdt})\text{L}]$  ( $\text{L} = \text{CO}$ ,  $\text{PR}_3$ ,  $\text{Ga}(\text{ddp})$ ),<sup>347-349</sup> treatment of the temperature-labile  $[\text{Ni}(\text{cdt})]$  with equimolar amounts of GaCp\* in *n*-hexane at low temperatures results in the immediate precipitation of an orange solid which was identified as  $[\text{Ni}(\text{cdt})(\text{GaCp}^*)]$  (**7**; Scheme 5) by means of NMR and IR spectroscopy, elemental analysis and single crystal X-ray diffraction studies. **7** is air- and moisture sensitive, and decomposes rapidly upon exposure to air as indicated by colour change from orange to black. It is well soluble in unpolar organic solvents and can be purified by crystallization from saturated *n*-hexane or toluene solutions.

#### Spectroscopic characterization of $[\text{Ni}(\text{cdt})(\text{GaCp}^*)]$ (**7**)

$^1\text{H}$  NMR spectroscopic characterization of **7** reveals a set of three signals at 4.37, 2.33 and 1.92 ppm corresponding to the olefinic and methanediyl hydrogen atoms of the cdt ligands whereat the signal splitting of the latter is attributed to their relative proximity to the GaCp\* ligand. Note that similar NMR spectroscopic observations were made for phosphine and Ga(ddp) analogues.<sup>348, 349</sup> The additionally expected GaCp\* singlet arises at 1.95 ppm, and coincides with the cdt signal at 1.92 ppm. The  $^{13}\text{C}$  NMR spectrum of **7** comprises the

characteristic set of signals of the Cp\* ligand's inner and outer carbon atoms at 113.57 and 9.97 ppm, as well as two signals at 102.86 and 41.10 ppm which are attributed to the sp<sup>2</sup> and sp<sup>3</sup>-hybridized carbon atoms of the cdt ligand.

IR spectroscopic measurements of neat **7** clearly confirm the presence of both ligands, and reveal intense absorption bands from 2961 to 2789 cm<sup>-1</sup> corresponding to diverse ν<sub>C-H,sp<sup>3</sup></sub> vibrational modes. An additional very weak ν<sub>C-H,sp<sup>2</sup></sub> absorption stemming from the Ni-coordinated ethylene bridges is observed at 3004 cm<sup>-1</sup>. Characteristic symmetric and antisymmetric ν<sub>C-C/C-Me</sub> vibrations occur at 1470 and 1413 cm<sup>-1</sup>, and at 786 cm<sup>-1</sup>, along with signals at 1508 and 1366 cm<sup>-1</sup> stemming from CH<sub>3</sub> bending modes. Furthermore, two absorption bands of medium intensity are found close to the detection limit (450 and 408 cm<sup>-1</sup>, respectively) which are in a comparable range as reported Ni-ligand vibrations of Nickel olefin complexes, like [Ni(ethylene)<sub>3</sub>].<sup>350</sup>

Complementary mass spectrometric measurements of **7** using the mild liquid injection field desorption ionization (LIFDI) method reveal the full molecular ion peak [MI]<sup>+</sup> at *m/z* 425.4 (calc. 425.9) along with significant fragmentation under loss of the labile bound ligands. Accordingly, signals at *m/z* 221.9 and 206.8 are attributed to cleavage of the unsupported Ni-Ga bond giving [Ni(cdt)]<sup>+</sup> (calc. 221.0) and [GaCp\*]<sup>+</sup> (calc. 204.9), whereas the free cdt ligand [cdt]<sup>+</sup> (calc. 162.3) is found at *m/z* 162.8. Additionally identified fragments include [Ni(GaCp\*)CH]<sup>+</sup> (calc. 276.6, found 275.9) and [NiCp\*]<sup>+</sup> (calc. 193.9, found 197.9).

### Structural characterization of [Ni(cdt)(GaCp\*)] (**7**)

Single crystal X-ray diffraction measurements were performed on suitable crystals of **7** as obtained from saturated toluene solutions at -30 °C within few days. **7** crystallizes in form of intergrown orange plates in the monoclinic *Pm* space group with four independent molecules per asymmetric unit. The molecular structure of **7** comprises a central Ni atom which is embedded into the pocket of a η<sup>6</sup>-coordinated cdt ligand and bears one additional GaCp\* ligand (Figure 49). The latter is bound *via* a long Ni-Ga bond (av. 2.308 Å) which is significantly elongated with regards to [Ni(GaCp\*)<sub>4</sub>] (2.2188(5) Å)<sup>245</sup>, but similar to the Ni-Ga distance of [Ni(cdt)(Ga(ddp))] (2.3482(6) Å),<sup>349</sup> thus indicating a weak dative bonding. This is further supported by the Ga-Cp\*<sub>centr.</sub> distance of av. 2.017 Å which is slightly shorter than those of hexameric [GaCp\*]<sub>6</sub> in the solid state (2.081 Å)<sup>315</sup> and hints at only weak electron donation from the gallium atom to the nickel center.

The overall coordination geometry of the central Ni atom is probably best described as distorted tetrahedral with inner angles ranging from 104.6 to 111.7° (C=C centroids of the cdt ligands taking as reference points), and Ni-C distances (av. 2.094 Å) that are elongated with regards to [Ni(cdt)] (av. 2.02 Å). The C-C bonds of the ethylene bridges (av. 1.38 Å) are

comparable to those of the starting reagent (1.37 Å) or the closely related [Ni(cdt)(Ga(ddp))] (av. 1.36 Å), but visibly longer than the C-C bonds of [Ni(cdt)(PR<sub>2</sub>R')] (av. 1.31 Å).

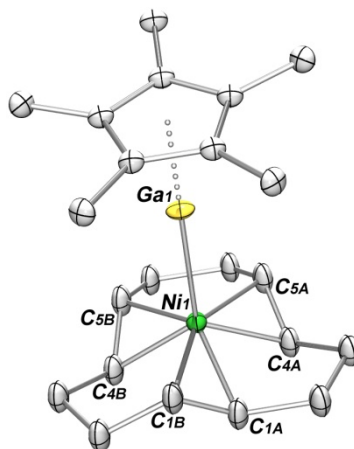
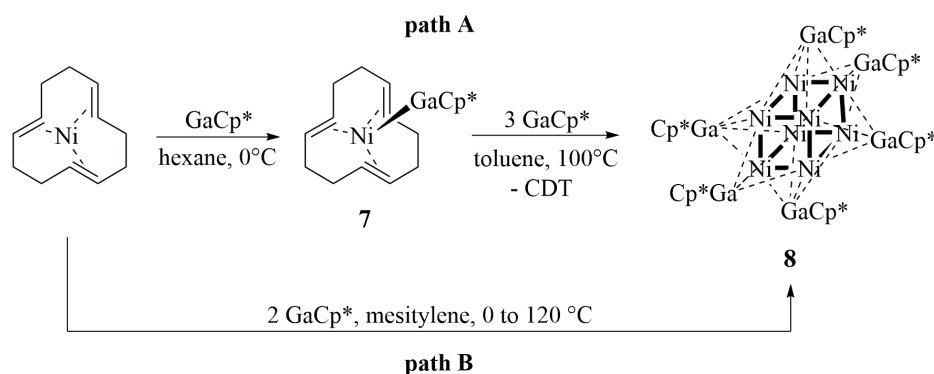


**Figure 49.** Molecular structure of [Ni(cdt)(GaCp\*)] (**7**) in the solid state (one of four crystallographically independent molecules of the asymmetric unit). Displacement ellipsoids are shown on the 50 % probability level, hydrogen atoms and disorder sites are omitted for clarity. Selected interatomic distances (Å) and angles (deg): Ni-Ga av. 2.308, Ga-Cp\*<sub>centr</sub> av. 2.017, Ni-C av. 2.094, C=C av. 1.38, Cp\*<sub>centr</sub>-Ga-Ni av. 167.6, (C=C)<sub>centr</sub>-Ni-Ga 104.6 - 111.7.

#### 4.5.3 Synthesis of [Ni<sub>8</sub>(GaCp\*)<sub>6</sub>] (**8**)

The labile cdt ligand of the closely related [Ni(cdt)(CO)] can easily be substituted by donor ligands, such as phosphines or isonitriles, to give complexes of the general formula [L<sub>3</sub>Ni(CO)] in subsequent reactions.<sup>347</sup> Likewise, [Ni(cdt)(Ga(ddp))] was reported to undergo facile cdt cleavage in the presence of suitable olefins, furnishing complexes of the type [Ni(Ga(ddp))(olefin)<sub>2</sub>] upon reaction with ethylene, styrene or dvds (dvds = 1,3-divinyl-(1,1,3,3-tetramethyl)disiloxane).<sup>349</sup> The obtained [Ni(Ga(ddp))(ethylene)<sub>2</sub>] is thermodynamically unstable and decomposes at room temperature in the absence of additional ethylene, further emphasizing the labile nature of the Ni-olefin coordination bond in such complexes.

Thus inspired, the controlled thermal decomposition of [Ni(cdt)(GaCp\*)] (**7**) in the presence of an excess of GaCp\* in toluene was found to effect cluster growth, giving the unprecedented intermetalloid Ni/Ga cluster [Ni<sub>8</sub>(GaCp\*)<sub>6</sub>] (**8**, Scheme 6, path A). Herein, preliminary *in situ* NMR spectroscopic data of mixtures of **7** with an excess of GaCp\* suggest the formation of intermediate products of the general formula [Ni(GaCp\*)<sub>x</sub>(cdt)] (x = 2,3) with η<sup>2</sup> or η<sup>4</sup>-coordinated cdt ligands, respectively.<sup>351</sup>



**Scheme 6.** Synthesis of [Ni<sub>8</sub>(GaCp\*)<sub>6</sub>] (**8**) from Ni(cdt) and GaCp\* via [Ni(cdt)(GaCp\*)] (**7**, path A). The two-step synthesis involving the isolation of intermediate **14** can be shortened by careful adjustment of the reaction conditions, which allows for the direct formation of **8** via *in-situ* formed **7** (path B).

Compound **8** crystallizes directly from the hot reaction mixture in form of dark red needles and is sparingly soluble in unpolar organic solvents. The highly air and moisture sensitive substance smolders upon exposure to air, but can be stored at room temperature under an inert atmosphere for months without apparent signs of decomposition. Further optimization of the synthetic access towards **8** afforded a feasible one-pot procedure which allows for its direct synthesis from [Ni(cdt)] and two equivalents of GaCp\* in mesitylene (Scheme 6, path B). Herein, systematic temperature control is required to allow for the initial *in situ* formation of **7** and its consecutive cluster growth reaction with surplus GaCp\*.

#### 4.5.4 Spectroscopic characterization of [Ni<sub>8</sub>(GaCp\*)<sub>6</sub>] (**8**)

Owing to the poor solubility of **8** in common organic solvents, like *n*-hexane, toluene or benzene at room temperature, its comprehensive characterization is largely dependent on techniques that are applicable to solid-state materials. Consequently, the composition of compound **8** was confirmed on the basis of solid-state MAS NMR, IR spectroscopy, elemental analysis and AAS, and single crystal X-ray diffraction analysis. Despite its poor solubility, additional LIFDI-MS measurements could be performed.

<sup>1</sup>H MAS NMR spectroscopic analysis of neat **8** at room temperature gives rise to a broad singlet at 2.15 ppm which correlates to the chemically equivalent Cp\* ligands. An additional signal at 6.71 ppm is attributed to the aromatic protons of small amounts of co-crystallized mesitylene, whereat the missing second signal of the methyl groups is superimposed by the intense Cp\* signal. This is supported by the <sup>13</sup>C MAS NMR spectrum of **8** which reveals two sharp signals resembling the Cp\* ring and methyl carbon atoms at 98.10 and 13.22 ppm as well as the full set of signals expected for mesitylene at 137.74, 129.12 and 22.33 ppm. The

IR spectrum of **8** shows  $\nu_{\text{C-H}}$  stretching modes at 2929, 2884 and 2843  $\text{cm}^{-1}$ , along with symmetric and antisymmetric  $\nu_{\text{C-C/C-Me}}$  vibrations at 1446, 1421 and 799  $\text{cm}^{-1}$  that are characteristic of the Cp\* ligand. An additional intense absorption is observed at 1372  $\text{cm}^{-1}$ , corresponding to the symmetric  $\text{CH}_3$  bending mode.

Surprisingly, LIFDI mass spectrometric measurements of **8** could be performed despite the poor solubility of the compound in organic solvents. Even though the low  $S/N$  ratio does not allow for a sufficient resolution of the molecular ion peak's isotopic pattern, its position at  $m/z$  1702.6 ( $[\text{MI}]^+$ , calc. 1699.2) supports the overall composition of **8** as  $[\text{Ni}_8(\text{GaCp}^*)_6]$ . An additional intense signal is observed at  $m/z$  1644.8, and was initially believed to resemble the molecular ion peak, whereat position and isotopic pattern match a composition of  $[\text{Ni}_7(\text{GaCp}^*)_6]$  (calc. 1640.5). However, the estimated Ni:Ga ratio of 6:8.4, as deduced from refinement of the highly disordered molecular structure of **8** (see below), and, more importantly, results from elemental analysis and AAS are in excellent agreement with the proposed composition of  $[\text{Ni}_8(\text{GaCp}^*)_6]$  which is why the observed signal at  $m/z$  1644.8 is attributed to fragmentation of **8**, i.e. loss of one nickel atom. A third, very weak signal at  $m/z$  1574.6 corresponds to the  $[\text{MI-Ni-Ga}]^+$  fragment (calc. 1570.8) which might form *via* Cp\* transfer from one GaCp\* ligand to the central nickel core of the  $[\text{MI-Ni}]^+$  fragment and subsequent loss of one gallium atom.

In line with these findings, the tendency of **8** to undergo significant fragmentation under mass spectrometric conditions was observed in complementary measurements using a mass spectrometer equipped with a LIFDI source and an Orbitrap ion trap mass analyzer (see experimental section for details). However, and in contrast to the measurements described above, a variety of signals stemming from fragmentation of the Cp\* ligands is observed while the inner  $\text{Ni}_8\text{Ga}_6$  unit appears to stay intact, as evident from the molecular ion peaks  $[\text{MI+Li}]^+$  and  $[\text{MI+Na}]^+$  at  $m/z$  1707.2 and 1723.7, respectively (Figure 50; Table 9). This significantly different fragmentation behaviour of **8** is attributed to the higher argon pressure inside the higher-energy collisional dissociation (HCD) cell of the herein employed mass spectrometric set-up which stimulates collision-induced fragmentation. Furthermore, signals whose isotopic distribution patterns suggest a low metal content are observed at values below  $m/z$  1500. These could not be identified as fragments of **8**, but are thought to result from the recombination of smaller fragments, for instance during their prolonged residence time in the ion trap.

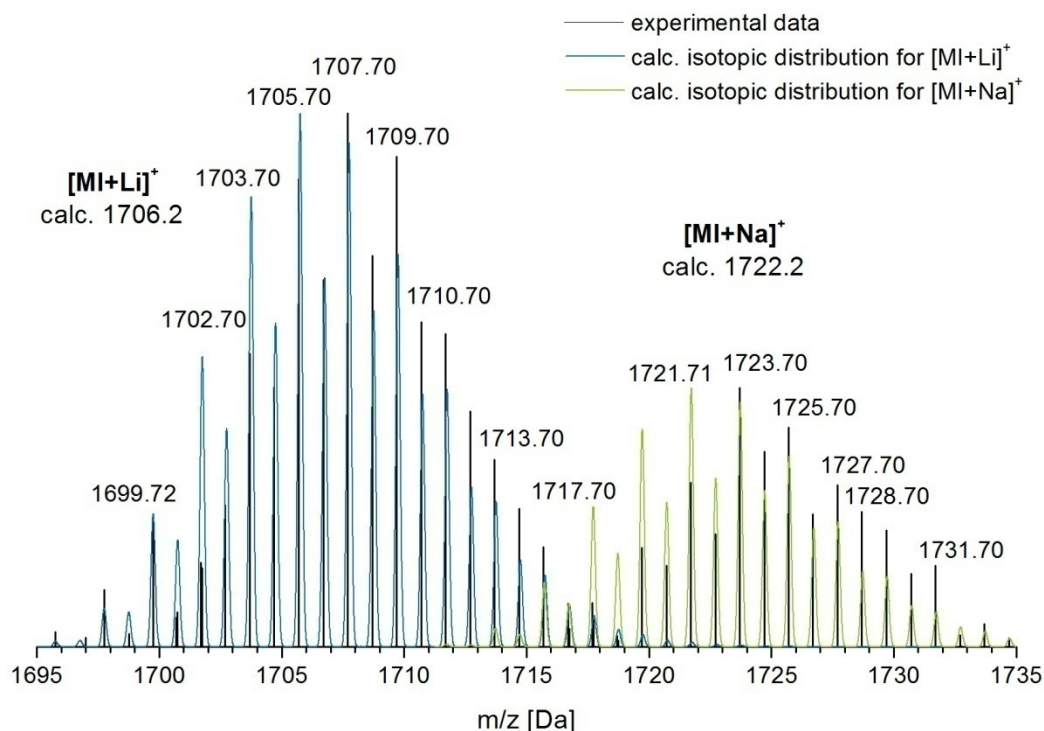


**Figure 50.** Experimental (black) and calculated isotopic distribution patterns of the molecular ion peaks  $[\text{MI}+\text{Na}]^+$  of  $[\text{Ni}_8(\text{GaCp}^*)_6]$  (**8**) at  $m/z$  1723.7 (calc. 1722.2; green), and  $[\text{MI}+\text{Li}]^+$  at  $m/z$  1707.7 (calc. 1706.2; blue).

**Table 9.** Masses detected during LIFDI-MS measurements of **8** and assigned fragments with calculated  $m/z$  values. Significant fragmentation of the Cp\* ligands is observed while the central  $\text{Ni}_8\text{Ga}_6$  core appears to stay intact.

$m/z_{\text{experimental}}$	fragment	$m/z_{\text{calculated}}$
1723.7	$[\text{MI}+\text{Na}]^+$	1722.2
1707.7	$[\text{MI}+\text{Li}]^+$	1706.2
1683.8	$[\text{MI}-\text{Me}]^+$	1684.2
1665.8	$[\text{MI}-2\text{Me}]^+$	1669.2
1649.8	$[\text{MI}-3\text{Me}]^+$	1654.1
1637.8	$[\text{MI}-4\text{Me}]^+$	1639.1
1531.6	$[\text{MI}-\text{Cp}^*-2\text{Me}]^+$	1533.9



#### 4.5.5 Structural characterization of $[\text{Ni}_8(\text{GaCp}^*)_6]$ (**8**)

Compound **8** crystallizes as dark red needles from saturated mesitylene solutions which are prepared by extraction of the substance with boiling mesitylene. Herein, controlled slow cooling of the resultant dark red solutions ( $\Delta T \approx 5^\circ\text{C/h}$ ) affords suitable crystals for single crystal X-ray diffraction studies. **8** crystallizes in the triclinic space group  $P-1$  with one molecule per unit cell under inclusion of two molecules of co-crystallized mesitylene. Its molecular structure features a significantly disordered central  $\text{Ni}_8$  core which is embedded inside the discrete octahedral arrangement of six  $\text{GaCp}^*$  ligands (Figure 51). Notably, the severe disorder of the metallic core renders a quantitative analysis of geometrical parameters impossible and even precludes the identification of the central structural motif. Nonetheless, refinement of all disordered Ni sites with individual occupation factors allows for sufficient data quality to support the proposed composition of **8** as  $[\text{Ni}_8(\text{GaCp}^*)_6]$ , and verify the compound's overall constitution. As indicated in chapter 4.3, this approach, which is commonly employed in the refinement of substitutional disorder and partial occupancy of crystallographic sites,<sup>300</sup> only provides an estimated sum formula with an approximated Ni:Ga ratio of 8.4:6 pointing towards an octanuclear rather than a heptanuclear central nickel unit. This is further supported by the elemental analysis which is in excellent agreement with the proposed composition of  $[\text{Ni}_8(\text{GaCp}^*)_6]$ , and mass spectrometric results.

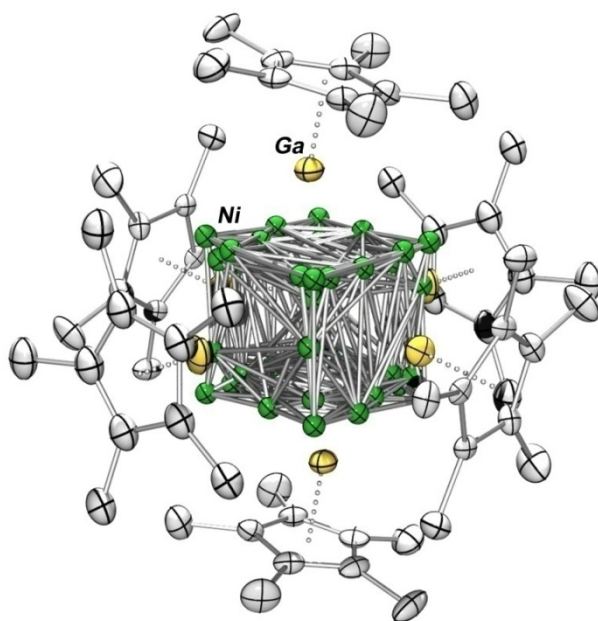


**Figure 51.** Severely disordered molecular structure of  $[\text{Ni}_8(\text{GaCp}^*)_6]$  (**8**) in the solid state (Ni, Ga, C depicted in green, yellow and grey, respectively). Displacement ellipsoids are shown on the 30% probability level, hydrogen atoms, co-crystallized solvent molecules and disorder sites of the  $\text{Cp}^*$  ligands are omitted for clarity. The unusually high degree of disorder of the central  $\text{Ni}_8$  unit precludes the identification of its core geometry as well as the quantification of structural parameters.



*Note:* Most interestingly, the severe disorder of the  $\text{Ni}_8$  kernel does not disrupt the otherwise discrete outer shell of six  $\text{GaCp}^*$  ligands. Hypothetically speaking, the resultant spherical ligand capsule might even account for the high degree of disorder as it is potentially able to compensate for small changes in the inner geometry, and host core structures of variable shapes. Given the variety of energetically accessible structures with increasing nuclearity, an inhomogeneous distribution of slightly variable molecular constitutions throughout the crystalline material of **8** is indeed conceivable, and might provide an explanation for the difficulties faced during the refinement of repeatedly compiled diffraction data. Such a (hypothetical) kind of system might be understood on the basis of snapshots of fluctuating core structures which are conserved during the crystallization process.

The discrete outer shell of six  $\text{GaCp}^*$  ligands displays an almost ideal octahedral arrangement of the gallium atoms with Ga-Ga-Ga angles close to the optimum value of  $90^\circ$ , and an average Ga-Ga distance of 4.210 Å. Interestingly, these are in a comparable range like those found for hexameric aggregates of  $\text{GaCp}^*$  in the solid state (4.073 and 4.172 Å).<sup>315</sup> While the latter is reported to be primarily stabilized by the van der Waals interactions of its organic envelope of  $\text{Cp}^*$  ligands, the noticeably shortened Ga-Cp\*<sub>centroid</sub> distances of **8** (av. 1.752 Å) in comparison to  $[\text{GaCp}^*]_6$  (av. 2.081 Å) provide evidence for significant electron donation from the Ga centers to the central  $\text{Ni}_8$  core, thus indicating a potential involvement of the gallium atoms in effective cluster bonding. Similar observations were made for the earlier introduced, closely related  $[\text{Pd}_3(\text{AlCp}^*)_6]$  whose bonding situation was rationalized following classical cve counting concepts.<sup>257</sup> Although an implementation of these concepts is hampered by the ill-defined geometry of the central  $\text{Ni}_8$  motif, careful analysis of reasonable limiting cases indeed supports viewing **8** as  $[(\text{Ni}_8\text{Ga}_6)\text{Cp}^*_6]$  rather than  $[\text{Ni}_8(\text{GaCp}^*)_6]$ . To begin with, conceivable geometries of the central  $\text{Ni}_8$  kernel include a cubic arrangement as well as the star-shaped stella quadrangula which is constructed from two interpenetrating, inversely oriented tetrahedra. Considering  $\text{GaCp}^*$  as a pure two-electron donating ligand, the expected cve counts for both structures (cube 120 cve; stella quadr. 108 cve) are distinctly higher than the *de facto* observed 92 cve. This also holds true for the cve count expected for a square antiprism (114 cve). In contrast, treatment of all gallium atoms as part of an inner  $\text{Ni}_8\text{Ga}_6$  core gives an actual electron count of 188 ( $8 \cdot 10 + 6 \cdot 13 + 6 \cdot 5$ ) which is higher than the calculated 180 cve for a multiply capped, star-shaped  $\text{Ni}_8$  unit, but in the range of 180 to 192 cves calculated for a multiply capped  $\text{Ni}_8$  cube. Note that these values were calculated following the cluster capping and -fusion rules introduced earlier: For a  $\text{Ni}_8\text{Ga}_6$  cluster featuring a star-shaped inner  $\text{Ni}_8$  geometry, a cve count of 180 is obtained by multiple capping of the innermost  $\text{Ni}_4$  tetrahedron under the assumption of radial bonding alone ( $60 + 4 \cdot 12 + 6 \cdot 12 = 180$ ), whereas the cve count of a hexacapped, cuboidal arrangement of Ni atoms is derived from fusion of a central cube with six square planar pyramids and

subtraction of the shared basal planes. Depending on the employed count for a square (62 vs. 64 cve), an expected value between 180 and 192 cve is obtained (Figure 52).

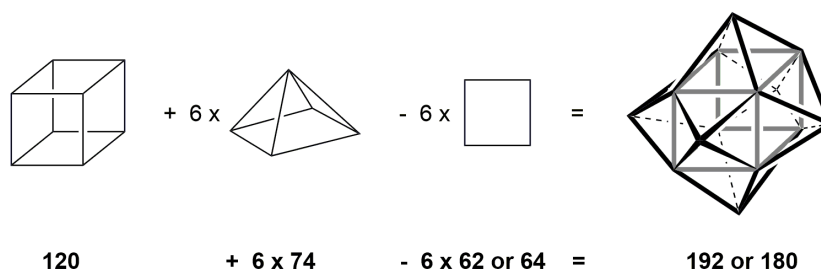


**Figure 52.** Calculation of the expected cve count of a hexacapped  $\text{Ni}_8$  cube on the basis of the cluster fusion principle. Depending on the employed count for a square, stable clusters are expected to feature 180 or 192 cve, respectively.

*Note:* With regards to a potential cubic structure featuring six two-electron donating  $\text{GaCp}^*$  ligands, it is of note that cubic metal clusters on the borderline between molecular compounds and solid-state materials take an exceptional position amongst systems that can be rationalized by simple electron counting rules. In fact, known stable clusters of this kind exhibit cve counts in a broad range from 99 (e.g. in  $[\text{I}_8\text{Fe}_8\text{Se}_6]^{3-}$ )<sup>352</sup> to 120 cve (e.g. in  $[\text{Ni}_8(\text{CO})_8(\mu^4\text{-PPh})_6]$ ).<sup>353</sup> This is attributed to their particular MO structure, as exemplary discussed for  $[\text{Ni}_8(\text{CO})_8(\mu^4\text{-PPh})_6]$ . Here, twenty-two orbitals of the highest lying blocks of filled MOs with mainly d-metal character resemble non-bonding or weakly antibonding orbitals whereas Ni-Ni bonding is primarily associated with the ensuing, lower-lying set of twelve MOs.<sup>135</sup> As a consequence, cubic metal clusters are in theory predicted to be stable for diminished cve counts down to 76 cve, which resembles clearance of the uppermost 22 MOs.

#### 4.5.6 Relation of $[\text{Ni}_8(\text{GaCp}^*)_6]$ (**8**) to the solid state structures of binary NiGa phases

Correlation of the molecular structure of **8** to solid state structures of binary NiGa phases reveals a certain resemblance between the nested polyhedra of the latter and the central  $\text{Ni}_8\text{Ga}_6$  unit of **8** with regards to both, composition and constitution. Within this context it is of note that, while cuboidal arrangements correlating to the hypothetical structure of a  $\text{Ni}_8$  cube inside a  $\text{Ga}_6$  octahedron are indeed found in a variety of NiGa intermetallics, structural motifs reminiscent of the star-shaped  $\text{Ni}_8$  kernel were not found. For example, in the bcc  $\beta$ -NiGa phase,  $\text{Ni}_8$  cubes can be envisioned inside  $\text{Ga}_6$  octahedra with Ga-Ga distances (4.083 Å) that are in a comparable size regime as those found in the molecular structure of **8**

(Figure 53a).<sup>354</sup> The inverse structural motif of a Ga<sub>8</sub> cube inside a Ni<sub>6</sub> octahedron is found in the gallium-rich Ni<sub>3</sub>Ga<sub>7</sub> binary phase which adopts the body-centered cubic Ir<sub>3</sub>Ge<sub>7</sub> structure.<sup>355</sup> Its topology comprises two interpenetrating frameworks of edge-sharing "barrels", each being constructed from two condensed, centered square antiprisms. Herein, fusion of these barrels *via* the common edges of their terminal square faces creates a cubic Ga<sub>8</sub> junction unit which is surrounded by an octahedral arrangement of six Ni atoms (Figure 53b). In an alternative view, the structure of Ni<sub>3</sub>Ga<sub>7</sub> can be understood on the basis of interconnected Ga<sub>4</sub>Ni<sub>2</sub> and Ga<sub>8</sub>@Ni<sub>6</sub> clusters.

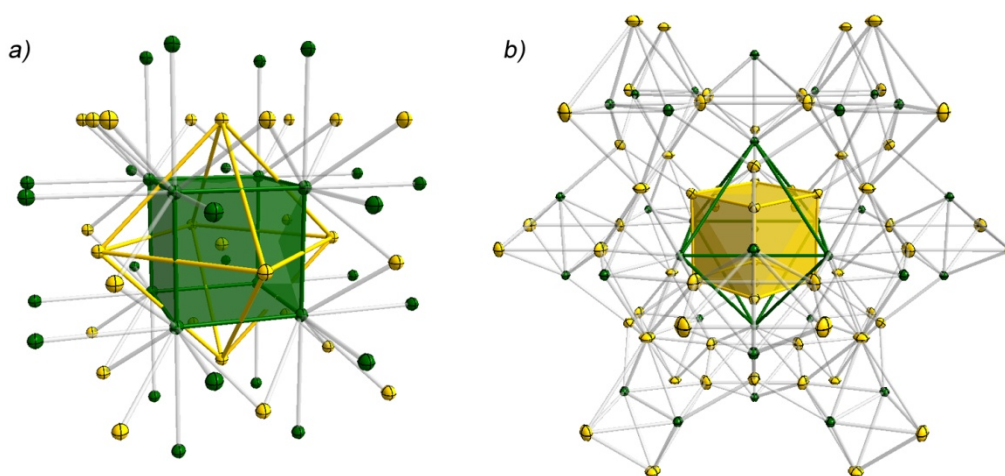


**Figure 53.** Crystal structures of the binary NiGa phases a)  $\beta$ -NiGa and b) Ni<sub>3</sub>Ga<sub>7</sub> (ICSD-reference no. 103854 and 408313) with Ni, Ga depicted in green, yellow. Both phases contain structural motifs comprising a cube inside an octahedron, albeit with different element distributions. The resulting M<sub>8</sub>M'<sub>6</sub> unit can be correlated to the conceivable cuboidal molecular structure of **8**.

#### 4.5.7 Theoretical investigations on the structure of [Ni<sub>8</sub>(GaCp\*)<sub>6</sub>] (**8**)

*The quantum chemical calculations presented in the following paragraph were performed by M.Sc. Julius Hornung, Chair of Inorganic and Metal-Organic Chemistry, TUM, and are part of his PhD studies.*

In an attempt to elucidate the molecular structure of **8**, DFT calculations were performed using the simplified model compound [Ni<sub>8</sub>(GaMe)<sub>6</sub>] (**8'**). In this context, replacement of sterically demanding ligands by methyl groups is an established procedure to minimize computational costs, and was reported to provide reasonably good approximations of the respective parent systems.<sup>356</sup> Starting from a cubic structure, geometry optimization of **8'** was performed at the BP86-D3/TZVPP level, whereat the result was confirmed as a local minimum by frequency calculations. The thus derived molecular structure is depicted in figure 54. It features a star-shaped Ni<sub>8</sub> kernel which is constructed from two almost ideal,

intersecting Ni<sub>4</sub> tetrahedra with Ni-Ni distances (av. 2.447 Å) that are close to the interatomic distances in bulk Ni (2.49 Å),<sup>357</sup> but noticeably shorter than those of Ni clusters of comparable sizes, such as [Ni<sub>8</sub>(μ<sub>4</sub>-PPh)<sub>6</sub>(CO)<sub>8</sub>] (2.65 Å)<sup>353</sup> or [Ni<sub>8</sub>(μ<sub>4</sub>-PPh)<sub>6</sub>(PPh<sub>3</sub>)<sub>8</sub>] (2.53 Å).<sup>358</sup> This is attributed to their distinctly less compact cubic core geometries, and more suitable reference systems are found amongst the, albeit smaller, deltahedral complexes [Ni<sub>4</sub>(CO)<sub>6</sub>L<sub>4</sub>] (L = GaCp\*, PMe<sub>3</sub>) with average Ni-Ni distances of 2.58 and 2.492 Å, respectively.<sup>244, 359</sup> Interestingly, the octahedral arrangement of the GaMe ligands remains largely unperturbed upon reconstruction of the central Ni<sub>8</sub> motif throughout the proceeding geometry optimization, and only slight bending of the methyl groups is observed. The resulting Ni-Ga distances (av. 2.436 Å) are significantly elongated in comparison to [Ni(GaCp\*)<sub>4</sub>] (2.2188(5) Å),<sup>245</sup> but in the same range as those of the bridging GaCp\* ligands in [Ni<sub>4</sub>(GaCp\*)<sub>4</sub>(CO)<sub>6</sub>] (av. 2.455(1) Å).<sup>244</sup>

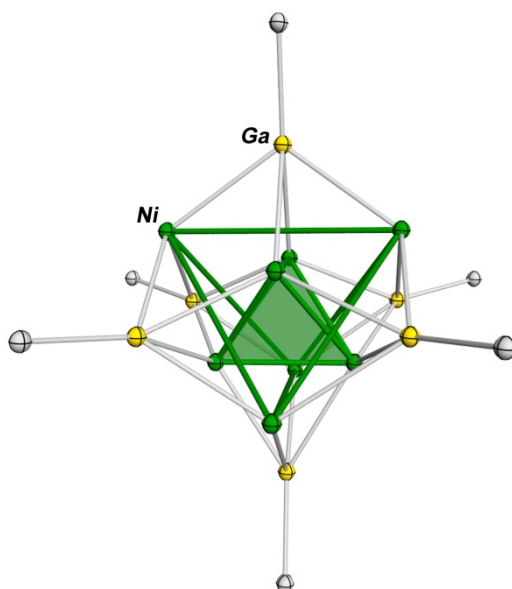


**Figure 54.** Optimized molecular structure of [Ni<sub>8</sub>(GaMe)<sub>6</sub>] (**8'**) as obtained from geometry optimization at the BP86-D3/TZVPP level of theory. The result was confirmed as a local minimum by frequency calculations. The intermetallic core is governed by the star-shaped Ni<sub>8</sub> stella quadrangula which is embedded into the octahedrally arranged shell of six GaCp\* ligands.

Comparison with the molecular structure of **8** reveals that the long Ga-Ga distances (av. 4.093 Å) of the outer Ga<sub>6</sub> octahedron of **8'** are in a comparable range as those of compound **8** (av. 4.210 Å), thus providing a first resemblance to the experimentally determined parent structure. Likewise, the dimensions of the highly disordered Ni kernel of **8** are large enough to host different orientations of the structure-optimized Ni<sub>8</sub> stella quadrangula. Here, the Ni-Ni distances of the outer Ni<sub>4</sub> tetrahedron of **8'** amount to an average of 4.064 Å, whereas the largest, diagonal Ni-Ni spacings in **8** range from 4.115(3) to

4.307(4) Å. However, these are mere indications and a reliable correlation of the optimized and experimentally determined structures is not possible on the basis of the available data. Although nickel pairings featuring the calculated short direct Ni-Ni distances of av. 2.447 Å are indeed found in the highly disordered skeleton of the experimental structure, coherent deltahedral (sub-)structures could not be identified. Likewise, attempts at a refinement of the compiled X-ray diffraction data based on the pre-modelled Ni<sub>8</sub> central unit, and the software assisted search for potential disorder sites remained inconclusive, thus making **8** a structural chameleon which evades structure elucidation.

#### 4.5.8 Concluding remarks

The reaction of the mixed-metal precursor [Ni(cdt)(GaCp\*)] (**7**) to form the intermetalloid NiGa cluster [Ni<sub>8</sub>(GaCp\*)<sub>6</sub>] (**8**) *via* mild thermal treatment in the presence of an excess of GaCp\* gives a first glimpse at the potential of pre-assembled TM-E complexes bearing residual labile co-ligands, e.g. hydrocarbons, for the synthesis of larger, metalloid TM<sub>x</sub>E<sub>y</sub> assemblies. In contrast to prior experiments at our chair involving the protolytic or oxidative cleavage of Cp\*H from TM-coordinated GaCp\* ligands, this approach preserves the integrity of the GaCp\* ligand and creates unsaturated Ni centers *via* removal of the labile cdt ligand for subsequent cluster assembly. While the thus synthesized [Ni<sub>8</sub>(GaCp\*)<sub>6</sub>] features a core-shell-type structure comprising a naked Ni<sub>8</sub> core exclusively stabilized by GaCp\* ligands, the well-documented tendency of ECp\*-ligands to undergo Cp\* transfer reactions to coordinatively unsaturated early transition metal centers might even allow for the formation of Hume-Rothery type clusters with truly mixed, intermetallic core geometries featuring the incorporation of naked group 13 metal atoms.

Notably, the unusually disordered molecular structure of [Ni<sub>8</sub>(GaCp\*)<sub>6</sub>] (**8**) could not be fully elucidated by means of single crystal X-ray diffraction studies and theoretical investigations, and the geometry of the central Ni<sub>8</sub> core remains equivocal. In an admittedly hypothetical scenario, this could potentially be attributed to an inhomogeneous distribution of slightly variable molecular constitutions throughout the crystalline material of **8** which would defy established structure characterization techniques. Irrespective of the validity of this hypothesis, the elaborate characterization of **8** clearly pinpoints upcoming challenges arising upon approaching the intermetalloid cluster size regime. Not only does the low solubility of **8** hamper its characterization by "classical" wet-chemical methods commonly employed in organometallic chemistry, additional unprecedented phenomena like the observed partial disorder demand for a revision of established routines and the exploitation of emergent new strategies, such as total X-ray scattering methods and pair distribution function analysis for the given example of a coherent structure elucidation of **8**.

## 4.6 Diverse Reactivity of ECp\* towards low-coordinate transition metal amides [TM(btsa)<sub>2</sub>] (TM = Mn, Fe, Co, Zn): Insertion, Cp\* transfer, and orthometalation

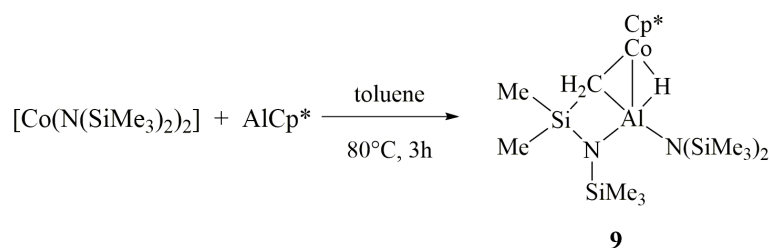
### 4.6.1 Introductory remarks

The application of small, heterometallic complexes with preformed metal-metal bonds as single-source precursors in the bottom-up preparation of intermetallic compounds and materials is widespread among the disciplines, and has also been applied in the synthesis of Hume-Rothery type materials, e.g. in the metalorganic chemical vapor deposition (MOCVD) of  $\beta$ -CoGa or NiGa thin films,<sup>360-363</sup> or the fabrication of NiGa nanoparticles.<sup>273</sup> Along these lines, the synthesis of small TM/E complexes with pre-formed Hume-Rothery-type nuclei exclusively bearing readily cleavable ligands appears of interest for controlled cluster growth reactions *via* well established chemical triggers. The following chapter discusses the synthesis and characterization of a small library of novel, mixed-metal complexes [TM<sub>1</sub>E<sub>b</sub>(Cp\*)<sub>n</sub>(btsa)<sub>m</sub>] (TM = Fe, Co, Zn; E = Al, Ga; btsa = bis(trimethylsilyl)amido ligand), as well as first investigations of their follow-up chemistry. Although the reactivity of ECp\* in the presence of amide co-ligands is still insufficiently investigated, such compounds are assumed to be of interest for subsequent, selective ligand removal, and might provide new pathways to higher nuclearity clusters or mixed TM/E nanoparticles. The particular potential of btsa-stabilized precursors for such purposes has already been demonstrated with the synthesis of transition metal nanoparticles,<sup>364, 365</sup> e.g. Fe nanoparticles *via* hydrogenation of [Fe(btsa)<sub>2</sub>],<sup>365</sup> and, more recently, with the synthesis of a series of cobalt cluster compounds from [Co(btsa)<sub>2</sub>] upon cleavage of the btsa ligand by pinacolborane (also compare chapter 4.4).<sup>313</sup> Furthermore, the bulky btsa ligand is commonly employed for the stabilization of metalloid group 13 and 14 cluster compounds, including Schnöckel's most prominent [Al<sub>x</sub>R<sub>y</sub>]<sup>n-</sup>.<sup>5, 162</sup> The results presented herein are largely covered in the following reference.<sup>250</sup>

### 4.6.2 Synthesis and characterization of [Cp\*Co( $\mu$ -H)(Al( $\kappa^2$ -(CH<sub>2</sub>SiMe<sub>2</sub>)NSiMe<sub>3</sub>)(btsa))] (**9**)

The reaction of [Co(btsa)<sub>2</sub>] with one equivalent of AlCp\* in toluene at 80°C results in an immediate colour change from green to brown and progressive AlCp\* consumption, as evident from the decreasing amounts of undissolved AlCp\*. Standard work-up of the reaction mixture after 3h by removal of all volatiles *in vacuo* and re-crystallization of the crude product from cold *n*-hexane yields dark-red, orthorhombic crystals of **9** in high yields around 85% (Scheme 7). Compound **9** is well soluble in non-polar solvents, like *n*-hexane, toluene or

benzene, and forms stable solutions without any indication of composition for several days. Isolated crystals of **9** can be stored under an inert atmosphere at room temperature for several weeks, and even for months at  $-30^{\circ}\text{C}$ . The composition as  $[\text{Cp}^*\text{Co}(\mu\text{-H})(\text{Al}(\kappa^2\text{-(CH}_2\text{SiMe}_2)\text{NSiMe}_3)(\text{btsa}))]$  was experimentally derived from single crystal X-Ray diffraction studies, and confirmed for the bulk phase by means of NMR and IR spectroscopy, along with elemental analysis and AAS. Owing to its paramagnetic nature, additional magnetic measurements and EPR studies were performed.

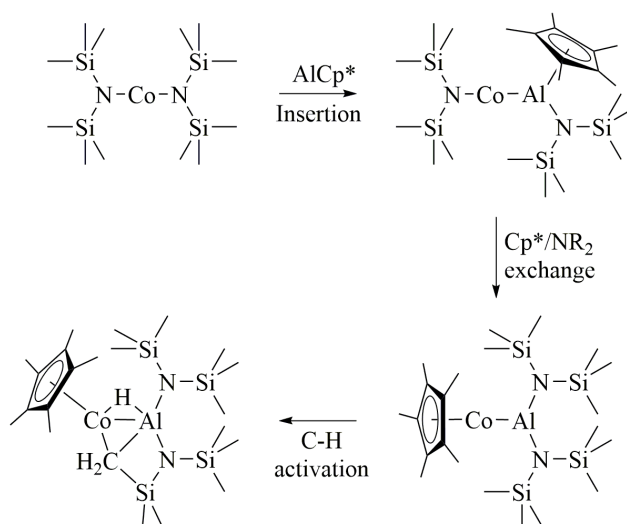


**Scheme 7.** Synthesis of  $[\text{Cp}^*\text{Co}(\mu\text{-H})(\text{Al}(\kappa^2\text{-(CH}_2\text{SiMe}_2)\text{NSiMe}_3)(\text{btsa}))]$  (**9**).

In accordance with the analytical data as discussed below, **9** features a complete ligand exchange between the two metal centers upon formation of the Co-Al bond, accompanied by the CH-activation of a methyl group at one btsa ligand. The resulting structural motif can be described as a [2.1.0] metallacycle with five different heteroatoms. A possible mechanistic pathway leading to this unusual structure is proposed in Scheme 8. It involves the insertion of one  $\text{AlCp}^*$  ligand into the polarized Co-amide bond, quite comparable to the mechanistic observations made for the reactivity of  $\text{ECp}^*$  ligands towards polarized TM-X bonds ( $\text{X} = \text{halide}$ ). For example,  $\text{GaCp}^*$  was found to insert into the Fe-Cl bond of iron(ii) chloride, and  $[\text{Cp}^*(\text{CO})_2\text{FeCl}]$ .<sup>249</sup> In both cases, subsequent ligand exchange and  $\sigma/\pi$ -rearrangement of the  $\text{Cp}^*$  ligand lead to the formation of  $[\text{Cp}^*(\text{Cp}^*\text{Ga})_2\text{FeGaCl}_2\cdot\text{THF}]$  and  $[\text{Cp}^*(\text{CO})_2\text{FeGa}(\eta^2\text{-Cp}^*)\text{Cl}]$ , respectively. Similarly, in the given case,  $\text{Cp}^*$  transfer from the Al center to the Co atom is mechanistically obvious, and accompanied by  $\text{N}(\text{SiMe}_3)_2$  transfer from the Co atom to the nitrogen-affine aluminium. Note that  $\text{Cp}^*$  transfer reactions are commonly observed in our group, particularly for reactions with metal complexes of the comparably lewis-acidic first row transition metals, and were reported to be relevant side reactions in numerous examples.<sup>319, 366</sup> Due to the absence of further stabilizing ligands, the thus generated, coordinatively unsaturated Co center facilitates the C-H activation of one methyl group, formally giving a Co(II) and an oxidized Al(III) center. A comparable orthometalation step occurs in the formation of  $[\text{FeCp}^*(\mu^3\text{-H})(\kappa\text{-(C}_6\text{H}_4)\text{PPh}_2)(\text{AlCp}^*)(\text{AlBr}_2)]$  from  $[\text{Fe}(\text{PPh}_3)_2\text{Br}_2]$  and  $\text{AlCp}^*$ .<sup>366</sup> Whether this C-H activation is to be considered the result of a synergetic effect stemming from the Co-Al bond, or occurs on one distinct metal site is



essentially speculative and remains open for discussion. One conceivable pathway, however, is the C-H bond activation at the coordinatively unsaturated cobalt center with subsequent migration of the activated fragments into Co-Al-bridging positions. A similar behaviour has been proposed for the C-H activation of benzene at the reactive, under-coordinated fragment  $[\text{Ni}(\text{AlCp}^*)_3]$  to give  $[(\text{AlCp}^*)_3\text{Ni}(\mu\text{-H})\text{AlCp}^*\text{Ph}]$ .<sup>367</sup> In addition, Co-mediated bond activation, e.g. at  $\text{CpCo}(\text{I})$  fragments, is a common phenomenon observed in the literature, for instance during the assembly of hydrocarbon-bridged  $[\text{Co}(\text{C}_5\text{R}_5)_n\text{L}_m]$  clusters.<sup>368, 369</sup>



**Scheme 8.** One possible mechanistic pathway leading to the formation of the unusual [2.1.0] metallacycle as observed in compound **9**. Insertion of  $\text{AlCp}^*$  into the polarized Co-N bond with subsequent ligand exchange between the metal centers formally creates a coordinatively unsaturated Co(I) center which stimulates C-H activation of one methyl group.

### Structural characterization of $[\text{Cp}^*\text{Co}(\mu\text{-H})(\text{Al}(\kappa^2\text{-(CH}_2\text{SiMe}_2)\text{NSiMe}_3)(\text{btsa}))]$ (**9**)

Suitable crystals for single crystal XRD studies are obtained from saturated *n*-hexane solutions of **9** within a few days. **9** crystallizes in the monoclinic space group  $P2_1/n$  with an asymmetric unit that comprises one single molecule. Its molecular structure features a central Co-Al bond which is formed between the disordered  $\text{CoCp}^*$  fragment and the almost perfectly trigonal planar-coordinated Al atom bearing two btsa ligands. Activation of the methyl group of one of these btsa ligands, and the orientation of the resulting methylene group in a Co-Al bridging position leads to the formation of an unusual heterometallic [2.1.0] metallacycle which consists of a distorted Al-N(2)-Si(4)-C(12) square and an almost symmetric Co-C(12)-Al triangle (Figure 55).



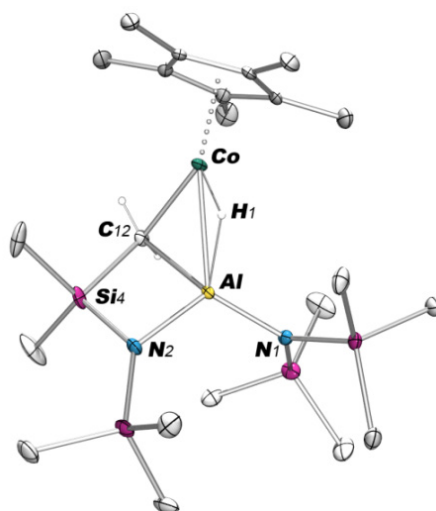


**Figure 55.** Molecular structure of  $[\text{Cp}^*\text{Co}(\mu\text{-H})(\text{Al}(\kappa^2\text{-(CH}_2\text{SiMe}_2\text{)NSiMe}_3\text{)(btsa))}]$  (**9**) in the solid state. Displacement ellipsoids are shown on the 20% probability level, hydrogen atoms and the disorder of the Cp\* ligand are omitted for clarity. Selected interatomic distances (Å) and angles (deg): Co-Al 2.402(2), Co-Cp\*<sub>centr</sub> 1.709 (1.689 for PART 2), Co-C(12) 2.095(2), Co-H(1) 1.566, Al-N(1) 1.818(4), Al-N(2) 1.827(4), Al-C(12) 2.149(2), Al-H(1) 1.705, Cp\*<sub>centr</sub>-Co-Al 162.6, Co-Al-N(1) 120.4(2), Co-Al-N(2) 120.6(2), N(1)-Al-N(2) 119.1(2). Reprinted with permission from J. Weßing, C. Göbel, B. Weber, C. Gemel, R. A. Fischer, *Inorg. Chem.* **2017**, 56 (6), 3517-3525. Copyright 2017 American Chemical Society.

The observed Co-Al bond distance of 2.402(2) Å is longer than comparable bonds found in  $[(\mu\text{-AlCp}^*)_2\text{Co}_2(\text{CO})_6]$  (av. 2.377 Å)<sup>370</sup> or  $[(\mu\text{-AlEt})_2(\text{Co}(\text{ethylene})\text{Cp}^*_2)]$  (av. 2.335 Å),<sup>371</sup> which might be a result of the unusual overall structure and the thus induced ring strain on the atoms of the central fused heterocycles. Likewise, it is significantly shorter than the sum of the *van der Waals* radii (Co 2.0; Al 2.1 Å)<sup>372</sup> and below the interatomic distances found in intermetallic CoAl phases, such as Co<sub>2</sub>Al<sub>5</sub> (2.43 Å) or Co<sub>2</sub>Al<sub>9</sub> (2.47 Å).<sup>373</sup> The formal assignment of the oxidation state +II for the Co center is derived from the overall ligand sphere of the complex and the apparent oxidation of Al(I) to Al(III). It is supported by the length of the Co-Cp\*<sub>centr</sub> distance of 1.709 Å (1.689 Å for the second disorder site) which is almost identical to the Co-Cp\*<sub>centr</sub> distance of CoCp\*<sub>2</sub> (1.714 Å),<sup>374</sup> and elongated with regard to trivalent cobaltocenium salts [CoCp\*<sub>2</sub>][X] (e.g. 1.623 Å for X = PF<sub>6</sub><sup>-</sup>).<sup>375</sup> Note, that additional evidence for the formal oxidation state Co(II) is provided by magnetic measurements. The coordination geometry of the Al atom is best described as trigonal planar (angular sum of 359.9°) under negligence of the additionally coordinated hydride and the methylene group. These are formed by the C-H activation, or orthometalation, of one btsa ligand and are found in Cu-Al bridging positions. The thus formed Co-C(12)-Al triangle is almost symmetrical with Co-C(12) and Al-C(12) bond lengths of 2.095(2) Å and 2.149(2) Å, respectively, displaying typical values for M-C bonds. The additionally spanned Al-N(2)-Si(4)-C(12) square is strongly distorted and adopts angles ranging from 80.02(2) to 98.51(2)°,

and edge lengths between 1.723(2) Å and 2.149(2) Å. Owing to the overall good quality of the crystallographic data, the hydride could be located on the Fourier density map and was allowed to refine freely. The Co-H distance is 1.566 Å; the Al-H distance of 1.705 Å is slightly elongated.

#### Spectroscopic characterization of [Cp\*Co( $\mu$ -H)(Al( $\kappa^2$ -(CH<sub>2</sub>SiMe<sub>2</sub>)NSiMe<sub>3</sub>)(btsa))] (**9**)

In accordance with the assumed d<sup>7</sup> configuration of the Co center, compound **9** displays paramagnetic behaviour in NMR studies with regards to large paramagnetic shifts of the NMR signals and significant broadening of signals which are close to the paramagnetic cobalt atom. Consequently, NMR spectra were recorded with wide spectral ranges and short delay times to ensure a sufficiently high resolution of all signals. The <sup>1</sup>H NMR spectrum of **9** shows three clearly resolved signals at 1.15, 0.46 and -0.55 ppm which correspond to the chemically non-equivalent protons of the asymmetric btsa ligands. Owing to the short delay times employed during the acquisition of the spectrum, a reliable quantitative integration of the signals is rendered impossible, as small delay times decrease the pulse repetition time and, with this, prohibit a full relaxation of non- or less paramagnetically influenced, excited nuclear spins. An additional broad, underlying signal is observed at 81.01 ppm, most likely resulting from the Co-bound Cp\* moiety, as indicated by the significant paramagnetic shift. Despite all efforts, no signal corresponding to the hydride could be observed. The paramagnetic, non-proton decoupled <sup>13</sup>C NMR spectrum displays several overlapping signals in the range of 4.30 to 9.58 ppm. Keeping in mind the strong paramagnetic influence observed for the <sup>1</sup>H NMR signals attributed to the Cp\* unit, these are likely to arise from the methyl groups of the btsa ligands. Attempts to resolve additional signals in spectral ranges from -150 to 500 ppm remained unsuccessful.

FT-IR spectroscopic analysis of neat **9** reveals the characteristic vibrational modes that are usually observed for Cp\* ligands: the  $\nu_{C-H}$  modes at 2924, 2882 and 2835 cm<sup>-1</sup>, and the  $\nu_{C-C}$  and  $\nu_{C-Me}$  vibrations at 1423, 1386, and 1368 cm<sup>-1</sup>.<sup>165</sup> Additional intense contributions arise from the presence of the btsa ligands, such as the  $\nu_{Si-C}$  and  $\nu_{Si-N-Si}$  absorptions at 667 and 613 cm<sup>-1</sup>, and 918 cm<sup>-1</sup>, respectively.<sup>376, 377</sup> While no signal attributing to the hydride could be observed in the <sup>1</sup>H NMR spectrum, its presence is unambiguously clear from the IR spectrum which shows a broad signal at 1632 cm<sup>-1</sup>. This is in good agreement with the location of the hydride in a Co-Al bridging position as derived from the molecular structure, as bridging M-H-M vibrational modes were reported to undergo signal broadening and a shift to lower frequencies with regard to the corresponding terminal M-H vibrations.<sup>323</sup> Literature values for the distinct signals of terminal Co-H and Al-H modes are usually reported in a range of 2000 to 1900 cm<sup>-1</sup>,<sup>323, 378</sup> and 1890 to 1750 cm<sup>-1</sup>,<sup>165, 311</sup> respectively.

Temperature-dependent susceptibility measurements of **9** between 50 and 300 K reveal Marie-Curie paramagnetism of the sample with the  $\chi_M^{-1}$  over T plot meeting the Curie-Weiss law for paramagnetic compounds. The Curie constant was determined to be  $0.58 \text{ cm}^3 \text{ K mol}^{-1}$ , the Weiss temperature to be  $-12.87 \text{ K}$ . At ambient temperature, the effective magnetic moment of 2.1 is slightly higher than the expected 1.7 for a low spin Co(II) center which is attributed to potential additional contributions originating from the Co-Al bond, like temperature-independent Van Vleck paramagnetism.<sup>379-382</sup> Notably, signs of decomposition were observed for temperatures above 250 K.

The average g-factor of **9** amounts to 2.06, and was determined based on EPR measurements of frozen toluene solutions of **7** at 133.15 K. Notably, the herein observed hyperfine coupling of the EPR signal could not be rationalized by simulation.

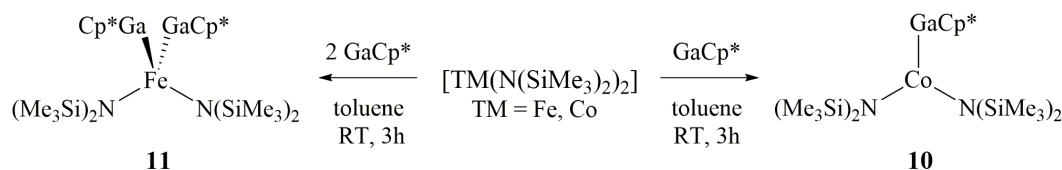
#### 4.6.3 Synthesis and characterization of $[(\text{Cp}^*\text{Ga})\text{Co}(\text{btsa})_2]$ (**10**) and $[(\text{Cp}^*\text{Ga})_2\text{Fe}(\text{btsa})_2]$ (**11**)

Motivated by the interesting reactivity of  $\text{AlCp}^*$  towards  $[\text{Co}(\text{btsa})_2]$  and the availability of a whole range of bis(trimethylsilyl)amide-stabilized first row transition metal complexes, the scope of reactions was extended to include the readily available  $[\text{TM}(\text{btsa})_2]$  with  $\text{TM} = \text{Mn}, \text{Fe}, \text{Co},$  and  $\text{Zn}$ , and their behaviour upon exposure to  $\text{ECp}^*$  ( $\text{E} = \text{Al}, \text{Ga}$ ) was systematically investigated. Interestingly, and in contrast to the formation of **9**, the strictly analogous reaction of  $[\text{Fe}(\text{btsa})_2]$  with  $\text{AlCp}^*$  does not result in Fe-Al bond formation, but instead furnishes the literature-known compounds  $\text{FeCp}^*_2$ <sup>383, 384</sup> and  $[\text{Al}_4\text{Cp}^*_3(\text{btsa})]$ ,<sup>385</sup> as identified by means of single-crystal X-ray diffraction analysis and NMR spectroscopy. Likewise, the reaction of  $[\text{Mn}(\text{btsa})_2]$  with  $\text{ECp}^*$  proceeds *via*  $\text{Cp}^*$  transfer to give  $\text{MnCp}^*_2$ .<sup>383</sup> In all cases, initial insertion of  $\text{ECp}^*$  into the TM-N bond with subsequent transfer of the  $\text{Cp}^*$  ligand to the transition metal, quite similar to the assumed mechanism for the formation of **9**, appears likely. However, and irrespective of the employed stoichiometries, eventual full ligand exchange to give  $\text{TMCP}^*_2$  occurs, presumably because of the higher Lewis acidity of manganese and iron with regards to the later transition metal cobalt.

An entirely different reaction behaviour is observed in the analogous reactions of  $[\text{TM}(\text{btsa})_2]$  ( $\text{TM} = \text{Fe}, \text{Co}$ ) with  $\text{GaCp}^*$  in toluene (Scheme 9). Both reactions proceed already at room temperature as indicated by the immediate colour change of the reaction mixture. This is attributed to  $\text{GaCp}^*$  being monomeric in solution, whereas  $\text{AlCp}^*$  forms  $[\text{AlCp}^*]_4$  tetramers whose dissociation enthalpy usually needs to be compensated by slightly elevated reaction temperatures.<sup>386</sup> Removal of all volatiles under reduced pressure afforded the crude products  $[(\text{Cp}^*\text{Ga})\text{Co}(\text{btsa})_2]$  (**10**) and  $[(\text{Cp}^*\text{Ga})_2\text{Fe}(\text{btsa})_2]$  (**11**) as wax-like green

(TM = Co) or yellow-brown (TM = Fe) solids, respectively. The latter can be further purified by re-crystallization as brown blocks from saturated *n*-hexane solutions.

Owing to its overall chemical lability, crude **10** can be stored under an inert atmosphere at  $-30^{\circ}\text{C}$  for a couple of days only, whereas **11** can be stored under argon a room temperature without any signs of decompositions for a couple of months. Both compounds are well soluble in non-polar solvents, like *n*-hexane, toluene or benzene.



**Scheme 9.** Synthesis of  $[(\text{Cp}^*\text{Ga})\text{Co}(\text{btsa})_2]$  (**10**) and  $[(\text{Cp}^*\text{Ga})_2\text{Fe}(\text{btsa})_2]$  (**11**). In contrast to  $\text{AlCp}^*$ ,  $\text{GaCp}^*$  does not insert into the polarized TM-N bond but forms 1:1 and 2:1 adducts, instead.

In the following, **10** and **11** will be discussed in a joint subchapter due to their overall similarity. Both compounds illustrate nicely the striking difference between the reactivities of  $\text{GaCp}^*$  versus  $\text{AlCp}^*$  towards TM amides. While  $\text{AlCp}^*$  was found to insert into the TM-amide bond of  $[\text{Co}(\text{btsa})_2]$ , thus triggering a complex cascade of ligand re-arrangement and orthometalation steps,  $\text{GaCp}^*$  shows no such behaviour but instead forms simple adducts with  $[\text{Co}(\text{btsa})_2]$  and  $[\text{Fe}(\text{btsa})_2]$ , and retains its formal oxidation state +I. A possible explanation for the completely different reaction behaviour might be the lower nitrogen affinity of gallium in comparison to aluminium as a consequence of its higher electronegativity, or its higher ability to stabilize the monovalent oxidation state more effectively. In general, the tendency of  $[\text{TM}(\text{btsa})_2]$  to form of adducts of the general formula  $[\text{TM}(\text{btsa})_m(\text{L})_n]$  in the presence of lewis basic,  $\sigma$ -donating ligands is well documented, and examples like  $[\text{Co}(\text{btsa})_2(\text{PPh}_3)]$ ,  $[\text{TM}(\text{btsa})_2(\text{thf})_n]$  ( $n = 2$  for Mn,  $n = 1$  for Fe), and  $[\text{TM}(\text{btsa})_2(\text{py})_n]$  ( $\text{py} = \text{pyridine}$ ;  $n = 2$  for Mn,  $n = 1$  for Fe, Co) have been reported.<sup>314, 387-389</sup>

### Structural characterization of $[(\text{Cp}^*\text{Ga})\text{Co}(\text{btsa})_2]$ (**10**) and $[(\text{Cp}^*\text{Ga})_2\text{Fe}(\text{btsa})_2]$ (**11**)

Single crystal X-ray diffraction measurements were performed on crystals of **10** and **11** which were grown from saturated *n*-hexane solutions. While **10** crystallizes in the monoclinic space group  $P2_1/c$  with two independent molecules per asymmetric unit cell, **11** exhibits an orthorhombic unit cell with the space group  $Pbcn$  in the solid state. As discussed above, both molecules represent simple 1:1 and 2:1  $\text{GaCp}^*$  adducts of the starting reagent  $[\text{TM}(\text{btsa})_2]$ . Their respective molecular structures are depicted in figure 56.

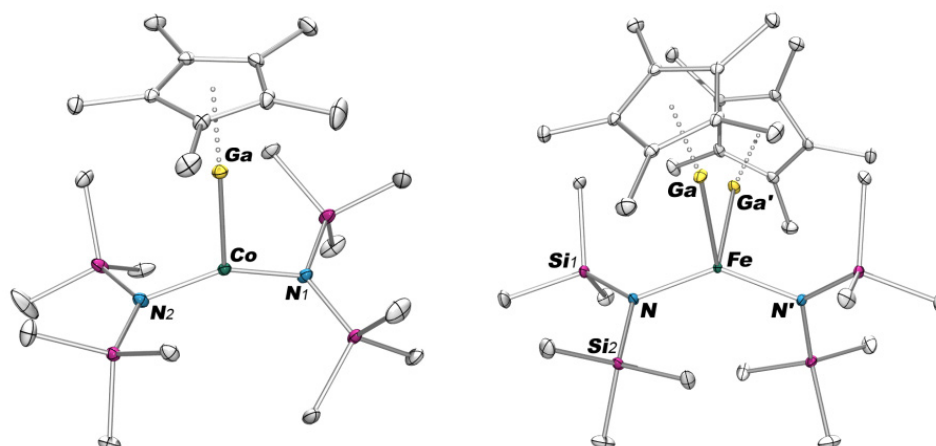


**Figure 56.** Molecular structures of  $[\text{Cp}^*\text{GaCo}(\text{btsa})_2]$  (**10**) (left, one independent molecule of the asymmetric unit) and  $[(\text{Cp}^*\text{Ga})_2\text{Fe}(\text{btsa})_2]$  (**11**) (right) in the solid state. Displacement ellipsoids are shown on the 20% probability level, hydrogen atoms are omitted for clarity. Selected interatomic distances (Å) and angles (deg) of **10**: Co(1)-Ga(1) 2.533(2), Ga(1)-Cp\*<sub>centr</sub> 1.939, Co(1)-N(1) 1.887(5), Co(1)-N(2) 1.894(2), N-Si av. 1.720, Cp\*<sub>centr</sub>-Ga(1)-Co(1) 175.0, Ga(1)-Co(1)-N(1) 109.3(2), Ga(1)-Co(1)-N(2) 104.5(2), N(1)-Co(1)-N(2) 146.1(2). Selected interatomic distances (Å) and angles (deg) of **11**: Fe-Ga 2.599(1), Ga-Cp\*<sub>centr</sub> 1.979, Fe-N 1.956(3), N-Si(1) 1.716(3), N-Si(2) 1.720(3), Cp\*<sub>centr</sub>-Ga-Fe 170.7, Ga-Fe-Ga' 94.3(2), Ga-Fe-N 96.4(2), N-Fe-N' 140.9(3). Reprinted with permission from J. Weßing, C. Göbel, B. Weber, C. Gemel, R. A. Fischer, *Inorg. Chem.* **2017**, 56 (6), 3517-3525. Copyright 2017 American Chemical Society.

The molecular structures of **10** and **11** in the solid state are dominated by the strong  $\pi$ -donating properties of the btsa ligands, prompting the significant distortion of both structures from an ideal trigonal planar (for **10**) or tetrahedral (for **11**) coordination geometry around the central metal atom. For **10**, the resulting coordination sphere of Co is probably best described as a planar three-coordinate geometry featuring significant distortion toward a T-shape with a wide N-Co-N' angle of 146.1(2)°. Similar effects were reported for other three-coordinated bisamido complexes of the  $d^5$  to  $d^7$  transition metals, such as the closely related  $[\text{Co}(\text{btsa})_2(\text{L})]$  (L = PPh<sub>3</sub>, pyridine) with N-Co-N' angles of 130.7(7) and 140.7(2)°, respectively.<sup>314, 387</sup> In the case of **11**, the large N-Fe-N' angle of 140.9(3)° results in an unusually small Ga-Fe-Ga' angle of 94.3(2)°, only. The significant electron donation from the btsa ligands is further shown by the obvious  $sp^2$  hybridization of the amides featuring almost perfectly planar coordination environments of the N atoms with triangular sums close to the ideal 360°. The TM-Ga bond distances are notably elongated, which indicates a relatively weak dative bonding in both cases. In detail, the long Co-Ga distance of **10** amounts to 2.533(2) Å, and the Fe-Ga bond length of **11** is 2.599(1) Å. Comparable literature values for the albeit rare Co-Ga bonds range between 2.297 Å in  $[\text{Cp}^*\text{Co}(\text{GaCp}^*)_3][\text{BAR}_4^{\text{F}}]_2$ <sup>319</sup> and

2.389 Å in  $[(\text{CO})_3\text{Co}(\mu\text{-GaCp}^*)_2\text{Co}(\text{CO})_3]$ ,<sup>244</sup> whereas reported Fe-Ga bond distances for terminal GaCp\* motifs, e.g. in  $[(\text{CO})_4\text{Fe}(\text{GaCp}^*)]$ ,<sup>244</sup>  $[\text{Cp}^*\text{Fe}(\text{GaCp}^*)_3][\text{BAr}_4^{\text{F}}]$ ,<sup>319</sup> or  $[\text{Cp}^*(\text{GaCp}^*)_2\text{Fe}(\text{GaCl}_2)\cdot\text{THF}]$ ,<sup>249</sup> vary from 2.273 to 2.314 Å.

### Spectroscopic characterization of $[(\text{Cp}^*\text{Ga})\text{Co}(\text{btsa})_2]$ (**10**) and $[(\text{Cp}^*\text{Ga})_2\text{Fe}(\text{btsa})_2]$ (**11**)

The <sup>1</sup>H NMR spectra of **10** and **11** show essentially identical patterns, that is two paramagnetically shifted singlets corresponding to the methyl groups of the Cp\*, and the btsa ligands, respectively. For **10** these are found at 16.86 and -11.29 ppm, whereat the former is ascribed to the Cp\* ligand, and the latter to the btsa ligand. The equivalent signals for **11** are observed at 45.74 and 0.38 ppm. It is of note that both, compounds **10** and **11**, show paramagnetic behaviour in NMR spectroscopic studies, which is in accordance with the d<sup>7</sup> configuration of the central Co(II) atom of **10** and the assumed high spin d<sup>6</sup> configuration of Fe(II) in **11**. However, the influence of the paramagnetic centers is not as pronounced as for **9**, owing to the larger distance of the NMR active groups of the ligands. Consequently, the efficient pulse delay times employed for the acquisition of NMR data of **10** and **11** are longer, which allows for a full relaxation of all nuclear spins, and thus a quantitative evaluation of the obtained spectra. The integration of the spectra supports the signal assignment as discussed above.

<sup>13</sup>C NMR spectroscopic measurements of **10** give rise to one slightly broadened signal of the Cp\* ligand's methyl groups at 32.62 ppm, and a sharp signal at 2.66 ppm which attributes to the btsa ligand. Similarly, the non-proton-decoupled <sup>13</sup>C NMR spectrum of **11** shows only two signals at 245.28 and 5.52 ppm, corresponding to the Cp\* and btsa ligand, respectively. In both cases, the missing second signal of the Cp\* ligand could not be resolved in spectral ranges from 500 to -150 ppm, even though a very broad, underlying signal was observed at 85.45 ppm for **11**.

IR spectra recorded for neat **10** and **11** show the characteristic vibrational modes of the Cp\* ligand, along with the intense absorptions of the btsa ligands. For **10**, the  $\nu_{\text{C-H}}$ ,  $\nu_{\text{C-C}}$ , and  $\nu_{\text{C-Me}}$  vibrations of the Cp\* unit are found at 2950, 2896 and 2857 cm<sup>-1</sup> ( $\nu_{\text{C-H}}$ ), and 1423, 1386 and 1368 cm<sup>-1</sup> ( $\nu_{\text{C-C/C-Me}}$ ), respectively. The  $\nu_{\text{Si-C}}$  and  $\nu_{\text{Si-N-Si}}$  vibrations are observed at 667 and 618 cm<sup>-1</sup>, and 999 cm<sup>-1</sup>. For **11**, the same set of signals with only small deviations of the absolute frequencies is found ( $\nu_{\text{C-H}}$  at 2920, 2889, 2839 cm<sup>-1</sup>;  $\nu_{\text{C-C/C-Me}}$  at 1469, 1409, 1375 cm<sup>-1</sup>;  $\nu_{\text{Si-C}}$  at 663, 608 cm<sup>-1</sup>;  $\nu_{\text{Si-N-Si}}$  at 958 cm<sup>-1</sup>).

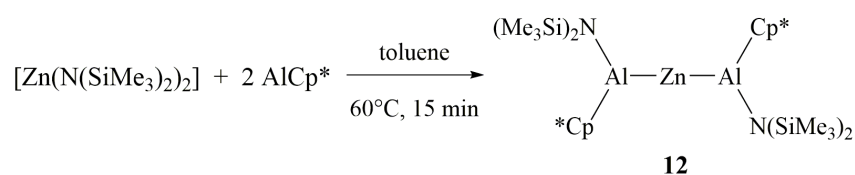
Additionally, the magnetic properties of **11** were investigated in temperature-dependent susceptibility measurements between 50 and 300 K. The experimentally determined  $\mu_{\text{eff}}$  of 4.5 is conceivably lower than the expected value for a high spin Fe(II) center (calc. 4.9). Based on



the linear correlation observed in the  $\chi_M^{-1}$  over T plot, the Curie constant was determined to  $2.75 \text{ cm}^3 \text{ K mol}^{-1}$ . The low Weiss temperature of  $-27.36 \text{ K}$ , in combination with the earlier mentioned low  $\mu_{\text{eff}}$ , indicate weak antiferromagnetic coupling between the metal centers. EPR spectroscopic measurements on frozen toluene solutions of **11** remained inconclusive.

#### 4.6.4 Synthesis and characterization of $[(\text{Zn}(\text{Al}(\eta^2\text{-Cp}^*)(\text{btsa}))_2)]$ (**12**)

Moving towards the far right side of the transition metal block, the reaction of  $[\text{Zn}(\text{btsa})_2]$  with two equivalents of  $\text{AlCp}^*$  proceeds rapidly at  $60^\circ\text{C}$  in toluene, giving  $[(\text{Zn}(\text{Al}(\eta^2\text{-Cp}^*)(\text{btsa}))_2)]$  (**12**) (Scheme 10). Contrary to **9**, **12** features the insertion of  $\text{AlCp}^*$  into the Zn-N bond without any subsequent ligand rearrangement steps. Instead, the generated low-valent zinc center is stabilized by the formation of unsupported Zn-Al bonds only, and the low coordination number of two is retained. Consequently,  $\text{AlCp}^*$  does not only serve as a reducing agent upon bond insertion, but also acts as a sufficient stabilizing ligand for the formal Zn(0) center itself. In this regards, the generated steric bulk of the  $\text{Al}(\eta^2\text{-Cp}^*)(\text{btsa})$  fragment is certainly beneficial for the stabilization of **12**.



**Scheme 10.** Synthesis of  $[(\text{Zn}(\text{Al}(\eta^2\text{-Cp}^*)(\text{btsa}))_2)]$  (**12**). In contrast to **9**, no ligand rearrangement occurs after the insertion of  $\text{AlCp}^*$  into the TM-N bond.

Compound **12** is unstable under the reaction conditions employed, and undergoes decomposition shortly after its formation in the reaction mixture, as indicated by metal precipitation from the yellow solution. Unfortunately, the reaction does not proceed at temperatures below  $60^\circ\text{C}$ , most likely due to the low solubility of  $\text{AlCp}^*$  and its tendency to form tetramers in solution, whose dissociation energy needs to be overcome, e.g. by elevated reaction temperatures. Thus, decomposition cannot be fully avoided, and attempts to reduce the reaction time to a minimum and employ subsequent purification steps at low-temperatures showed only limited success for the isolation of pure **12**.

In order to avoid the elevated reaction temperature required for the formation of **12**,  $\text{AlCp}^*$  was replaced with the well soluble  $\text{Cp}^*\text{AlH}_2$  which was found to serve as a suitable precursor for the formation of  $\text{AlCp}^*$ -ligated TM complexes *via* redox-active pathways.<sup>390</sup> Surprisingly, in the reaction of  $[\text{Zn}(\text{btsa})_2]$  with two equivalents of  $\text{Cp}^*\text{AlH}_2$  no ZnAl complex was

obtained. Instead, the isolated product was identified as  $[\text{Zn}_2\text{Cp}^*_2]$  by single crystal X-ray diffraction studies and  $^1\text{H}$  NMR spectroscopy. In addition, the formation of  $[\text{H}_x\text{Al}(\text{btsa})_{3-x}]$  species was observed by *in situ* NMR spectroscopic analysis of the respective reaction mixtures. Apparently, the ancillary hydrides at  $\text{Cp}^*\text{AlH}_2$  prompt ligand exchange between the aluminium and zinc centers *via* mechanisms still to be elucidated, thus generating partially reduced Zn which is subsequently stabilized by Zn-Zn bond formation.

### Structural characterization of $[(\text{Zn}(\text{Al}(\eta^2\text{-Cp}^*)(\text{btsa}))_2)]$ (**12**)

X-ray quality crystals of **12** were grown from saturated *n*-hexane solutions at  $-30^\circ\text{C}$  within few days. **12** crystallizes in the monoclinic space group *P*-1, featuring a centrosymmetric molecular structure with two unsupported Zn-Al bonds in a perfectly linear Al-Zn-Al bonding motif (Figure 57). In fact, **12** is the first reported example of a molecular Zn/Al complex featuring an unsupported Zn-Al bond, although a handful of Zn-gallyl complexes with unsupported Zn-Ga bonds are known.<sup>391-393</sup> The Zn-Al bond of 2.448(2) Å is well below the sum of the respective *van der Waals* radii (Zn 1.39; Ga 1.87 Å)<sup>284, 372</sup> and distinctly shorter than the calculated values of intermetallic Zn-Al hydride model complexes which were found to vary between 2.60 and 2.79 Å.<sup>394</sup>

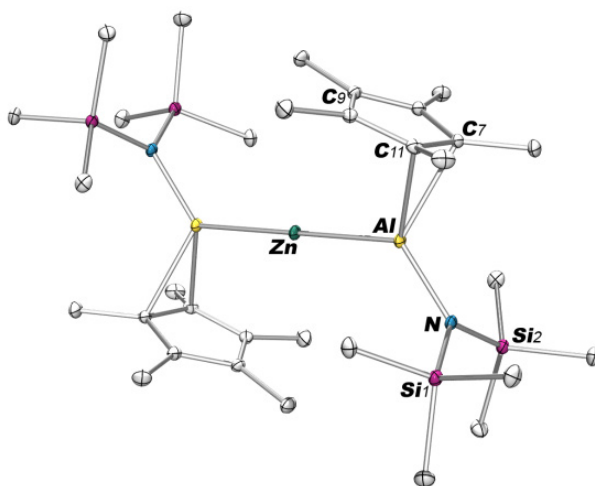


**Figure 57.** Molecular structure of  $[(\text{Zn}(\text{Al}(\eta^2\text{-Cp}^*)(\text{btsa}))_2)]$  (**12**) in the solid state. Displacement ellipsoids are shown on the 20% probability level, hydrogen atoms are omitted for clarity. Selected interatomic distances (Å) and angles (deg): Zn-Al 2.448(2), Al-C(7) 2.210(2), Al-C(11) 2.181(2), Al-N 1.850(5), N-Si  $\emptyset$  1.728, Zn-Al-C<sub>7/11</sub> 115.6, Zn-Al-N 127.6(2), C<sub>7/11</sub>-Al-N 116.7. Reprinted with permission from J. Weßing, C. Göbel, B. Weber, C. Gemel, R. A. Fischer, *Inorg. Chem.* **2017**, 56 (6), 3517-3525. Copyright 2017 American Chemical Society.



Resulting from the insertion of AlCp\* into the Zn-amide bond, the Al atoms exhibit a pseudo trigonal planar coordination geometry, bearing one  $\eta^2$ -coordinated Cp\* and one btsa ligand. The Zn-Al-N and Zn-Al-C<sub>7/11</sub> (C<sub>7/11</sub> = C7-C11 centroid) angles approach the optimum value of 120° and the angular sum adds up to 359.8°. The change in hapticity observed for the Cp\* ligand is probably a result of steric overcrowding, as additionally indicated by the Al-C and Al-N bonds (Al-C 2.181(2) and 2.210(2) Å; Al-N 1.850(5) Å) being slightly elongated with regards to comparable bond lengths in [Al(btsa)<sub>3</sub>] (Al-N 1.78 Å)<sup>395</sup> or [Fe(AlCp\*)<sub>5</sub>] (Al-C of the  $\eta^2$ -coordinated Cp\* 2.030(5) Å).<sup>396</sup> Notably, the observed tilting of the ligand towards the Zn center rather than away from the complex seems counter-intuitive, and might result from packing effects in the solid state. However, weak intramolecular interactions cannot be completely excluded given the comparably short Zn-C(9) distance of 3.051(1) Å, and the close proximity of the protons of the nearest methyl group (Zn-H 2.858(2) Å).

#### Spectroscopic characterization of [(Zn(Al( $\eta^2$ -Cp\*)(btsa))<sub>2</sub>)] (**12**)

Owing to its thermal instability in solution and the resulting difficulties in obtaining compound **10** in an analytically pure form, characterization of **12** is restricted to <sup>1</sup>H and <sup>29</sup>Si NMR, and IR spectroscopy. The <sup>1</sup>H NMR spectrum of **12** shows two singlets at 2.08 and 0.31 ppm which correspond to the fluctuating Cp\* ligand and the btsa ligand, respectively. Note that a splitting of the Cp\* signal as expected for the  $\eta^2$ -coordinated ligand was not observed, not even for spectra recorded at low temperatures down to -80°C. The <sup>29</sup>Si NMR spectrum gives rise to one sharp signal at -3.96 ppm. Further attempts to collect meaningful <sup>13</sup>C NMR spectroscopic data failed because of significant decomposition of **12** during the measurements.

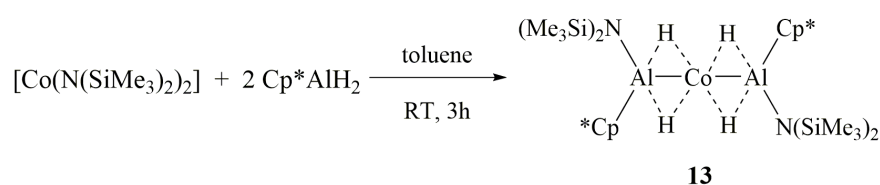
Complementary IR spectroscopic measurements of neat **12** confirm the presence of btsa and Cp\* ligands, and display distinctive signals corresponding to the symmetric  $\nu_{C-H}$  vibrations at 2946, 2901, and 2859 cm<sup>-1</sup>, along with a  $\nu_{C-C}$  band at 1419 cm<sup>-1</sup>. In addition, the strong  $\nu_{Si-C}$  and  $\nu_{Si-N-Si}$  vibrational modes are observed at 672 and 616, and 939 cm<sup>-1</sup>.

#### 4.6.5 Synthesis and characterization of [(Co( $\mu$ -H)<sub>4</sub>(Al( $\eta^2$ -Cp\*)(btsa))<sub>2</sub>)] (**13**)

Given its diverse reactivity towards [Co(btsa)<sub>2</sub>] and [Zn(btsa)<sub>2</sub>] in the syntheses of **9** and **12**, the tendency of AlCp\* to undergo Cp\* transfer reactions appears to be largely dependent on the nature of the transition metal center, particularly its Lewis acidity and its ability to stabilize unsaturated coordination spheres. This is further supported by the formation of [TMCp\*<sub>2</sub>] as the only isolable product in the reactions of [Mn(btsa)<sub>2</sub>] and [Fe(btsa)<sub>2</sub>] with AlCp\*, irrespective of the stoichiometric ratio employed.

Thus inspired, attempts at an inhibition of Cp\* transfer reactions by artificially increasing the electron density at the transition metal center were made by reacting the trivalent [Cp\*AlH<sub>2</sub>] with [TM(bt<sub>2</sub>sa)<sub>2</sub>] (TM = Fe, Co). Here, the assumedly preferred transfer of the agile hydride co-ligands rather than the bulky Cp\* group was expected to effectively lower the electron affinity of the respective transition metal center, consequently preventing undesirable subsequent ligand re-arrangements. It is of note, that the integrity of hydride ligands in the presence of reactive ECp\* fragments had already been demonstrated by a series of ECp\*-ligated ruthenium polyhydride complexes, like [Ru(cod)(H)(GaCp\*)<sub>3</sub>][BAR<sub>4</sub><sup>F</sup>], [Cp\*Ru(μ-H)(H)(μ-ECp\*)]<sub>2</sub> or [(Cp\*Ru)<sub>3</sub>(μ-H)<sub>5</sub>(μ<sub>3</sub>-ECp\*)].<sup>397</sup>

While the reaction of [Cp\*AlH<sub>2</sub>] with [Fe(bt<sub>2</sub>sa)<sub>2</sub>] proceeds unchanged to give the ligand exchange product [FeCp\*<sub>2</sub>], the reaction of [Co(bt<sub>2</sub>sa)<sub>2</sub>] with two equivalents of [Cp\*AlH<sub>2</sub>] in toluene at room temperature yields the pure insertion product [(Co(μ-H)<sub>4</sub>(Al(η<sup>2</sup>-Cp\*)(bt<sub>2</sub>sa))<sub>2</sub>)] (**13**, Scheme 11) featuring formal insertion of an AlCp\* fragment into the Co-amide bond. Compound **13** crystallizes immediately from the reaction mixture and is obtained in its analytically pure form following standard work-up procedures. It is scarcely soluble in common organic solvents, like benzene or toluene, and decomposes under hydrogen evolution in THF. The isolated compound is air- and moisture sensitive, but can be stored under an inert atmosphere for weeks without signs of decomposition.



**Scheme 11.** Synthesis of [(Co(μ-H)<sub>4</sub>(Al(η<sup>2</sup>-Cp\*)(bt<sub>2</sub>sa))<sub>2</sub>)] (**13**). In contrast to the formation of **9**, no Cp\* transfer occurs after the formal insertion of an AlCp\* fragment into the Co-N bond. Instead, the additionally introduced hydrides appear to sufficiently stabilize the low-valent Co center.

### Structural characterization of [(Co(μ-H)<sub>4</sub>(Al(η<sup>2</sup>-Cp\*)(bt<sub>2</sub>sa))<sub>2</sub>)] (**13**)

Compound **13** crystallizes in the triclinic space group *P*-1 with one molecule per unit cell. Its molecular structure (Figure 58) is essentially isostructural to the molecular structure of **12** with a Co-Al bond distance of 2.386(1) Å that is slightly shorter than the Co-Al bond in **9** (2.402(2) Å), and elongated with regards to [(μ-AlCp\*)<sub>2</sub>Co<sub>2</sub>(CO)<sub>6</sub>] (av. 2.377 Å)<sup>370</sup> or [(μ-AlEt)<sub>2</sub>(Co(ethylene)Cp\*<sub>2</sub>)] (av. 2.335 Å).<sup>371</sup> The pseudo trigonal planar coordination geometry of the Al atoms features angles close to the optimum values of 120° with Al-N and Al-C distances in the expected ranges. Selected interatomic distances and angles are given below.

In contrast to the molecular structure of **12**, complex **13** bears four hydrides which could be located on the Fourier density map and were allowed to refine freely. These are found in  $\mu_2$ -bridging positions above the Co-Al bonds, formally creating Co(II) and Al(III) centers. Considering the, albeit still underdeveloped, bonding modes of multiply bridged heterobimetallic hydride complexes which formally distinguish between true metal-metal adducts, oxidative addition products and M-H-M  $\sigma$ -complexes, compound **13** can be clearly categorized as the former on the basis of the reasonably short Co-Al interatomic distance indicating substantial metal-metal interactions.<sup>398</sup> This is further supported by the Al-H distance of av. 1.758 Å which is distinctly shorter than expected values > 2.0 Å for the hypothetical oxidative addition product featuring hydride transfer to the cobalt center. The Co-H distance averages to 1.510 Å.

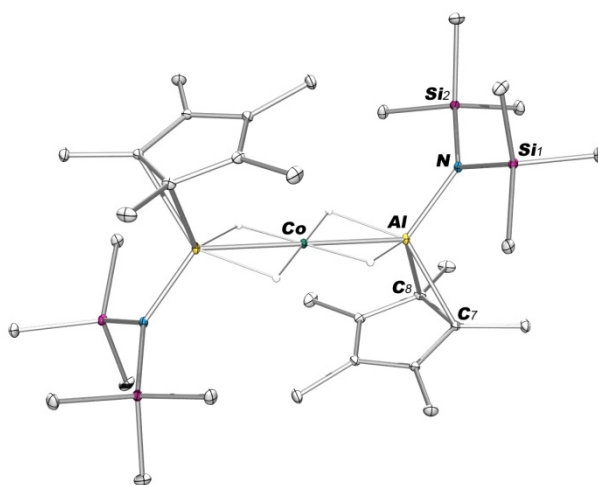


**Figure 58.** Molecular structure of  $[(\text{Co}(\mu\text{-H})_4(\text{Al}(\eta^2\text{-Cp}^*)(\text{btsa}))_2)]$  (**13**) in the solid state. Displacement ellipsoids are shown on the 20% probability level, hydrogen atoms are omitted for clarity. Selected interatomic distances (Å) and angles (deg): Co-Al 2.386(1), Al-C  $\bar{\text{O}}$  2.167, Al-N 1.833(1), Co-H av. 1.510, Al-H  $\bar{\text{O}}$  1.758, Co-Al-C<sub>7/8</sub> 123.3, Co-Al-N 120.5(2), C<sub>7/8</sub>-Al-N 116.2. Reprinted with permission from J. Weßing, C. Göbel, B. Weber, C. Gemel, R. A. Fischer, *Inorg. Chem.* **2017**, 56 (6), 3517-3525. Copyright 2017 American Chemical Society.

### Spectroscopic characterization of $[(\text{Co}(\mu\text{-H})_4(\text{Al}(\eta^2\text{-Cp}^*)(\text{btsa}))_2)]$ (**13**)

Compound **13** was characterized by means of NMR spectroscopy, IR spectroscopy, elemental analysis and AAS. In addition, the magnetic properties of **13** were assessed in temperature-dependent magnetic susceptibility measurements.

Owing to its low solubility in conventional deuterated solvents, like benzene- $d_6$ , toluene- $d_8$  or acetonitrile- $d_3$ , and its decomposition in chlorinated NMR solvents like  $\text{CDCl}_3$  or  $\text{CD}_2\text{Cl}_2$ , characterization of compound **13** by NMR spectroscopy proved to be non-trivial and furnished inconclusive results. Following its dissolution in THF- $d_8$ , rapid  $\text{H}_2$  evolution

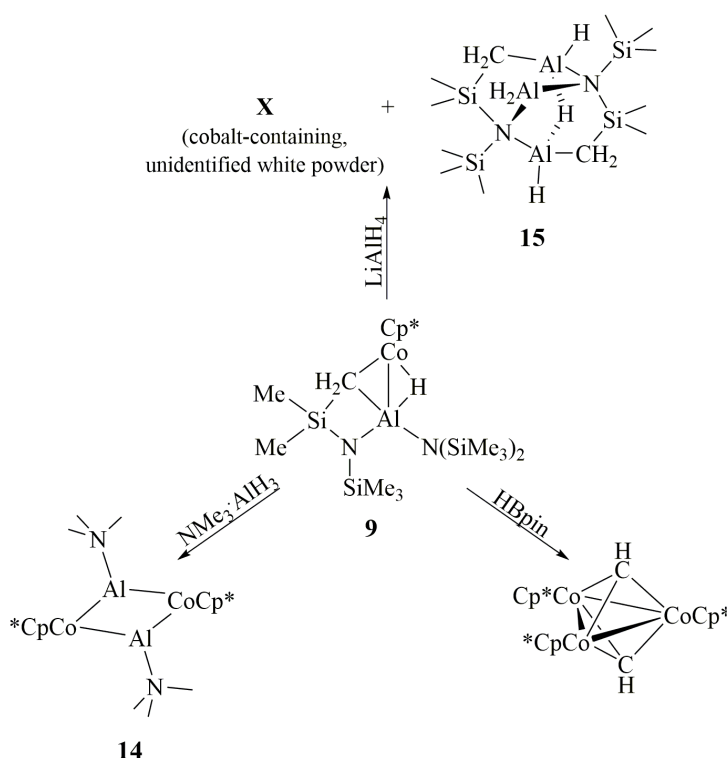
accompanied by a colour change from yellow to orange was observed, reproducibly and quantitatively yielding a yet non-identified diamagnetic species which gives rise to a distinct  $^1\text{H}$  NMR spectrum. The latter shows clearly distinguishable signals at 1.85 and 1.80 ppm, which are indicative of a  $\eta^1$ - or  $\eta^2$ -coordinated Cp\* ligand under the assumption of a third signal underlying the residual solvent peak. Additional signals are observed in the range from 0.40 to 0.04 ppm and might attribute to chemically non-equivalent protons of one or more btsa ligands. Keeping in mind the unusual formation mechanism of  $[\text{Cp}^*\text{Co}(\mu\text{-H})(\text{Al}(\kappa^2\text{-(CH}_2\text{SiMe}_2)\text{NSiMe}_3)(\text{btsa}))]$  (**9**) and the involved C-H activation of the btsa ligand to stabilize the interim, lowly coordinated cobalt center, a comparable bond activation reaction appears conceivable for **13** upon (partial) loss of its hydride ligands. Comparable results are obtained from  $^{13}\text{C}$  NMR spectroscopic analysis of **13** in THF- $d_8$  which reveals a set of signals corresponding to the inner carbons of an asymmetrically bound Cp\* ligand at 119.31, 90.38 and 89.96 ppm, along with signals stemming from the respective methyl groups at 13.10, 13.04 and 12.35 ppm. Additionally observed peaks in the range from 6.25 to 5.68 ppm are attributed to chemically non-equivalent aliphatic carbons of the btsa ligands.

Irrespective of the difficulties arising in the NMR spectroscopic characterization of **13**, its composition as  $[(\text{Co}(\mu\text{-H})_4(\text{Al}(\eta^2\text{-Cp}^*)(\text{btsa}))_2)]$  could be confirmed by elemental analysis and AAS, along with IR spectroscopic results. The latter provide clear evidence for the presence of both, btsa and Cp\* ligands, by revealing characteristic symmetric  $\nu_{\text{C-H}}$  and  $\nu_{\text{C-C}}$  vibrational modes of the Cp\* ligand at 2927, 2879, 2839 and 1430  $\text{cm}^{-1}$ , along with typical absorptions at 905, 667 and 613  $\text{cm}^{-1}$  corresponding to the  $\nu_{\text{Si-C}}$  and  $\nu_{\text{Si-N-Si}}$  vibrations of the btsa ligands. An additional broad  $\nu_{\text{M-H}}$  band is observed at 1672  $\text{cm}^{-1}$  which is in good agreement with the  $\mu_2$ -bridging positions of the hydrides as concluded from single crystal X-ray diffraction analysis.

The magnetic properties of **13** were determined by temperature-dependent susceptibility measurements in a temperature range from 50 to 300 K whereat paramagnetic behaviour deviating from classical Marie-Curie paramagnetism was observed. Within this context, the nonlinear correlation of the  $\chi_{\text{M}}^{-1}$  over T curve precludes a reliable determination of the Curie constant or the Weiss temperature. The effective magnetic moment  $\mu_{\text{eff}}$  was determined to 2.7 at ambient temperature, and differs significantly from the expected values for a Co(II) center. For comparison,  $\mu_{\text{eff}}$  was calculated to 1.7 for a low spin, and 3.9 for a high spin Co(II) complex, respectively. Instead, the experimentally obtained value is in good agreement with the calculated value for Co(I) (2.82). This, along with an evident colour change of the sample during the measurement, indicated the reduction of the compound, most likely by liberation of hydrogen.

#### 4.6.6 Preliminary reactivity studies - attempts at the initiation of cluster growth by selective ligand abstraction

Following up on the initially proposed perspective of initiating cluster growth by selective ligand removal, the reactivity of the herein presented TM/E complexes  $[\text{TM}_1\text{E}_b(\text{Cp}^*)_n(\text{btsa})_m]$ , particularly of  $[\text{Cp}^*\text{Co}(\mu\text{-H})(\text{Al}(\kappa^2\text{-(CH}_2\text{SiMe}_2)\text{NSiMe}_3)(\text{btsa}))]$  (**9**), towards hydride-bearing reducing agents, like  $\text{LiAlH}_4$ ,  $[\text{NMe}_3 \rightarrow \text{AlH}_3]$  or pinacolborane (HBpin), was investigated (Scheme 12). The latter was recently shown to undergo metathesis-type reactions with btsa-ligated TM complexes, in which replacement of the amide by a small hydride ligand furnishes coordinatively unsaturated TM hydride intermediates which tend to undergo assembly processes, in parts accompanied by the reductive elimination of  $\text{H}_2$ . For instance, treatment of  $[\text{Cp}^*\text{Fe}(\text{btsa})]$  with half an equivalent of HBpin was found to yield the dinuclear  $[\text{Cp}_2^*\text{Fe}_2(\mu\text{-H})(\mu\text{-N}(\text{SiMe}_3)_2)]$  which is anticipated to form *via* the reaction of *in situ* generated "Cp\*FeH" and remaining starting material.<sup>399</sup> Quite comparably, the reaction of  $[\text{Co}(\text{btsa})_2]$  with HBpin in the absence or presence of tris(isopropyl)phosphine gives the tetranuclear, amide-bridged  $[\text{Co}_4(\text{btsa})_4]$  or the hexanuclear cobalt-hydride cluster  $[\text{Co}_6(\text{P}^i\text{Pr}_3)_6\text{H}_8]$ , respectively.<sup>313</sup>



**Scheme 12.** Reactivity of  $[\text{Cp}^*\text{Co}(\mu\text{-H})(\text{Al}(\kappa^2\text{-(CH}_2\text{SiMe}_2)\text{NSiMe}_3)(\text{btsa}))]$  (**9**) towards hydride bearing reducing agents. In all cases, cleavage of the supported Co-Al bond of **9** occurs, furnishing coordinatively unsaturated  $[\text{Cp}^*\text{Co}]$  and  $[(\text{btsa})\text{Al}]$  fragments which undergo further reaction.

Reaction of  $[\text{Cp}^*\text{Co}(\mu\text{-H})(\text{Al}(\kappa^2\text{-(CH}_2\text{SiMe}_2)\text{NSiMe}_3)(\text{btsa}))]$  (**9**) with HBpin

Treatment of  $[\text{Cp}^*\text{Co}(\mu\text{-H})(\text{Al}(\kappa^2\text{-(CH}_2\text{SiMe}_2)\text{NSiMe}_3)(\text{btsa}))]$  (**9**) with two equivalents of HBpin results in the formation of the literature-known  $[(\text{Cp}^*\text{Co})_3(\mu\text{-CH})_2]$ ,<sup>322</sup> which was identified by single crystal X-ray diffraction analysis,  $^1\text{H}$  and  $^{13}\text{C}$  NMR spectroscopy, and IR spectroscopy. Here, the exchange of the sterically demanding btsa by the small hydride ligand appears to evoke ligand-redistribution within the molecule which eventually destabilizes the formerly supported Co-Al bond. It is assumed that the thus induced cleavage of the metal-metal bond furnishes low-coordinate  $[\text{Cp}^*\text{Co}]$  and  $[(\text{btsa})\text{Al}]$  species, whereat the former is stabilized by subsequent formation of the trinuclear cobalt cluster  $[(\text{Cp}^*\text{Co})_3(\mu\text{-CH})_2]$ . Note that evidence for the selective replacement of the btsa ligand with H<sup>-</sup> is provided by *in situ*  $^1\text{H}$  NMR spectra of the reaction mixture giving rise to gradually increasing, characteristic signals of (btsa)Bpin at 1.03 and 0.37 ppm. Furthermore, the involvement of chemically distinct hydride intermediates is indicated by correspondent signals around -16 ppm.

Reaction of  $[\text{Cp}^*\text{Co}(\mu\text{-H})(\text{Al}(\kappa^2\text{-(CH}_2\text{SiMe}_2)\text{NSiMe}_3)(\text{btsa}))]$  (**9**) with  $[\text{NMe}_3\text{-AlH}_3]$ 

Interestingly, quite similar mechanisms appear to take effect in the reactions of  $[\text{Cp}^*\text{Co}(\mu\text{-H})(\text{Al}(\kappa^2\text{-(CH}_2\text{SiMe}_2)\text{NSiMe}_3)(\text{btsa}))]$  (**9**) with  $\text{LiAlH}_4$  and  $[\text{NMe}_3\text{-AlH}_3]$ , respectively. In both cases, hydride transfer is anticipated to evoke Co-Al bond cleavage *via* mechanisms still to be elucidated, thus creating reactive (btsa)Al and  $\text{Cp}^*\text{Co}$  fragments *in situ*. In the presence of  $[\text{NMe}_3\text{-AlH}_3]$ , the latter is trapped as the hydride-rich  $[(\text{Cp}^*\text{Co})_2(\mu\text{-AlNMe}_3)_2\text{H}_4]$  (**14**) which can be isolated as a red, microcrystalline powder in moderate yields, and has been preliminary characterized by single crystal X-ray diffraction studies,  $^1\text{H}$  and  $^{13}\text{C}$  NMR spectroscopy, IR spectroscopy and elemental analysis. Note that its sensitive chemical nature precludes a characterization by LIFDI-MS.

The molecular structure of **14** comprises a flat-angle  $\text{Co}_2\text{Al}_2$  butterfly geometry, with each cobalt atom bearing an additional  $\text{Cp}^*$  group, and each aluminium atom being coordinated by one trimethylamine ligand (Figure 59). The Co-Al distances (av. 2.414 Å) are in a similar range as those in **9** (2.402(2) Å) or **13** (2.386(1) Å), but visibly elongated with regards to the structurally closely related  $[(\mu\text{-AlCp}^*)_2\text{Co}_2(\text{CO})_6]$  (av. 2.377 Å)<sup>370</sup> and  $[(\mu\text{-AlEt})_2(\text{Co}(\text{ethylene})\text{Cp}^*_2)]$  (av. 2.335 Å).<sup>371</sup> The Al-Al distance of 2.784(2) Å is well below the sum of the *van der Waals* radii (Al 1.84 Å),<sup>284</sup> thus indicating direct intermetallic interactions, like in  $[(\mu\text{-AlEt})_2(\text{Co}(\text{ethylene})\text{Cp}^*_2)]$  ( $d_{\text{Al-Al}}$  2.663(3) Å). Notably, the unusual angles of the  $\text{Cp}^*$  and trimethylamine ligands which are tilted towards opposite sides of the central  $\text{Co}_2\text{Al}_2$  motif indicate the presence of additional hydride ligands. These could not be located on the Fourier density map due to large termination effects causing significant residual electron densities around the metal atoms. However, based on the coordination geometries around the cobalt and aluminium centers, respectively, the presence of four

additional hydrides in terminal positions is suggested. This is in good agreement with electron counting procedures, and matches the experimental data of  $^1\text{H}$  NMR and IR spectroscopy. Assuming four additional hydride ligands, the observed cve count meets the expected 62 cve ( $2\cdot 9 + 2\cdot 13 + 2\cdot 5 + 2\cdot 2 + 4\cdot 1$ ) of a butterfly geometry.

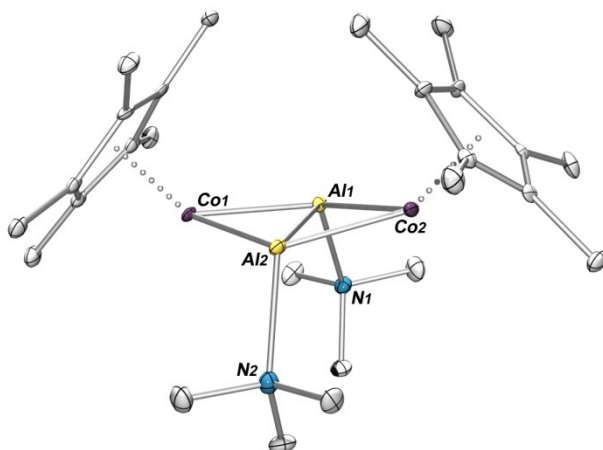


**Figure 59.** Preliminary molecular structure of  $[(\text{Cp}^*\text{Co})_2(\mu\text{-AlNMe}_3)_2\text{H}_4]$  (**14**) in the solid state with Co, Al, N, C depicted in violet, yellow, blue and grey, respectively. Displacement ellipsoids are shown on the 30% probability level, hydrogen atoms are omitted for clarity. Selected interatomic distances (Å) and angles (deg): Co(1)-Al(1) 2.403(2), Co(1)-Al(2) 2.421(2), Co(2)-Al(1) 2.417(2), Co(2)-Al(2) 2.416(2), Al(1)-Al(2) 2.784(3), Al(1)-N(1) 2.160(6), Al(2)-N(2) 2.142(6), Co-Cp\*<sub>centr.</sub> av. 1.705, N-C av. 1.480, Co(1)-Al(1)-Co(2) 108.8(1), Co(1)-Al(2)-Co(2) 108.3(2), Al(1)-Co(1)-Al(2) 70.5(1), Al(1)-Co(2)-Al(2) 70.3(2), N(1)-Al(1)-Al(2) 125.9(2), N(2)-Al(2)-Al(1) 125.0(2), Cp\*<sub>centr.</sub>-Co(1)-Al<sub>1/2centr.</sub> 143.5, Cp\*<sub>centr.</sub>-Co(2)-Al<sub>1/2centr.</sub> 143.9, Co(1)-Al<sub>1/2centr.</sub>-Co(2) 167.5.

The  $^1\text{H}$  NMR spectrum of **14** gives rise to two overlapping singlets at 2.08 and 2.07 ppm, resembling the Cp\* and NMe<sub>3</sub> ligands, respectively. An additional signal at -19.97 ppm corresponds to the hydride ligands, with the integral ratio matching the proposed amount of four hydrides.  $^{13}\text{C}$  NMR spectroscopic measurements reveal the expected set of signals for Cp\* ligands at 88.86 and 11.95 ppm, along with the methyl carbons of the amine group at 47.70 ppm. In agreement with the conclusions drawn from its molecular structure, IR spectroscopic data of **14** show characteristic metal-hydride stretches at 1910 and 1716  $\text{cm}^{-1}$ , whereat wave number and shape indicate terminal M-H rather than bridging M-H-M bonding modes, and match literature-reported values of Co-hydride and Al-hydride complexes. For comparison, terminal Co-H stretches are usually reported between 1970 and 1880  $\text{cm}^{-1}$ ,<sup>323</sup> while Al-H vibrational modes are found at slightly lower values ranging from 1700 to 1800  $\text{cm}^{-1}$ .<sup>165, 309, 310</sup>



Reaction of  $[\text{Cp}^*\text{Co}(\mu\text{-H})(\text{Al}(\kappa^2\text{-(CH}_2\text{SiMe}_2)\text{NSiMe}_3)(\text{btsa}))]$  (**9**) with  $\text{LiAlH}_4$ 

In line with the experimental findings for the reactions of  $[\text{Cp}^*\text{Co}(\mu\text{-H})(\text{Al}(\kappa^2\text{-(CH}_2\text{SiMe}_2)\text{NSiMe}_3)(\text{btsa}))]$  (**9**) with HBpin and  $[\text{NMe}_3\text{AlH}_3]$ , respectively, treatment of **7** with  $\text{LiAlH}_4$  results in cleavage of the Co-Al bond under formation of a yet to be identified off-white powder and the byproduct  $[\text{Al}_3\text{H}_4(\mu\text{-H})(\kappa^2\text{-(CH}_2\text{SiMe}_2)\text{NSiMe}_3)_2]$  (**15**). In this context, the obtained powder is anticipated to be a cobalt complex of low nuclearity, as indicated by the absence of intense coloration. Its IR spectroscopic analysis reveals the presence of Cp\* and btsa moieties, as well as metal hydrides; the latter being concluded from a broad absorption around  $1683\text{ cm}^{-1}$ . This is further supported by the  $^1\text{H}$  NMR spectrum giving rise to two singlets at 1.77 and 0.04 ppm with an integral ratio of 15:18, along with a broad singlet of low intensity at -21.97 ppm. While the peak at 1.77 ppm is attributed to a cobalt-bound Cp\* unit, the low-field signal at 0.04 ppm is assigned to the methyl groups of a btsa ligand. The corresponding  $^{13}\text{C}$  NMR spectrum shows three signals resembling the  $\text{sp}^2$ - and  $\text{sp}^3$ -hybridized carbon atoms of the Cp\* ligand and the chemically equivalent btsa carbons at 83.35, 8.12 and 2.42 ppm, respectively. Accordingly, conceivable reaction products include hydride-bearing mononuclear complexes, like  $[\text{Cp}^*\text{Co}(\text{btsa})\text{H}_x]$ , whereat  $^1\text{H}$  NMR spectroscopic results suggest that  $x = 2$ . Note that the related iron complex  $[\text{Cp}^*\text{Fe}(\text{btsa})]^{400}$  is indeed literature-known.

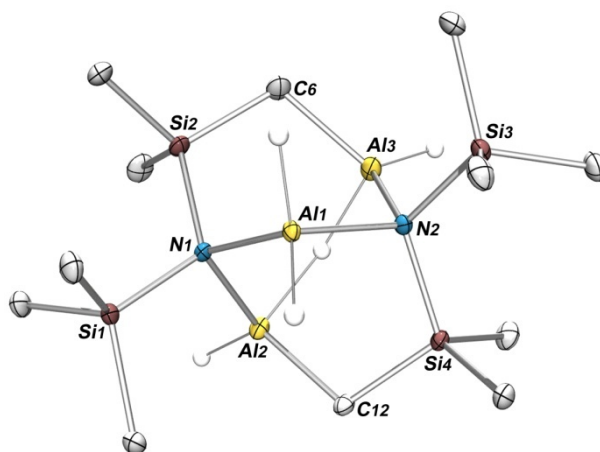


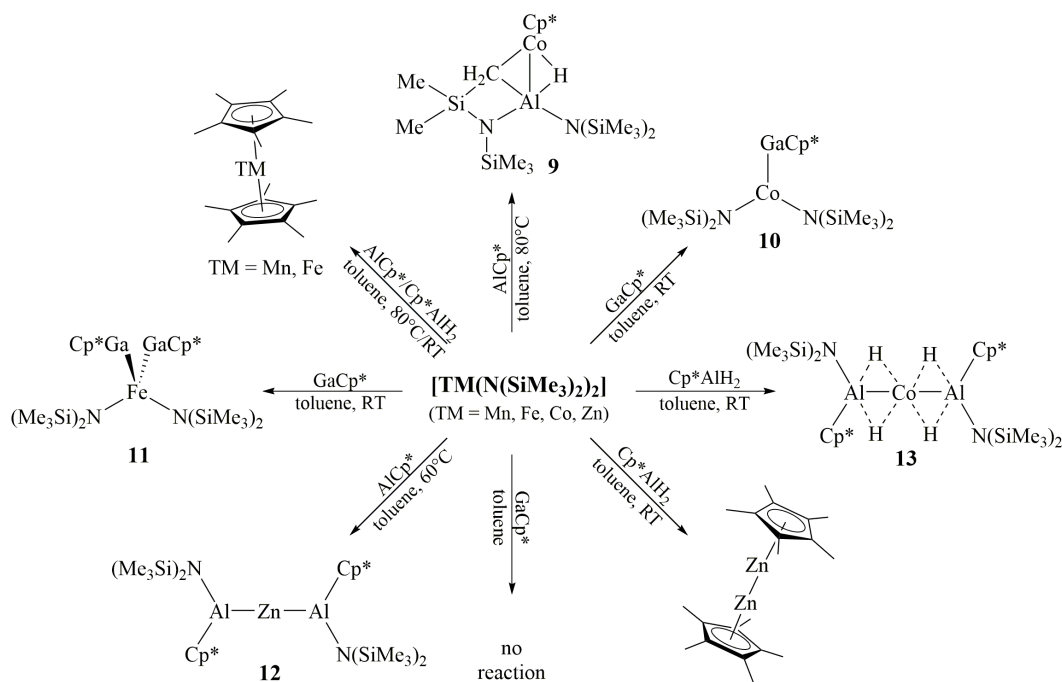
**Figure 60.** Molecular structure of  $[\text{Al}_3\text{H}_4(\mu\text{-H})(\kappa^2\text{-(CH}_2\text{SiMe}_2)\text{NSiMe}_3)_2]$  (**15**) in the solid state with Al, N, Si, C, H depicted in yellow, blue, violet, grey and white, respectively. Displacement ellipsoids are shown on the 30% probability level, hydrogen atoms except the hydride ligands are omitted for clarity. These could be located on the Fourier density map and were allowed to refine freely. Selected interatomic distances (Å) and angles (deg): Al(1)-N(1) 1.957(2), Al(1)-N(2) 1.977(1), Al(2)-N(1) 1.944(2), Al(3)-N(2) 1.942(2), Al-C av. 1.956, Al-H<sub>term.</sub> av. 1.47, Al(2)-H(3) 1.78(2), Al(3)-H(3) 1.69(2), N-Si<sub>term.</sub> av. 1.808, N-Si<sub>bdg.</sub> 1.829, Si(2)-C(6) 1.848(3), Si(4)-C(12) 1.850(2), N(1)-Al(1)-N(2) 107.1(1), H(1)-Al(1)-H(2) 114.9(2), Al(1)-N(1)-Al(2) 103.5(1), Al(1)-N(2)-Al(3) 104.3(1), N(1)-Al(2)-C(12) 104.3(1), H(3)-Al(2)-H(4) 107.2(2), N(2)-Al(3)-C(6) 109.9(1), H(3)-Al(3)-H(5) 106.5(2), Si(1)-N(1)-Si(2) 115.7(1), Si(3)-N(2)-Si(4) 115.8(1).



Small amounts of the side product  $[\text{Al}_3\text{H}_4(\mu\text{-H})(\kappa^2\text{-(CH}_2\text{SiMe}_2\text{)NSiMe}_3)_2]$  (**15**) crystallize from the combined, and concentrated hexane filtrates at  $-30^\circ\text{C}$  after several days. Although a bulk characterization of the compound was not possible due to the low amount of isolated material, its molecular structure as determined by single-crystal X-ray diffraction analysis serves as a proof-of-principle for the dismounting of **7** and cleavage of the inherent Co-Al bond. Compound **15** crystallizes in the monoclinic space group  $P2(1)$  with one molecule per unit cell. Its molecular structure contains three independent aluminium centers which are connected *via* two C-H activated btsa and one  $\mu_2$ -bridging hydride ligand, formally creating a [3.3.1.1<sup>2,6</sup>] metalla-tricycle (Figure 60). Herein, each aluminium atom is coordinated to both btsa ligands with Al(1) being bound *via* the amide nitrogen atoms, and Al(2) and Al(3) being coordinated by one nitrogen center and one methylene group, respectively. The distorted tetrahedral coordination sphere of all aluminium atoms is completed by two additional hydride ligands each, one of which adopts a  $\mu_2$ -bridging position between Al(2) and Al(3). The Al-N distances range from 1.942(2) to 1.977(1) Å, and are significantly longer than those of the starting material **7** (av. 1.823 Å) or  $[\text{Al}(\text{btsa})_3]$  (1.78(2) Å),<sup>395</sup> but comparable to those of other annular alane oligomers, like the dimethylaminoalanes  $[\text{H}_{3-x}\text{Al}(\text{NMe}_2)_x]_n$ .<sup>309</sup> The Al-C distances (av. 1.956 Å) and Al-H distances of terminal (av. 1.47 Å) and bridging hydrides (1.69(2) and 1.78(2) Å) are in the expected ranges.<sup>311, 401, 402</sup>

#### 4.6.7 Concluding remarks

By systematically probing the reactivity of  $\text{ECp}^*$  towards lowly coordinated first row transition metal complexes  $[\text{TM}(\text{btsa})_2]$ , a small library of heterometallic TM/E complexes of the general formula  $[\text{TM}_1\text{E}_b(\text{Cp}^*)_n(\text{btsa})_m]$  was obtained whereat substantially different reactivity patterns were revealed for  $\text{E} = \text{Al}, \text{Ga}$  respectively (Scheme 13). While  $\text{GaCp}^*$  was found to preferably undergo simple adduct formation,  $\text{AlCp}^*$  inserts into the TM-amide bond, in certain cases followed by complex cascades of ligand re-arrangement steps, i.e.  $\text{Cp}^*$  transfer reactions. Accordingly, the reactions of  $[\text{TM}(\text{btsa})_2]$  ( $\text{TM} = \text{Fe}, \text{Co}$ ) with  $\text{GaCp}^*$  furnish the 1:2 and 1:1 adducts  $[(\text{GaCp}^*)_2\text{Fe}(\text{btsa})_2]$  (**11**) and  $[(\text{GaCp}^*)\text{Co}(\text{btsa})_2]$  (**10**), respectively, whereas the analogous reactions with  $\text{AlCp}^*$  give  $\text{FeCp}^*_2$  and the unusual bicyclic CoAl complex  $[\text{Cp}^*\text{Co}(\mu\text{-H})(\text{Al}(\kappa^2\text{-(CH}_2\text{SiMe}_2\text{)NSiMe}_3)(\text{btsa}))]$  (**9**). As indicated by the formation of the pure insertion product  $[\text{Zn}(\text{Al}(\eta^2\text{-Cp}^*)(\text{btsa}))_2]$  (**12**) from  $[\text{Zn}(\text{btsa})_2]$ , the tendency of  $\text{AlCp}^*$  to undergo further  $\text{Cp}^*$  transfer reactions upon insertion into the TM-N bond appears to be largely dependent on the nature of the TM center, e.g. its Lewis acidity and ability to stabilize low coordination numbers. In the reaction of  $[\text{Co}(\text{btsa})_2]$  with  $[\text{Cp}^*\text{AlH}_2]$ , the presence of the anionic hydride ligands appears to inhibit further ligand re-arrangements, thus facilitating formal insertion of an  $\text{AlCp}^*$  unit into the Co-N bond to give  $[\text{Co}(\mu\text{-H})_4(\text{Al}(\eta^2\text{-Cp}^*)(\text{btsa}))_2]$  (**13**).



Scheme 13. Reactivity of  $\text{ECp}^*$  ( $\text{E} = \text{Al, Ga}$ ) towards  $[\text{TM}(\text{btsa})_2]$  ( $\text{TM} = \text{Mn, Fe, Co, Zn}$ ).

First experiments aiming at the initiation of cluster growth reactions by selective abstraction of the btsa ligand in the presence of hydride donating agents were performed on  $[\text{Cp}^*\text{Co}(\mu\text{-H})(\text{Al}(\kappa^2\text{-(CH}_2\text{SiMe}_2)\text{NSiMe}_3)(\text{btsa}))]$  (**9**) which was exposed to HBpin,  $[\text{NMe}_3\text{AlH}_3]$  and  $\text{LiAlH}_4$ , respectively. In all cases, hydride transfer to **9** evokes cleavage of the apparently labile Co-Al bond to form reactive  $[\text{Cp}^*\text{Co}]$  and  $[(\text{btsa})\text{Al}]$  fragments which undergo subsequent assembly processes to form low-nuclearity cluster compounds like  $[(\text{Cp}^*\text{Co})_3(\mu\text{-CH})_2]$ ,  $[(\text{Cp}^*\text{Co})_2(\mu\text{-AlNMe}_3)_2\text{H}_4]$  (**14**) or the side product  $[\text{Al}_3\text{H}_4(\mu\text{-H})(\kappa^2\text{-(CH}_2\text{SiMe}_2)\text{NSiMe}_3)_2]$  (**15**). Albeit accompanied by the unintended degradation of the pre-formed CoAl unit in the given reactions, the liability of **9** to ligand removal might allow for directed TM/E cluster growth provided an efficient stabilization of reactive intermediates by suitable additives, e.g. an excess of  $\text{ECp}^*$ . In this context, it is of note that  $[(\text{GaCp}^*)_2\text{Fe}(\text{btsa})_2]$  (**11**) and  $[(\text{GaCp}^*)\text{Co}(\text{btsa})_2]$  (**10**) also react readily with HBpin under formation of  $(\text{btsa})\text{Bpin}$  with yet unidentified reaction products. Furthermore, alternative strategies, like the protolytic or oxidative cleavage of the  $\text{Cp}^*$  ligand, e.g. in the presence of  $[\text{FeCp}_2][\text{BAR}_4^{\text{F}}]$ , or mild hydrogenolysis might turn out to effectively promote cluster growth.

## References

5. A. Schnepf, H. Schnöckel, *Angew. Chem. Int. Ed.* **2002**, 41 (19), 3532-3554.
7. H. Banh, K. Dilchert, C. Schulz, C. Gemel, R. W. Seidel, R. Gautier, S. Kahlal, J.-Y. Saillard, R. A. Fischer, *Angew. Chem.* **2016**, 128 (10), 3344-3349.
9. R. Jin, C. Zeng, M. Zhou, Y. Chen, *Chem. Rev.* **2016**, 116 (18), 10346-10413.
10. T.-A. D. Nguyen, Z. R. Jones, D. F. Leto, G. Wu, S. L. Scott, T. W. Hayton, *Chem. Mater.* **2016**, 28 (22), 8385-8390.
11. C. Ganesamoorthy, J. Weßing, C. Kroll, R. W. Seidel, C. Gemel, R. A. Fischer, *Angew. Chem. Int. Ed.* **2014**, 53 (30), 7943-7947.
80. A. Mackay, *Acta Crystallogr.* **1962**, 15 (9), 916-918.
135. T. P. Fehlner, J.-F. Halet, J.-Y. Saillard, *Molecular Clusters - A Bridge to Solid State Chemistry*, Cambridge University Press, Cambridge, **2007**.
143. G. Schmid, R. Pfeil, R. Boese, F. Bandermann, S. Meyer, G. H. M. Calis, J. W. A. van der Velden, *Chem. Ber.* **1981**, 114 (11), 3634-3642.
144. G. Schmid, *Chem. Soc. Rev.* **2008**, 37 (9), 1909-1930.
150. J. D. Erickson, E. G. Mednikov, S. A. Ivanov, L. F. Dahl, *J. Am. Chem. Soc.* **2016**, 138 (5), 1502-1505.
151. N. T. Tran, D. R. Powell, L. F. Dahl, *Angew. Chem. Int. Ed.* **2000**, 39 (22), 4121-4125.
152. E. G. Mednikov, M. C. Jewell, L. F. Dahl, *J. Am. Chem. Soc.* **2007**, 129 (37), 11619-11630.
154. A. Dass, S. Theivendran, P. R. Nimmala, C. Kumara, V. R. Jupally, A. Fortunelli, L. Sementa, G. Barcaro, X. Zuo, B. C. Noll, *J. Am. Chem. Soc.* **2015**, 137 (14), 4610-4613.
159. J. Vollet, J. R. Hartig, H. Schnöckel, *Angew. Chem. Int. Ed.* **2004**, 43 (24), 3186-3189.
162. A. Schnepf, *New J. Chem.* **2010**, 34 (10), 2079-2092.
165. H.-J. Himmel, J. Vollet, *Organometallics* **2002**, 21 (26), 5972-5977.
166. D. Michael, P. Mingos, R. L. Johnston. In *Theoretical Approaches*; Springer Berlin Heidelberg, **1987**, pp 29-87.
191. M. Walter, J. Akola, O. Lopez-Acevedo, P. D. Jadzinsky, G. Calero, C. J. Ackerson, R. L. Whetten, H. Grönbeck, H. Häkkinen, *PNAS* **2008**, 105 (27), 9157-9162.
197. C. Zeng, H. Qian, T. Li, G. Li, N. L. Rosi, B. Yoon, R. N. Barnett, R. L. Whetten, U. Landman, R. Jin, *Angew. Chem. Int. Ed.* **2012**, 51 (52), 13114-13118.
242. X.-K. Wan, X.-L. Cheng, Q. Tang, Y.-Z. Han, G. Hu, D.-e. Jiang, Q.-M. Wang, *J. Am. Chem. Soc.* **2017**, 139 (28), 9451-9454.
244. P. Jutzi, B. Neumann, G. Reumann, H.-G. Stammler, *Organometallics* **1998**, 17 (7), 1305-1314.
245. P. Jutzi, B. Neumann, L. O. Schebaum, A. Stammler, H.-G. Stammler, *Organometallics* **1999**, 18 (21), 4462-4464.
249. P. Jutzi, B. Neumann, L. O. Schebaum, A. Stammler, H.-G. Stammler, *Organometallics* **2000**, 19 (7), 1445-1447.
250. J. Weßing, C. Göbel, B. Weber, C. Gemel, R. A. Fischer, *Inorg. Chem.* **2017**, 56 (6), 3517-3525.
251. S. González-Gallardo, T. Bollermann, R. A. Fischer, R. Murugavel, *Chem. Rev.* **2012**, 112 (6), 3136-3170.
257. T. Steinke, C. Gemel, M. Winter, R. A. Fischer, *Chem. Eur. J.* **2005**, 11 (5), 1636-1646.
269. M. Cokoja, B. R. Jagirdar, H. Parala, A. Birkner, R. A. Fischer, *Eur. J. Inorg. Chem.* **2008**, 2008 (21), 3330-3339.

270. M. Cokoja, H. Parala, A. Birkner, R. A. Fischer, O. Margeat, D. Ciuculescu, C. Amiens, B. Chaudret, A. Falqui, P. Lecante, *Eur. J. Inorg. Chem.* **2010**, 2010 (11), 1599-1603.
271. M. Cokoja, H. Parala, A. Birkner, O. Shekhah, M. W. E. van den Berg, R. A. Fischer, *Chem. Mater.* **2007**, 19 (23), 5721-5733.
272. M. Cokoja, H. Parala, M.-K. Schröter, A. Birkner, M. W. E. van den Berg, W. Grünert, R. A. Fischer, *Chem. Mater.* **2006**, 18 (6), 1634-1642.
273. K. Schutte, A. Doddi, C. Kroll, H. Meyer, C. Wiktor, C. Gemel, G. van Tendeloo, R. A. Fischer, C. Janiak, *Nanoscale* **2014**, 6 (10), 5532-5544.
274. M. Armbrüster, K. Kovnir, M. Behrens, D. Teschner, Y. Grin, R. Schlögl, *J. Am. Chem. Soc.* **2010**, 132 (42), 14745-14747.
275. M. Armbrüster, K. Kovnir, M. Friedrich, D. Teschner, G. Wowsnick, M. Hahne, P. Gille, L. Szentmiklósi, M. Feuerbacher, M. Heggen, F. Girgsdies, D. Rosenthal, R. Schlögl, Y. Grin, *Nat. Mater.* **2012**, 11, 690.
277. M. Molon, T. Bollermann, C. Gemel, J. Schaumann, R. A. Fischer, *Dalton Trans.* **2011**, 40 (40), 10769-10774.
278. T. Cadenbach, C. Gemel, T. Bollermann, R. A. Fischer, *Inorg. Chem.* **2009**, 48 (11), 5021-5026.
279. S. A. Bezman, M. R. Churchill, J. A. Osborn, J. Wormald, *J. Am. Chem. Soc.* **1971**, 93 (8), 2063-2065.
280. T.-A. D. Nguyen, Z. R. Jones, B. R. Goldsmith, W. R. Buratto, G. Wu, S. L. Scott, T. W. Hayton, *J. Am. Chem. Soc.* **2015**, 137 (41), 13319-13324.
281. J. F. Moulder, W. F. Stickle, P. E. Sobol, K. D. Bomben, *Handbook of X-ray Photoelectron Spectroscopy*, Perkin Elmer Corporation, Eden Prairie, Minnesota, USA, **1992**.
282. C. D. Wagner, *Faraday Discuss. Chem. Soc.* **1975**, 60 (0), 291-300.
283. A. Bondi, *J. Phys. Chem.* **1964**, 68 (3), 441-451.
284. M. Mantina, A. C. Chamberlin, R. Valero, C. J. Cramer, D. G. Truhlar, *J. Phys. Chem. A* **2009**, 113 (19), 5806-5812.
285. R. W. G. Wyckoff, *Crystal Structures*, 2nd ed.; Interscience Publishers, New York, **1963**; Vol. 1.
286. Y. Grin, F. R. Wagner, M. Armbrüster, M. Kohout, A. Leithe-Jasper, U. Schwarz, U. Wedig, H. Georg von Schnering, *J. Solid State Chem.* **2006**, 179 (6), 1707-1719.
287. L. Arnberg, S. Westman, *Acta Crystallogr., Sect. A* **1978**, 34 (3), 399-404.
288. G. D. S. Douglas, M. C. Henrique, G. R. Gustavo, F. d. O. Marcelo, L. F. D. S. Juarez, *J. Phys.: Condens. Matter* **2016**, 28 (17), 175302.
289. C. Ganesamoorthy, *Unpublished results*. Chair of Inorganic Chemistry II, Ruhr-University Bochum, **2013**.
290. D. Bono, J. Hartig, M. Huber, H. Schnöckel, L. J. de Jongh, *J. Clust. Sci.* **2007**, 18 (1), 319-331.
291. K. K. Chakrahari, J.-H. Liao, S. Kahlal, Y.-C. Liu, M.-H. Chiang, J.-Y. Saillard, C. W. Liu, *Angew. Chem. Int. Ed.* **2016**, 55 (47), 14704-14708.
292. O. Kahn, *Molecular Magnetism*, VCH Weinheim, **1993**.
293. C. Binns, *Nanomagnetism: Fundamentals and Applications*, Elsevier, Oxford, **2014**; Vol. 6.
294. A. P. Guimarães, *The principles of nanomagnetism*, Springer Berlin Heidelberg, **2009**.
295. J. Crangle, *Solid-state magnetism*, Springer, New York, **1991**.
296. A. Sacco, M. Rossi, F. Bottomley, A. D. Allen. In *Inorg. Synth.*; John Wiley & Sons, Inc., **2007**, pp 18-22.
297. D. H. Gerlach, W. G. Peet, E. L. Muetterties, *J. Am. Chem. Soc.* **1972**, 94 (13), 4545-4549.

298. E. Y. Tsui, P. Müller, J. P. Sadighi, *Angew. Chem. Int. Ed.* **2008**, 47 (46), 8937-8940.
299. S. Gaillard, P. Nun, A. M. Z. Slawin, S. P. Nolan, *Organometallics* **2010**, 29 (21), 5402-5408.
300. P. Müller, R. Herbst-Irmer, A. Spek, T. Schneider, M. Sawaya, *Crystal Structure Refinement - A Crystallographer's Guide to Shelxl*, Oxford University Press, New York, **2006**.
301. D. M. P. Mingos, *J. Chem. Soc., Dalton Trans.* **1996**, (5), 561-566.
302. K. Konishi. In *Gold Clusters, Colloids and Nanoparticles I*, D. M. P. Mingos, Ed.; Springer International Publishing, Cham, **2014**, pp 49-86.
303. C. Dohmeier, C. Robl, M. Tacke, H. Schnöckel, *Angew. Chem.* **1991**, 103 (5), 594-595.
304. S. Martinez-Salvador, L. R. Falvello, A. Martin, B. Menjon, *Chem. Sci.* **2015**, 6 (10), 5506-5510.
305. D. Michael, P. Mingos, *Polyhedron* **1984**, 3 (12), 1289-1297.
306. V. G. Albano, P. L. Bellon, M. Manassero, M. Sansoni, *J. Chem. Soc., Chem. Comm.* **1970**, (18), 1210-1211.
307. C. E. Briant, B. R. C. Theobald, J. W. White, L. K. Bell, D. M. P. Mingos, A. J. Welch, *J. Chem. Soc., Chem. Commun.* **1981**, (5), 201-202.
308. J. W. A. Van der Velden, P. T. Beurskens, J. J. Bour, W. P. Bosman, J. H. Noordik, M. Kolenbrander, J. A. K. M. Buskes, *Inorg. Chem.* **1984**, 23 (2), 146-151.
309. K. Ouzounis, H. Riffel, H. Hess, U. Kohler, J. Weidlein, *Z. Anorg. Allg. Chem.* **1983**, 504 (9), 67-76.
310. A. E. Nako, S. J. Gates, A. J. P. White, M. R. Crimmin, *Dalton Trans.* **2013**, 42 (42), 15199-15206.
311. C. Ganesamoorthy, S. Loerke, C. Gemel, P. Jerabek, M. Winter, G. Frenking, R. A. Fischer, *Chem. Commun.* **2013**, 49 (28), 2858-2860.
312. X. Wang, L. Andrews, *J. Am. Chem. Soc.* **2001**, 123 (51), 12899-12900.
313. Y. Ohki, Y. Shimizu, R. Araake, M. Tada, W. M. C. Sameera, J.-I. Ito, H. Nishiyama, *Angew. Chem. Int. Ed.* **2016**, 55 (51), 15821-15825.
314. D. C. Bradley, M. B. Hursthouse, R. J. Smallwood, A. J. Welch, *J. Chem. Soc., Chem. Commun.* **1972**, (15), 872-873.
315. D. Loos, E. Baum, A. Ecker, H. Schnöckel, A. J. Downs, *Angew. Chem. Int. Ed. Engl.* **1997**, 36 (8), 860-862.
316. G. Linti, S. Çoban, D. Dutta, *Z. Anorg. Allg. Chem.* **2004**, 630 (2), 319-323.
317. B. Quillian, P. Wei, C. S. Wannere, P. v. R. Schleyer, G. H. Robinson, *J. Am. Chem. Soc.* **2009**, 131 (9), 3168-3169.
318. R. Wolf, W. Uhl, *Angew. Chem. Int. Ed.* **2009**, 48 (37), 6774-6776.
319. T. Bollermann, A. Puls, C. Gemel, T. Cadenbach, R. A. Fischer, *Dalton Trans.* **2009**, (8), 1372-1377.
320. M. Molon, *Unpublished results*. Chair of Inorganic Chemistry II, Ruhr-University Bochum, **2011**.
321. M. Kehrwald, W. Köstler, A. Rodig, G. Linti, T. Blank, N. Wiberg, *Organometallics* **2001**, 20 (5), 860-867.
322. M. E. Smith, R. A. Andersen, *Organometallics* **1996**, 15 (12), 2680-2682.
323. H. D. Kaesz, R. B. Saillant, *Chem. Rev.* **1972**, 72 (3), 231-281.
324. C. Jones, D. P. Mills, R. P. Rose, *J. Organomet. Chem.* **2006**, 691 (13), 3060-3064.
325. A. J. Downs, M. J. Goode, C. R. Pulham, *J. Am. Chem. Soc.* **1989**, 111 (5), 1936-1937.
326. S. Aldridge, A. J. Downs, *Chem. Rev.* **2001**, 101 (11), 3305-3366.
327. S. Guo, R. Hauptmann, S. Losi, P. Zanello, J. Schneider, *J. Clust. Sci.* **2007**, 18, 237-251.

328. M. W. Howard, S. F. Kettle, I. A. Oxton, D. B. Powell, N. Sheppard, P. Skinner, *J. Chem. Soc., Faraday Trans. 2* **1981**, 77 (2), 397-404.
329. M. Moselage, J. Li, L. Ackermann, *ACS Catal.* **2016**, 6 (2), 498-525.
330. B. Su, Z.-C. Cao, Z.-J. Shi, *Acc. Chem. Res.* **2015**, 48 (3), 886-896.
331. T. Zheng, H. Sun, Y. Chen, X. Li, S. Dürr, U. Radius, K. Harms, *Organometallics* **2009**, 28 (19), 5771-5776.
332. D. Zell, Q. Bu, M. Feldt, L. Ackermann, *Angew. Chem. Int. Ed.* **2016**, 55 (26), 7408-7412.
333. E. Ozkal, B. Cacherat, B. Morandi, *ACS Catal.* **2015**, 5 (11), 6458-6462.
334. L. Souillart, N. Cramer, *Chem. Rev.* **2015**, 115 (17), 9410-9464.
335. T. Cadenbach, C. Gemel, R. Schmid, S. Block, R. A. Fischer, *Dalton Trans.* **2004**, (20), 3171-3172.
336. T. Cadenbach, C. Gemel, R. Schmid, R. A. Fischer, *J. Am. Chem. Soc.* **2005**, 127 (48), 17068-17078.
337. C. D. Keefe, J. L. MacDonald, *Spectrochim. Acta, Part A* **2006**, 64 (2), 483-494.
338. J. L. Bourque, M. C. Biesinger, K. M. Baines, *Dalton Trans.* **2016**, 45 (18), 7678-7696.
339. R. L. Holland, J. M. O'Connor, A. L. Rheingold, *J. Clust. Sci.* **2009**, 20 (2), 261-265.
340. R. D. Adams, S. Miao, *Inorg. Chim. Acta* **2005**, 358 (5), 1401-1406.
341. Y. Nishihara, K. J. Deck, M. Shang, T. P. Fehlner, B. S. Haggerty, A. L. Rheingold, *Organometallics* **1994**, 13 (11), 4510-4522.
342. D. Sharmila, R. Ramalakshmi, K. K. Chakrahari, B. Varghese, S. Ghosh, *Dalton Trans.* **2014**, 43 (26), 9976-9985.
343. F. Jiang, T. P. Fehlner, A. L. Rheingold, *J. Am. Chem. Soc.* **1987**, 109 (6), 1860-1861.
344. R. Beck, M. Shoshani, S. A. Johnson, *Angew. Chem.* **2012**, 124 (47), 11923-11926.
345. T. Cadenbach, C. Gemel, D. Zacher, R. A. Fischer, *Angew. Chem. Int. Ed.* **2008**, 47 (18), 3438-3441.
346. M. Halbherr, T. Bollermann, C. Gemel, R. A. Fischer, *Angew. Chem. Int. Ed.* **2010**, 49 (10), 1878-1881.
347. K. R. Pörschke, G. Wilke, *Chem. Ber.* **1984**, 117 (1), 56-68.
348. K.-R. Pörschke, G. Wilke, R. Mynott, *Chem. Ber.* **1985**, 118 (1), 298-312.
349. A. Kempfer, C. Gemel, T. Cadenbach, R. A. Fischer, *Organometallics* **2007**, 26 (17), 4257-4264.
350. P. Csaszar, P. L. Goggin, J. Mink, J. L. Spencer, *J. Organomet. Chem.* **1989**, 379 (3), 337-349.
351. T. Steinke, *Unpublished results*. Chair of Inorganic Chemistry II, Ruhr-University Bochum, **2003**.
352. W. Saak, S. Pohl, *Angew. Chem.* **1991**, 103 (7), 869-870.
353. L. D. Lower, L. F. Dahl, *J. Am. Chem. Soc.* **1976**, 98 (16), 5046-5047.
354. H. Ipsen, A. Mikula, W. Schuster, *Monatsh. Chem.* **1989**, 120 (4), 283-289.
355. U. Häussermann, M. Elding-Pontén, C. Svensson, S. Lidin, *Chem. Eur. J.* **1998**, 4 (6), 1007-1015.
356. J. Uddin, C. Boehme, G. Frenking, *Organometallics* **2000**, 19 (4), 571-582.
357. J. Donohue, *The Structures of the Elements*, John Wiley & Sons Incorporated, **1974**.
358. D. Fenske, J. Hachgenei, F. Rogel, *Angew. Chem.* **1984**, 96 (12), 959-960.
359. M. Bochmann, I. Hawkins, L. J. Yellowlees, M. B. Hursthouse, R. L. Short, *Polyhedron* **1989**, 8 (10), 1351-1355.
360. R. A. Fischer, A. Miehr, M. M. Schulte, *Adv. Mater.* **1995**, 7 (1), 58-61.
361. R. A. Fischer, A. Miehr, T. Metzger, *Thin Solid Films* **1996**, 289 (1), 147-152.
362. R. A. Fischer, A. Miehr, *Chem. Mater.* **1996**, 8 (2), 497-508.

363. B. Fraser, L. Brandt, W. K. Stovall, H. D. Kaesz, S. I. Khan, F. Maury, *J. Organomet. Chem.* **1994**, 472 (1), 317-328.
364. B. Cormary, F. Dumestre, N. Liakakos, K. Soulantica, B. Chaudret, *Dalton Trans.* **2013**, 42 (35), 12546-12553.
365. L.-M. Lacroix, S. Lachaize, A. Falqui, T. Blon, J. Carrey, M. Respaud, F. Dumestre, C. Amiens, O. Margeat, B. Chaudret, P. Lecante, E. Snoeck, *J. Appl. Phys.* **2008**, 103 (7), 07D521.
366. B. Buchin, C. Gemel, A. Kempter, T. Cadenbach, R. A. Fischer, *Inorg. Chim. Acta* **2006**, 359 (15), 4833-4839.
367. T. Steinke, C. Gemel, M. Cokoja, M. Winter, R. A. Fischer, *Angew. Chem. Int. Ed.* **2004**, 43 (17), 2299-2302.
368. H. Wadepohl, S. Gebert, *Coord. Chem. Rev.* **1995**, 143, 535-609.
369. H. Wadepohl, T. Borchert, H. Pritzkow, *Chem. Ber.* **1997**, 130 (5), 593-603.
370. C. Üffing, A. Ecker, R. Köppe, H. Schnöckel, *Organometallics* **1998**, 17 (11), 2373-2375.
371. J. J. Schneider, C. Krüger, M. Nolte, I. Abraham, T. S. Ertel, H. Bertagnolli, *Angew. Chem.* **1994**, 106 (23-24), 2537-2540.
372. S. S. Batsanov, *Inorg. Mater.* **2001**, 37 (9), 871-885.
373. P. J. Black, *Acta Metall.* **1956**, 4 (2), 172-179.
374. M. M. Clark, W. W. Brennessel, P. L. Holland, *Acta Crystallogr., Sect. E* **2009**, 65 (4), m391.
375. M. A. Laffey, P. Thornton, *J. Chem. Soc., Dalton Trans.* **1982**, (2), 313-318.
376. H. Bürger, W. Sawodny, U. Wannagat, *J. Organomet. Chem.* **1965**, 3 (2), 113-120.
377. K. J. Fisher, D. C. Bradley, *J. Am. Chem. Soc.* **1971**, 93 (8), 2058-2059.
378. S. S. Kristjansdottir, J. R. Norton, A. Moroz, R. L. Sweany, S. L. Whittenburg, *Organometallics* **1991**, 10 (7), 2357-2361.
379. S. T. Liddle, *Molecular Metal-Metal Bonds: Compounds, Synthesis, Properties*, Wiley-VCH, Weinheim, Germany, **2015**.
380. S. L. Bartley, M. J. B. Jr, R. Clerac, H. Zhao, X. Ouyang, K. R. Dunbar, *Dalton Trans.* **2003**, (14), 2937-2944.
381. D. J. M. F. E. Mabbs, *Magnetism and Transition Metal Complexes*, Chapman and Hall, London, UK, **1973**.
382. A. F. Orchard, *Magnetochemistry*, Oxford University Press, USA, **2003**.
383. D. P. Freyberg, J. L. Robbins, K. N. Raymond, J. C. Smart, *J. Am. Chem. Soc.* **1979**, 101 (4), 892-897.
384. C. M. Lousada, S. S. Pinto, J. N. Canongia Lopes, M. F. Minas da Piedade, H. P. Diogo, M. E. Minas da Piedade, *J. Phys. Chem. A* **2008**, 112 (13), 2977-2987.
385. H. Sitzmann, M. F. Lappert, C. Dohmeier, C. Üffing, H. Schnöckel, *J. Organomet. Chem.* **1998**, 561 (1-2), 203-208.
386. A. Haaland, K.-G. Martinsen, S. A. Shlykov, H. V. Volden, C. Dohmeier, H. Schnöckel, *Organometallics* **1995**, 14 (6), 3116-3119.
387. A. Panda, M. Stender, M. M. Olmstead, P. Klavins, P. P. Power, *Polyhedron* **2003**, 22 (1), 67-73.
388. S. Alvarez, *Coord. Chem. Rev.* **1999**, 193-195, 13-41.
389. P. G. Eller, D. C. Bradley, M. B. Hursthouse, D. W. Meek, *Coord. Chem. Rev.* **1977**, 24 (1), 1-95.
390. J. Kim, *Dissertation*, Ruhr-University Bochum, Bochum, **2017**.
391. C. Jones, R. P. Rose, A. Stasch, *Dalton Trans.* **2007**, (28), 2997-2999.
392. A. Kempter, C. Gemel, T. Cadenbach, R. A. Fischer, *Inorg. Chem.* **2007**, 46 (22), 9481-9487.

393. K. Freitag, H. Banh, C. Gemel, P. Jerabek, R. W. Seidel, G. Frenking, R. A. Fischer, *Inorg. Chem.* **2015**, 54 (1), 352-358.
394. H. Kayi, T. Clark, *J. Mol. Model.* **2007**, 13 (9), 965-979.
395. G. M. Sheldrick, W. S. Sheldrick, *J. Chem. Soc. A* **1969**, (0), 2279-2282.
396. T. Steinke, M. Cokoja, C. Gemel, A. Kempter, A. Krapp, G. Frenking, U. Zenneck, R. A. Fischer, *Angew. Chem. Int. Ed.* **2005**, 44 (19), 2943-2946.
397. T. Cadenbach, T. Bollermann, C. Gemel, R. A. Fischer, *Dalton Trans.* **2009**, (2), 322-329.
398. M. J. Butler, M. R. Crimmin, *Chem. Commun.* **2017**, 53 (8), 1348-1365.
399. Y. Ohki, Y. Takikawa, T. Hatanaka, K. Tatsumi, *Organometallics* **2006**, 25 (13), 3111-3113.
400. U. Siemeling, U. Vorfeld, B. Neumann, H.-G. Stammler, *Organometallics* **1998**, 17 (3), 483-484.
401. J. C. Huffman, W. E. Streib, *J. Chem. Soc., Chem. Comm.* **1971**, (16), 911-912.
402. W. Uhl, E. Schnepf, J. Wagner, *Z. Anorg. Allg. Chem.* **1992**, 613 (7), 67-75.



## 5 OUTLOOK

Inspired by the conceptual understanding of intermetallic clusters as spatially confined representatives of intermetallic phases, or molecular alloys, whose structural and compositional diversity might be just as rich as that of their macroscopic parent materials, the declared objective of this thesis was the development of reliable synthetic strategies for a systematic wet-chemical access on Hume-Rothery phase-inspired, ligand-stabilized group 13/transition metal cluster compounds. The herein presented successful syntheses of a small library of these novel metal atom-rich cluster compounds  $[TM_aE_b](Cp^*)_n(H)_x$  with Cu/Al, Au/Al, Co/Ga and Ni/Ga combinations prove their access to be feasible, but synthetically challenging. In particular, the direct access *via* reaction of carefully chosen, suitable organometallic precursors of low-nuclearity was found to be extraordinarily prone to factors like the chemical nature and purity of precursors, ancillary ligands, solvents, reaction times and temperature, and more, resulting in complex, and competitive reaction pathways of limited reproducibility. This is impressively illustrated by the synthesis of  $[Cu_{43}(AlCp^*)_{12}]$  (**3**) from  $[CuMes]_5$  and  $AlCp^*$  which is known in our group for a long time but took years to optimize to the current stage. Likewise, the structurally diverse AuAl clusters  $[Au_a(AlCp^*)_6H_x]$  (**4**) and  $[Au_8(AlCp^*)_5(IMes)H_x]$  (**5**) are obtained upon just small variation of the ancillary ligand of the precursor  $[(NHC)AuH]$  with  $NHC = IPr$  or  $IMes$ , respectively. Potentially more selective, alternative pathways include ligand exchange reactions at precast polynuclear  $TM_a$  kernels, or the directed stimulation of cluster growth at pre-formed  $TM/E$  complexes, e.g. by selective ligand removal. The former is supported by the synthesis of  $[Cu_6(AlCp^*)_6H_4]$  (**1**)<sup>11</sup> and  $[(Cp^*Co)_3Ga_6(Cp^*_3Co_3(\mu^3-CH))H_x]$  (**6**) from  $[PPh_3CuH]_6$  and  $[(P^iPr_3)_6Co_6H_8]$ , respectively. Why should comparable clusters with Ni/E, Rh/E, or even the long-time aspired Fe/E combination not be accessible from further representatives of this class of hydride-bearing phosphine transition metal clusters, like the pentanuclear  $[(P^iPr_3)_5Ni_5H_6]$ ,<sup>344</sup> the hydride-rich cationic  $[(P^iPr_3)_6Rh_6H_{12}]^{2+}$ ,<sup>403</sup> or the very recent  $[(PMe_3)_{10}Fe_6H_{12}]$ ?<sup>404</sup> For the early transition metals, the tendency of  $ECp^*$  to undergo  $Cp^*$  transfer, as also observed for **6**, might eventually even allow for the formation of truly mixed intermetallic core systems, rather than the usually observed segregation of transition metal core and peripheral group 13-ligand shell. Furthermore, the stimulation of cluster growth of all-labile  $TM/E$  complexes by selective removal of their stabilizing ligand shell might turn out effective. While initial experiments on the cleavage of *btsa* ligands from mononuclear  $[TM_1E_b(Cp^*)_n(btsa)_m]$  complexes fail to provide polynuclear cluster compounds, no attempts were made on the removal of the likewise cleavable  $Cp^*$  ligand. Precedence for the well feasible removal of  $Cp^*$  ligands from  $ECp^*$ -ligated  $TM$  complexes is for instance provided by reports on the protolytic cleavage of  $Cp^*H$  in the reaction of  $[(GaCp^*)Rh(Ga(Me)Cp^*)]$  with  $[H(OEt_2)_2][BAR_4^F]$  to furnish  $[(GaCp^*)_4Rh(GaMe)]$ ,<sup>345</sup> or the formation of  $[(\mu_2-Ga)Pt_3(\mu_3GaCp^*)_2(GaCp^*)_4][BAR_4^F]$  upon oxidative cleavage of the  $Cp^*$  ligand from  $[Pt(GaCp^*)_4]$  with  $[FeCp_2][BAR_4^F]$ .<sup>346</sup> Such strategies are not only of interest for the formation of  $TM/E$  clusters from small building units, but also with regards to an investigation of the

follow-up chemistry of readily accessible representatives, like **1** or **6**, upon removal of the sterically encumbering, and thus passivating Cp\* ligand shell.

With suitable synthesis strategies and a first small library of homoleptic  $[\text{TM}_a\text{E}_b](\text{Cp}^*)_n(\text{H})_x$  clusters in hand, additional studies should further be directed towards the chemistry of these novel compounds. The reaction of **1** with benzonitrile to give  $[\text{Cu}_6(\text{AlCp}^*)_6(\text{NCHPh})\text{H}_3]$  (**2**) which serves as a molecular model of conceivable surface-bound intermediates in semi-hydrogenation reactions at TM/E nanophases, shows the potential of these well-defined systems to study catalytically relevant processes on a molecular level. However, a systematic investigation on the behaviour of **1** towards further unsaturated organic molecules is still pending. With the mixed CoGa cluster **6**, a second, readily accessible example of this class of compounds showing interesting reaction behaviour has been found. The unprecedented coordination of a capping methin ligand of yet unclarified origin at the peripheral  $[\text{Cp}^*_3\text{Co}_3]$  fragment indicates the involvement of C-C bond activation in the formation of **6**. In fact, related C-C bond activation at TM/E complexes have already been observed in the reactions of  $[\text{Cp}^*\text{Rh}(\text{CH}_3)_2\text{L}]$  (L = dmsO, pyridine) with  $\text{ECp}^*$ .<sup>335</sup> For  $\text{GaCp}^*$ , formation of an intermediate  $[\text{Cp}^*\text{Rh}(\text{CH}_3)_2\text{GaCp}^*]$  occurs which undergoes further reaction to give  $[\text{Cp}^*\text{Rh}(\text{CpMe}_4)\text{Ga}(\text{CH}_3)_3]$ . While the actual C-C bond activation step was found to occur at the gallium center, DFT calculations revealed decisive cooperative effects between the electron-rich rhodium atom and the electrophilic gallium center.<sup>336</sup> Supposing comparable synergistic effects in **6**, the identification of the CH group's origin and the mechanistic pathways involved in its formation and trapping at the  $\text{Co}_3$  site might provide us with a rationale that can be utilized for the development of further catalytically relevant model reactions.

## References

11. C. Ganesamoorthy, J. Weßing, C. Kroll, R. W. Seidel, C. Gemel, R. A. Fischer, *Angew. Chem. Int. Ed.* **2014**, 53 (30), 7943-7947.
335. T. Cadenbach, C. Gemel, R. Schmid, S. Block, R. A. Fischer, *Dalton Trans.* **2004**, (20), 3171-3172.
336. T. Cadenbach, C. Gemel, R. Schmid, R. A. Fischer, *J. Am. Chem. Soc.* **2005**, 127 (48), 17068-17078.
344. R. Beck, M. Shoshani, S. A. Johnson, *Angew. Chem.* **2012**, 124 (47), 11923-11926.
345. T. Cadenbach, C. Gemel, D. Zacher, R. A. Fischer, *Angew. Chem. Int. Ed.* **2008**, 47 (18), 3438-3441.
346. M. Halbherr, T. Bollermann, C. Gemel, R. A. Fischer, *Angew. Chem. Int. Ed.* **2010**, 49 (10), 1878-1881.
403. P. J. Dyson, J. S. McIndoe, *Angew. Chem. Int. Ed.* **2004**, 43 (45), 6028-6030.
404. R. Araake, K. Sakadani, M. Tada, Y. Sakai, Y. Ohki, *J. Am. Chem. Soc.* **2017**, 139 (15), 5596-5606.

## 6 EXPERIMENTAL PART

## 6.1 Materials and Methods

### General techniques

Manipulation of air and moisture-sensitive compounds was performed under an atmosphere of purified argon using conventional Schlenk and glovebox techniques. Herein, argon was purified by successively passing it over a heated copper(I) catalyst, and activated molecular sieves (4 Å) to remove residual oxygen and water contents.

All glassware was flame dried in vacuum and silylated prior to usage. To this end, small amounts of 1,1,1,3,3,3-hexamethyldisilazane were heated to reflux inside the closed apparatus using a hot air gun, and allowed to condense at the glass surfaces. Excess 1,1,1,3,3,3-hexamethyldisilazane was removed under reduced pressure.

Common organic solvents, like *n*-hexane, *n*-pentane, toluene, tetrahydrofuran, diethyl ether were dried using an MBraun solvent purification system (SPS) in which solvents were passed through consecutive filter columns containing suitable adsorbents by application of argon pressure gradients. Used adsorbent materials included a copper catalyst and molecular sieve for *n*-hexane or *n*-pentane, and activated alumina for toluene, tetrahydrofuran and diethyl ether. Benzene and mesitylene were dried using standard purification procedures, i.e. by passing the solvent over a column of activated alumina under an inert atmosphere. Thus treated solvents exhibited a purity above 99 % and water contents below 5 ppm, as verified by Karl-Fischer titration. Deuterated solvents for NMR spectroscopic measurements were dried above activated molecular sieve (3 Å) and degassed using a minimum of three freeze-pump-thaw cycles.

Air and moisture-sensitive research chemicals were stored in a glovebox with an argon atmosphere and standard oxygen/water contents below 0.5 ppm, whereat temperature sensitive chemicals were kept in an integrated freezer at -30 °C.

Low temperature reactions were performed in cooled isopropanol/liquid nitrogen baths at the appropriate temperatures.

### Nuclear Magnetic Resonance (NMR) Spectroscopy

Standard NMR spectroscopic measurements were performed in gastight Y-Joung NMR tubes using a Bruker Advance DPX-250 or a Bruker Advance III AV400 US spectrometer operating at the appropriate frequencies. For paramagnetic NMR spectroscopic measurements, specifically adapted pulse programs with broad spectral ranges, short relaxation times, and short prescan delays were employed, using a Bruker DRX400 spectrometer. Unless otherwise noted, <sup>13</sup>C NMR spectra were measured in fully proton-

decoupled mode. Spectra are referenced relative to the residual solvent signals ( $^1\text{H}$ :  $\text{C}_6\text{D}_6$  7.16 ppm,  $\text{THF-d}_8$  3.58 ppm;  $^{13}\text{C}$  NMR:  $\text{C}_6\text{D}_6$  128.06 ppm,  $\text{THF-d}_8$  67.57 ppm) with exception of  $^{29}\text{Si}$  NMR spectra which are referenced to TMS as an internal standard.

Solid state magic angle spinning (MAS) NMR spectroscopic measurements were performed in 2.5 mm  $\text{ZrO}_2$  rotors using a Bruker Advance 300 spectrometer operating at the appropriate frequencies.  $^1\text{H}$  NMR spectra were measured using the single-pulse technique, whereas high-power decoupling (HPDEC) pulse programs were used for  $^{13}\text{C}$  NMR spectroscopic measurements. Spectra were referenced to the external standard adamantane ( $^1\text{H}$ : 2.00 ppm,  $^{13}\text{C}$  29.47 ppm, downfield shifted from TMS).

In the following, chemical shifts ( $\delta$ ) are given in ppm (parts per million) downfield shifted from TMS, and consecutively denoted as position ( $\delta_{\text{H}}$ ,  $\delta_{\text{C}}$  or  $\delta_{\text{Si}}$ ), relative integral, multiplicity, coupling constant ( $J$  in Hz), and assignment. Multiplicities are abbreviated as s = singlet, d = doublet, t = triplet, sept = septet and m = multiplet. Spectral data was processed using TopSpin 2.1 software packages, and manipulated using the software MestReNova (Mestrelab Research S.L.), version 9.0.1.

## Infrared (IR) spectroscopy

IR spectra were acquired on a Bruker Alpha FT-IR spectrometer with an attenuated total reflection (ATR) geometry, using a diamond ATR unit under argon atmosphere. Spectral data was processed using the software OPUS 6.5 (Bruker Optics GmbH), and edited using the data analysis software OriginPro 8 (OriginLab Corporation). Absorption bands are consecutively reported as position (wave number  $\nu$  in  $\text{cm}^{-1}$ ) and relative band intensity (vs = very strong, s = strong, m = medium, w = weak).

## Liquid injection field desorption ionization mass spectrometry (LIFDI-MS)

Mass spectrometric measurements were performed using a Waters LCT Classic orthogonal acceleration reflectron time of flight (TOF) mass spectrometer equipped with a LIFDI ionization source by Linden CMS GmbH. The mild ionization technique is particularly suitable for air sensitive, labile substances, and allows for mass spectrometric measurements of such samples with minimized fragmentation under an inert atmosphere. In a standard measuring procedure, samples are dissolved in suitable medium to high boiling point solvents, like toluene, in septum-capped glass vials, and deposited on a micro graphite dendrite-coated tungsten emitter *via* a glass fibre with an applied pressure gradient. After evaporation of the

solvent, a potential of 10kV is applied between the emitter and the counter electrode which effects mild ionization of the sample and acceleration of the ions towards the counter electrode, and eventually the detector. Additionally, an electrical current of up to 120 mA can be applied to effectively heat the emitter and increase the mobility of the molecules as well as their energetic excitation.

Complementary LIFDI-MS measurements of **6** and **8** were performed in the group of Prof. Dr. Todd B. Marder, Julius-Maximilians-University Würzburg, Germany, using a Thermo Scientific Exactive Plus instrument, equipped with an Orbitrap detector and a “LIFDI 700” ionization source.

Spectrometric data was analyzed using the software MestReNova (Mestrelab Research S.L.), version 9.0.1.

### Elemental analysis (EA) and atom absorption spectrometry (AAS)

Elemental analysis and AAS measurements were performed by the Microanalytical Laboratoy Kolbe, Mülheim an der Ruhr, Germany using an Elementar CHNOS-Analyzer (Vario-EL) and a Perkin Elmer AAS Analyst200. Additional measurements were performed at the Microanalytical Laboratory of the Technical University of Munich, Germany on a HEKAtech Euro EA CHNSO-Analyzer and a Varian AA280FS fast sequential AAS spectrometer.

### Magnetic susceptibility measurements

*Magnetic susceptibility measurements were conducted in the group of Prof. Dr. Birgit Weber, University of Bayreuth, Germany, (compounds **3**, **9**, **11**, and **13**) and the group of Prof. Dr. Olivier Cador, Institut des Sciences Chimiques de Rennes, France (advanced magnetic measurements on **3**), respectively. For more detailed information on the experimental procedure and set-up, please refer to Prof. Dr. Birgit Weber (weber@uni-bayreuth.de) or Prof. Dr. Olivier Cador (olivier.cador@univ-rennes1.fr) directly.*

Magnetic susceptibility data on **3**, **9**, **11**, and **13** was collected using a Quantum Design MPMSXL-5 SQUID magnetometer under an applied field of 0.5 T over the respective temperature ranges in the settle mode. Field-dependent measurements of **3** were performed at 10, 50 and 200 K in a range from -3- to 3 T. Samples were either prepared in a gelatine capsule (**9**, **11**, **13**), or in a quartz glass tube (**3**) held within a plastic straw. Data was corrected for diamagnetic contributions of the ligands using tabulated Pascal's constants, and of the sample holder.

Additional dc magnetic susceptibility measurements were performed on a solid polycrystalline sample of **3** which was sealed in a quartz glass tube, using a Quantum Design MPMS-XL SQUID magnetometer between 2 and 300 K. Herein, a magnetic field of 0.2 T was applied for temperatures of 2 to 20 K, and a magnetic field of 1 T was applied for temperatures of 20-300 K. All measurements were corrected for diamagnetic contributions as calculated with Pascal's constants. In addition, data was corrected for ferromagnetic impurities on the basis of magnetization versus field curves which were performed every 50 K.

### Electron paramagnetic resonance (EPR) spectroscopy

EPR measurements were performed in the group of Prof. Dr. Klaus Köhler, Technical University of Munich, Germany. EPR data of frozen toluene solutions (approx.  $10^{-3}$  to  $10^{-4}$  mol/l) was recorded on a Jeol JES-FA200 at 133.15K.

### X-ray photoelectron spectroscopy (XPS)

*XPS measurements were performed in the group of Prof. Dr. Sebastian Günther, Technical University of Munich, Germany.*

X-ray photoelectron spectra were recorded on a Leybold-Heraeus LHS 10 spectrometer using a non-monochromatized Al- $K_{\alpha}$  source (1486.7 eV). To this end, powder samples of **1** and **6** were suspended in benzene and coated on a sample holder inside a glovebox by drop-casting. The analyzer was operated at a constant pass energy of 100 eV leading to an energy resolution with a full width at half-maximum (fwhm) of  $\sim 1.1$  eV. The energy scale of the spectra was corrected for sample charging using the C1s signal (284.6 eV, amorphous carbon) as a reference signal. The oxidation states of copper (for **1**) and gallium (for **6**) were assessed on the basis of the Auger parameters  $\alpha = E_B(\text{Cu}2p_{3/2}) + E_{\text{kin}}(\text{Cu} L_3M_{45}M_{45})$  and  $\alpha = E_B(\text{Ga}2p_{3/2}) + E_{\text{kin}}(\text{Ga} L_3M_{45}M_{45})$ , respectively. All spectra were recorded in an ultra-high vacuum chamber at a pressure below  $5 \times 10^{-8}$  mbar. Core level spectra were deconvoluted by using Voigt functions and linear background subtraction.



## Single crystal X-ray diffraction (XRD)

Single crystal X-ray diffraction data for compounds **1-3**, **5** and **9-12** was collected on an Oxford SuperNova diffractometer with an Atlas CCD, using Cu-K $\alpha$  ( $\lambda = 1.54178 \text{ \AA}$ ) radiation from multilayer X-ray optics, whereat a continuously updated version of CrysAlisPro (Agilent Technologies) was used for data acquisition and processing.<sup>405</sup> If necessary, multi-scan absorption corrections were performed using the implemented ABSPACK.

For compounds **6**, **7**, **13**, and **14**, X-ray diffraction intensities were collected on a Bruker X-ray single crystal diffractometer equipped with a CMOS detector (Bruker Photon-100), an IMS microsource with Mo-K $\alpha$  radiation ( $\lambda = 0.71073 \text{ \AA}$ ) or Cu-K $\alpha$  radiation ( $\lambda = 1.54178 \text{ \AA}$ ), respectively, and a Helios mirror optic. X-ray intensity data of compounds **4**, **8** and **15** was collected on a Bruker diffractometer equipped with a CMOS detector (Bruker Photon-100), a TXS rotating anode with Mo K $\alpha$  radiation ( $\lambda = 0.71073 \text{ \AA}$ ) and a Helios mirror optic. Diffraction data was acquired and processed with the APEX-III program package.<sup>406</sup> In a routine experiment, suitable crystals were coated in perfluoropolyether, and mounted in the cooled nitrogen stream of the diffractometer on a loop or micro sampler. Lattice parameters were determined with an initial matrix scan. Reflections were merged and corrected for Lorenz and polarization effects, as well as scan speed and background using SAINT. Multiscan absorption corrections were performed with SADABS.<sup>407</sup>

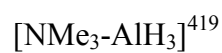
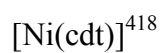
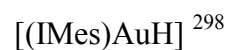
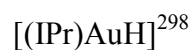
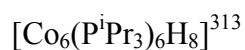
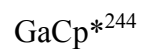
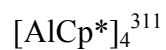
Molecular structures were solved by direct methods and refined using the program package SHELXLE in conjunction with SHELXS-97 and a continuously updated version of SHELXL.<sup>408-410</sup> For **7**, the crystal studied was a two-component, non-merohedral twin with the twin law:

$$\begin{pmatrix} -1.001 & 0.003 & 0.001 \\ -0.009 & -1.000 & -0.001 \\ 0.135 & -0.002 & 1.000 \end{pmatrix}$$

Twinning was taken into account during the data reduction process, and a reflection file in the HKLF-5 format was generated as a basis for subsequent data refinement. Full-matrix least squares refinement against all data was performed by minimization of  $\Delta w(F_o^2 - F_c^2)^2$  with the SHELXL weighting scheme. Disordered regions were modelled using standard similar distance restraints and constraints on atomic displacement parameters. If necessary, contributions of disordered, co-crystallized solvent molecules which could not be modelled accordingly were removed using the SQUEEZE routine implemented in PLATON.<sup>411-413</sup> Hydrogen atoms were calculated in ideal positions (riding model) with exception of the hydrides of compounds **9**, **13** and **15**. The latter could be located in the differential Fourier maps and were allowed to refine freely.

## Starting reagents

Unless otherwise noticed, starting reagents were obtained from commercial sources and used without further purification. The following compounds were synthesized according to literature procedures or modifications thereof.



## 6.2 Synthetic procedures

### $[\text{Cu}_6(\text{AlCp}^*)_6\text{H}_4]$ (**1**).<sup>11</sup>

A mixture of  $[\text{PPh}_3\text{CuH}]_6$  (1.007 g, 0.51 mmol) and  $\text{AlCp}^*$  (0.500 g, 3.08 mmol) was suspended in benzene (7 ml) and heated to 70°C for 7 h. The resulting dark brown suspension was allowed to settle overnight at room temperature, and filtrated to afford a black crystalline solid which was washed with a small amount of benzene (2 ml) and dried *in vacuo*. Yield: 0.539 mg, 0.39 mmol, 77 %.  $^1\text{H}$  NMR ( $\text{C}_6\text{D}_6$ , r.t.):  $\delta_{\text{H}}$  [ppm] = 2.01 (s, 90 H,  $\text{Cp}^*$ ), -2.86 (br s, 4 H, *hydride*);  $^{13}\text{C}$  NMR ( $\text{C}_6\text{D}_6$ , r.t.):  $\delta_{\text{C}}$  [ppm] = 115.92 ( $\text{C}_5\text{Me}_5$ ), 12.15 ( $\text{C}_5\text{Me}_5$ ); IR (ATR, neat,  $\text{cm}^{-1}$ ): 2941 (w), 2879 (m), 2831 (m), 2695 (w), 1466 (w), 1409 (m), 1361 (m), 1020 (w), 789 (w), 668 (m), 578 (w), 426 (s); MS (LIFDI, toluene):  $m/z$  1355.6  $[\text{MI-3H}]^+$ . *Anal.* calc. for  $\text{C}_{60}\text{H}_{94}\text{Al}_6\text{Cu}_6$  ( $M = 1358.55 \text{ g mol}^{-1}$ ): C 53.04; H 6.97; Al 11.92; Cu 28.06. Found: C 53.14; H 6.48; Al 11.69; Cu 28.22.

### $[\text{Cu}_6(\text{AlCp}^*)_6\text{H}_3(\text{N}=\text{CHPh})]$ (**2**).<sup>11</sup>

A suspension of  $[(\text{Cp}^*\text{AlCu})_6\text{H}_4]$  (**1**) (0.200 g, 0.15 mmol) and benzonitrile (0.091 g, 0.88 mmol) in benzene (4 ml) was reacted at room temperature for 24 h. The resulting brown crystalline material was isolated by means of filtration, washed with a minimal amount of benzene (1 ml) and dried *in vacuo*. An additional amount of pure **2** was obtained by further crystallization from the combined filtrates. Yield: 0.183 g, 0.13 mmol, 85 %.  $^1\text{H}$  NMR ( $\text{C}_6\text{D}_6$ , r.t.):  $\delta_{\text{H}}$  [ppm] = 8.06 (d, 2H,  $\text{C}_6\text{H}_5$ ), 7.70 (s, 1H,  $\text{N}=\text{CHPh}$ ), 7.29 (m, 3H,  $\text{C}_6\text{H}_5$ ), 2.20 (s, 30H,  $\text{Cp}^*$ ), 2.00 (s, 30H,  $\text{Cp}^*$ ), 1.93 (s, 15H,  $\text{Cp}^*$ ), 1.83 (s, 15H,  $\text{Cp}^*$ ), -2.50 (br s, 3H, *hydride*);  $^{13}\text{C}$  NMR ( $\text{C}_6\text{D}_6$ , r.t.):  $\delta_{\text{C}}$  [ppm] = 164.55 ( $\text{N}=\text{CHPh}$ ), 137.68 ( $\text{C}_6\text{H}_5$ ), 131.93 ( $\text{C}_6\text{H}_5$ ), 128.92 ( $\text{C}_6\text{H}_5$ ), 118.26 ( $\text{C}_5\text{Me}_5$ ), 117.24 ( $\text{C}_5\text{Me}_5$ ), 116.02 ( $\text{C}_5\text{Me}_5$ ), 116.00 ( $\text{C}_5\text{Me}_5$ ), 13.47 ( $\text{C}_5\text{Me}_5$ ), 12.62 ( $\text{C}_5\text{Me}_5$ ), 12.11 ( $\text{C}_5\text{Me}_5$ ), 12.07 ( $\text{C}_5\text{Me}_5$ ); IR (ATR, neat,  $\text{cm}^{-1}$ ): 2885 (m), 2824 (m), 1600 (w), 1414 (m), 1364 (m), 1188 (w), 1024 (w), 788 (w), 743 (m), 672 (m), 639 (m), 579 (w), 425 (s); *Anal.* calc. for  $\text{C}_{67}\text{H}_{99}\text{NAl}_6\text{Cu}_6$  ( $M = 1461.67 \text{ g mol}^{-1}$ ): C 55.05; H 6.83; N 0.96; Al 11.08; Cu 26.08. Found: C 52.93; H 7.22; N 0.94; Al 10.89; Cu 25.73.

### $[\text{Cu}_{43}(\text{AlCp}^*)_{12}]$ (**3**).

A mixture of  $[\text{Cu}(\text{Mes})]_5$  (205 mg, 0.961 mmol) and  $\text{AlCp}^*$  (120 mg, 0.740 mmol) was suspended in freshly distilled benzene (4 ml) and heated to 78°C for 48 h, whereat the reaction mixture was stirred for an initial 30 min and left to react without stirring afterwards. The resulting brown-black mixture was slowly cooled to room temperature and left to

crystallize for an additional 48 h. The black crystalline material was isolated by careful decantation using a narrow teflon cannula ( $d < 1$  mm) and repeatedly washed with benzene. For this, the black residue was suspended in freshly distilled benzene (4 ml), rigorously stirred and left to settle for several minutes. Subsequently, the solvent was removed by careful decantation. This procedure was repeated until the supernatant remained colourless and the resulting black solid was dried *in vacuo*. Yield: 17 mg, 0.004 mmol, 17 %.  $^1\text{H}$  MAS NMR (neat, r.t.):  $\delta_{\text{H}}$  [ppm] = 1.72 (s, Cp\*);  $^{13}\text{C}$  MAS NMR (neat, r.t.):  $\delta_{\text{C}}$  [ppm] = 117.94 ( $\text{C}_5\text{Me}_5$ ), 14.27 ( $\text{C}_5\text{Me}_5$ );  $^{27}\text{Al}$  MAS NMR (neat, r.t.):  $\delta_{\text{Al}}$  [ppm] = -97.25 (AlCp\*), not reproduced in this work. IR (neat, r.t.): 2936 (w), 2872 (w), 2818 (w), 1463 (w), 1412 (m), 1358 (m), 1157 (w), 1017 (w), 839 (w), 792 (w), 668 (m), 586 (m), 391 (s)  $\text{cm}^{-1}$ . Anal. calcd. for  $\text{Cu}_{43}\text{Al}_{12}\text{C}_{120}\text{H}_{180}\cdot 3\text{C}_6\text{H}_6$  ( $M = 4885.30$  g/mol): C 33.90, H 4.08, Al 6.63, Cu 55.39; found: C 33.83, H 4.13, Al 6.07, Cu 55.61%.

*Note: If small amounts of brown powder precipitate during the crystallization process, the washing procedure can be effectively used to remove these impurities. For this purpose, freshly distilled benzene is added to the residue and the suspension is rigorously stirred before it is briefly allowed to settle. While the black crystalline material sinks to the ground of the flask within a short time, the brown powder takes more time to do so and can be removed by decantation.*



**Figure 61.** Preparative steps in the synthesis of  $[\text{Cu}_{43}(\text{AlCp}^*)_{12}]$  (**3**). The synthesis was always conducted in the depicted Schlenk flasks with a high surface to volume ratio (left, outer diameter: 1.3 cm). Starting reagents were weighed into the reaction vessel inside a glovebox. Freshly distilled benzene was added outside the GB, and the closed Schlenk flask was disconnected from the Schlenk line and placed in an oil bath which was pre-heated to  $78^\circ\text{C}$  (middle left). After completed reaction and crystallization time, the product was isolated by slow and careful decantation using a narrow teflon cannula ( $d < 1$  mm; middle right). Repeated washing steps with benzene were performed analogously until the supernatant liquid remained colourless (right).

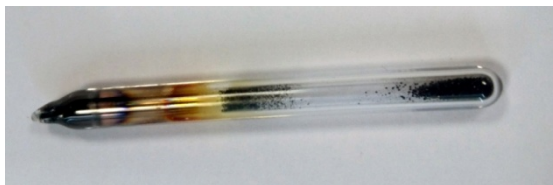


Figure 62. Analytically pure  $[\text{Cu}_{43}(\text{AlCp}^*)_{12}]$  (**3**) in a sealed quartz glass ampulla.

### $[\text{Au}_a(\text{AlCp}^*)_6\text{H}_x]$ (**4**).

A mixture of  $[(\text{IPr})\text{AuH}]$  (250 mg, 0.426 mmol) and  $\text{AlCp}^*$  (52 mg, 0.320 mmol) was suspended in benzene (8 ml) and heated to  $70^\circ\text{C}$  for 7 h. The resultant dark brown suspension was cooled to room temperature and left to settle over night. Cannula filtration afforded a black, microcrystalline material which was washed with small amounts of benzene (2 x 1 ml) and dried *in vacuo*. Yield: 39 mg (0.017 mmol, 32 %, for a composition of  $[\text{Au}_7(\text{AlCp}^*)_6\text{H}_x]$ ; 0.018 mmol, 34 %, for a composition of  $[\text{Au}_6(\text{AlCp}^*)_6\text{H}_x]$ ; yields were determined with regards to  $\text{AlCp}^*$ ).  $^1\text{H}$  MAS NMR (neat, r.t.):  $\delta_{\text{H}} [\text{ppm}] = 7.44$  (s,  $\text{C}_6\text{H}_6$ ), 1.85 (br s,  $\text{Cp}^*$ ), 1.09 (s);  $^{13}\text{C}$  MAS NMR (neat, r.t.):  $\delta_{\text{C}} [\text{ppm}] = 137.63$  ( $\text{C}_5\text{Me}_5$ ), 134.61 ( $\text{C}_5\text{Me}_5$ ), 14.42 ( $\text{C}_5\text{Me}_5$ ), 11.88 ( $\text{C}_5\text{Me}_5$ ); IR (ATR, neat,  $\text{cm}^{-1}$ ): 2962 (w), 2903 (m), 2847 (m), 2713 (w), 1747 (w), 1426 (m), 1370 (m), 1259 (w), 1026 (w), 847 (br, m), 799 (m), 672 (s), 589 (m), 492 (w), 424 (s). *Anal. calc.* for  $\text{C}_{60}\text{H}_{90}\text{Al}_6\text{Au}_7$  ( $M = 2352.01 \text{ g mol}^{-1}$ ): C 30.64; H 3.86; Al 6.88; Au 58.62. *Anal. calc.* for  $\text{C}_{60}\text{H}_{90}\text{Al}_6\text{Au}_6$  ( $M = 2155.05 \text{ g mol}^{-1}$ ): C 33.44; H 4.21; Al 7.51; Au 54.84. Found: C 32.47; H 4.59; Al 7.43; Au 54.16.

### $[\text{Au}_8(\text{AlCp}^*)_5(\text{IMes})\text{H}_x]$ (**5**).

In an NMR scale reaction, a mixture of  $[(\text{IMes})\text{AuH}]$  (15 mg, 0.03 mmol) and  $\text{AlCp}^*$  (3 mg, 0.02 mmol) was suspended in benzene- $\text{d}_6$  (0.5 ml) and heated to  $70^\circ\text{C}$  for 5 h. Crystals of **5** were obtained directly from the reaction mixture.

At preparative scale, a mixture of  $[(\text{IMes})\text{AuH}]$  (250 mg, 0.498 mmol) and  $\text{AlCp}^*$  (51 mg, 0.311 mmol) was suspended in benzene (8 ml) and heated to  $60^\circ\text{C}$  for 9 h. The dark brown reaction mixture was cooled to room temperature, and left to settle overnight. The resultant black precipitate was isolated by means of cannula filtration, washed with minimal amounts of benzene and dried *in vacuo*. Yield: 26 mg (0.010 mmol, 16 % for the anticipated formula). IR (ATR, neat,  $\text{cm}^{-1}$ ): 3117 (br w), 3013 (br w), 2962 (m), 2919 (w), 2853 (w), 1669 (br sh), 1609 (m), 1485 (m), 1440 (m), 1380 (m), 1261 (m), 1089 (br m), 1018 (m), 929 (w), 847 (m), 797 (s), 682 (m), 648 (m), 569 (m), 499 (sh).

The compound could not be further characterized due to limited reproducibility and insolubility in common organic solvents. Whether the given IR data reflects the data of analytically pure **5** cannot be reliably determined.

### $[(\text{Cp}^*\text{Co})_3\text{Ga}_6(\text{Cp}^*_3\text{Co}_3(\mu^3\text{-CH}))\text{H}_x]$ (**6**).

GaCp\* (124 mg, 0.605 mmol, 8 eq.) was added dropwise to a solution of  $[\text{Co}_6(\text{P}^i\text{Pr}_3)_6\text{H}_8]$  (100 mg, 0.075 mmol, 1 eq.) in toluene (5 ml) at room temperature. The reaction mixture was heated to 70 °C overnight (16h) and cooled to room temperature. Removal of all volatiles in vacuo afforded a microcrystalline black solid which was washed with small amounts of *n*-hexane and dried *in vacuo*. Further purification can be achieved by recrystallization from boiling mesitylene. Yield: 95 mg (0.06 mmol, 80 %).  $^1\text{H}$  NMR ( $\text{C}_6\text{D}_6$ , r.t.):  $\delta_{\text{H}}$  [ppm] = 6.72 (s, mesitylene-CH), 2.20 (s, 30H, Cp\*), 2.16 (overlapping signals, s, mesitylene-CH<sub>3</sub>/Cp\*), 2.04 (s, 15H, Cp\*); -15.29 (s, 0.5H, hydride);  $^{13}\text{C}$  NMR ( $\text{C}_6\text{D}_6$ , r.t.):  $\delta_{\text{C}}$  [ppm] = 137.63 (mesitylene-C<sub>arom.</sub>), 127.38 (mesitylene-CH<sub>arom.</sub>), 93.01 (C<sub>5</sub>Me<sub>5</sub>), 90.11 (C<sub>5</sub>Me<sub>5</sub>), 84.60 (C<sub>5</sub>Me<sub>5</sub>), 21.33 (mesitylene-CH<sub>3</sub>), 13.44 (C<sub>5</sub>Me<sub>5</sub>), 13.16 (C<sub>5</sub>Me<sub>5</sub>), 13.10 (C<sub>5</sub>Me<sub>5</sub>). IR (ATR, neat, cm<sup>-1</sup>): 2964 (w), 2886 (m), 2849 (m), 2711 (w), 1674 (w), 1454 (m), 1371 (s), 1258 (w), 1154 (w), 1065 (w), 1023 (s), 985 (sh), 832 (vw), 795 (vw), 680 (w), 599 (w), 537 (w). MS (LIFDI, toluene): *m/z* 1599.9 ( $[\text{MI}]^+$ , calc. 1600.3 for x = 4), 1583.9 ( $[\text{MI-CH}]^+$ , calc. 1584.3 for x = 1), 1516.0 ( $[\text{MI-CH-Ga}]^+$ , calc. 1514.6 for x = 1), 1447.7 ( $[\text{MI-CH-Cp}^*]^+$ , calc. 1448.1). Anal. calc. for C<sub>61</sub>H<sub>91</sub>Co<sub>6</sub>Ga<sub>6</sub> (*M* = 1596.31 g mol<sup>-1</sup>): C 45.89; H 5.74; Co 22.15; Ga 26.21. Found: C 45.39; H 5.77; Co 22.12; Ga 26.37.

### Reaction of $[\text{Co}_6(\text{P}^i\text{Pr}_3)_6\text{H}_8]$ with AlCp\*.

A mixture of AlCp\* (37 mg, 0.227 mmol, 6 eq.) and  $[\text{Co}_6(\text{P}^i\text{Pr}_3)_6\text{H}_8]$  (50 mg, 0.038 mmol, 1 eq.) was suspended in benzene (4 ml) and heated to 60°C for 24h. The reaction mixture was allowed to settle for an additional 24h, upon which a black microcrystalline solid forms. The latter was isolated by cannula filtration, washed with small amounts of benzene and dried *in vacuo*. Yield: 12 mg. IR (ATR, neat, cm<sup>-1</sup>): 2960 (w), 2896 (m), 2851 (m), 1448 (m), 1371 (m), 1259 (w), 1152 (w), 1069 (w), 1022 (m), 797 (s), 707 (m), 672 (s), 478 (w), 447 (m). MS (LIFDI, toluene): *m/z* 838.9 ( $[\text{MI}]^+$ , unassigned), 610.6 ( $[\text{Co}_3\text{Cp}^*_3(\text{CH})_2]^+$ , calc. 608.5), 596.7 ( $[\text{Co}_3\text{Cp}^*_3(\text{CH})]^+$ , calc. 595.5), 584.4 ( $[\text{Co}_3\text{Cp}^*_3]^+$ , calc. 582.5).



**[Ni(cdt)(GaCp\*)] (7).**

GaCp\* (463 mg, 2.262 mmol) was added dropwise to a solution of [Ni(cdt)] (0.500 g, 2.262 mmol) in *n*-hexane (10 mL) at 0°C, whereupon an orange precipitate formed. The reaction mixture was stirred for 10 min and allowed to settle at -50°C. The orange precipitate was isolated by means of cannula filtration, washed twice with a small amount of *n*-hexane and dried *in vacuo*. For further purification, the product was dissolved in toluene and crystallized by slow cooling to -30°C. Yield: 0.771 g (1.810 mmol, 80.1%). Dec. 167°C. <sup>1</sup>H NMR (C<sub>6</sub>D<sub>6</sub>, r.t.):  $\delta_H$  [ppm] = 4.37 (m, 6H, CH), 2.33 (m, 6H, CH<sub>2</sub>), 1.95 and 1.92 (overlapping signals, 21H, Cp\*/CH<sub>2</sub>). <sup>13</sup>C NMR (C<sub>6</sub>D<sub>6</sub>, r.t.):  $\delta_C$  [ppm] = 113.57 (C<sub>5</sub>Me<sub>5</sub>), 102.86 (CH), 41.10 (CH<sub>2</sub>), 9.97 ppm (C<sub>5</sub>Me<sub>5</sub>). IR (ATR, neat, cm<sup>-1</sup>): 3004 (vw), 2961 (w), 2938 (w), 2880 (s), 2837 (s), 2816 (s), 2789 (s), 1508 (m), 1470 (w), 1413 (m), 1366 (m), 1312 (w), 1296 (m), 1262 (m), 1231 (m), 1187 (w), 1164 (w), 1016 (w), 969 (w), 935 (m), 902 (w), 878 (w), 862 (m), 840 (m), 786 (m), 585 (w), 541 (w), 499 (w), 449 (w), 408 (m). MS (LIFDI, toluene): *m/z* 425.4 ([MI]<sup>+</sup>, calc. 425.9), 275.9 ([Ni(GaCp\*)CH]<sup>+</sup>, calc. 276.6), 221.9 ([Ni(cdt)]<sup>+</sup>, calc. 221.0), 206.8 ([GaCp\*]<sup>+</sup>, calc. 204.9), 197.9 ([NiCp\*]<sup>+</sup>, calc. 193.9), 162.8 ([cdt]<sup>+</sup>, calc. 162.3). Anal. calc. for C<sub>22</sub>H<sub>33</sub>GaNi (M = 425.91 g/mol): C 62.04, H 7.81, Ga 16.37, Ni 13.78. Found: C 61.97, H 7.66, Ga, Ni not determined.

**[Ni<sub>8</sub>(GaCp\*)<sub>6</sub>] (8).**

Pathway A: A solution of [Ni(cdt)GaCp\*] (300 mg, 0.705 mmol) and GaCp\* (432 mg, 2.114 mmol) in toluene (6 ml) was heated to 120°C for 4h, whereupon a red microcrystalline precipitate formed. After cooling the resultant dark red reaction mixture to room temperature, the precipitate was isolated by means of cannula filtration, washed twice with a small amount of cold hexane and dried *in vacuo*. Purification of the crude product was achieved by slow crystallization from saturated solutions of **8** in mesitylene. Yield: 0.082 g (0.048 mmol, 54.8%). Pathway B: GaCp\* (288 mg, 1.41 mmol, 2.0 eq.) was added dropwise to a pre-cooled solution of [Ni(cdt)] (156 mg, 0.70 mmol, 1 eq.) in mesitylene (7 ml) at 0 °C. Stirring for 1h afforded a red suspension which was heated to 120 °C for an additional 4h. The resultant black precipitate was isolated by means of cannula filtration, washed with *n*-hexane and dried *in vacuo*. Purification of the crude product was achieved by extraction with boiling mesitylene. Analytically pure **8** crystallized as dark red needles upon slow cooling to room temperature. Yield: 31 mg (0.018 mmol, 20.5%). <sup>1</sup>H MAS NMR (neat, r.t.):  $\delta_H$  [ppm] = 6.71 (s, mesitylene-CH), 2.15 (br s, overlapping signals of Cp\*, mesitylene-CH<sub>3</sub>); <sup>13</sup>C MAS NMR (neat, r.t.):  $\delta_C$  [ppm] = 137.74 (mesitylene-C<sub>arom.</sub>), 129.12(mesitylene-C<sub>arom.</sub>), 98.10 (C<sub>5</sub>Me<sub>5</sub>), 22.33 (mesitylene-CH<sub>3</sub>), 13.22 (C<sub>5</sub>Me<sub>5</sub>). IR (ATR, neat, cm<sup>-1</sup>): 2986 (w), 2929 (w), 2881 (m), 2842 (m), 1421 (m), 1371 (s), 1258 (w), 1062 (w), 1019 (s), 941 (w), 797 (m), 679 (m). MS (LIFDI-TOF, toluene): *m/z* 1702.6 ([MI]<sup>+</sup>, calc. 1699.2),

1644.8 ( $[MI-Ni]^+$ , calc. 1640.5), 1574.6 ( $[MI-Ni-Ga]^+$ , calc. 1570.8). MS (LIFDI-Orbitrap, toluene):  $m/z$  1723.7 ( $[MI+Na]^+$ , calc. 1722.2), 1707.7 ( $[MI+Li]^+$ , calc. 1706.2), 1683.8 ( $[MI-Me]^+$ , calc. 1684.2), 1665.8 ( $[MI-2Me]^+$ , calc. 1669.2), 1649.8 ( $[MI-3Me]^+$ , calc. 1654.1), 1637.8 ( $[MI-4Me]^+$ , calc. 1639.1), 1531.6 ( $[MI-Cp^*-2Me]^+$ , calc. 1533.9). *Anal.* Calc. for  $C_{60}H_{90}Ga_6Ni_8$  ( $M = 1699.24$  g mol<sup>-1</sup>): C 42.41; H 5.34; Ga 24.62; Ni 27.63. Found: C 42.7, H 5.52, Ni 27.1, Ga 24.6.

### $[Cp^*Co(\mu-H)(Al(\kappa^2-(CH_2SiMe_2)NSiMe_3)(btsa))]$ (**9**).

A mixture of  $[Co(btsa)_2]$  (600 mg, 1.59 mmol) and  $AlCp^*$  (255 mg, 1.59 mmol) was suspended in toluene (15 ml) and heated to 80°C for 3h. After cooling to room temperature, all volatiles were removed under reduced pressure and the residue was dissolved in *n*-hexane (10 ml) and filtered. The red filtrate was concentrated *in vacuo* and kept at -30°C for crystallization. **9** was obtained as dark red needles within few days. Yield: 730 mg (1.35 mmol, 85 %). <sup>1</sup>H NMR ( $C_6D_6$ , r.t.):  $\delta_H$  [ppm] = 81.01 (vbr s,  $Cp^*$ ), 1.15 (s, *btsa*), 0.46 (s, *btsa*), -0.55 (s, *btsa*); <sup>13</sup>C NMR ( $C_6D_6$ , r.t.):  $\delta_C$  [ppm] = 9.58 - 4.30 (overlapping multiplets, *btsa*). IR (ATR, neat, cm<sup>-1</sup>): 2924 (m), 2882 (w), 2835 (w), 1632 (w), 1423 (w), 1386 (w), 1368 (w), 1232 (s), 1020 (s), 918 (m), 888 (s), 862 (s), 821 (vs), 770 (s), 741 (s), 667 (s), 632 (m), 613 (m), 561 (w), 527 (w), 478 (w), 443 (m), 396 (m), 374 (m). *Anal.* calc. for  $C_{22}H_{51}N_2CoAlSi_4$  ( $M = 541.91$  g mol<sup>-1</sup>): C 48.76; H 9.49; N 5.17; Si 20.73; Co 10.88; Al 4.98. Found: C 48.61; H 10.34; N 4.99; Si 20.41; Co 10.54; Al 4.84.

### $[(GaCp^*)Co(btsa)_2]$ (**10**).

At room temperature,  $GaCp^*$  (162 mg, 0.79 mmol) was added dropwise *via* syringe to a solution of  $[Co(btsa)_2]$  (300 mg, 0.79 mmol) in toluene (9 ml). The resulting green solution was stirred for 3h. Subsequent removal of all volatiles *in vacuo* gave crude **10** as a wax-like green solid with slight impurities. Attempts on further purification *via* crystallization failed due to the lability of the compound. Yield: 266 mg (0.45 mmol, 86 %). <sup>1</sup>H NMR ( $C_6D_6$ , r.t.):  $\delta_H$  [ppm] = 16.86 (br s, 15H,  $Cp^*$ ), -11.29 (br s, 36H, - $SiMe_3$ ); <sup>13</sup>C NMR ( $C_6D_6$ , r.t.):  $\delta_C$  [ppm] = 32.62 ( $C_5Me_5$ ), 2.66 (- $SiMe_3$ ). IR (ATR, neat, cm<sup>-1</sup>): 2950 (m), 2896 (m), 2857 (sh), 1475 (w), 1378 (m), 1246 (m), 1180 (w), 1079 (w), 999 (m), 927 (m), 818 (s), 750 (m), 717 (m), 667 (m), 618 (m), 488 (w).



### $[(\text{GaCp}^*)_2\text{Fe}(\text{btsa})_2]$ (**11**).

At room temperature, GaCp\* (385 mg, 1.88 mmol) was added dropwise *via* syringe to a solution of [Fe(btsa)<sub>2</sub>] (354 mg, 0.94 mmol) in toluene (8 ml). The resulting yellow-green solution was stirred for 3h. All volatiles were removed *in vacuo* and the wax-like, yellow-brown residue was dissolved in *n*-hexane and filtered. The filtrate was concentrated and kept at -30°C for crystallization. After isolation *via* cannula filtration and drying *in vacuo*, **11** was obtained as violet-brown crystals. Repeated concentration and work-up of the filtrate yields an additional amount of analytically pure **11**. Yield: 458 mg (0.58 mmol, 62 %). <sup>1</sup>H NMR (C<sub>6</sub>D<sub>6</sub>, r.t.):  $\delta_{\text{H}}$  [ppm] = 45.74 (br s, 30H, Cp\*), 0.38 (s, 36H, -SiMe<sub>3</sub>); <sup>13</sup>C NMR (C<sub>6</sub>D<sub>6</sub>, r.t.):  $\delta_{\text{C}}$  [ppm] = 245.5 (s, C<sub>5</sub>Me<sub>5</sub>), 88.7 (vbr s, C<sub>5</sub>Me<sub>5</sub>), 5.5 (q, -SiMe<sub>3</sub>); IR (ATR, neat, cm<sup>-1</sup>): 2920 (m), 2889 (w), 2839 (w), 1469 (w), 1409 (w), 1375 (w), 1227 (m), 958 (s), 818 (s), 770(m), 739 (m), 696 (m), 663 (m), 653 (m), 608 (m), 582 (m), 511(w). *Anal. calc.* for C<sub>32</sub>H<sub>66</sub>N<sub>2</sub>FeGa<sub>2</sub>Si<sub>4</sub> (*M* = 786.51 g mol<sup>-1</sup>): C 48.87; H 8.46; N 3.56; Si 14.28; Fe 7.10; Ga 17.73. Found: C 47.80; H 8.36; N 3.50; Si 13.44; Fe 8.13; Ga 15.60.

### $[\text{Zn}(\text{Al}(\eta^2\text{-Cp}^*)(\text{btsa}))_2]$ (**12**).

At room temperature, [Zn(btsa)<sub>2</sub>] (300 mg, 0.78 mmol) was added to a suspension of AlCp\* (252 mg, 1.55 mmol) in toluene (6 ml). The reaction mixture was heated to 60°C for 30 min. After cooling to room temperature, the resulting green suspension was filtered and kept at -30°C for crystallization. **12** was obtained in form of yellow plates, which were isolated *via* cannula filtration and dried *in vacuo*. Yield: 73 mg (0.11 mmol, 14 %). <sup>1</sup>H NMR (C<sub>6</sub>D<sub>6</sub>, r.t.):  $\delta_{\text{H}}$  [ppm] = 2.08 (s, 30H, Cp\*), 0.31 (s, 36H, -SiMe<sub>3</sub>); <sup>13</sup>C NMR (C<sub>6</sub>D<sub>6</sub>, r.t.): decomposition; <sup>29</sup>Si NMR (C<sub>6</sub>D<sub>6</sub>, r.t.):  $\delta_{\text{Si}}$  [ppm] = -4.08. IR (ATR, neat, cm<sup>-1</sup>): 2946 (m), 2901 (m), 2859 (w), 1419 (br, w), 1246 (s), 1028 (w), 939 (m), 867 (m), 826 (s), 756 (m), 719 (m), 672 (m), 641 (m), 616 (m), 595 (m), 455 (m), 433 (m).

### $[\text{Co}(\mu\text{-H})_4(\text{Al}(\eta^2\text{-Cp}^*)(\text{btsa}))_2]$ (**13**).

A mixture of [Co(btsa)<sub>2</sub>] (200 mg, 0.53 mmol) and [Cp\*AlH<sub>2</sub>] (173 mg, 1.05 mmol) was dissolved in toluene (6 ml), resulting in immediate gas evolution. The dark red solution was stirred at room temperature for 3h and the yellow, micro-crystalline precipitate was allowed to settle prior to filtration. Washing with toluene (2 x 1 ml) and drying *in vacuo* gave **13** in form of a yellow powder. Yield: 51 mg (0.07 mmol, 14 %). <sup>1</sup>H NMR (THF-d<sub>8</sub>, r.t.):  $\delta_{\text{H}}$  [ppm] = 1.85 (s, 6H), 1.80 (s, 6H), 1.73 (3H, overlapping with solvent residual signal), 0.40 (s, 2H), 0.19 (s, 3H), 0.11 (s, 9H), 0.04 (s, 3H); <sup>13</sup>C NMR (THF-d<sub>8</sub>, r.t.):

$\delta_C$  [ppm] = 119.3 (s), 90.3 (s), 90.0 (s), 13.1 (s), 13.0 (s), 12.4 (s), 6.3 (s), 6.1 (s), 6.0 (s), 5.7 (s). IR (ATR, neat,  $\text{cm}^{-1}$ ): 2927 (m), 2879 (w), 2839 (w), 1672 (m), 1430 (w), 1386 (w), 1366 (w), 1238 (m), 1126 (w), 1020 (w), 905 (m), 869 (s), 823 (s), 751 (m), 667 (m), 639 (m), 613 (w), 470 (m), 416 (m), 383 (m). *Anal.* calc. for  $\text{C}_{32}\text{H}_{70}\text{N}_2\text{CoAl}_2\text{Si}_4$  ( $M = 708.15 \text{ g mol}^{-1}$ ): C 54.27; H 9.96; N 3.96; Si 15.86; Co 8.32; Al 7.62. Found: C 54.22; H 9.84; N 3.95; Si 13.81; Co 8.26; Al 7.60.

### Reaction of $[\text{Cp}^*\text{Co}(\mu\text{-H})(\text{Al}(\kappa^2\text{-(CH}_2\text{SiMe}_2)\text{NSiMe}_3)(\text{btsa}))]$ (9) with HBpin - Synthesis of $[\text{Cp}^*_3\text{Co}_3(\mu\text{-CH})_2]$ .

At room temperature, HBpin (0.054 ml, 0.37 mmol) was added dropwise to a solution of  $[\text{Cp}^*\text{Co}(\mu\text{-H})(\text{Al}(\kappa^2\text{-(CH}_2\text{SiMe}_2)\text{NSiMe}_3)(\text{btsa}))]$  (100 mg, 0.18 mmol) in toluene (3 ml). The resulting dark red solution was stirred at  $80^\circ\text{C}$  for 8h. It was then cooled to room temperature, reduced to approx. 1/3 of its volume by partial evaporation of the solvent *in vacuo* and kept at  $-30^\circ\text{C}$  for crystallization.  $[\text{Cp}^*_3\text{Co}_3(\mu\text{-CH})_2]$  was obtained as almost black, rhombohedral crystals within few days. Yield: 21 mg (0.03 mmol, 56 %).  $^1\text{H}$  NMR ( $\text{C}_6\text{D}_6$ , r.t.):  $\delta_H$  [ppm] = 21.00 (br s, CH), 1.81 (s,  $\text{C}_5\text{Me}_5$ );  $^{13}\text{C}$  NMR ( $\text{C}_6\text{D}_6$ , r.t.):  $\delta_C$  [ppm] = 92.35 ( $\text{C}_5\text{Me}_5$ ), 12.05 ( $\text{C}_5\text{Me}_5$ ); IR (ATR, neat,  $\text{cm}^{-1}$ ): 2977 (m), 2892 (m), 2853 (sh), 2402 (m), 1428 (m), 1368 (s), 1248 (m), 1147 (m), 1069 (w), 1022 (m), 946 (m), 915 (m), 840 (s), 762 (m), 725 (m), 667 (m), 583 (w), 531 (w).

$[\text{Cp}^*_3\text{Co}_3(\mu\text{-CH})_2]$  is literature-known<sup>322</sup> and has been identified as such by single crystal X-ray diffraction analysis,  $^1\text{H}$  and  $^{13}\text{C}$  NMR spectroscopy and IR spectroscopy. The obtained analytical data is in good agreement with literature-reported data.

### Reaction of $[\text{Cp}^*\text{Co}(\mu\text{-H})(\text{Al}(\kappa^2\text{-(CH}_2\text{SiMe}_2)\text{NSiMe}_3)(\text{btsa}))]$ (9) with $[\text{NMe}_3\text{-AlH}_3]$ - Synthesis of $[\text{Cp}^*_2\text{Co}_2(\mu\text{-AlNMe}_3)_2\text{H}_4]$ (14).

A mixture of  $[\text{Cp}^*\text{Co}(\mu\text{-H})(\text{Al}(\kappa^2\text{-(CH}_2\text{SiMe}_2)\text{NSiMe}_3)(\text{btsa}))]$  (100 mg, 0.18 mmol) and  $[\text{NMe}_3\text{-AlH}_3]$  (33 mg, 0.37 mmol) was dissolved in toluene (1.5 ml), and stirred at room temperature for 2h. The resultant red-brown, microcrystalline solid was isolated by means of cannula filtration, washed with a minimal amount of toluene and dried *in vacuo*. Yield: 33 mg (0.06 mmol, 32 %).  $^1\text{H}$  NMR ( $\text{C}_6\text{D}_6$ , r.t.):  $\delta_H$  [ppm] = 2.08 (overlapping s, 30H,  $\text{C}_5\text{Me}_5$ ), 2.07 (overlapping s, 18H,  $\text{NMe}_3$ ), -19.97 (s, 4H, hydride);  $^{13}\text{C}$  NMR ( $\text{C}_6\text{D}_6$ , r.t.):  $\delta_C$  [ppm] = 88.56 ( $\text{C}_5\text{Me}_5$ ), 47.70 ( $\text{NMe}_3$ ), 11.95 ( $\text{C}_5\text{Me}_5$ ); IR (ATR, neat,  $\text{cm}^{-1}$ ): 2969 (w), 2948 (w), 2894 (m), 2845 (m), 1910 (br, w), 1716 (m), 1475 (m), 1454 (m), 1376 (m), 1248 (m), 1098 (w), 1067 (w), 1026 (w), 1005 (m), 802 (m), 748 (m), 694 (m), 639 (s),

480 (m), 433 (w); *Anal.* calc. for  $C_{26}H_{52}N_2CoAl_2$  ( $M = 564.53 \text{ g mol}^{-1}$ ): C 55.31; H 9.28; N 4.96; Co 20.88; Al 9.56. Found: C 52.74; H 9.21; N 4.39; Co, Al not determined.

Reaction of  $[Cp^*Co(\mu-H)(Al(\kappa^2-(CH_2SiMe_2)NSiMe_3)(btsa))]$  (**9**) with  $LiAlH_4$  -side formation of  $[Al_3H_4(\mu-H)(\kappa^2-(CH_2SiMe_2)NSiMe_3)_2]$  (**15**).

At  $-80^\circ\text{C}$ ,  $LiAlH_4$  (4M in  $Et_2O$ , 0.065 ml) was added dropwise to a solution of  $[Cp^*Co(\mu-H)(Al(\kappa^2-(CH_2SiMe_2)NSiMe_3)(btsa))]$  (70.0 mg, 0.13 mmol) in toluene (5 ml), whereupon gas evolution occurred. The deep red solution was stirred for 10 min at  $-80^\circ\text{C}$ , and allowed to warm up to room temperature. Stirring for an additional 1h affords an off-white precipitate which was isolated by removal of all volatiles in vacuo, washed with *n*-hexane and dried *in vacuo*. Yield: 51 mg.  $^1\text{H}$  NMR (THF- $d_8$ , r.t.):  $\delta_H$  [ppm] = 1.77 (s, 15H,  $C_5Me_5$ ), 0.04 (s, 18H,  $SiMe_3$ ), -21.97 (br s, 2H, *hydride*);  $^{13}\text{C}$  NMR (THF- $d_8$ , r.t.):  $\delta_C$  [ppm] = 83.35 ( $C_5Me_5$ ), 8.12 ( $C_5Me_5$ ), 2.42 ( $SiMe_3$ ); IR (ATR, neat,  $\text{cm}^{-1}$ ): 2955 (w), 2901 (w), 1683 (br m), 1469 (br m), 1384 (m), 1248 (m), 902 (s), 838 (s), 667 (vs), 595 (s), 422 (w).

Few crystals of **15** were obtained from the combined hexane filtrates, which were reduced in volume and kept at  $-30^\circ\text{C}$  for several days.

## 6.3 Supplementary data

### 6.3.1 Computational details

#### Computational details for the theoretical investigation of $[\text{Cu}_{43}(\text{AlCp}^*)_{12}]$ (**3**)

*Quantum chemical calculations on the model compound  $[\text{Cu}_{43}(\text{AlCp})]$  (**3'**) were performed by the group of Prof. Dr. Jean-Yves Saillard, particularly involving Dr. Rémi Marchal and Dr. Samia Kahlal, Institut des Sciences Chimiques de Rennes, France. For more detailed information on, please refer to Prof. Dr. Jean-Yves Saillard ([jean-yves.saillard@univ-rennes1.fr](mailto:jean-yves.saillard@univ-rennes1.fr)) directly.*

Density functional theory (DFT) calculations were carried out by using the ADF code.<sup>420-422</sup> The Becke-Perdew (BP86) exchange functional<sup>423-426</sup> was employed, together with the standard STO-TZP basis set of ADF. Frozen core approximation was applied to the  $[1s^2-3p^6]$  inner electrons for Cu,  $[1s^2-2p^6]$  for Al and  $[1s^2]$  for C, leaving the remaining electrons to be treated variationally. Geometry optimizations were performed via the analytical energy gradient method implemented by Versluis and Ziegler.<sup>427</sup> Since the ADF program does not recognize the  $I_h$  symmetry, its  $D_{5d}$  subgroup was assumed for the computed models. Since no significant deviation away from  $I_h$  symmetry occurred, the results were analyzed within  $I_h$  symmetry.

#### Geometry optimizations of $[\text{Au}_7(\text{AlMe})_6\text{H}]$ (**4'**), $[\text{Au}_8(\text{AlMe})_6]$ (**4''**) and $[\text{Ni}_8(\text{GaMe}_3)_6]$ (**8'**)

*Geometry optimizations of **4'**, **4''** and **8'** were performed by M.Sc. Julius Hornung, Chair of Inorganic and Metal-Organic Chemistry, TUM, and are part of his PhD studies.*

Starting from the cubic shape obtained by single crystal X-ray diffraction analysis of **4** and **8**, respectively, the geometries of  $[\text{Au}_7(\text{AlMe})_6\text{H}]$  (**4'**),  $[\text{Au}_8(\text{AlMe})_6]$  (**4''**) and  $[\text{Ni}_8(\text{GaMe}_3)_6]$  (**8'**) were freely optimized using the ORCA 4.0 software package,<sup>428</sup> and Becke's exchange functional<sup>424</sup> with Perdew's correlation functional (BP86).<sup>425</sup> In addition, Grimme's Dispersion correction including Becke-Johnson damping (D3BJ) was used.<sup>429, 430</sup> After pre-optimization and analytical calculation of the Hessian using Ahlrich's def2-SVP basis set, the resulting structure was further optimized using the def2-TZVPP basis set.<sup>431</sup> To speed up the calculations, the resolution of identity approximation (RI) was applied.<sup>432</sup> The cartesian coordinates of the thus optimized structures are given in table 10-12, figure 63 shows the optimized structure of **4''**.

Table 10. Cartesian coordinates of the optimized structure of  $[\text{Au}_7(\text{AlMe})_6\text{H}]$  (**4'**).

	<b>x</b>	<b>y</b>	<b>z</b>
<b>Au</b>	14.581062	6.721404	5.828204
<b>Au</b>	14.791089	8.732275	3.893424
<b>Au</b>	14.640315	8.881916	8.290445
<b>Al</b>	16.688363	10.05797	2.927376
<b>Al</b>	13.235552	8.867047	6.071393
<b>Au</b>	17.336263	6.950053	5.396677
<b>Au</b>	17.816552	8.727046	7.505443
<b>H</b>	17.787209	8.56925	2.589001
<b>Al</b>	16.338336	10.790693	7.680221
<b>Al</b>	18.801553	8.578748	4.174289
<b>Au</b>	17.47793	10.397107	5.285038
<b>Al</b>	16.175923	6.806319	7.808953
<b>Au</b>	14.751233	10.875252	5.693245
<b>Al</b>	16.573429	7.197517	3.019789
<b>C</b>	11.402125	8.964777	6.78473
<b>C</b>	16.561157	5.925375	1.531442
<b>C</b>	20.691833	8.48397	3.672637
<b>C</b>	16.202109	11.942107	9.272499
<b>C</b>	16.781849	11.238521	1.368047
<b>C</b>	15.952675	5.776205	9.472952
<b>H</b>	10.68462	8.966534	5.949257
<b>H</b>	11.244691	9.881875	7.369963
<b>H</b>	11.172514	8.103651	7.428218
<b>H</b>	15.180033	12.322939	9.409205
<b>H</b>	16.874941	12.806304	9.157197
<b>H</b>	16.49284	11.404461	10.186152
<b>H</b>	20.987835	9.344265	3.055374
<b>H</b>	20.913967	7.564018	3.113106
<b>H</b>	21.319915	8.487196	4.575964
<b>H</b>	15.860741	5.104385	1.745659
<b>H</b>	17.555504	5.484494	1.371243
<b>H</b>	16.240199	6.404215	0.595264
<b>H</b>	14.903744	5.488505	9.632121
<b>H</b>	16.288565	6.347403	10.350012
<b>H</b>	16.553579	4.855079	9.415793
<b>H</b>	16.422694	10.736583	0.458203
<b>H</b>	17.810208	11.583854	1.189012

Table 11. Cartesian coordinates of the optimized structure of  $[\text{Au}_8(\text{AlMe})_6]$  (**4''**).

	<b>x</b>	<b>y</b>	<b>z</b>
<b>Au</b>	14.936469	7.044478	5.606051
<b>Au</b>	14.620313	8.740002	3.403494
<b>Au</b>	14.183931	8.869815	9.049717
<b>Au</b>	17.814688	10.734818	5.118979
<b>Au</b>	15.057427	10.497417	5.535813
<b>Au</b>	17.669095	6.599848	5.204147
<b>Au</b>	17.603675	8.710091	7.039577
<b>Au</b>	17.745312	8.616499	2.718669
<b>Al</b>	15.914099	10.362956	7.895212
<b>Al</b>	19.211204	8.610295	4.907396
<b>Al</b>	15.80467	7.214402	7.958841
<b>Al</b>	16.06803	6.647597	3.218648
<b>Al</b>	16.210621	10.716594	3.135269
<b>Al</b>	13.482323	8.844619	6.587305
<b>C</b>	11.523197	8.911333	6.493084
<b>C</b>	16.20018	5.496816	1.627771
<b>C</b>	21.060694	8.531544	4.239673
<b>C</b>	16.299591	11.89327	9.061859
<b>C</b>	16.419931	11.789339	1.498735
<b>C</b>	16.084975	5.709436	9.186841
<b>H</b>	11.214857	8.900608	5.435909
<b>H</b>	11.124198	9.826804	6.952826
<b>H</b>	11.061693	8.045554	6.989153
<b>H</b>	16.714589	11.574131	10.028596
<b>H</b>	15.400507	12.496244	9.253467
<b>H</b>	17.043276	12.540022	8.570475
<b>H</b>	21.295874	9.401164	3.609518
<b>H</b>	21.233716	7.621991	3.646861
<b>H</b>	21.763641	8.524768	5.087121
<b>H</b>	15.528254	4.631293	1.736048
<b>H</b>	17.223368	5.118316	1.49185
<b>H</b>	15.911701	6.039578	0.716271
<b>H</b>	15.146723	5.177987	9.401025
<b>H</b>	16.522062	6.037958	10.140609
<b>H</b>	16.781851	4.99388	8.723
<b>H</b>	15.810071	12.70324	1.570857
<b>H</b>	16.092775	11.231228	0.609852
<b>H</b>	17.466749	12.089838	1.348658

Table 12. Cartesian coordinates of the optimized structure of  $[\text{Ni}_8(\text{GaMe}_3)_6]$  (**8'**).

	<b>x</b>	<b>y</b>	<b>z</b>
<b>Ni</b>	-5.048441	1.95489	-0.588382
<b>Ni</b>	-2.74763	2.615561	-0.169644
<b>Ni</b>	-3.251369	0.271339	-0.617316
<b>Ni</b>	-5.514502	-0.325265	0.110888
<b>Ni</b>	-3.409093	1.920032	-2.425505
<b>Ni</b>	-2.792385	-0.393469	-2.924412
<b>Ni</b>	-5.76119	2.408355	-2.865943
<b>Ni</b>	-5.083151	0.139894	-2.25055
<b>Ga</b>	-3.971607	1.125871	1.425187
<b>Ga</b>	-7.094019	0.894151	-1.354201
<b>Ga</b>	-4.063799	-1.810985	-1.386336
<b>Ga</b>	-1.318268	1.124781	-1.693707
<b>Ga</b>	-4.214312	3.965161	-1.668748
<b>Ga</b>	-4.315073	0.892714	-4.348773
<b>C</b>	0.638378	1.423463	-1.489471
<b>C</b>	-4.676362	1.070329	-6.296572
<b>C</b>	-9.055363	1.121979	-1.122051
<b>C</b>	-4.089479	1.437916	3.385624
<b>C</b>	-4.280429	-3.753043	-1.010777
<b>C</b>	-4.461364	5.934247	-1.548257
<b>H</b>	-4.028427	0.37616	-6.846702
<b>H</b>	-4.46513	2.096652	-6.619562
<b>H</b>	-5.725522	0.827142	-6.502585
<b>H</b>	-5.316227	-4.05504	-1.206176
<b>H</b>	-4.026898	-3.959748	0.035813
<b>H</b>	-3.607345	-4.321472	-1.66535
<b>H</b>	0.889868	2.448388	-1.787246
<b>H</b>	1.178042	0.716222	-2.132093
<b>H</b>	0.930808	1.260202	-0.445475
<b>H</b>	-5.212211	6.151406	-0.777903
<b>H</b>	-4.808312	6.325192	-2.512272
<b>H</b>	-3.513423	6.413184	-1.275528
<b>H</b>	-4.825917	2.228947	3.575914
<b>H</b>	-3.112281	1.75305	3.770917
<b>H</b>	-4.406259	0.518355	3.892075
<b>H</b>	-9.52808	1.291598	-2.096956
<b>H</b>	-9.238952	1.989353	-0.475334
<b>H</b>	-9.482218	0.225552	-0.656548

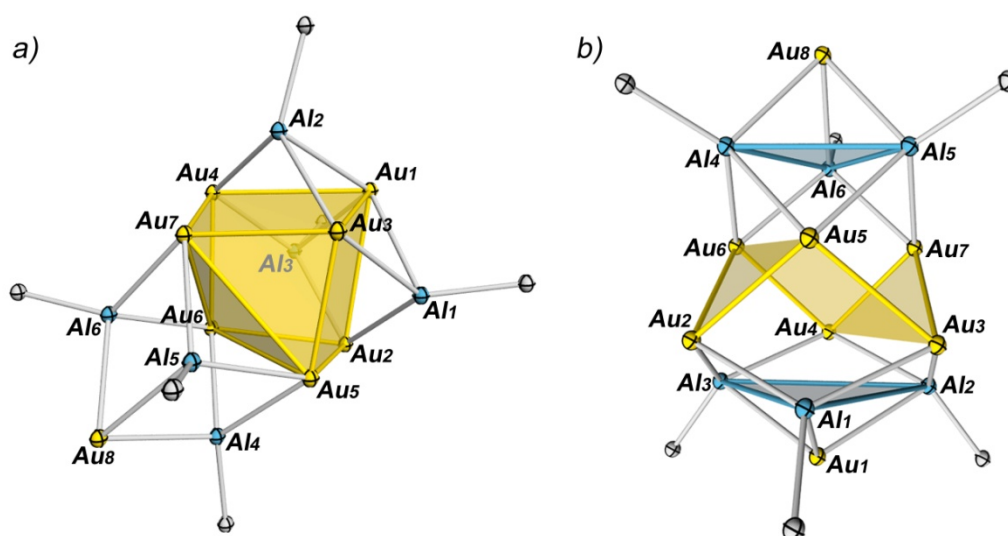


Figure 63. Different views on the optimized molecular structure of  $[\text{Au}_8(\text{AlMe}_6)]$  ( $4''$ ) as obtained from geometry optimization at the BP86-D3/TZVPP level of theory. The result was confirmed as a local minimum by frequency calculations.



## 6.3.2 Crystallographic data

Table 13. Crystallographic data of compounds 1-3.

	<b>1</b> · C <sub>6</sub> H <sub>6</sub> <sup>11</sup>	<b>2</b> · 3C <sub>6</sub> H <sub>6</sub> <sup>11</sup>	<b>3</b> · 6 C <sub>6</sub> H <sub>6</sub>
Empirical formula	C <sub>66</sub> H <sub>100</sub> Al <sub>6</sub> Cu <sub>6</sub>	C <sub>85</sub> H <sub>117</sub> Al <sub>6</sub> Cu <sub>6</sub> N	C <sub>156</sub> H <sub>216</sub> Al <sub>12</sub> Cu <sub>43</sub>
Formula weight	1436.58	1695.92	5147.26
Temperature [K]	100(2)	100(2)	101(2)
λ [Å]	1.54184	1.54184	1.54184
Crystal size [mm <sup>3</sup> ]	0.08 × 0.10 × 0.14	0.06 × 0.09 × 0.15	0.07 × 0.10 × 0.11
Crystal system	Monoclinic	Triclinic	Cubic
Space group	<i>I2/m</i>	<i>P-1</i>	<i>Im-3</i>
a [Å]	12.7283(2)	13.6197(4)	20.2549(1)
b [Å]	18.1126(3)	13.7220(3)	20.2549(1)
c [Å]	15.2699(3)	22.7748(5)	20.2549(1)
α [°]	90	92.374(2)	90
β [°]	91.013(1)	94.753(2)	90
γ [°]	90	95.926(2)	90
Volume [Å <sup>3</sup> ]	3519.91(11)	4213.70(18)	8309.79(12)
Z	2	2	2
ρ <sub>calc</sub> [g/cm <sup>3</sup> ]	1.355	1.337	2.057
μ [mm <sup>-1</sup> ]	2.963	2.565	6.643
F(000)	1496	1772	5110
θ range [°]	3.79 - 74.25	3.24 - 74.37	3.085 - 74.014
Index ranges	-15 ≤ h ≤ 15 -22 ≤ k ≤ 22 -18 ≤ l ≤ 18	-17 ≤ h ≤ 17 -17 ≤ k ≤ 17 -28 ≤ l ≤ 28	-23 ≤ h ≤ 24 -24 ≤ k ≤ 16 -17 ≤ l ≤ 17
Reflections collected/unique	54154/3686	28897/28897	11127/1494
R <sub>int</sub>	0.0697	0.0730	0.0197
Reflections observed [I ≥ 2σ]	3281	24849	1107
Data/restraints/parameters	3686/102/167	28897/96/918	1494/156/130
Goodness-of-fit on F <sup>2</sup>	1.075	1.096	1.909
Final R indexes [I ≥ 2σ]	0.0635	0.0635	0.1207
wR <sub>2</sub> [all data]	0.1674	0.1931	0.4290
ΔF <sub>max</sub> , ΔF <sub>min</sub> [e Å <sup>-3</sup> ]	0.794, -0.682	1.225, -0.939	3.942, -0.763

Table 14. Crystallographic data of compounds 4-6.

	<b>4</b>	<b>5</b>	<b>6</b>
Empirical formula	C <sub>60</sub> H <sub>90</sub> Al <sub>6</sub> Au <sub>6.44</sub>	C <sub>77</sub> H <sub>105</sub> Al <sub>5</sub> Au <sub>8</sub> N <sub>2</sub>	C <sub>61</sub> H <sub>91</sub> Co <sub>6</sub> Ga <sub>6</sub>
Formula weight	2241.66	2769.26	1596.23
Temperature [K]	100(2)	110(2)	100(2)
$\lambda$ [Å]	0.71073	1.54178	1.54178
Crystal size [mm <sup>3</sup> ]	0.091 × 0.117 × 0.168	0.050 × 0.058 × 0.134	0.027 × 0.046 × 0.137
Crystal system	Monoclinic	Triclinic	Monoclinic
Space group	<i>C2/m</i>	<i>P-1</i>	<i>C2/c</i>
a [Å]	19.8994(11)	13.8170(3)	44.0717(15)
b [Å]	17.4668(9)	14.4666(4)	13.3580(5)
c [Å]	12.9838(7)	20.4715(5)	22.7079(8)
$\alpha$ [°]	90	90.429(2)	90
$\beta$ [°]	124.475(2)	92.7636(17)	103.245(2)
$\gamma$ [°]	90	104.324(2)	90
Volume [Å <sup>3</sup> ]	3720.3(4)	3959.34(17)	13012.8(8)
Z	2	2	8
$\rho_{\text{calc}}$ [g/cm <sup>3</sup> ]	2.001	2.323	1.630
$\mu$ [mm <sup>-1</sup> ]	12.751	27.966	14.575
F(000)	2074	2556	6440
$\theta$ range [°] of data collection	2.332 - 25.022	3.306 - 74.271	3.465 - 66.595
Index ranges	-23 ≤ h ≤ 23 -20 ≤ k ≤ 20 -15 ≤ l ≤ 15	-11 ≤ h ≤ 17 -17 ≤ k ≤ 18 -25 ≤ l ≤ 25	-52 ≤ h ≤ 52 -15 ≤ k ≤ 15 -26 ≤ l ≤ 26
Reflections collected/unique	67711/3408	28599/15630	61000/11494
R <sub>int</sub>	0.0723	0.0320	0.0715
Reflections observed [I ≥ 2σ]	2819	13765	9373
Data/restraints/parameters	3408/178/363	15630/602/1040	11494/765/995
Goodness-of-fit on F <sup>2</sup>	1.083	1.029	1.041
Final R indexes [I ≥ 2σ]	0.0286	0.0309	0.0544
wR <sub>2</sub> [all data]	0.0713	0.0799	0.1416
$\Delta F_{\text{max}}, \Delta F_{\text{min}}$ [e Å <sup>-3</sup> ]	1.198, -0.809	2.537, -2.936	1.014 - -0.913

Table 15. Crystallographic data of compounds 7-9.

	7	8· 2(C <sub>9</sub> H <sub>12</sub> )	9
Empirical formula	C <sub>22</sub> H <sub>33</sub> GaNi	C <sub>78</sub> H <sub>114</sub> Ga <sub>6</sub> Ni <sub>8.37</sub>	C <sub>22</sub> H <sub>51</sub> AlCoN <sub>2</sub> Si <sub>4</sub>
Formula weight	425.91	1961.22	541.92
Temperature [K]	100(2)	100(2)	110(2)
$\lambda$ [Å]	1.54178	0.71073	1.54184
Crystal size [mm <sup>3</sup> ]	0.080 × 0.129 × 0.217	0.035 × 0.073 × 0.111	0.08 × 0.09 × 0.20
Crystal system	Monoclinic	Triclinic	Monoclinic
Space group	<i>Pm</i>	<i>P-1</i>	<i>P2<sub>1</sub>/n</i>
a [Å]	8.453(4)	12.481(11)	12.4018(2)
b [Å]	13.432(4)	12.756(10)	18.4650(3)
c [Å]	17.910(6)	14.179(12)	14.0269(2)
$\alpha$ [°]	90	88.05(4)	90.00
$\beta$ [°]	91.894	63.73(4)	104.914(2)
$\gamma$ [°]	90	66.35(3)	90.00
Volume [Å <sup>3</sup> ]	2032.5(12)	1910(3)	3103.94(8)
Z	4	1	4
$\rho_{\text{calc}}$ [g/cm <sup>3</sup> ]	1.384	1.705	1.160
$\mu$ [mm <sup>-1</sup> ]	2.742	4.125	6.167
F(000)	890	1002	1172
$\theta$ range [°] of data collection	3.290 - 74.518	2.189 - 25.011	4.05 - 76.24
Index ranges	-10 ≤ h ≤ 10 0 ≤ k ≤ 16 0 ≤ l ≤ 22	-14 ≤ h ≤ 14 -15 ≤ k ≤ 15 -16 ≤ l ≤ 16	-15 ≤ h ≤ 14 -20 ≤ k ≤ 23 -17 ≤ l ≤ 12
Reflections collected/unique	7470/7470	41532/6697	14115/6364
R <sub>int</sub>	0.0563	0.0452	0.0257
Reflections observed [I ≥ 2σ]	6266	5511	5554
Data/restraints/parameters	7470/434/582	6697/538/672	6364/145/395
Goodness-of-fit on F <sup>2</sup>	1.020	1.124	1.047
Final R indexes [I ≥ 2σ]	0.0607	0.0697	0.0350
wR <sub>2</sub> [all data]	0.1598	0.1677	0.0902
$\Delta F_{\text{max}}, \Delta F_{\text{min}}$ [e Å <sup>-3</sup> ]	0.901, -1.156	1.101, -1.379	0.327, -0.697

Table 16. Crystallographic data of compounds **10-12**.

	<b>10</b>	<b>11</b>	<b>12</b>
Empirical formula	C <sub>22</sub> H <sub>5</sub> GaCoN <sub>2</sub> Si <sub>4</sub>	C <sub>32</sub> H <sub>66</sub> FeGa <sub>2</sub> N <sub>2</sub> Si <sub>4</sub>	C <sub>32</sub> H <sub>66</sub> Al <sub>2</sub> N <sub>2</sub> Si <sub>4</sub> Zn
Formula weight	584.66	786.52	710.56
Temperature [K]	108(2)	112(2)	113(2)
$\lambda$ [Å]	1.54184	1.54184	1.54184
Crystal size [mm <sup>3</sup> ]	0.12 × 0.17 × 0.23	0.14 × 0.17 × 0.26	0.06 × 0.12 × 0.17
Crystal system	Monoclinic	Orthorhombic	Triclinic
Space group	<i>P2<sub>1</sub>/c</i>	<i>Pbcn</i>	<i>P-1</i>
a [Å]	16.8275(2)	16.3997(3)	8.5944(5)
b [Å]	21.4098(2)	15.1616(2)	9.6962(5)
c [Å]	18.8062(2)	16.9223(3)	14.0679(9)
$\alpha$ [°]	90.00	90.00	93.962(5)
$\beta$ [°]	106.8760(10)	90.00	106.393(5)
$\gamma$ [°]	90.00	90.00	112.654(5)
Volume [Å <sup>3</sup> ]	6483.59(12)	4207.66(11)	1016.74(10)
Z	8	4	1
$\rho_{\text{calc}}$ [g/cm <sup>3</sup> ]	1.198	1.242	1.160
$\mu$ [mm <sup>-1</sup> ]	6.518	5.469	2.545
F(000)	2488	1664	384
$\theta$ range [°] of data collection	3.43 - 76.33	3.97 - 76.31	3.34 - 76.35
Index ranges	-21 ≤ h ≤ 21 -22 ≤ k ≤ 26 -22 ≤ l ≤ 23	-11 ≤ h ≤ 20 -17 ≤ k ≤ 18 -18 ≤ l ≤ 21	-10 ≤ h ≤ 7 -12 ≤ k ≤ 11 -16 ≤ l ≤ 17
Reflections collected/unique	31094/13339	11783/4346	7520/4172
R <sub>int</sub>	0.0279	0.0193	0.0278
Reflections observed [I ≥ 2 $\sigma$ ]	11306	4004	3490
Data/restraints/parameters	13339/6/575	4346/0/197	4172/0/198
Goodness-of-fit on F <sup>2</sup>	1.023	1.037	1.044
Final R indexes [I ≥ 2 $\sigma$ ]	0.0338	0.0252	0.0354
wR <sub>2</sub> [all data]	0.0880	0.0683	0.0970
$\Delta F_{\text{max}}, \Delta F_{\text{min}}$ [e Å <sup>-3</sup> ]	0.889, -0.531	0.318, -0.408	0.681/-0.484

Table 17. Crystallographic data of compounds **13-15**.

	<b>13</b>	<b>14</b>	<b>15</b>
Empirical formula	C <sub>32</sub> H <sub>7</sub> Al <sub>2</sub> CoN <sub>2</sub> Si <sub>4</sub>	C <sub>26</sub> H <sub>48</sub> Al <sub>2</sub> Co <sub>2</sub> N <sub>2</sub>	C <sub>12</sub> H <sub>39</sub> Al <sub>3</sub> N <sub>2</sub> Si <sub>4</sub>
Formula weight [g/mol]	708.16	560.48	404.75
Temperature [K]	100(2)	100(2)	100(2)
$\lambda$ [Å]	0.71073	0.71073	0.71073
Crystal size [mm <sup>3</sup> ]	0.04 × 0.10 × 0.17	0.029 × 0.031 × 0.072	0.079 × 0.133 × 0.522
Crystal system	Triclinic	Triclinic	Monoclinic
Space group	<i>P</i> -1	<i>P</i> -1	<i>P</i> 2(1)
a [Å]	8.6323(3)	9.1431(8)	9.042(4)
b [Å]	106.1040(10)	9.3554(8)	10.825(5)
c [Å]	13.9237(5)	17.9644(14)	12.268(6)
$\alpha$ [°]	94.067(2)	104.600(4)	90
$\beta$ [°]	106.8760(10)	102.012(4)	92.76(2)
$\gamma$ [°]	113.1350(10)	91.311(4)	90
Volume [Å <sup>3</sup> ]	1001.20(6)	1449.8(2)	119.4(9)
Z	1	2	2
$\rho_{\text{calc}}$ [g/cm <sup>3</sup> ]	1.175	1.284	1.121
$\mu$ [mm <sup>-1</sup> ]	0.615	1.220	0.355
F(000)	385	596	440
$\theta$ range [°] for data collection	2.35 - 35.63	2.257 - 25.350	1.662 - 25.391
Index ranges	-14 ≤ h ≤ 14 -15 ≤ k ≤ 15 -22 ≤ l ≤ 22	-11 ≤ h ≤ 11 -11 ≤ k ≤ 11 -21 ≤ l ≤ 21	-10 ≤ h ≤ 10 -12 ≤ k ≤ 13 -14 ≤ l ≤ 14
Reflections collected/unique	64049/9232	48687/5299	42479/4367
R <sub>int</sub>	0.0473	0.0500	0.0283
Reflections observed [I ≥ 2σ]	7434	4693	4216
Data/restraints/parameters	9232/0/206	5299/60/306	4367/1/220
Goodness-of-fit on F <sup>2</sup>	1.035	1.108	1.073
Final R indexes [I ≥ 2σ]	0.0344	0.0684	0.0186
wR <sub>2</sub> [all data]	0.0776	0.2188	0.0481
$\Delta F_{\text{max}}, \Delta F_{\text{min}}$ [e Å <sup>-3</sup> ]	0.613/-0.421	2.699, -0.898	0.233, -0.130

### 6.3.3 Synthetic procedure and molecular structure of $[\text{Ga}_{10}(\text{CoCp}^*)_6]^{320}$

Single crystal X-ray diffraction data of  $[\text{Ga}_{10}(\text{CoCp}^*)_6]$  was collected and refined by Dr. Mariusz Molon during his PhD studies under supervision of Prof. Dr. Roland A. Fischer at the Chair of Inorganic Chemistry II, Ruhr-University Bochum.

#### Synthetic protocol for $[\text{Ga}_{10}(\text{CoCp}^*)_6]$ :

At  $-70\text{ }^\circ\text{C}$ , a solution of  $\text{GaCp}^*$  (369 mg, 1.80 mmol) in THF (3 ml) was added dropwise to as suspension of  $\text{CoCl}_2$  (58 mg, 0.45 mmol) and activated Mg turnings (20 mg, 0.83 mmol) in THF (2 ml). The reaction mixture was allowed to warm up to room temperature and stirred for 2h. Removal of all volatiles *in vacuo* and extraction of the residue with pentane (2 x 5 ml) afforded a blue solution which was reduced in volume and kept at  $-30\text{ }^\circ\text{C}$  for crystallization. Black prisms of  $[\text{Ga}_{10}(\text{CoCp}^*)_6]$  were obtained within few days.

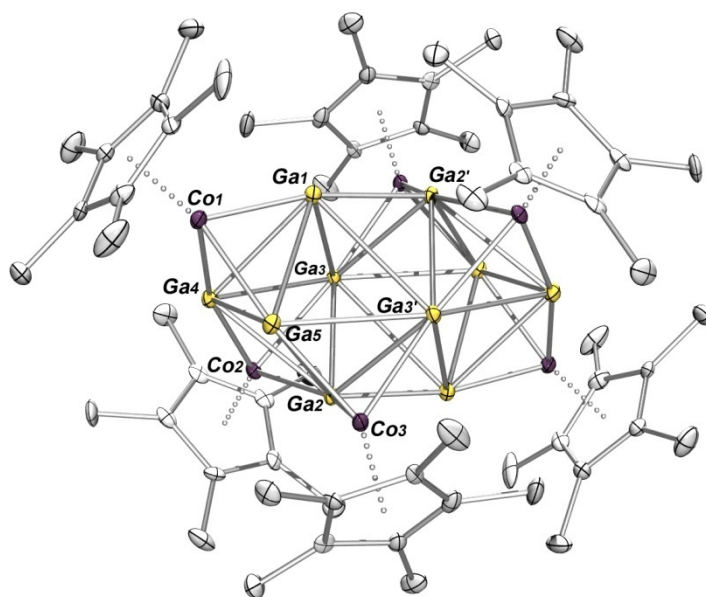


**Figure 64.** Molecular structure of  $[\text{Ga}_{10}(\text{CoCp}^*)_6]$  in the solid state with Ga, Co and C depicted in yellow, violet and grey, respectively. Displacement ellipsoids are shown on the 30 % probability level, hydrogen atoms are omitted for clarity. Selected interatomic distances ( $\text{\AA}$ ) and angles (deg): Ga(1)-Ga(2') 2.481(2), Ga(1)-Ga(3) 3.109(1), Ga(1)-Ga(3') 3.115(1), Ga(1)-Ga(4) 2.814(1), Ga(1)-Ga(5) 2.792(2), Ga(2)-Ga(3) 2.840(2), Ga(2)-Ga(3') 2.891(2), Ga(2)-Ga(4) 2.875(2), Ga(2)-Ga(5) 2.848(2), Ga(3)-Ga(3') 4.087(1), Ga(3)-Ga(4) 2.965(1), Ga(3')-Ga(5) 2.965(1), Ga(4)-Ga(5) 2.842(1), Co-Ga av. 2.311, Co-Cp\*<sub>centr.</sub> av. 1.708, Ga(3)-Ga(1)-Ga(5) 98.78(4), Ga(3')-Ga(1)-Ga(4) 100.14(4), Ga(3)-Ga(2)-Ga(5) 104.07(4), Ga(3')-Ga(2)-Ga(4) 104.22(4), Ga(4)-Ga(3)-Ga(5) 155.74(4), Ga(3)-Ga(4)-Ga(5) 101.09(4), Ga(3')-Ga(5)-Ga(4) 103.16(4), Ga<sub>plane</sub>-Co-Cp\*<sub>centr.</sub> 173.4.

Table 18. Crystallographic data of  $[\text{Ga}_{10}(\text{CoCp}^*)_6]$ .

	<b><math>[\text{Ga}_{10}(\text{CoCp}^*)_6]</math></b>
Empirical formula	$\text{C}_{60}\text{H}_{90}\text{Co}_6\text{Ga}_6$
Formula weight [g/mol]	1862.10
Temperature [K]	105(2)
$\lambda$ [Å]	0.71073
Crystal size [ $\text{mm}^3$ ]	0.09 × 0.22 × 0.23
Crystal system	Monoclinic
Space group	$P\ 21/n$
a [Å]	12.6873(6)
b [Å]	14.5039(8)
c [Å]	19.3928(10)
$\alpha$ [°]	90
$\beta$ [°]	94.409(5)
$\gamma$ [°]	90
Volume [Å <sup>3</sup> ]	3558.0(3)
Z	2
$\rho_{\text{calc}}$ [g/cm <sup>3</sup> ]	1.738
$\mu$ [mm <sup>-1</sup> ]	5.104
F(000)	1844
$\theta$ range [°] for data collection	2.91 - 25.00
Index ranges	-15 ≤ h ≤ 15 -17 ≤ k ≤ 17 -23 ≤ l ≤ 21
Reflections collected/unique	37233/6257
$R_{\text{int}}$	0.1158
Reflections observed [ $I \geq 2\sigma$ ]	4485
Data/restraints/parameters	6257/0/343
Goodness-of-fit on $F^2$	1.059
Final R indexes [ $I \geq 2\sigma$ ]	0.0628
wR <sub>2</sub> [all data]	0.1370
$\Delta F_{\text{max}}, \Delta F_{\text{min}}$ [e Å <sup>-3</sup> ]	0.941, -0.761

## 6.3.4 Supplementary analytical data

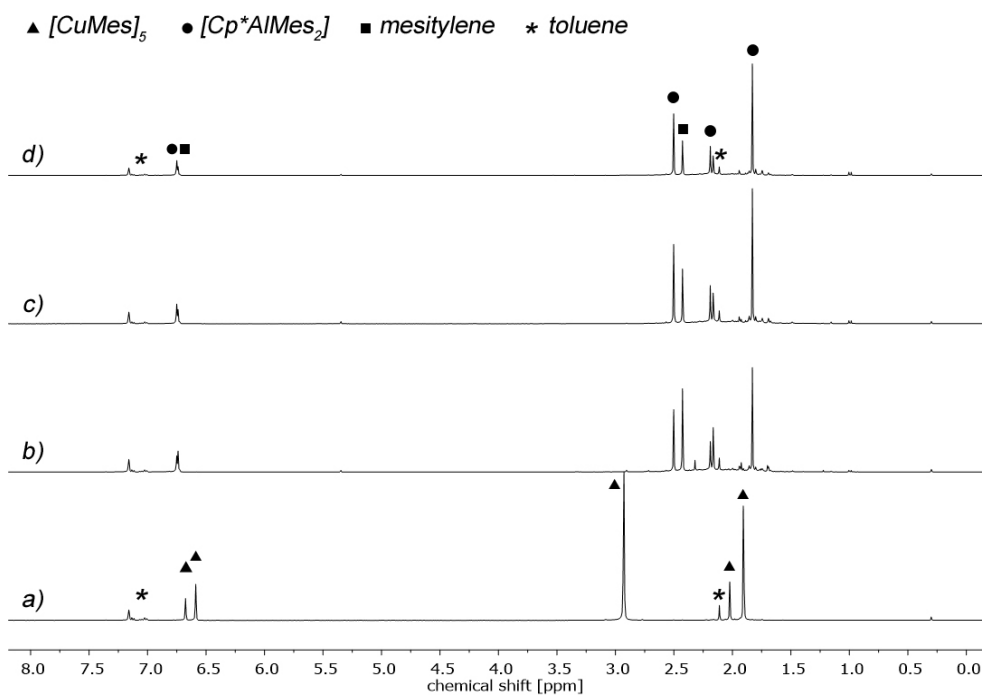
Supplementary data for  $[\text{Cu}_{43}(\text{AlCp}^*)_{12}]$  (**3**)

Figure 65. *In situ*  $^1\text{H}$  NMR spectroscopic measurements of a 1:1 mixture of  $[\text{CuMes}_5]$  and  $\text{AlCp}^*$  in  $\text{C}_6\text{D}_6$  at room temperature (a), and after thermal treatment at  $78^\circ\text{C}$  for 1h (b), 3h (c) and 10h (d), respectively.

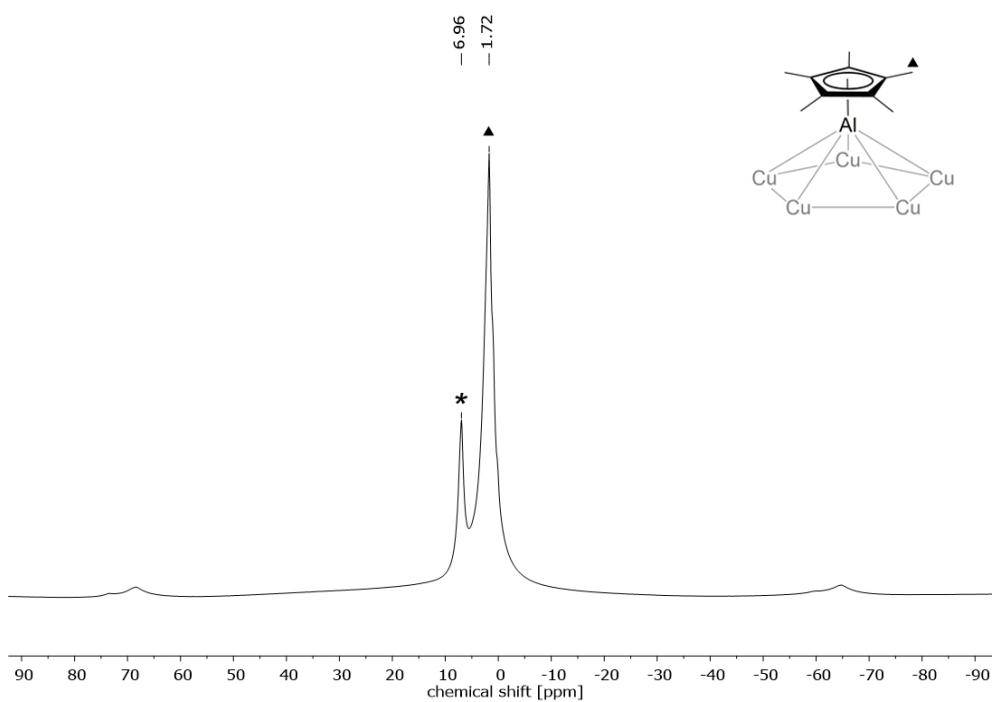


Figure 66.  $^1\text{H}$  MAS NMR spectrum of neat  $[\text{Cu}_{43}(\text{AlCp}^*)_{12}]$  (**3**). The signal marked with an asterisk is attributed to co-crystallized benzene.



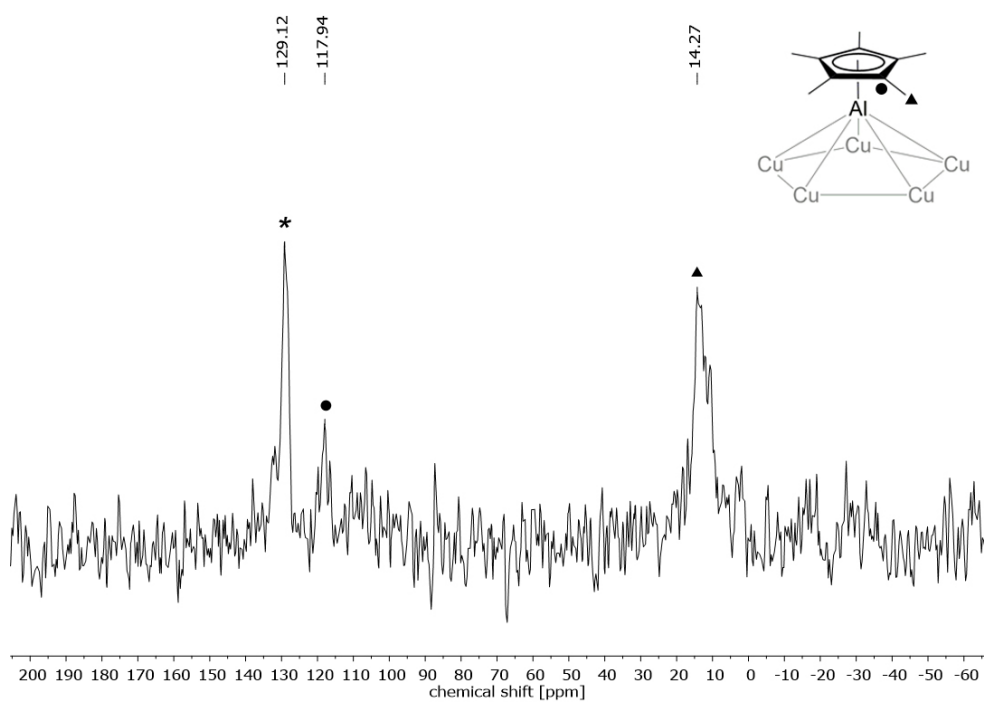


Figure 67.  $^{13}\text{C}$  MAS NMR (CPMAS) spectrum of neat  $[\text{Cu}_{43}(\text{AlCp}^*)_{12}]$  (**3**). The signal marked with an asterisk is attributed to co-crystallized benzene.

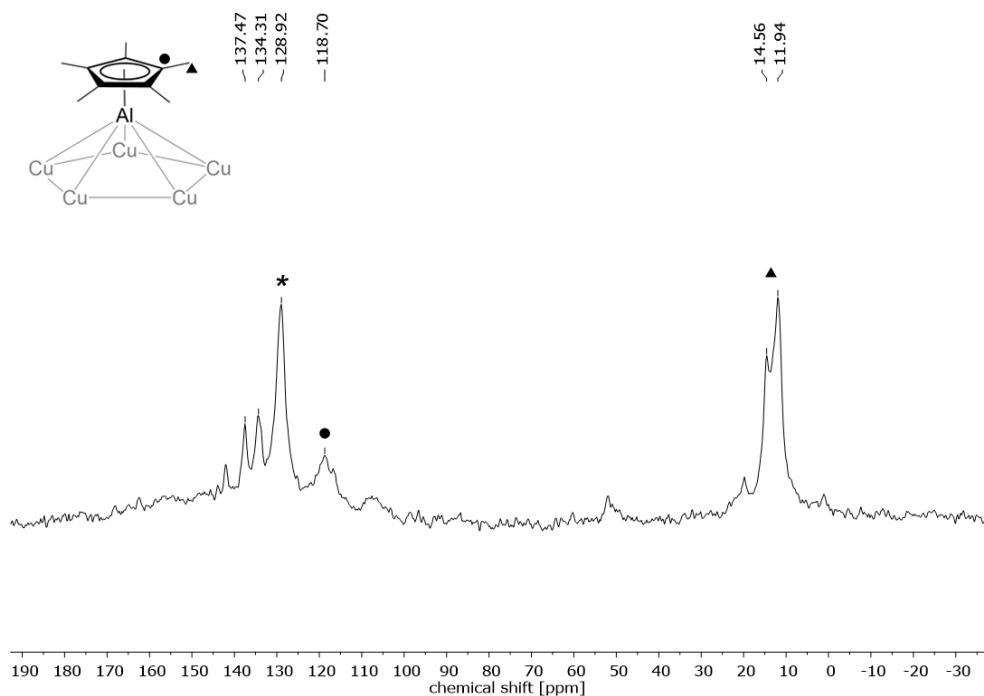


Figure 68.  $^{13}\text{C}$  MAS NMR (HPDEC) spectrum of neat  $[\text{Cu}_{43}(\text{AlCp}^*)_{12}]$  (**3**). Signal splitting around 128.92 ppm (marked with an asterisk) is attributed to unsymmetrically distributed, co-crystallized benzene.

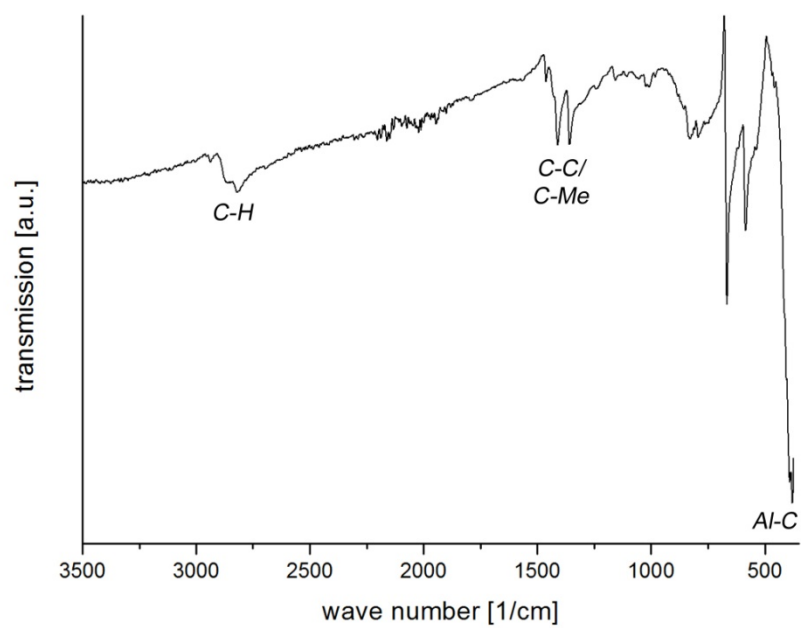


Figure 69. IR spectrum of neat  $[\text{Cu}_{43}(\text{AlCp}^*)_{12}]$  (**3**).

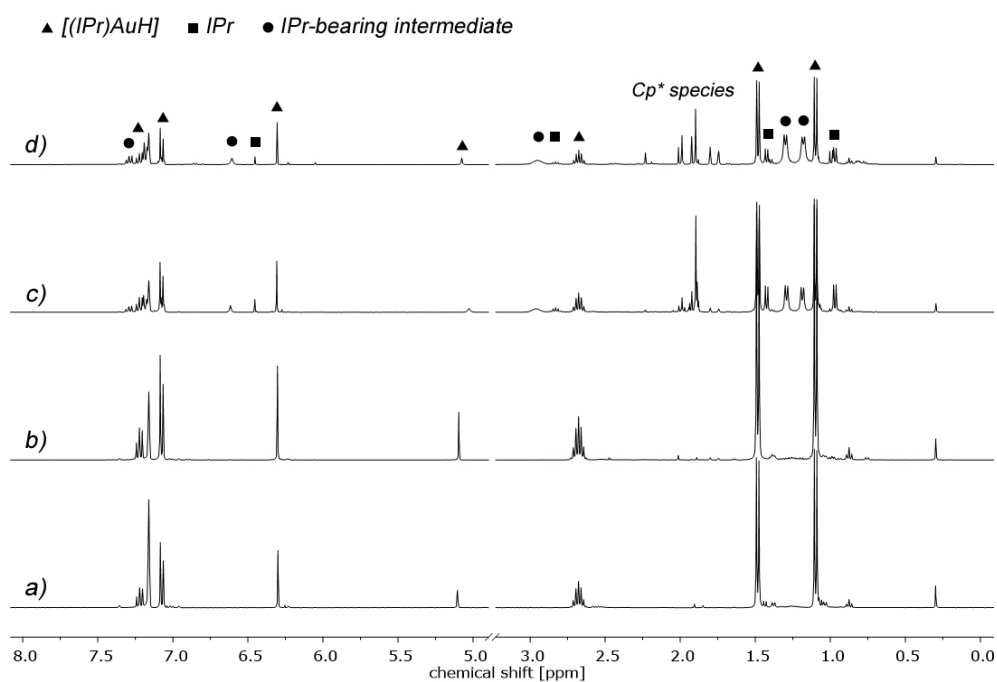
Supplementary data for  $[\text{Au}_a(\text{AlCp}^*)_6\text{H}_x]$  (4)

Figure 70. *In situ*  $^1\text{H}$  NMR spectroscopic measurements of a 4:3 mixture of  $[(\text{IPr})\text{AuH}]$  and  $\text{AlCp}^*$  in  $\text{C}_6\text{D}_6$  at room temperature (a), and after mild thermal treatment at  $60^\circ\text{C}$  for 1h (b), 4h (c) and 24h (d), respectively.

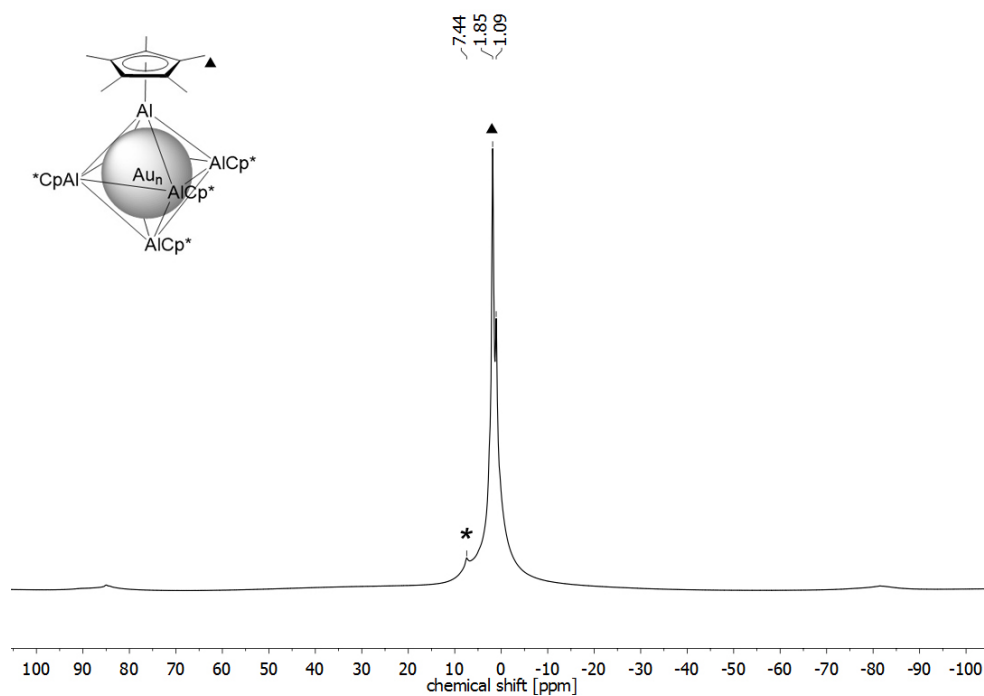


Figure 71.  $^1\text{H}$  MAS NMR spectrum of neat  $[\text{Au}_a(\text{AlCp}^*)_6\text{H}_x]$  (4). The signal marked with an asterisk is attributed to co-crystallized benzene.

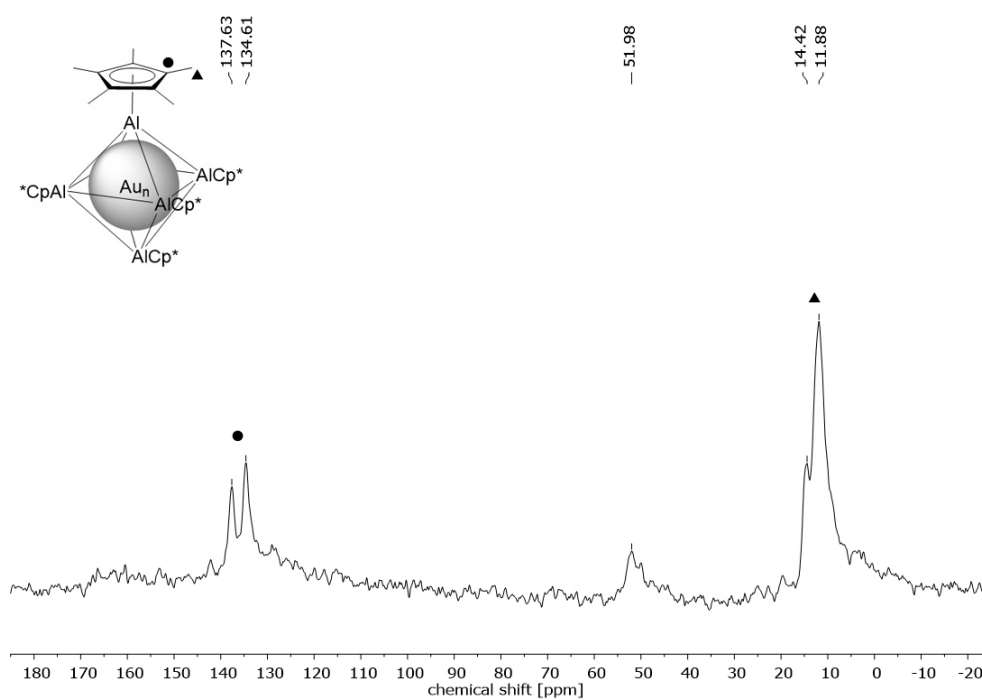


Figure 72.  $^{13}\text{C}$  MAS NMR (HPDEC) spectrum of neat  $[\text{Au}_a(\text{AlCp}^*)_6\text{H}_x]$  (4).

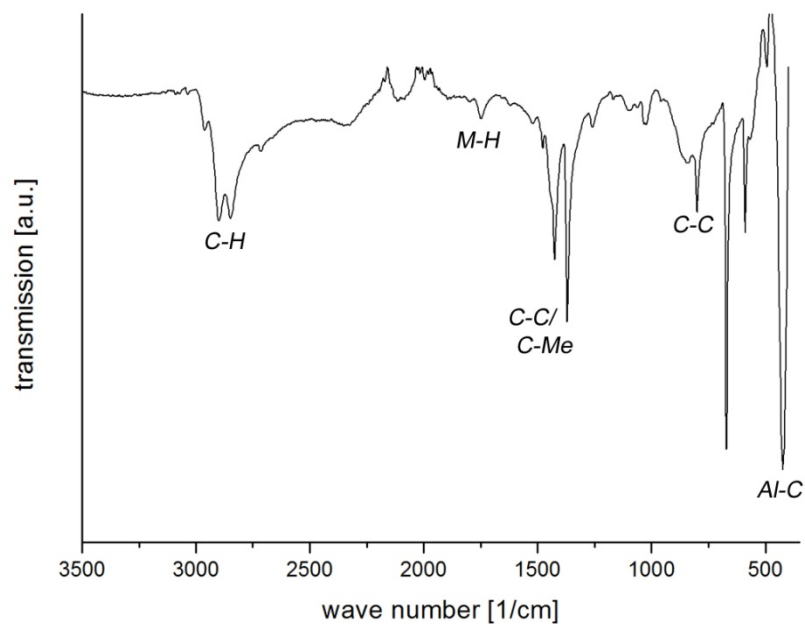


Figure 73. IR spectrum of neat  $[\text{Au}_a(\text{AlCp}^*)_6\text{H}_x]$  (4).

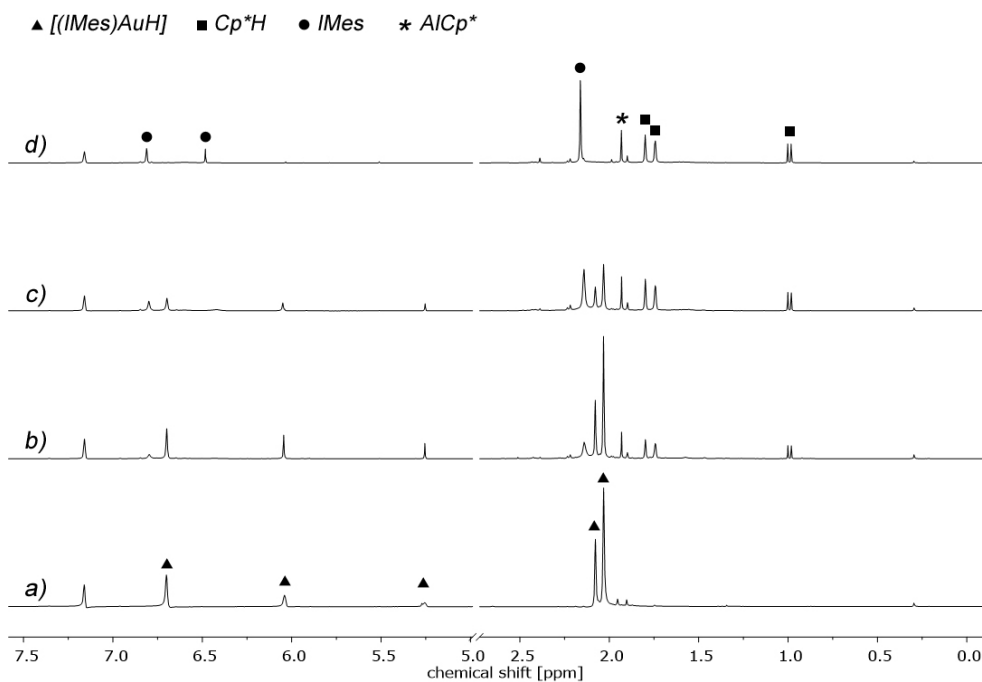
Supplementary data for  $[\text{Au}_8(\text{AlCp}^*)_5(\text{IMes})\text{H}_x]$  (5)

Figure 74. *In situ*  $^1\text{H}$  NMR spectroscopic measurements of a 4:3 mixture of [(IMes)AuH] and AlCp\* in  $\text{C}_6\text{D}_6$  at room temperature (a), and after mild thermal treatment at  $60^\circ\text{C}$  for 1h (b), 4h (c) and 24h (d), respectively.

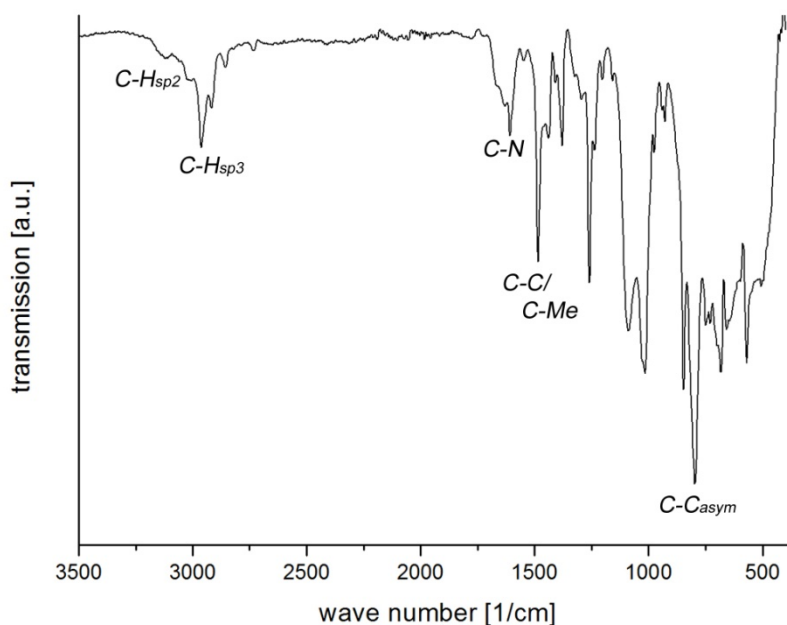


Figure 75. IR spectrum of neat  $[\text{Au}_8(\text{AlCp}^*)_5(\text{IMes})\text{H}_x]$  (5).

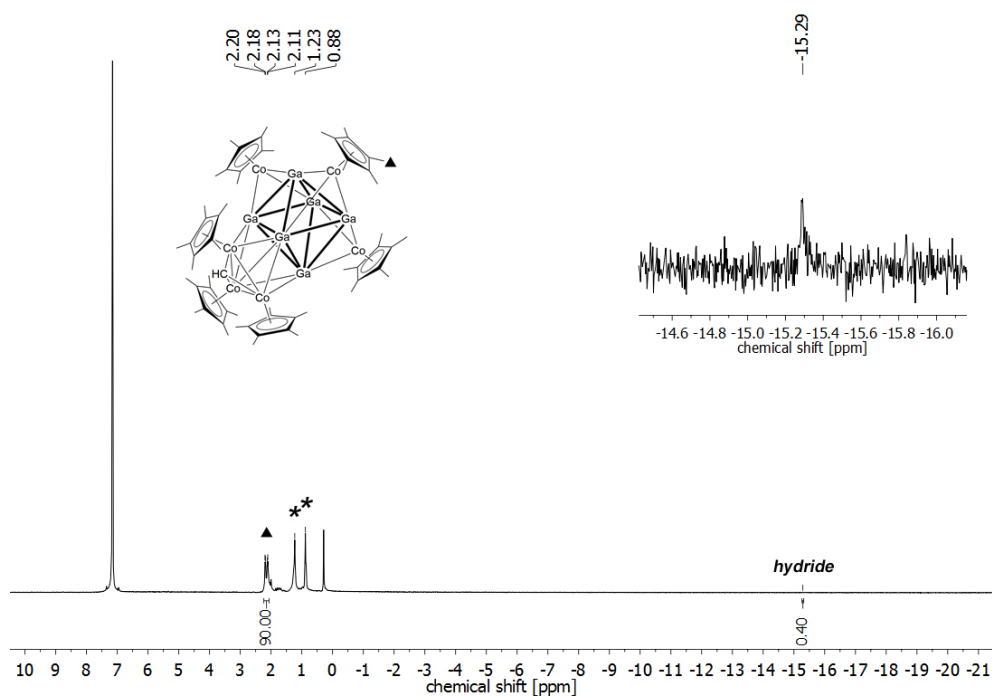
Supplementary data for  $[(\text{Cp}^*\text{Co})_3\text{Ga}_6(\text{Cp}^*_3\text{Co}_3(\mu^3\text{-CH}))\text{H}_x]$  (**6**)

Figure 76.  $^1\text{H}$  NMR spectrum of  $[(\text{Cp}^*\text{Co})_3\text{Ga}_6(\text{Cp}^*_3\text{Co}_3(\mu^3\text{-CH}))\text{H}_x]$  (**6**) in  $\text{C}_6\text{D}_6$ . Signals marked with an asterisk are attributed to residual *n*-hexane.

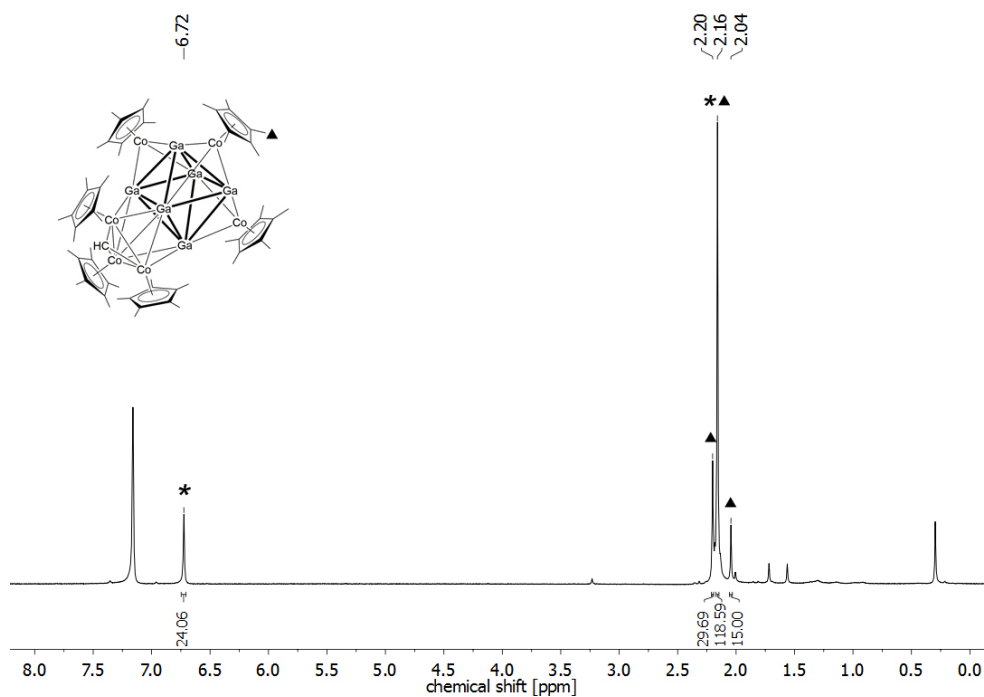


Figure 77.  $^1\text{H}$  NMR spectrum of  $[(\text{Cp}^*\text{Co})_3\text{Ga}_6(\text{Cp}^*_3\text{Co}_3(\mu^3\text{-CH}))\text{H}_x]$  (**6**) in  $\text{C}_6\text{D}_6$  after recrystallization from mesitylene. Signals marked with an asterisk are attributed to co-crystallized mesitylene.

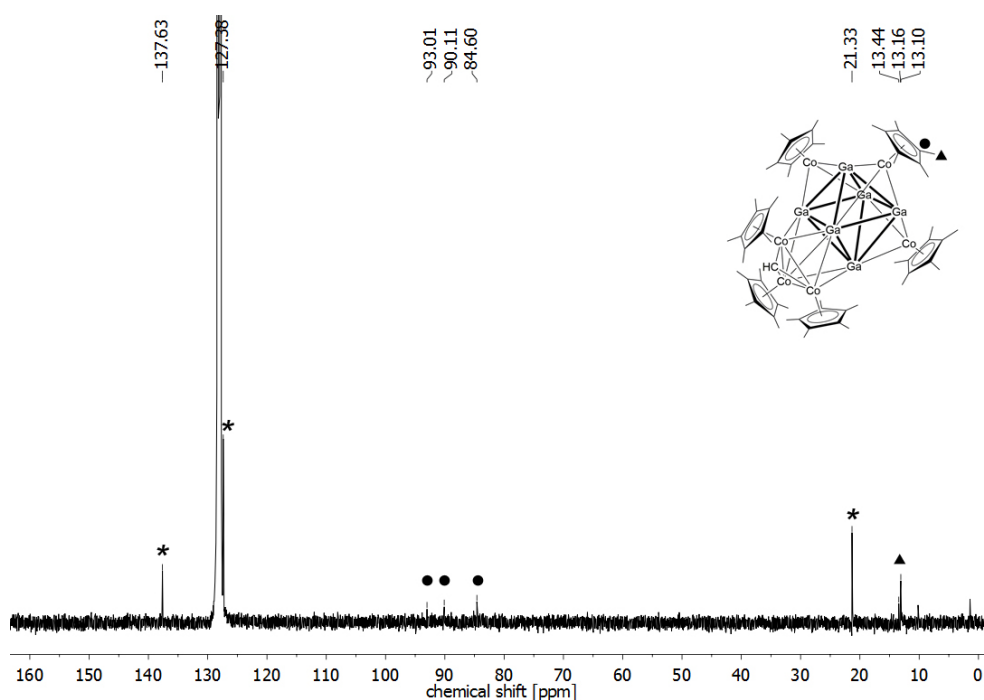


Figure 78.  $^{13}\text{C}$  NMR spectrum of  $[(\text{Cp}^*\text{Co})_3\text{Ga}_6(\text{Cp}^*_3\text{Co}_3(\mu^3\text{-CH}))\text{H}_x]$  (**6**) in  $\text{C}_6\text{D}_6$  after recrystallization from mesitylene. Signals marked with an asterisk are attributed to co-crystallized mesitylene.

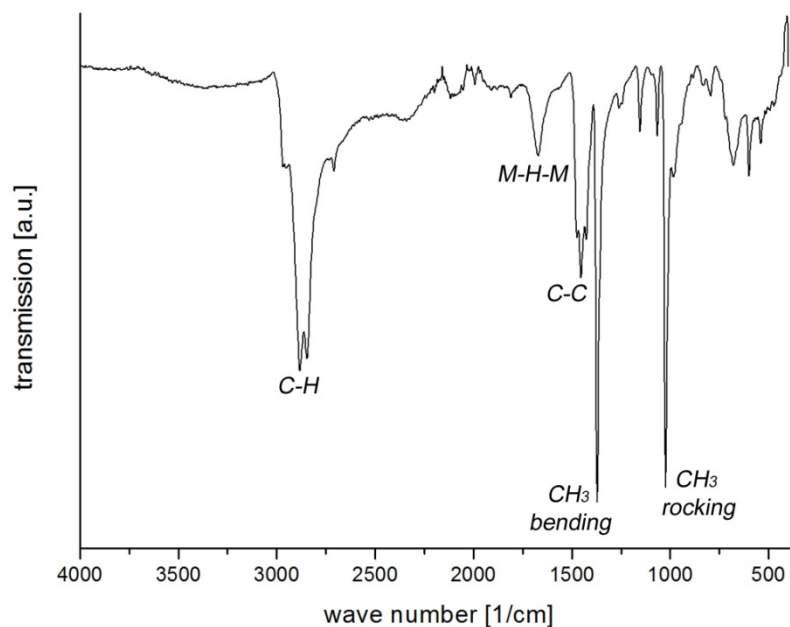


Figure 79. IR spectrum of neat  $[(\text{Cp}^*\text{Co})_3\text{Ga}_6(\text{Cp}^*_3\text{Co}_3(\mu^3\text{-CH}))\text{H}_x]$  (**6**). The absence of a sharp  $\nu_{\text{OH}}$  vibration around  $3650\text{ cm}^{-1}$  speaks in favour of a  $\mu^3$ -coordinated CH group.

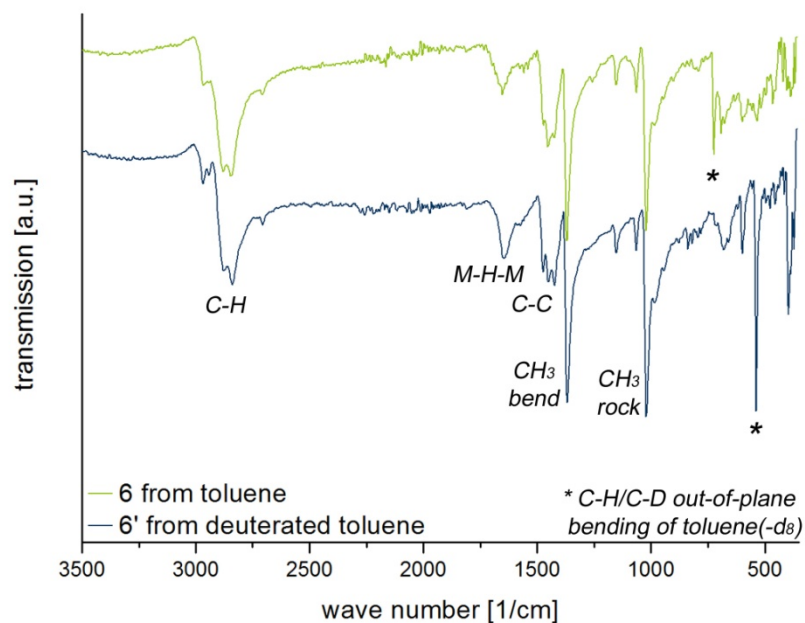


Figure 80. Comparison of the IR spectra of  $[(Cp^*Co)_3Ga_6(Cp^*_3Co_3(\mu^3-CH))H_x]$  (**6**) obtained from toluene (green) and deuterated toluene (blue), respectively.

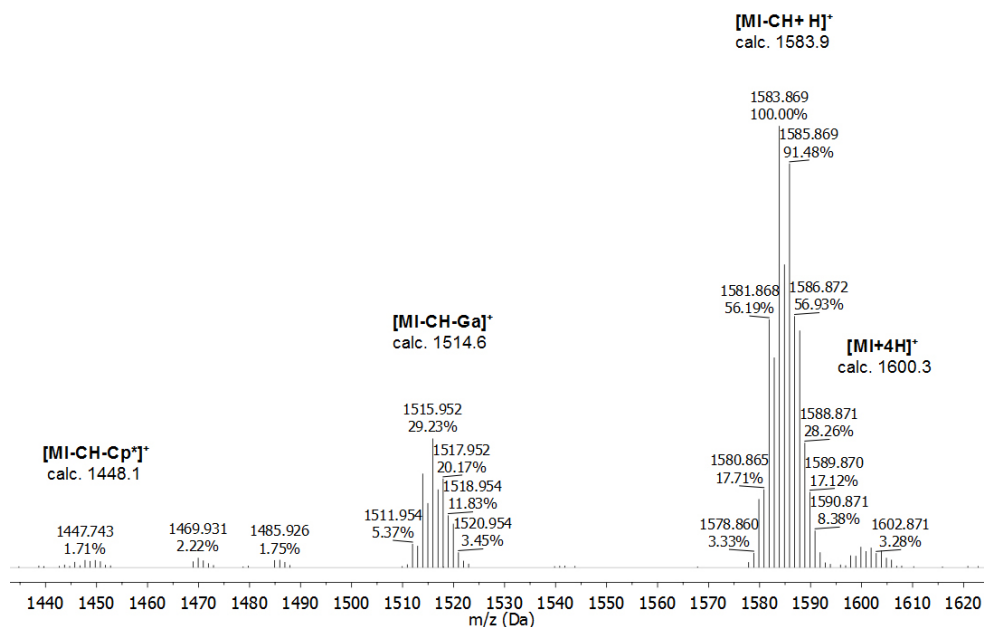


Figure 81. LIFDI-MS spectrum of  $[(Cp^*Co)_3Ga_6(Cp^*_3Co_3(\mu^3-CH))H_x]$  (**6**), measured with a Thermo Scientific Exactive Plus instrument, equipped with an Orbitrap detector and a “LIFDI 700” ionization source.



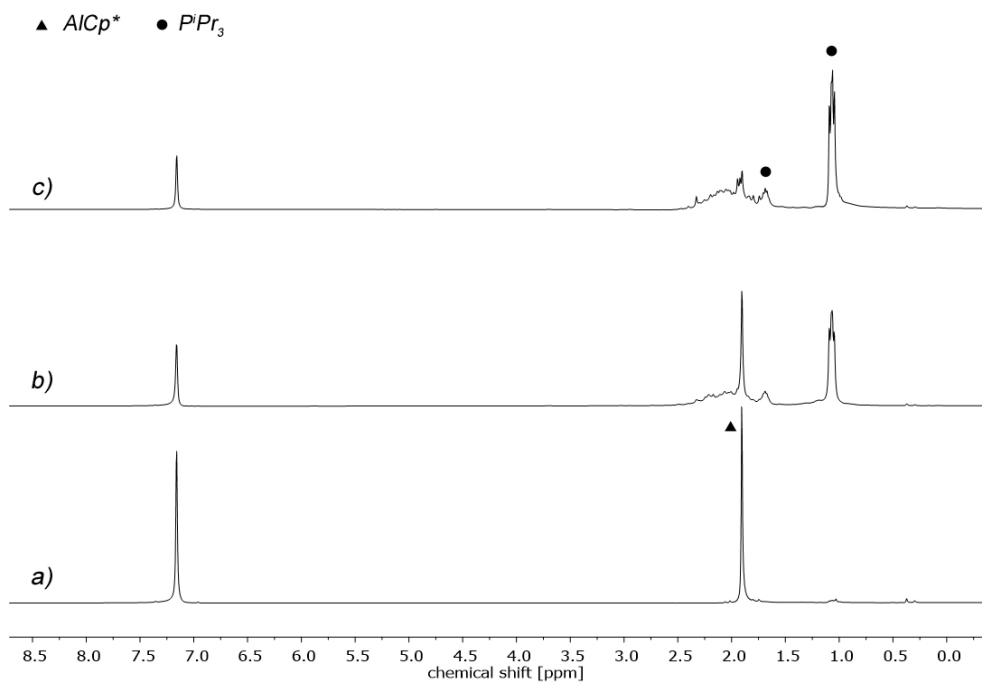
Reaction of  $[\text{Co}_6(\text{P}^i\text{Pr}_3)_6\text{H}_8]$  with  $\text{AlCp}^*$ 

Figure 82. *In situ*  $^1\text{H}$  NMR spectroscopic measurements of a 1:6 mixture of  $[(\text{P}^i\text{Pr}_3)_6\text{Co}_6\text{H}_8]$  and  $\text{AlCp}^*$  in  $\text{C}_6\text{D}_6$  at room temperature (a), and after thermal treatment at  $70^\circ\text{C}$  for 3h (b) and 16h, respectively. Additionally arising paramagnetically shifted signals at 108.39 and 58.60 ppm, as well as several signals around -17 ppm are too low in intensity to be properly depicted.

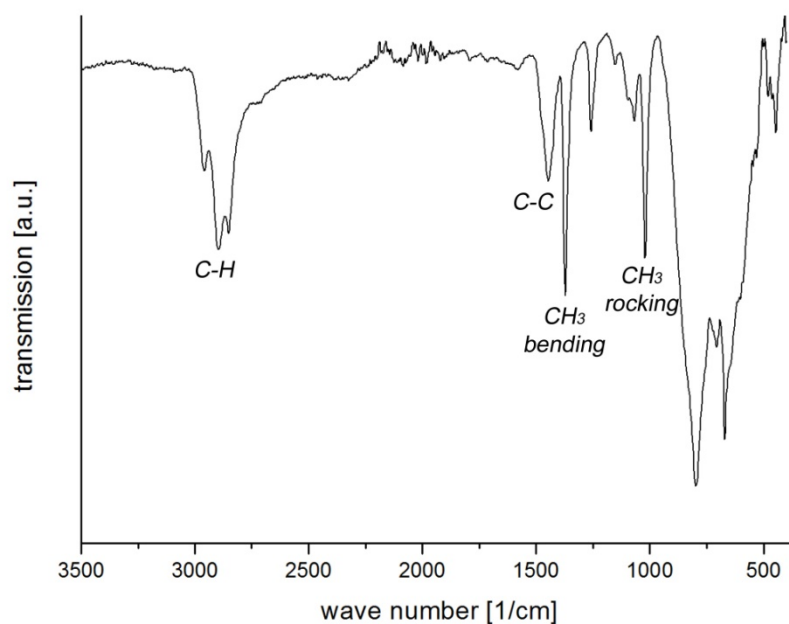


Figure 83. IR spectrum of the black microcrystalline solid obtained from the reaction of  $[\text{Co}_6(\text{P}^i\text{Pr}_3)_6\text{H}_8]$  with  $\text{AlCp}^*$ .

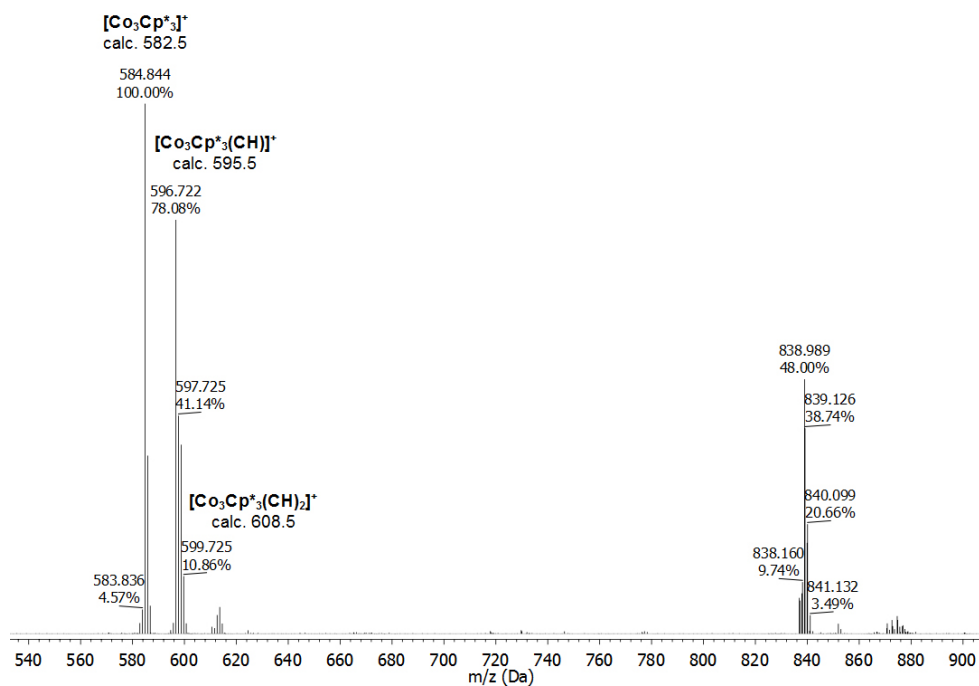
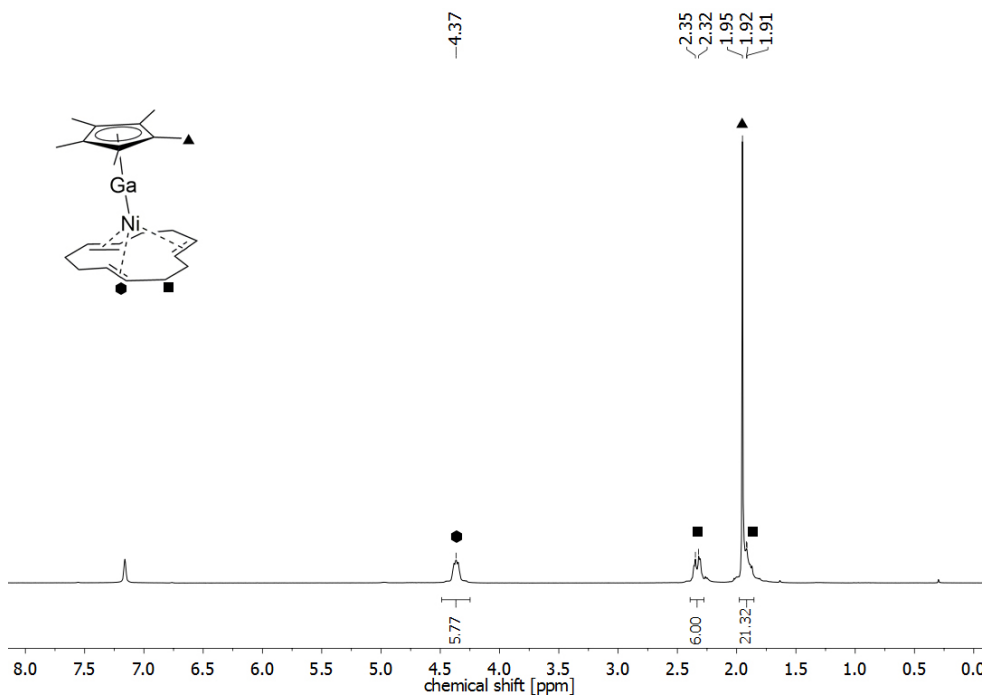
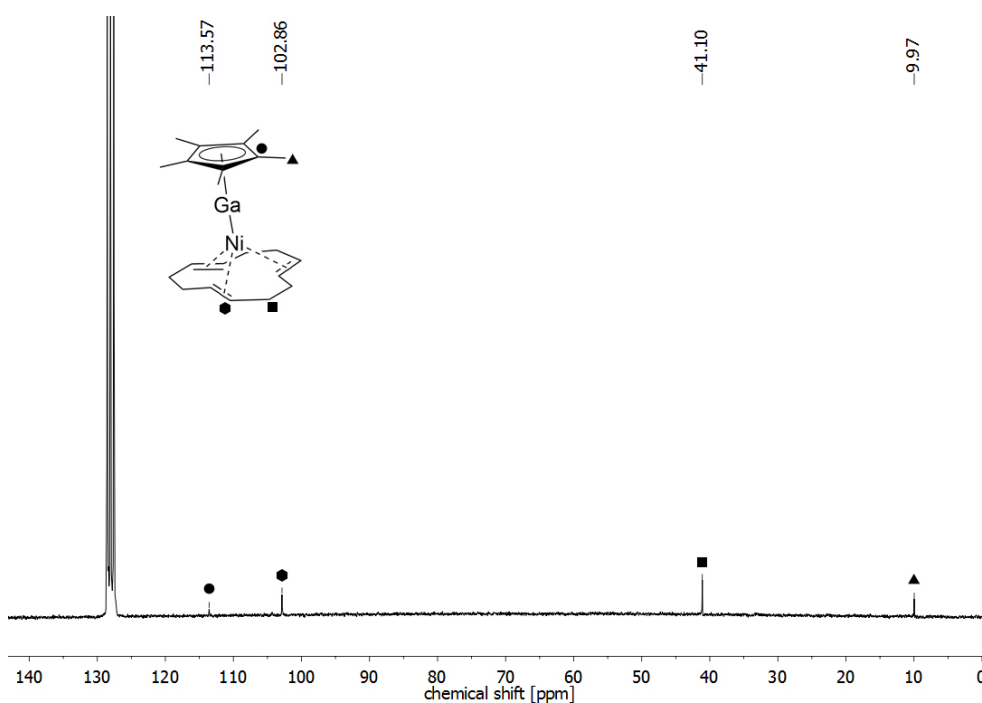
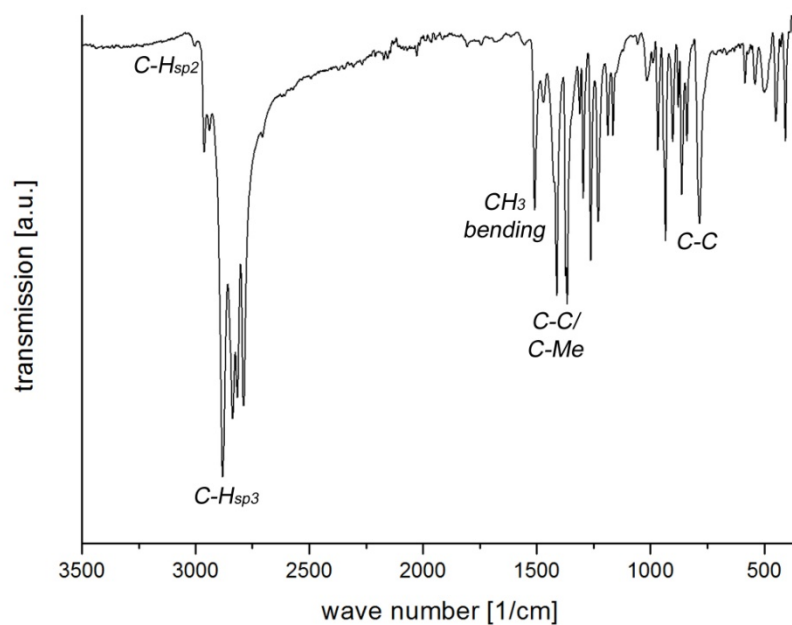
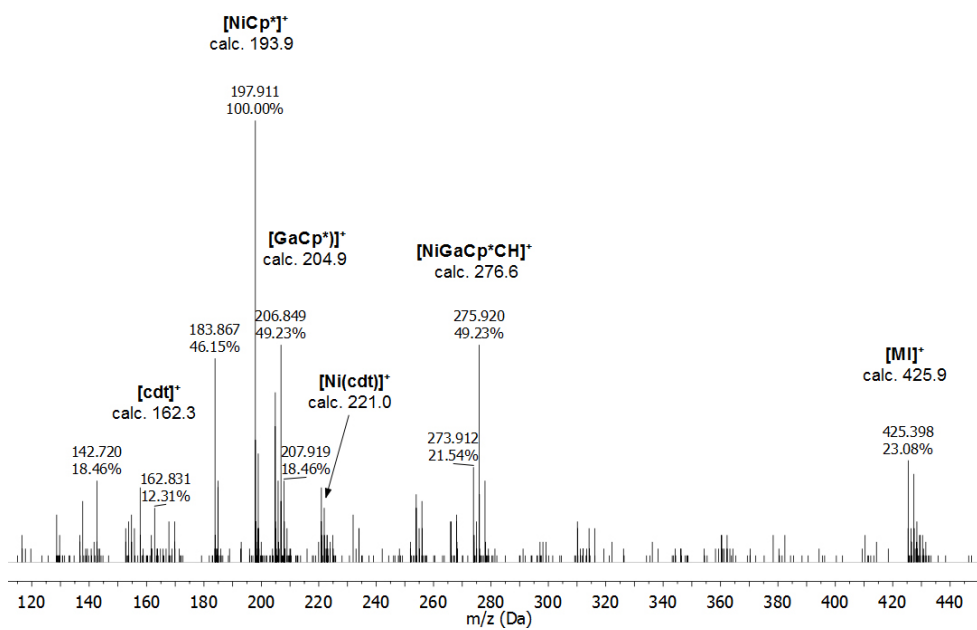


Figure 84. LIFDI-MS spectrum of the black microcrystalline solid obtained from the reaction of  $[\text{Co}_6(\text{P}^i\text{Pr}_3)_6\text{H}_8]$  with  $\text{AlCp}^*$ . The assumed molecular ion peak at  $m/z$  838.9 could not be reliably identified. However, compounds of the formal compositions  $[(\text{Cp}^*\text{Co})_4\text{Al}_2\text{H}_x]$  (calc. 834.6 for  $x = 4$ ) or  $[\text{Co}_5\text{Cp}^*_4]$  (calc. 835.6) are conceivable.

## Supplementary data for [Ni(cdt)(GaCp\*)] (7)

Figure 85.  $^1\text{H}$  NMR spectrum of [Ni(cdt)(GaCp\*)] (7) in  $\text{C}_6\text{D}_6$ .Figure 86.  $^{13}\text{C}$  NMR spectrum of [Ni(cdt)(GaCp\*)] (7) in  $\text{C}_6\text{D}_6$ .

Figure 87. IR spectrum of  $[\text{Ni}(\text{cdt})(\text{GaCp}^*)]$  (7).Figure 88. LIFDI-MS spectrum of  $[\text{Ni}(\text{GaCp}^*)(\text{cdt})]$  (7).

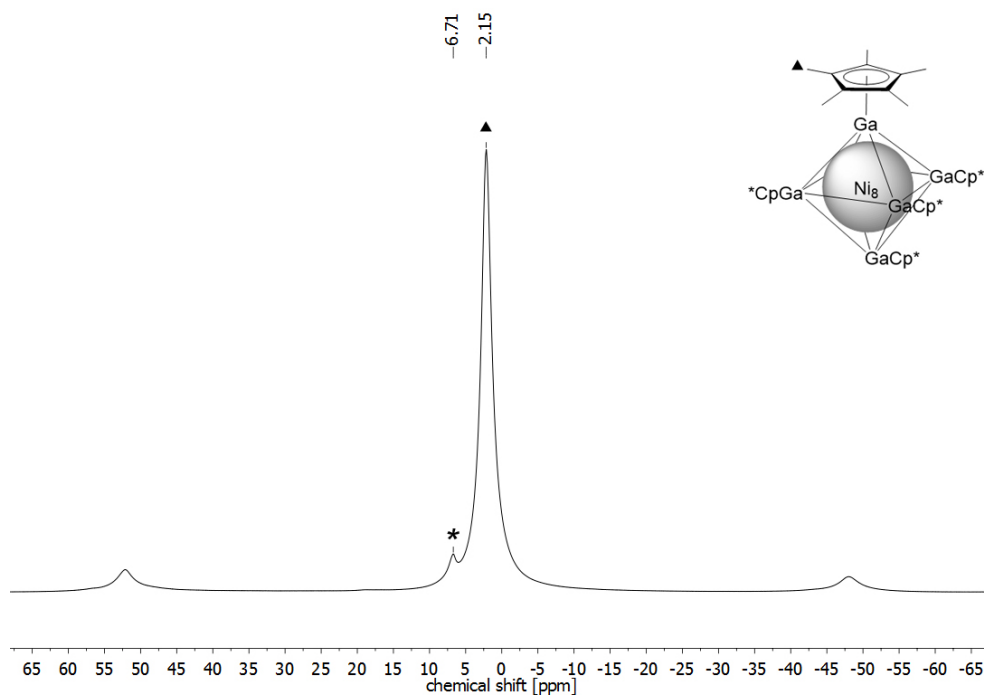
Supplementary data for  $[\text{Ni}_8(\text{GaCp}^*)_6]$  (**8**)

Figure 89.  $^1\text{H}$  MAS NMR spectrum of neat  $[\text{Ni}_8(\text{GaCp}^*)_6]$  (**8**). The signal marked with an asterisk is attributed to co-crystallized mesitylene.

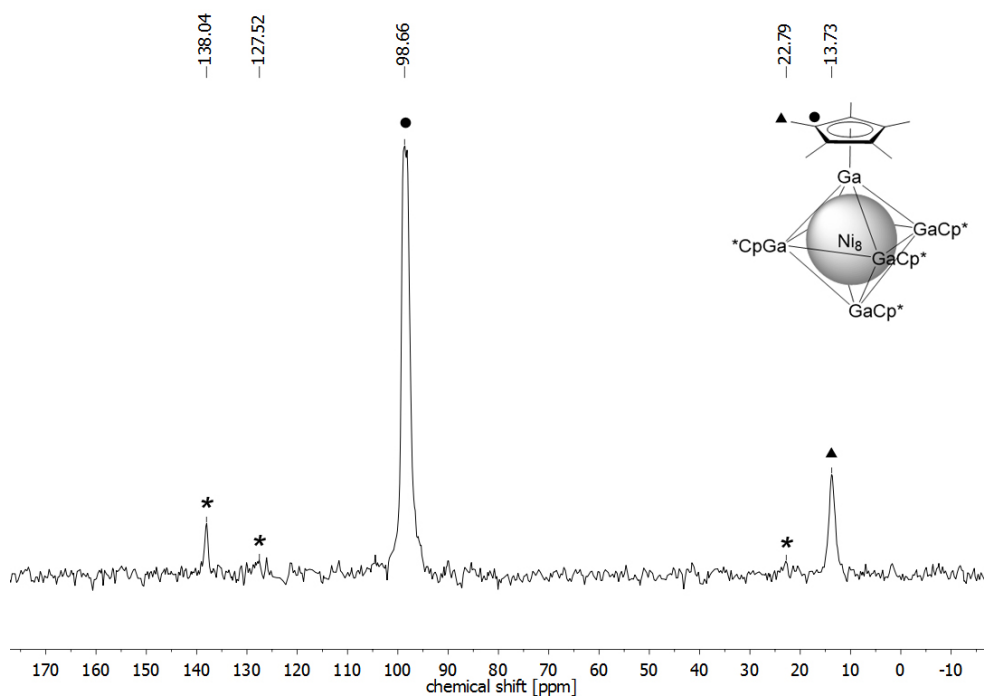


Figure 90.  $^{13}\text{C}$  MAS NMR (CPMAS) spectrum of neat  $[\text{Ni}_8(\text{GaCp}^*)_6]$  (**8**). Signals marked with an asterisk are attributed to co-crystallized mesitylene.

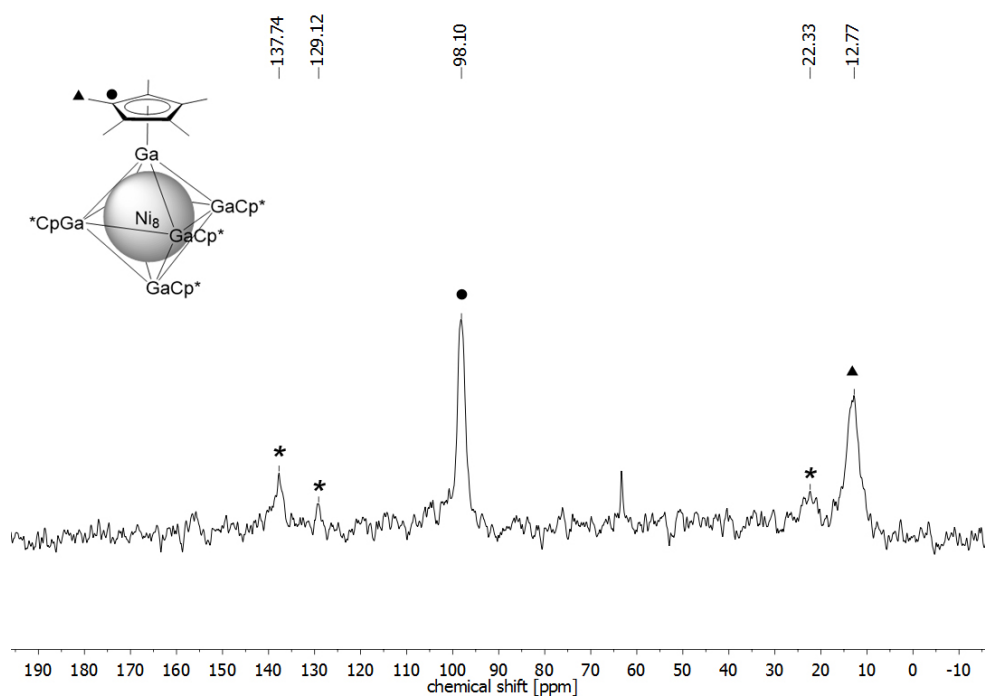


Figure 91.  $^{13}\text{C}$  MAS NMR (single-pulse technique) spectrum of neat  $[\text{Ni}_8(\text{GaCp}^*)_6]$  (**8**). Signals marked with an asterisk are attributed to co-crystallized mesitylene.

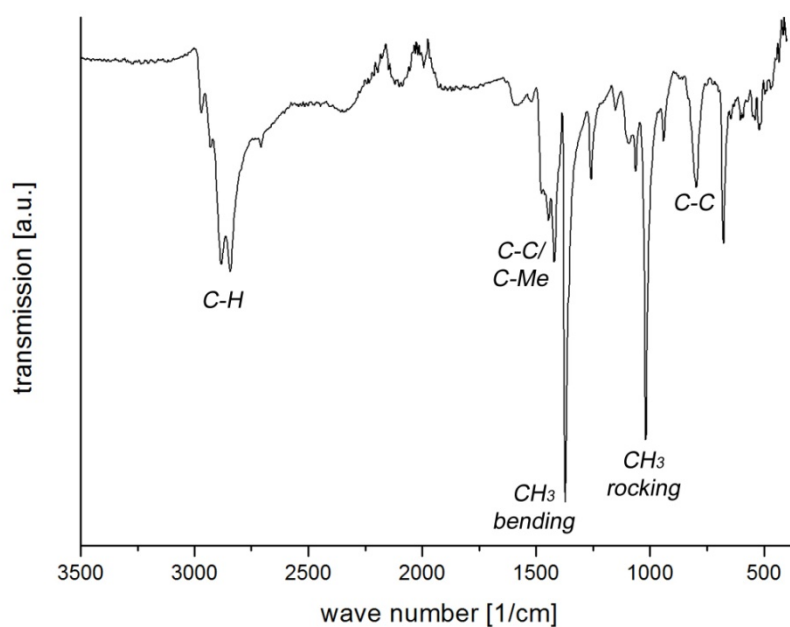


Figure 92. IR spectrum of neat  $[\text{Ni}_8(\text{GaCp}^*)_6]$  (**8**).

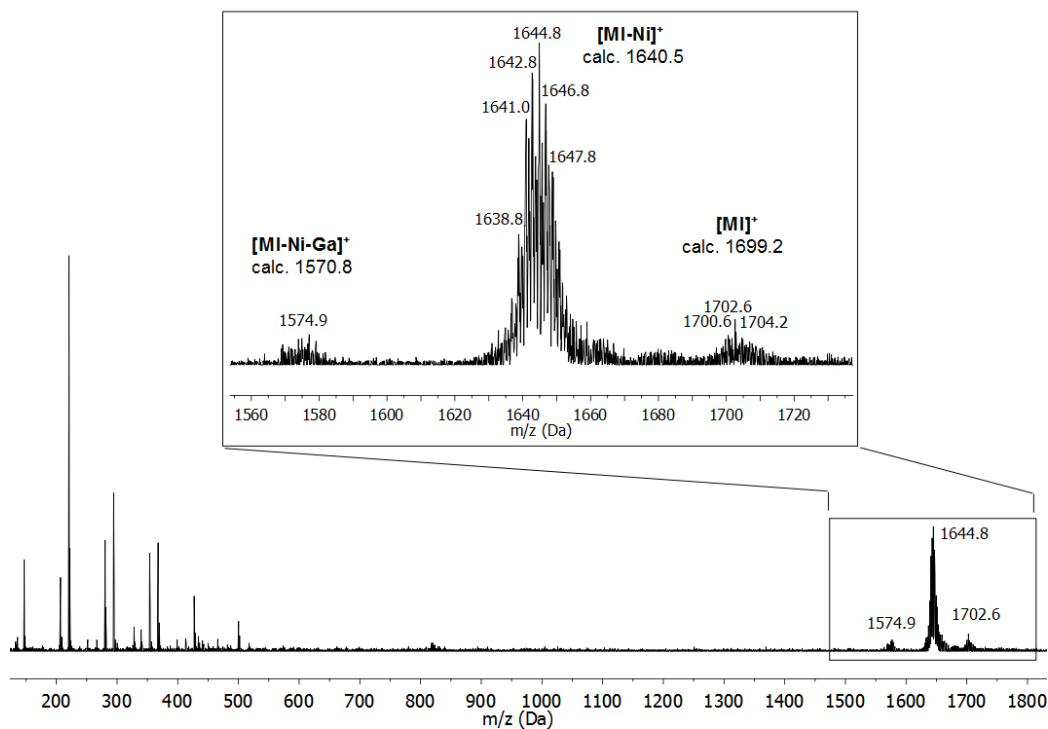


Figure 93. LIFDI-MS spectrum of  $[\text{Ni}_8(\text{GaCp}^*)_6]$  (**8**), measured with a Waters LCT Classic orthogonal acceleration time of flight (TOF) mass spectrometer equipped with a liquid injection field desorption ionization (LIFDI) source by Linden CMS GmbH.

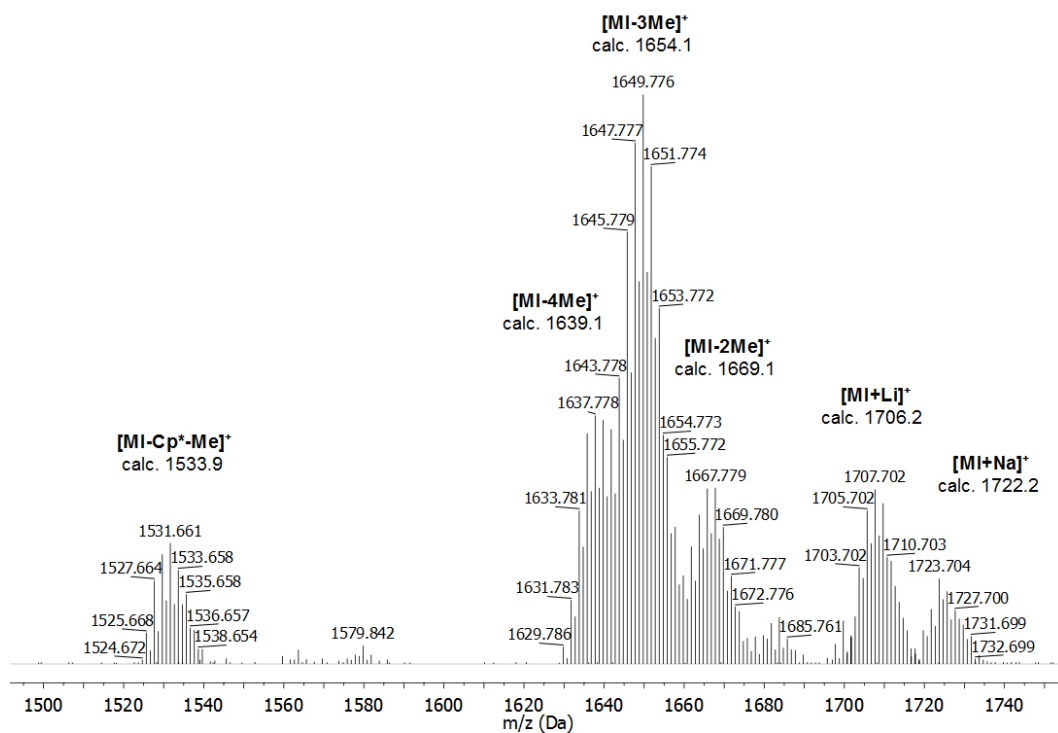
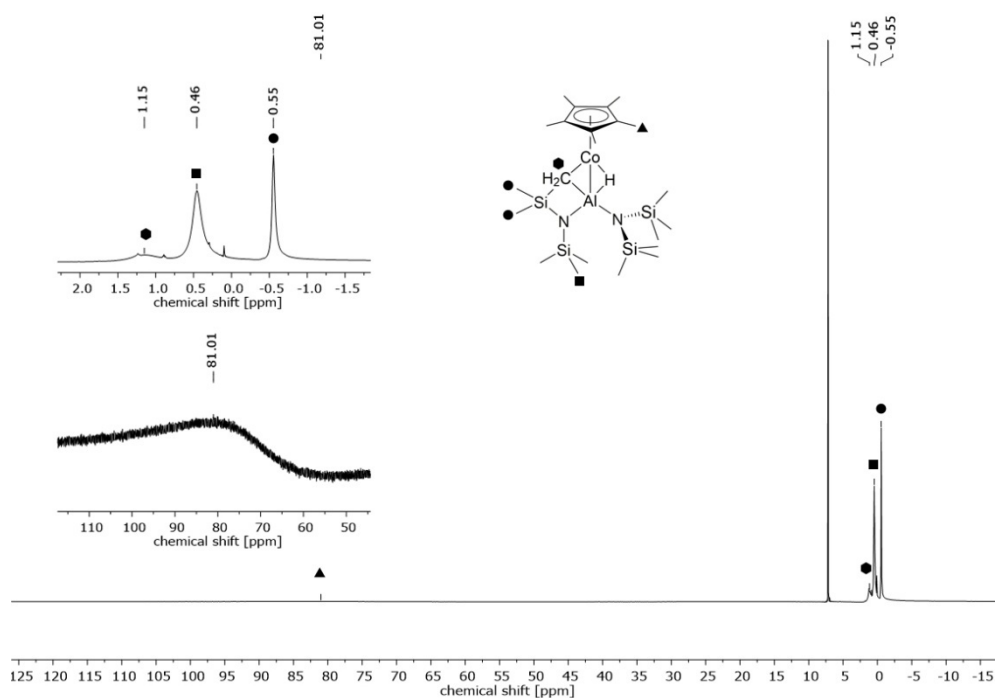
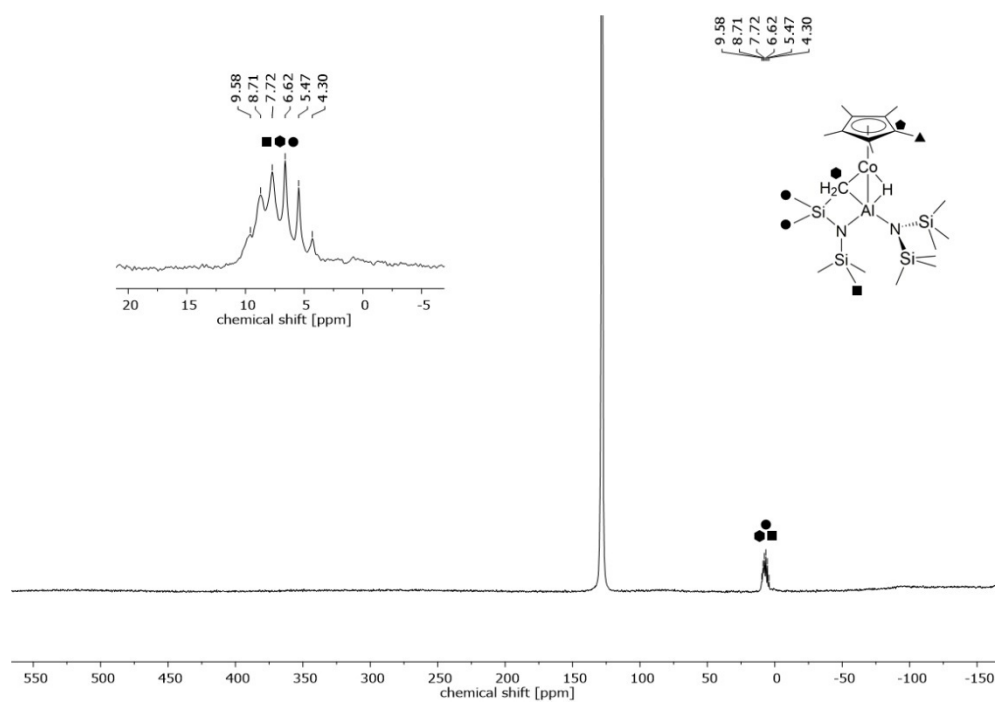


Figure 94. Detailed view of the LIFDI-MS spectrum of  $[\text{Ni}_8(\text{GaCp}^*)_6]$  (**8**) in the range  $m/z$  1500 to 1750, measured with a Thermo Scientific Exactive Plus instrument, equipped with an Orbitrap detector and a “LIFDI 700” ionization source.

Supplementary data for  $[\text{Cp}^*\text{Co}(\mu\text{-H})(\text{Al}(\kappa^2\text{-(CH}_2\text{SiMe}_2)\text{NSiMe}_3)(\text{btsa}))]$  (9)Figure 95.  $^1\text{H}$  NMR spectrum of  $[\text{Cp}^*\text{Co}(\mu\text{-H})(\text{Al}(\kappa^2\text{-(CH}_2\text{SiMe}_2)\text{NSiMe}_3)(\text{btsa}))]$  (9) in  $\text{C}_6\text{D}_6$ .Figure 96.  $^{13}\text{C}$  NMR spectrum of  $[\text{Cp}^*\text{Co}(\mu\text{-H})(\text{Al}(\kappa^2\text{-(CH}_2\text{SiMe}_2)\text{NSiMe}_3)(\text{btsa}))]$  (9) in  $\text{C}_6\text{D}_6$ .



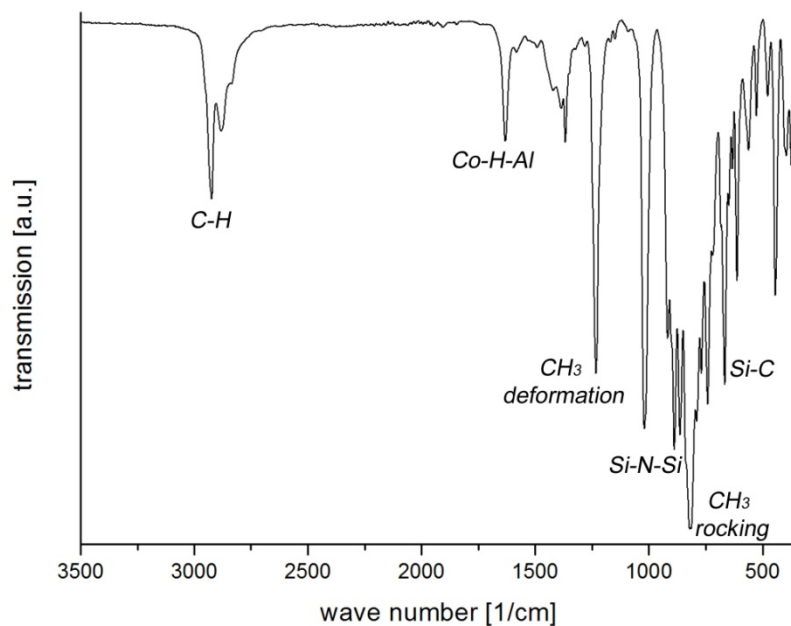


Figure 97. IR spectrum of  $[\text{Cp}^*\text{Co}(\mu\text{-H})(\text{Al}(\kappa^2\text{-(CH}_2\text{SiMe}_2\text{)NSiMe}_3\text{)(btsa))}]$  (**9**).

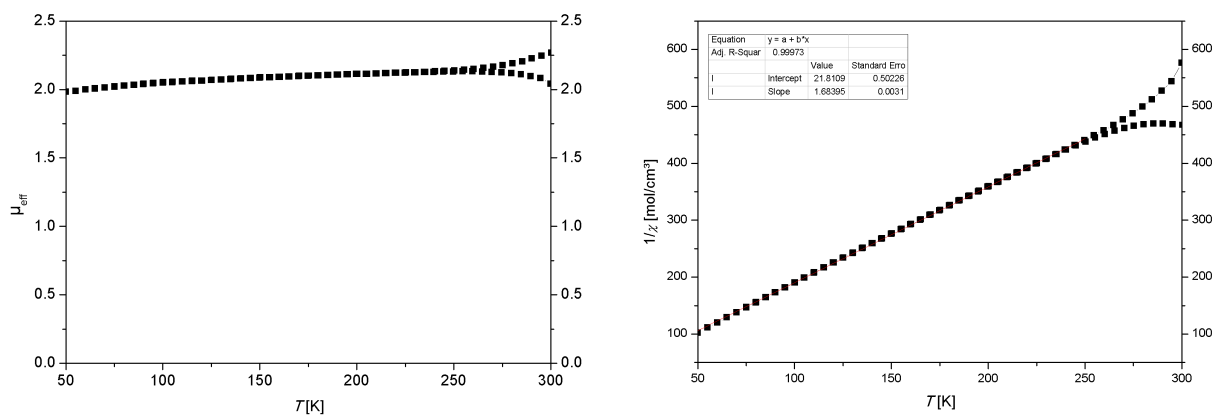


Figure 98. Temperature-dependent magnetic susceptibility measurements of  $[\text{Cp}^*\text{Co}(\mu\text{-H})(\text{Al}(\kappa^2\text{-(CH}_2\text{SiMe}_2\text{)NSiMe}_3\text{)(btsa))}]$  (**9**):  $\mu_{\text{eff}}$  vs.  $T$  plot (left) and Curie plot (right) displayed for  $T$  between 50 K and 300 K.

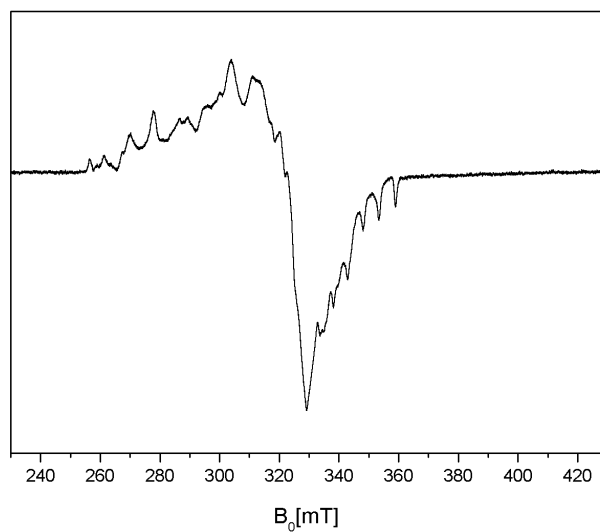
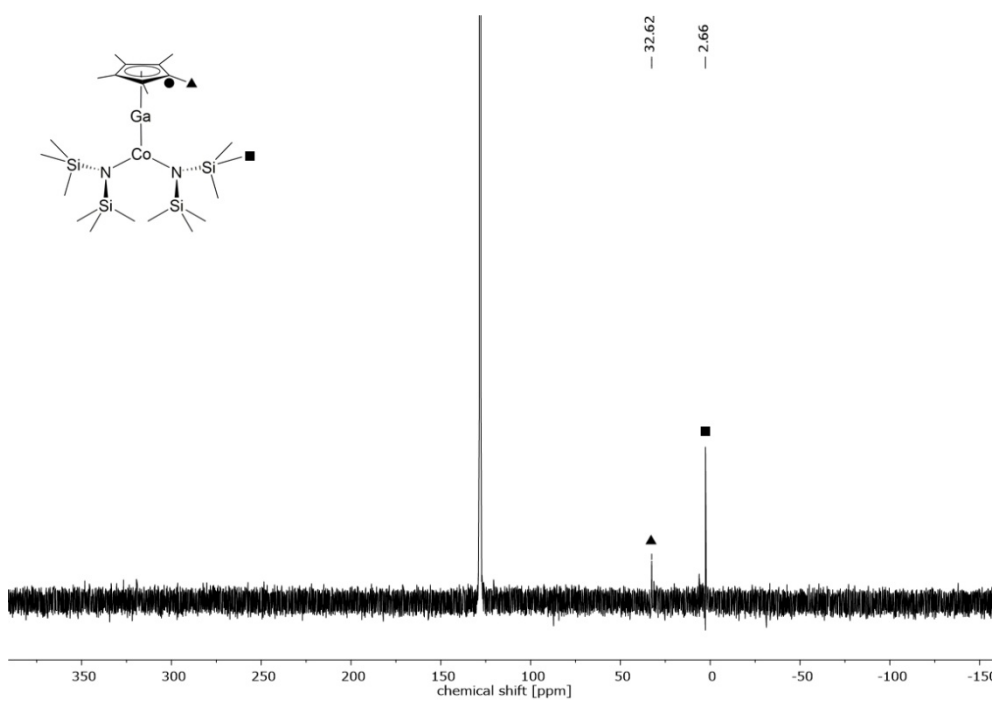
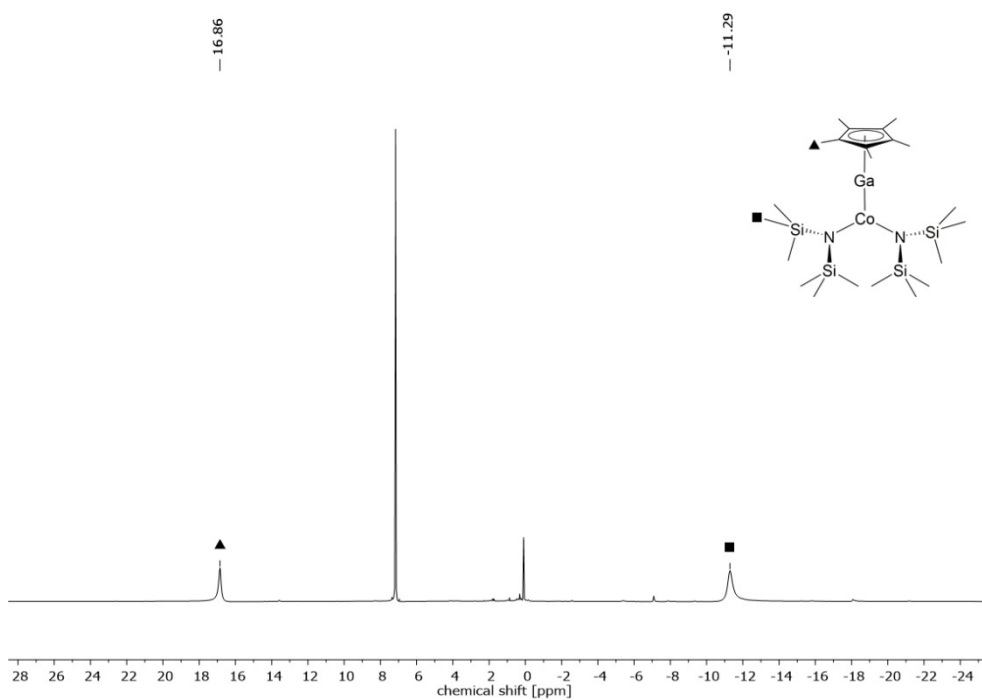


Figure 99. EPR spectrum of a frozen solution ( $c \approx 10^{-3}$  mol/l) of  $[\text{Cp}^*\text{Co}(\mu\text{-H})(\text{Al}(\kappa^2\text{-(CH}_2\text{SiMe}_2)\text{NSiMe}_3)(\text{btsa}))]$  (**9**) in toluene at 133.15 K.

Supplementary data for  $[(\text{GaCp}^*)\text{Co}(\text{btsa})_2]$  (**10**)

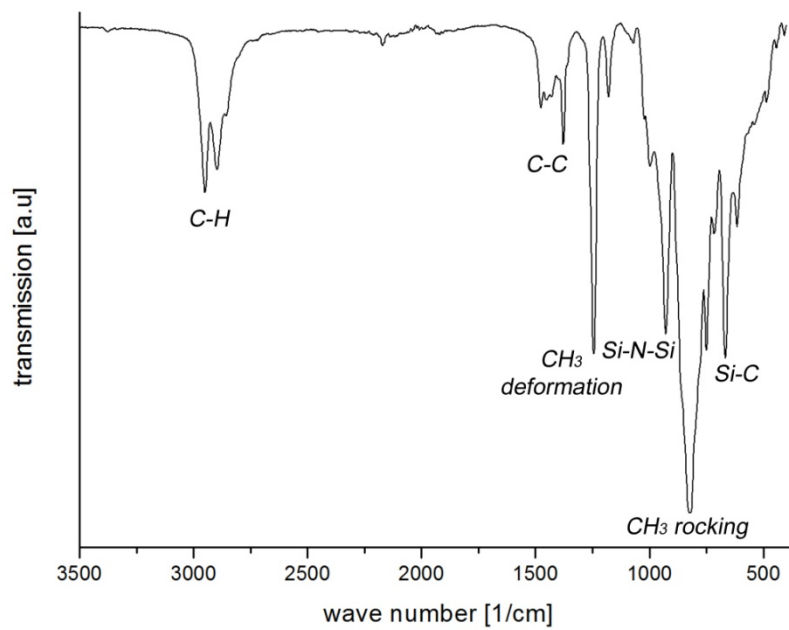
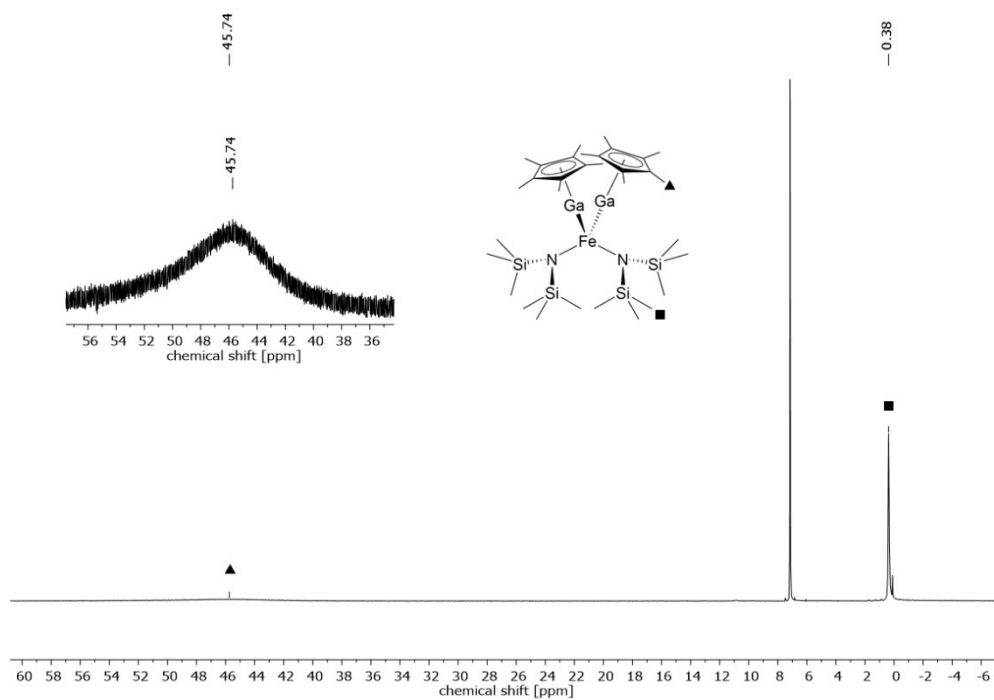
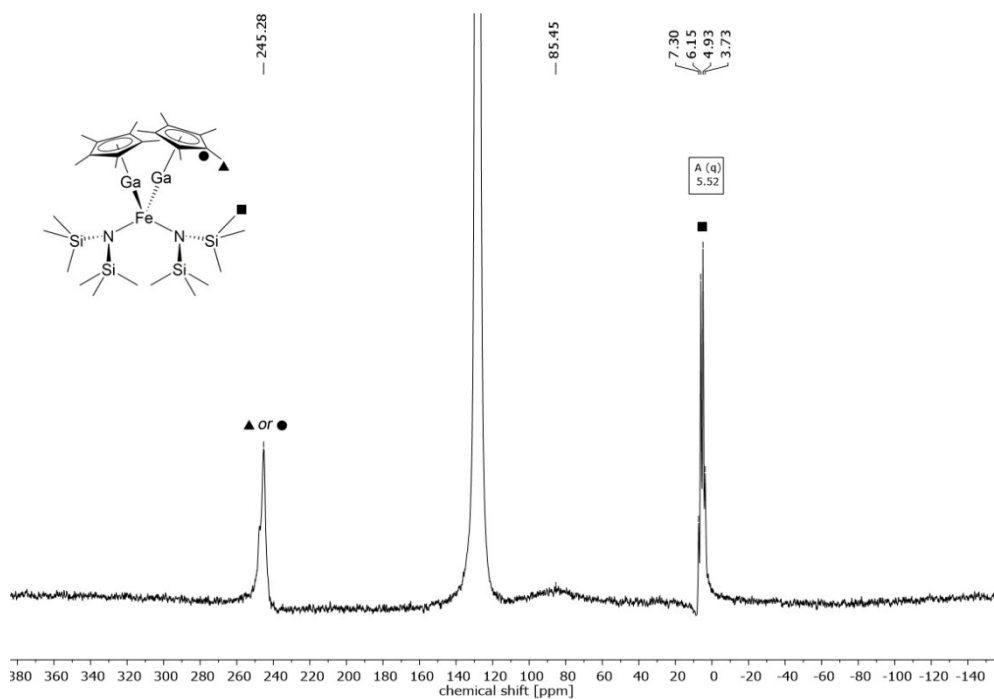
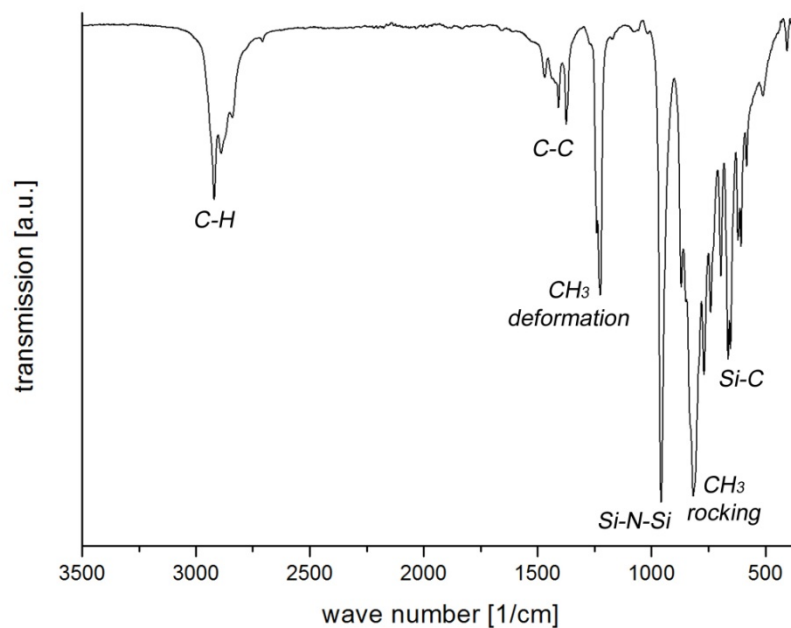
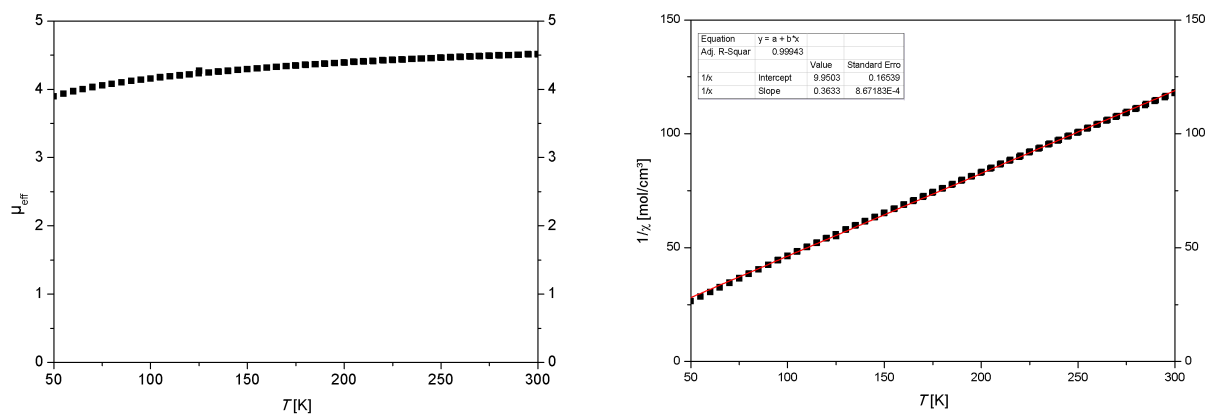
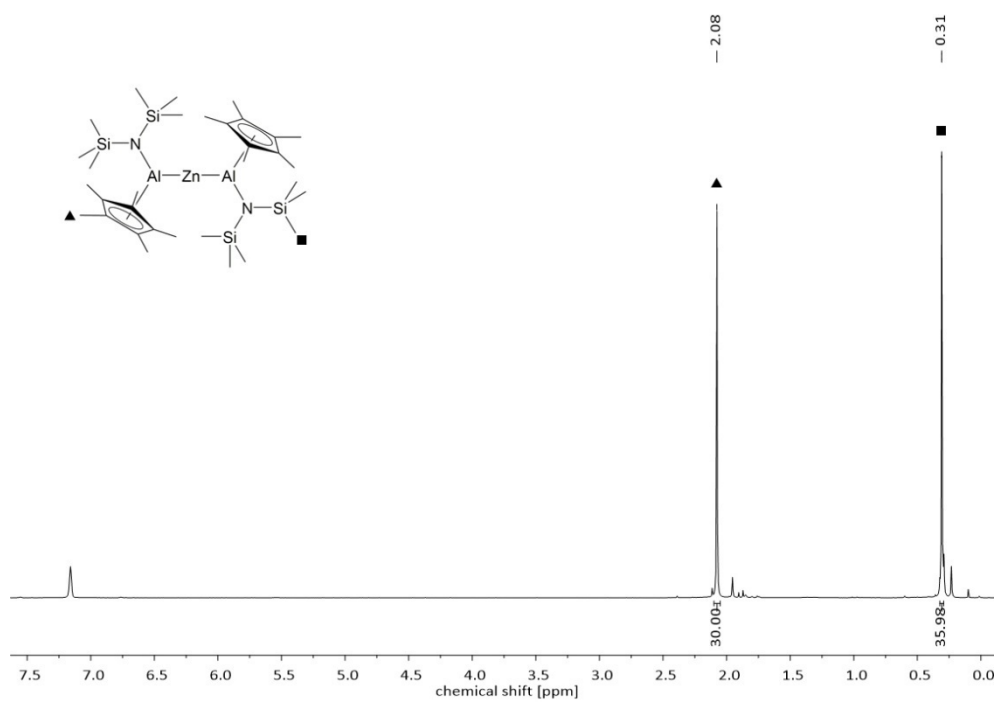
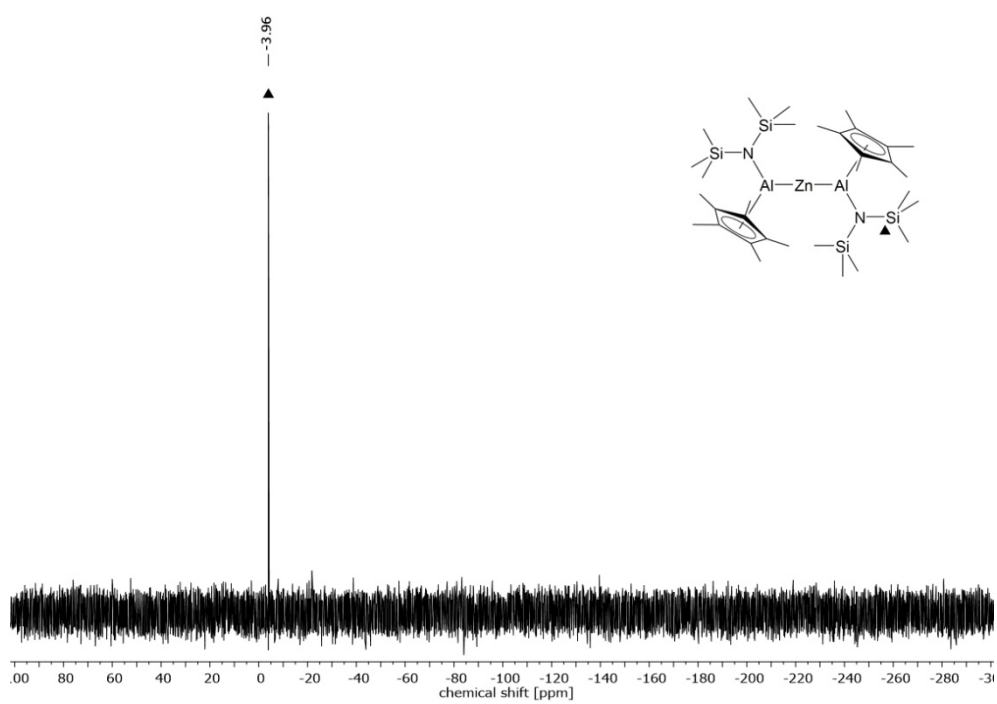


Figure 102. IR spectrum of  $[(\text{GaCp}^*)\text{Co}(\text{btsa})_2]$  (**10**).

Supplementary data for  $[(\text{GaCp}^*)_2\text{Fe}(\text{btsa})_2]$  (**11**)Figure 103.  $^1\text{H}$  NMR spectrum of  $[(\text{GaCp}^*)_2\text{Fe}(\text{btsa})_2]$  (**11**) in  $\text{C}_6\text{D}_6$ .Figure 104.  $^{13}\text{C}$  NMR spectrum of  $[(\text{GaCp}^*)_2\text{Fe}(\text{btsa})_2]$  (**11**) in  $\text{C}_6\text{D}_6$ .

Figure 105. IR spectrum of  $[(\text{GaCp}^*)_2\text{Fe}(\text{btsa})_2]$  (**11**).Figure 106. Temperature-dependent magnetic susceptibility measurements of  $[(\text{GaCp}^*)_2\text{Fe}(\text{btsa})_2]$  (**11**):  $\mu_{\text{eff}}$  vs.  $T$  plot (left) and Curie plot (right) displayed for  $T$  between 50 K and 300 K.

Supplementary data for  $[\text{Zn}(\text{Al}(\eta^2\text{-Cp}^*)(\text{btsa}))_2]$  (**12**)Figure 107.  $^1\text{H}$  NMR spectrum of  $[\text{Zn}(\text{Al}(\eta^2\text{-Cp}^*)(\text{btsa}))_2]$  (**12**).Figure 108.  $^{29}\text{Si}$  NMR spectrum of  $[\text{Zn}(\text{Al}(\eta^2\text{-Cp}^*)(\text{btsa}))_2]$  (**12**).

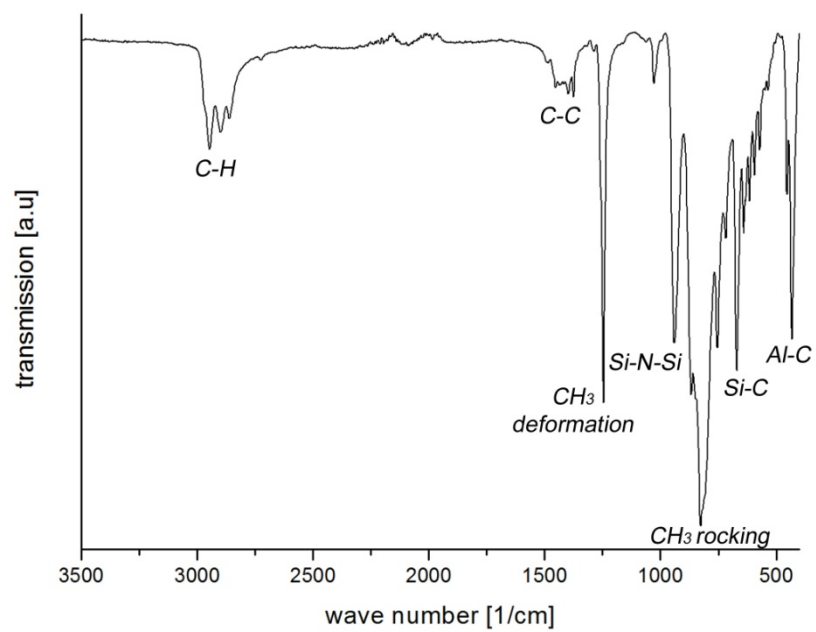


Figure 109. IR spectrum of  $[\text{Zn}(\text{Al}(\eta^2\text{-Cp}^*)(\text{btsa}))_2]$  (**12**).



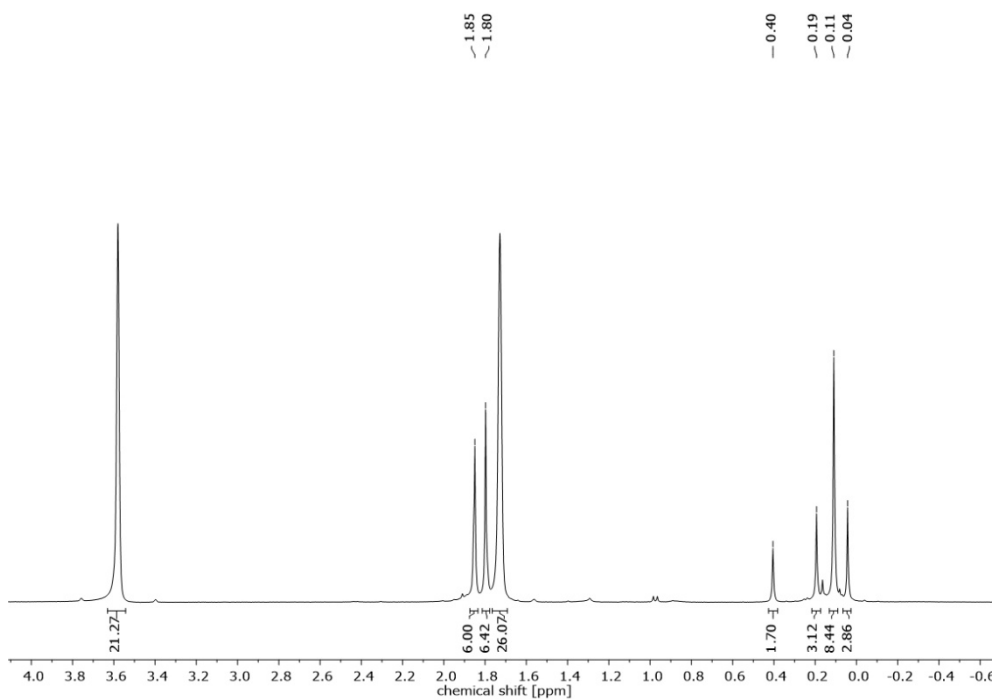
Supplementary data for  $[\text{Co}(\mu\text{-H})_4(\text{Al}(\eta^2\text{-Cp}^*)(\text{btsa}))_2]$  (**13**)

Figure 110.  $^1\text{H}$  NMR spectrum obtained upon dissolution of  $[\text{Co}(\mu\text{-H})_4(\text{Al}(\eta^2\text{-Cp}^*)(\text{btsa}))_2]$  (**13**) in  $\text{THF-}d_8$ , whereat **13** decomposes rapidly under liberation of  $\text{H}_2$  and reproducible formation of a yet unidentified species.

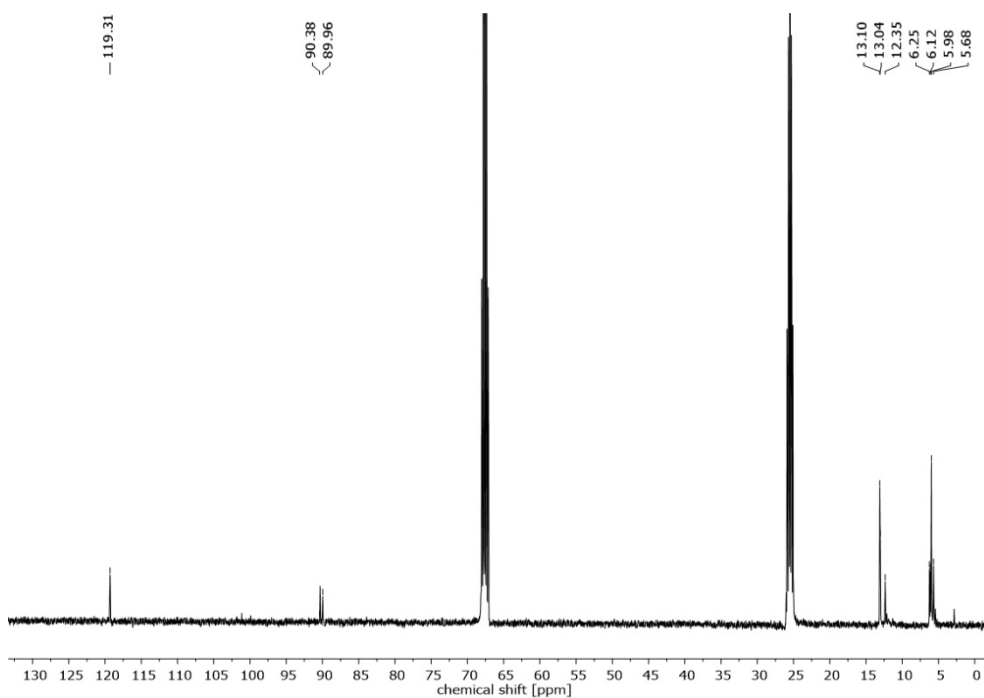


Figure 111.  $^{13}\text{C}$  NMR spectrum obtained upon dissolution of  $[\text{Co}(\mu\text{-H})_4(\text{Al}(\eta^2\text{-Cp}^*)(\text{btsa}))_2]$  (**13**) in  $\text{THF-}d_8$ , whereat **13** decomposes rapidly under liberation of  $\text{H}_2$  and reproducible formation of a yet unidentified species.

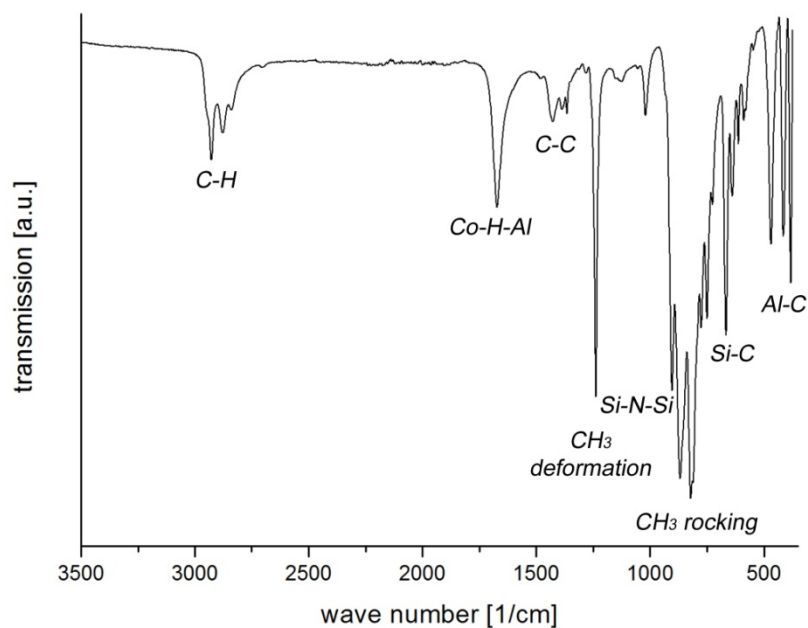


Figure 112. IR spectrum of  $[\text{Co}(\mu\text{-H})_4(\text{Al}(\eta^2\text{-Cp}^*)(\text{btsa}))_2]$  (**13**).

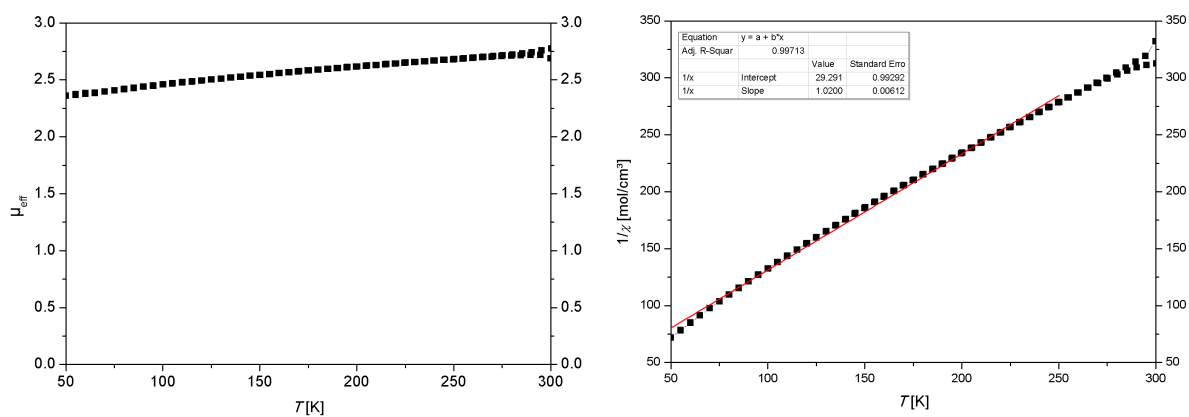
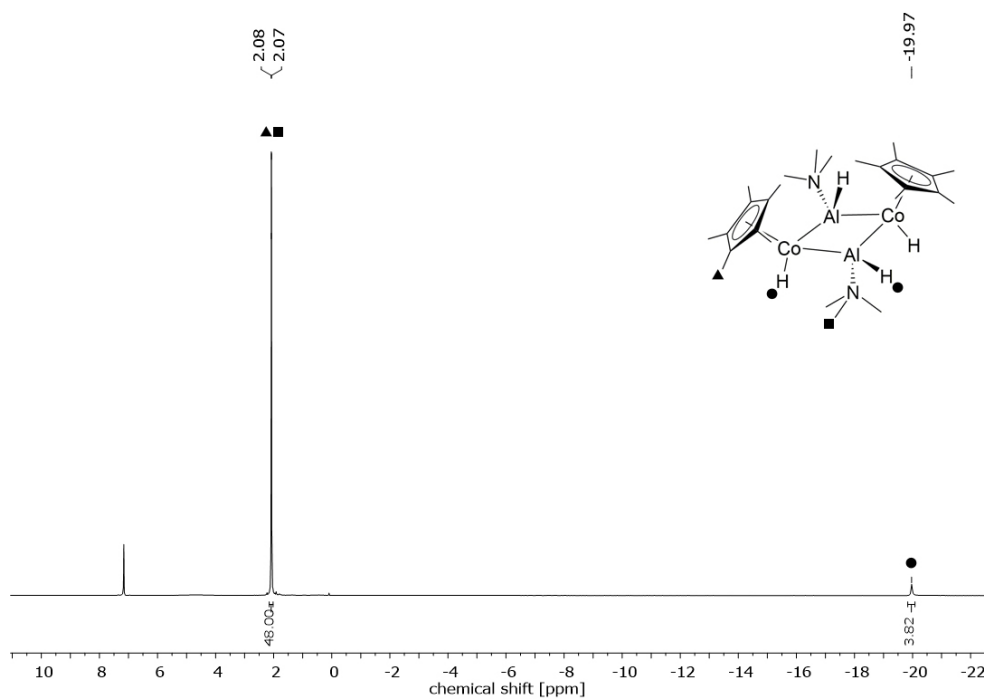
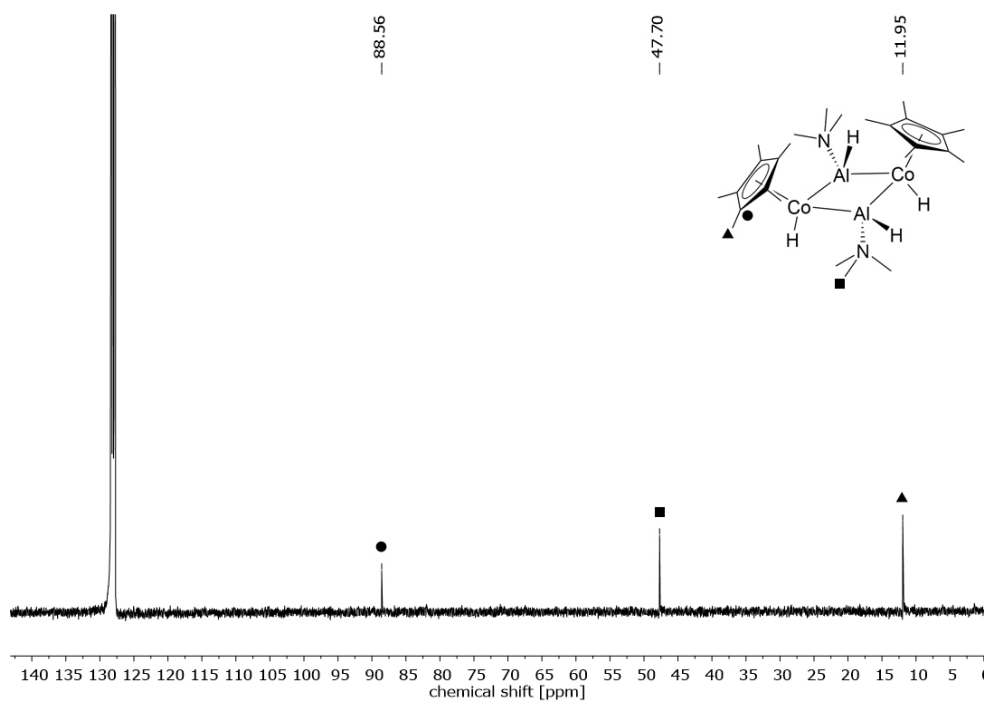


Figure 113. Temperature-dependent magnetic susceptibility measurements of  $[\text{Co}(\mu\text{-H})_4(\text{Al}(\eta^2\text{-Cp}^*)(\text{btsa}))_2]$  (**13**):  $\mu_{\text{eff}}$  vs.  $T$  plot (left) and Curie plot (right) displayed for  $T$  between 50 K and 300 K.

Supplementary data for  $[\text{Cp}^*_2\text{Co}_2(\mu\text{-AlNMe}_3)_2\text{H}_4]$  (**14**)Figure 114.  $^1\text{H}$  NMR spectrum of  $[\text{Cp}^*_2\text{Co}_2(\mu\text{-AlNMe}_3)_2\text{H}_4]$  (**14**) in  $\text{C}_6\text{D}_6$ .Figure 115.  $^{13}\text{C}$  NMR spectrum of  $[\text{Cp}^*_2\text{Co}_2(\mu\text{-AlNMe}_3)_2\text{H}_4]$  (**14**) in  $\text{C}_6\text{D}_6$ .

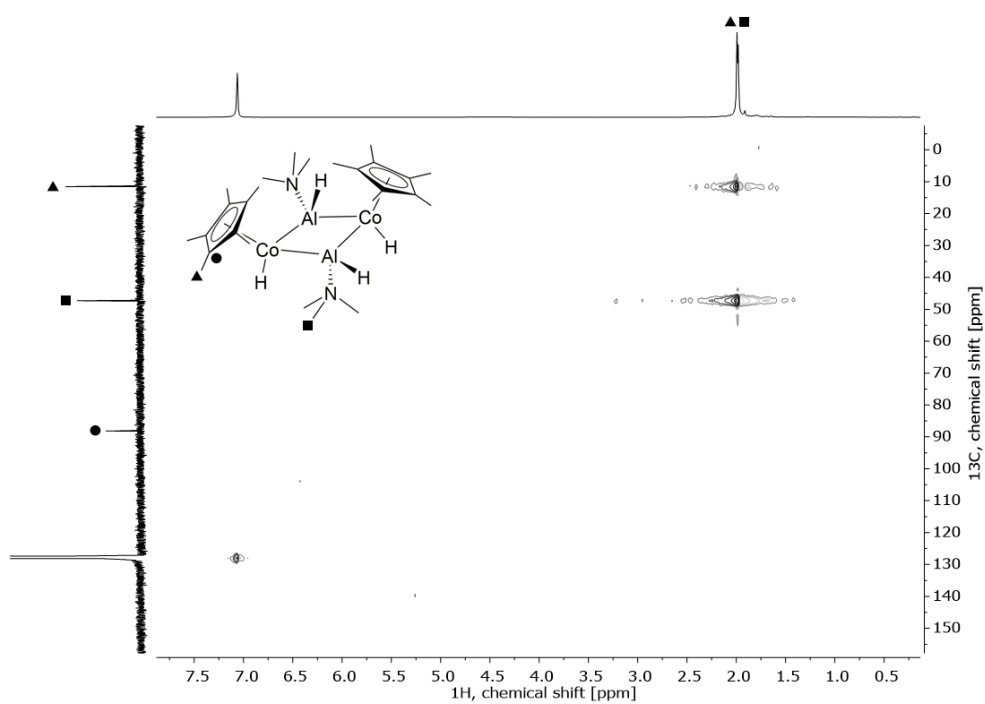


Figure 116. HSQC NMR spectrum of  $[\text{Cp}^*_2\text{Co}_2(\mu\text{-AlNMe}_3)_2\text{H}_4]$  (**14**) in  $\text{C}_6\text{D}_6$ .

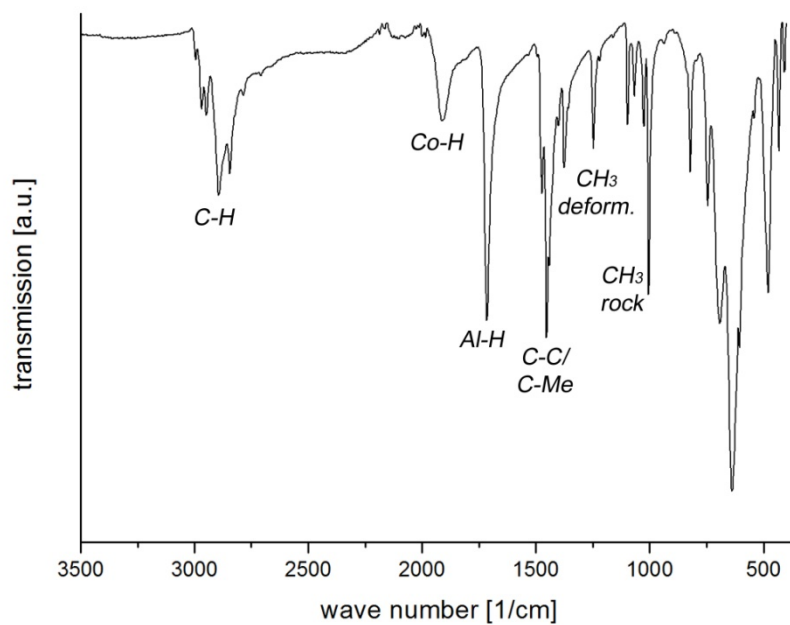


Figure 117. IR spectrum of neat  $[\text{Cp}^*_2\text{Co}_2(\mu\text{-AlNMe}_3)_2\text{H}_4]$  (**14**).

Supplementary data for the reaction of  $[\text{Cp}^*\text{Co}(\mu\text{-H})(\text{Al}(\kappa^2\text{-}(\text{CH}_2\text{SiMe}_2)\text{NSiMe}_3)(\text{btsa}))]$  (9) with  $\text{LiAlH}_4$

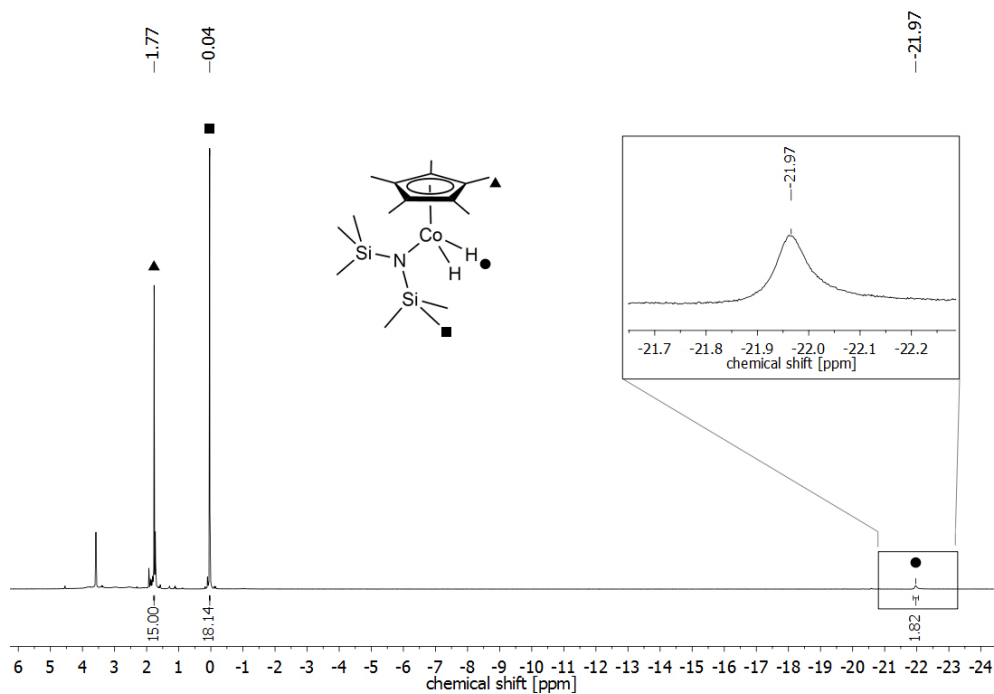


Figure 118.  $^1\text{H}$  NMR spectrum of the anticipated  $[\text{Cp}^*\text{Co}(\text{btsa})\text{H}_x]$  in  $\text{THF-d}_8$ .

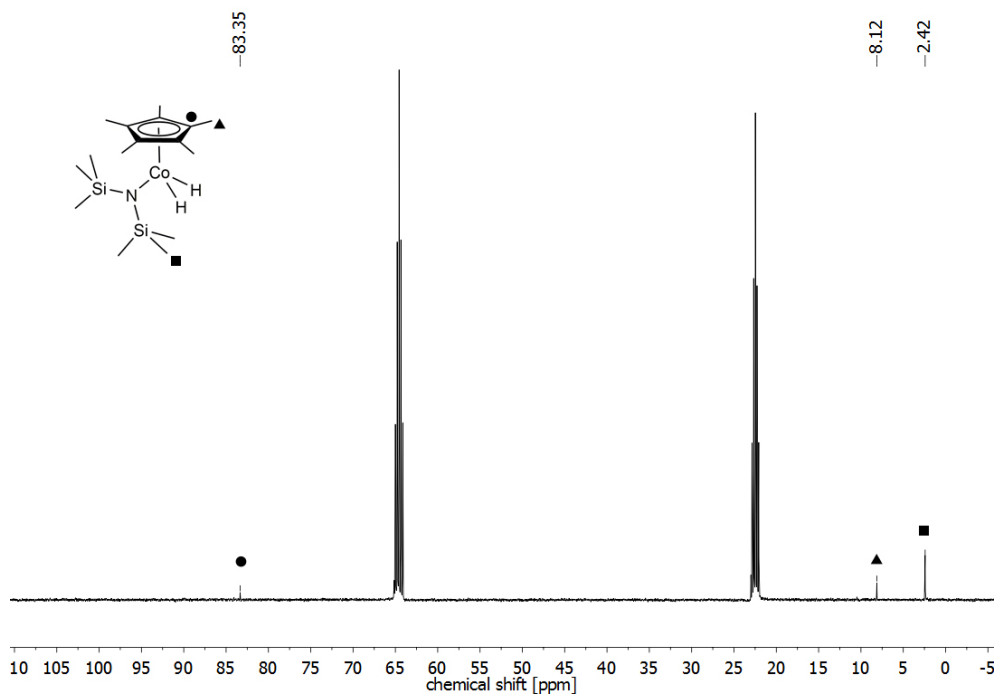


Figure 119.  $^{13}\text{C}$  NMR spectrum of the anticipated  $[\text{Cp}^*\text{Co}(\text{btsa})\text{H}_x]$  in  $\text{THF-d}_8$ .

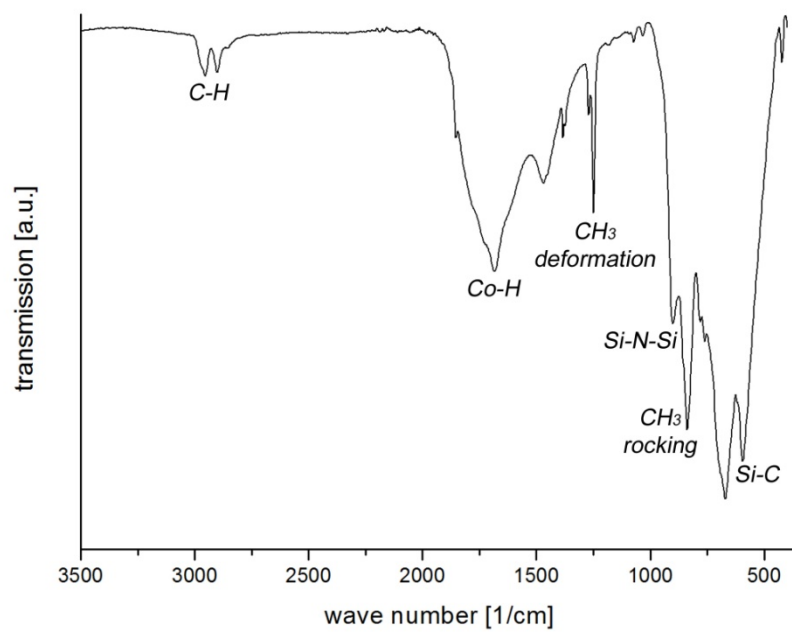


Figure 120. IR spectrum of the anticipated neat  $[\text{Cp}^*\text{Co}(\text{btsa})\text{H}_x]$ .

## References

11. C. Ganesamoorthy, J. Weßing, C. Kroll, R. W. Seidel, C. Gemel, R. A. Fischer, *Angew. Chem. Int. Ed.* **2014**, 53 (30), 7943-7947.
244. P. Jutzi, B. Neumann, G. Reumann, H.-G. Stammer, *Organometallics* **1998**, 17 (7), 1305-1314.
298. E. Y. Tsui, P. Müller, J. P. Sadighi, *Angew. Chem. Int. Ed.* **2008**, 47 (46), 8937-8940.
311. C. Ganesamoorthy, S. Loerke, C. Gemel, P. Jerabek, M. Winter, G. Frenking, R. A. Fischer, *Chem. Commun.* **2013**, 49 (28), 2858-2860.
313. Y. Ohki, Y. Shimizu, R. Araake, M. Tada, W. M. C. Sameera, J.-I. Ito, H. Nishiyama, *Angew. Chem. Int. Ed.* **2016**, 55 (51), 15821-15825.
320. M. Molon, *Unpublished results*. Chair of Inorganic Chemistry II, Ruhr-University Bochum, **2011**.
322. M. E. Smith, R. A. Andersen, *Organometallics* **1996**, 15 (12), 2680-2682.
376. H. Bürger, W. Sawodny, U. Wannagat, *J. Organomet. Chem.* **1965**, 3 (2), 113-120.
405. Agilent Technologies UK Ltd, *CrysAlisPro Software system*, version 1.171.35.19; Oxford, UK, **2011**.
406. Bruker AXS Inc., *APEX suite of crystallographic software, APEX 3 Version 2015-5.2*, Madison, Wisconsin, USA, **2015**.
407. Bruker AXS Inc., *SAINT, Version 8.34A and SADABS, Version 2014/5*, Madison, Wisconsin, USA, **2014**.
408. G. Sheldrick, *Acta Crystallogr., Sect. A* **2008**, 64 (1), 112-122.
409. C. B. Hubschle, G. M. Sheldrick, B. Dittrich, *J. Appl. Crystallogr.* **2011**, 44 (6), 1281-1284.
410. G. Sheldrick, *Acta Crystallogr., Sect. C* **2015**, 71 (1), 3-8.
411. P. van der Sluis, A. L. Spek, *Acta Crystallogr., Sect. A* **1990**, 46 (3), 194-201.
412. A. Spek, *J. Appl. Crystallogr.* **2003**, 36 (1), 7-13.
413. A. Spek, *Acta Crystallogr., Sect. D* **2009**, 65 (2), 148-155.
414. P. Chiu, Z. Li, K. C. M. Fung, *Tetrahedron Lett.* **2003**, 44 (3), 455-457.
415. R. A. Andersen, K. Faegri, J. C. Green, A. Haaland, M. F. Lappert, W. P. Leung, K. Rypdal, *Inorg. Chem.* **1988**, 27 (10), 1782-1786.
416. H. Bürger, U. Wannagat, *Monatsh. Chem.* **1963**, 94 (6), 1007-1012.
417. E. M. Meyer, S. Gambarotta, C. Floriani, A. Chiesi-Villa, C. Guastini, *Organometallics* **1989**, 8 (4), 1067-1079.
418. B. Bogdanović, M. Kröner, G. Wilke, *Liebigs Ann. Chem.* **1966**, 699 (1), 1-23.
419. J. K. Ruff, M. F. Hawthorne, *J. Am. Chem. Soc.* **1960**, 82 (9), 2141-2144.
420. C. Fonseca Guerra, J. G. Snijders, G. te Velde, E. J. Baerends, *Theor. Chem. Acc.* **1998**, 99 (6), 391-403.
421. G. te Velde, F. M. Bickelhaupt, E. J. Baerends, C. Fonseca Guerra, S. J. A. van Gisbergen, J. G. Snijders, T. Ziegler, *J. Comput. Chem.* **2001**, 22 (9), 931-967.
422. SCM, *ADF2017*, Theoretical Chemistry, Vrije Universiteit, Amsterdam, The Netherlands.
423. A. D. Becke, *J. Chem. Phys.* **1986**, 84 (8), 4524-4529.
424. A. D. Becke, *Phys. Rev. A* **1988**, 38 (6), 3098-3100.
425. J. P. Perdew, *Phys. Rev. B* **1986**, 33 (12), 8822-8824.
426. J. P. Perdew, *Phys. Rev. B* **1986**, 34 (10), 7406-7406.
427. L. Versluis, T. Ziegler, *J. Chem. Phys.* **1988**, 88 (1), 322-328.
428. F. Neese, *Wiley Interdiscip. Rev. Comput. Mol. Sci.* **2012**, 2 (1), 73-78.
429. S. Grimme, J. Antony, S. Ehrlich, H. Krieg, *J. Chem. Phys.* **2010**, 132 (15), 154104.
430. S. Grimme, S. Ehrlich, L. Goerigk, *J. Comput. Chem.* **2011**, 32 (7), 1456-1465.
431. F. Weigend, R. Ahlrichs, *PCCP* **2005**, 7 (18), 3297-3305.

432. F. Neese, F. Wennmohs, A. Hansen, U. Becker, *Chem. Phys.* **2009**, 356 (1), 98-109.



## 7 APPENDIX

## Active participation in scientific conferences

**J. Weßing**, C. Gemel, R. A. Fischer (**oral presentation**), *"On the way towards Hume-Rothery phase-inspired intermetalloid clusters: synthetic principles and precursor design"*, 27<sup>th</sup> International Conference on Organometallic Chemistry, Melbourne, Australia, 17<sup>th</sup>-22<sup>nd</sup> July **2016**.

**J. Weßing**, C. Ganesamoorthy, C. Gemel, R. A. Fischer (**oral presentation**), *"Intermetalloid transition metal/group 13 clusters – A novel approach on molecular congeners of Hume-Rothery Phases"*, 250<sup>th</sup> ACS National Meeting, Boston, USA, 16<sup>th</sup>-20<sup>th</sup> August **2015**.

**J. Weßing**, C. Gemel, R. A. Fischer (**oral presentation**), *"Organo(inter)metallics - Precursor development for bimetallic nanoparticle synthesis in ionic liquids"*, SPP 1708 Workshop - "Synthetic methods", Rostock, Germany, 18<sup>th</sup>-20<sup>th</sup> February **2015**.

**J. Weßing**, C. Ganesamoorthy, C. Gemel, R. A. Fischer (**poster presentation**), *"Hume-Rothery phase-inspired molecular chemistry – Synthesis of intermetalloid transition metal/group 13 clusters"*, 14<sup>th</sup> International Symposium on Inorganic Ring Systems, Regensburg, Germany, 26<sup>th</sup>-31<sup>st</sup> July **2015**.

**J. Weßing**, C. Ganesamoorthy, C. Gemel, R. A. Fischer (**poster presentation**), *"Intermetalloid Cu/Al clusters - Molecular Models of Hume-Rothery Nanophases"*, Dalton Division Poster Symposium, London, UK, 31<sup>st</sup> March **2015**.

## Publications in scientific journals

### Thesis-relevant publications:

**J. Weßing**, C. Göbel, B. Weber, C. Gemel, R. A. Fischer, "*Diverse Reactivity of ECp\* (E = Al, Ga) toward Low-Coordinate Transition Metal Amides [TM(N(SiMe<sub>3</sub>)<sub>2</sub>)<sub>2</sub>] (TM = Fe, Co, Zn): Insertion, Cp\* Transfer, and Orthometalation*", *Inorg. Chem.* **2017**, 56, 3517.

C. Ganesamoorthy, **J. Weßing**, C. Kroll, R. W. Seidel, C. Gemel, R. A. Fischer, "*The Intermetalloid Cluster [(Cp\*AlCu)<sub>6</sub>H<sub>4</sub>], Embedding a Cu<sub>6</sub> Core Inside an Octahedral Al<sub>6</sub> Shell: Molecular Models of Hume–Rothery Nanophases*", *Angew. Chem. Int. Ed.* **2014**, 53, 7943.

### Contributions in other scientific projects:

J. Hornung, **J. Weßing**, M. Molon, K. Dilchert, C. Gemel, R. A. Fischer, "*Chemistry of Hume-Rothery Inspired Organometallics: Selective Functionalization of [M(ZnCp\*)<sub>4</sub>(ZnCH<sub>3</sub>)<sub>4</sub>] (M = Ni, Pd, Pt) with Terminal Alkynes to yield [M(ZnCp\*)<sub>4</sub>(ZnCCSi<sup>*i*</sup>Pr)<sub>4</sub>]*", *J. Organomet. Chem.* **2018**, 860, 78.

S. B. Kalidindi, C. Wiktor, A. Ramakrishnan, **J. Weßing**, A. Schneemann, G. Van Tendeloo, R. A. Fischer, "*Lewis base mediated efficient synthesis and solvation-like host–guest chemistry of covalent organic framework-1*", *Chem. Commun.* **2013**, 49, 463.

*Note:* Following-up on this dissertation, first author manuscripts based on chapters 4.2 and 4.5 of this dissertation are currently under preparation.

## Curriculum vitae

## ■ PERSONAL DETAILS

---

Name Jana Weßing  
 Date, place of birth 26<sup>th</sup> June 1990, Essen  
 Nationality German  
 Contact Schlesierstraße 19  
 81669 München  
 jana.wessing@tum.de  
 +49 1522 1569535



## ■ ACADEMIC BACKGROUND

---

01/2014 - today **Doctoral Studies in Chemistry**  
 Under supervision of Prof. Dr. Roland A. Fischer  
 Technical University of Munich, Germany (04/2016 - today)  
 and Ruhr-University Bochum, Germany (01/2014 - 03/2016)  
 Dissertation topic: *"From Intermetallics to Intermetalloid Clusters  
 Molecular Alloying of Aluminum and Gallium with Transition Metals"*

10/2011 - 09/2013 **Master's Program (Chemistry)**  
 Ruhr-University Bochum, Germany  
 Focus: Inorganic Chemistry  
 Degree: Master of Science, overall grade 1.0

10/2008 - 09/2011 **Bachelor's Program (Chemistry)**  
 Ruhr-University Bochum, Germany  
 Degree: Bachelor of Science, overall grade 1.2

08/2000 - 07/2008 **Gymnasium Borbeck, Essen, Germany**  
 Degree: University Entrance Qualification, grade 1.0

## ■ PRACTICAL EXPERIENCE

---

01/2014 - today **Scientific Staff / PhD candidate**  
 Chair of Inorganic and Metal-Organic Chemistry  
 Technical University of Munich (04/2016 - today)  
 and Chair of Inorganic Chemistry II  
 Ruhr-University Bochum (01/2014 - 03/2016)

*Tasks: Interdisciplinary scientific cooperations, planning and development of research projects, instrumental analytics of inorganic coordination compounds, maintenance of technical equipment, supervision of students in various practical courses*

- 10/2012 - 12/2013      **Research Assistant**  
Ruhr-University Bochum  
*Tasks: Synthesis of organometallic compounds, Supervision of university practical courses*
- 04/2010 - 03/2011      **Student Assistant**  
Ruhr-University Bochum  
*Tasks: Supervision of university practical courses*

## ■ SCHOLARSHIPS AND AWARDS

---

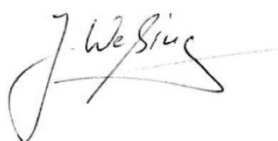
- 06/2016      **Scholarship for scientific conference participation**  
provided by the "Gesellschaft Deutscher Chemiker" (GDCh)
- 07/2014 - 06/2016      **Chemiefonds Scholarship**  
provided by the Chemical Industry Fonds (FCI)
- 10/2013      **GDCh prize**  
for the best MSc graduate in chemistry at the  
Ruhr-University Bochum  
provided by the "Gesellschaft Deutscher Chemiker" (GDCh)
- 10/2010 - 09/2012      **Deutschlandstipendium**  
sponsored by Sensolytics GmbH and the "Verein zur Förderung der  
Chemie und Biochemie an der Ruhr-Universität Bochum" (VFCh)
- 10/2009 - 09/2010      **Hermann-Specker Fellowship**  
sponsored by the "Verein zur Förderung der Chemie und Biochemie  
an der Ruhr-Universität Bochum" (VFCh)
- 06/2008      **GDCh prize**  
for the best graduate in chemistry at the Gymnasium Borbeck, Essen,  
Germany

## ■ MISCELLANEOUS

---

- Languages      German (mother tongue)  
English (proficient)  
French (basic)
- Hobbies      Sports (hiking, swimming), travelling, reading, sewing

Munich, 26<sup>th</sup> February, 2018



*“The only thing you really get to figure out after a lifetime of study is that there's more stuff to figure out. Frustrating and enlightening at the same time.”*

— Jasper Fforde